UNIVERSITY OF SOUTHAMPTON

FACULTY OF ENGINEERING, SCIENCE AND MATHEMATICS

SCHOOL OF CHEMISTRY

Atomistic Simulations of Semiconductor and Metallic Nanoparticles

by

Nicholas Zonias

Thesis for the degree of Doctor of Philosophy

July 2011

UNIVERSITY OF SOUTHAMPTON
FACULTY OF ENGINEERING, SCIENCE & MATHEMATICS
SCHOOL OF CHEMISTRY

Doctor of Philosophy

ATOMISTIC SIMULATIONS OF SEMICONDUCTOR AND METALLIC NANOPARTICLES

by Nicholas A. Zonias

Abstract

Semiconductor and metallic nanoparticles have recently become an attractive area of intensive research due to their unique and diverse properties, that differ significantly from bulk materials. With a wide range of applications and potential uses in nanoelectronics, catalysis, medicine, chemistry or physics an important amount of experimental and theoretical investigations aim to facilitate deeper understating in their physical and chemical behaviour.

Within this context, this thesis is focused on the theoretical investigation of silicon, gold and platinum nanoclusters and nanoalloys, in order to provide support for experimental data obtained from collaborating researchers and scientists. Modelled structures of the above nanoparticles were constructed and studied by using a variety of computational tools such as, classical force field MD (DL_POLY [1]), tight-binding DFT (DFTB+ [2]), conventional DFT (CASTEP [3]) and linear-scaling DFT (ONETEP [4]).

A brief introduction regarding some basic principles of quantum mechanics (QM) and of solid state physics is presented in the first chapter; followed by a general

chapter about the classical molecular dynamics (MD) method and its utilisation within the DL_POLY code [1]. The last part of the second chapter is devoted to the introduction, validation and implementation of a non-default force field in the source code of DL_POLY. The third chapter contains a brief description of some important theorems and terms used in density functional theory (DFT), with some basic information about linear-scaling DFT, as developed in the ONETEP code [4], and tight-binding DFT, reported in the last sections.

Chapter 4, includes the results of a series of DFT calculations performed on silicon nanorods, with diameters varying from 0.8 nm to 1.3 nm and about 5.0 nm long. While up to now, similar computational works were conducted on periodic nanowires, in our case, the calculations were performed on the entire nanorods without imposing any symmetry. The fifth chapter proposes a new methodology for calculating extended x-ray absorption fine structure (EXAFS) spectra from modelled geometries of gold nanoparticles by exploiting some of the capabilities of the FEFF code [5]. From several snap-shots of a classical MD simulation, a probability distribution function is calculated for sampling the photoabsorbing and the scattering atoms of the simulated system. The results are then compared with experimental EXAFS data showing a good agreement between the predicted and the measured structures.

Finally, in the last two chapters, classical MD simulations on gold and platinum nanoparticles and nanoalloys are reported, which have been performed to support the structural characterisation and analysis of synthesised gold and platinum nanoparticles. Within this framework, DFT calculations have also been attempted on ultrasmall gold nanoparticles and on gold nanosurfaces with one or two thiols attached to them, as a preliminary stage towards the application of linear-scaling DFT in simulating the properties of large metallic systems, currently being studied with semi-empirical quantum approaches or empirical force fields.

Contents

List of Figures

List of Tables

Declaration of authorship

I, **Nicholas Zonias**, declare that this thesis entitled, "Atomistic Simulations of Semiconductor and Metallic Nanoparticles" and the work presented in it are both my own, and have been generated by me as a result of my own original research. I confirm that:

- This work was done wholly or mainly while in candidature for a research degree at this University;
- Where any part of this thesis has previously been submitted for a degree or any other qualification at this University or any other institution, this has been clearly stated;
- Where I have consulted the published work of others, this is always clearly attributed;
- Where I have quoted from the work of others, the source is always given. With the exception of such quotations, this thesis is entirely my own work;
- I have acknowledged all main sources of help;
- Where the thesis is based on work done by myself jointly with others, I have made clear exactly what was done by others and what I have contributed myself;
- Parts of this work have been published as papers [21], [22].

Signed: _____

Date: _____

Acknowledgements

First and foremost, I offer my sincerest gratitude to my supervisor, Dr. Chris-Kriton Skylaris, for giving me this opportunity and more importantly, for his support, encouragement and inspiration throughout my PhD. I attribute this degree to his valuable knowledge, technical skills and effort that without, this thesis too, would not have been completed.

All the work carried out on the gold and platinum nanoparticles, has been initiated and extended by the innovative ideas of Dr Stephen W. Price, who has kindly provided me with all the necessary experimental information and input data for the first series of classical MD simulations performed on these systems. Our stimulating collaboration, exchange of ideas and mutual support during this work had a major impact to the successful completion of this project.

Needless to mention the significant contribution, at this point, of Dr Otello M. Roscioni, who deserves all the credits for the work done with the MDXAS code. His scientific approach and programming skills have given a whole new dimension to this project, by creating a better link, through an alternative path, between the theoretical and experimental EXAFS data. Many thanks also for the very useful programming tips and tricks. Special thanks to Prof. Andrea E. Russell, Dr Syma Khalid and Prof. Pavlos Lagoudakis too, for their valuable feedback regarding this work.

My humble gratitude, goes to Dr Quintin Hill, for his generous help and support, and all the time spent dealing with every annoying bug of the software used and all the technical issues of the hardware, mainly during my first and second year. A

pleasant surprise has marked the end of this era when Quintin and his beloved Tamsin were joined together in the sacred vows of matrimony. May their love be everlasting throughout their lifetimes.

The entirety of my thesis would not have been possible without the financial support provided by the Southampton Nanoforum, during the first three years of my postgraduate studies. Equally important was the technical support and expertise of the iSolutions staff at Southampton University, who maintain our computer clusters and take care of our personal workstations, where much of the computational work in this thesis has been conducted. The efficiency and capacity of the new Iridis3 supercomputer system has been of a great value for our computationally demanding calculations. Investment in such technologies, by our University, has been an enormous benefit for the research performed within this group.

In my daily work, I have been blessed with a friendly and cheerful group of fellow colleagues, Alvaro, Stephen, Jacek and Chris, who made our office a pleasant environment to work into. Particular thanks to my house-mates at "7 Kenilworth Road", Grant, Juan, George, Sonya and Sam, for all the fun and enjoyable moments spent together. They have definitely made life outside the office really amusing and memorable.

Last but not least, my special thanks and gratitude belongs to all the good friends made, throughout the four years living in Southampton: Stefanos and Ally, Eirini, Dimitris, Patrick, Yannis, Tonia, Maria and many more. Their genuine support and friendship has been a true blessing for me. They will always be part of my heart and soul.

Most of all, this thesis is attributed to my beloved parents, whose psychological and financial support was considerably worthwhile, in overcoming every difficulty throughout this journey and building up my self-confidence.

Πάντα στον νου να έχεις την Ιθάκη.
Το φθάσιμον εκεί ειν΄ ο προορισμός σου.
Αλλά μη βιάζεις το ταξείδι διόλου.
Καλλίτερα χρόνια πολλά να διαρκέσει
και γέρος πια ν΄ αράξεις στο νησί,
πλούσιος με όσα κέρδισες στο δρόμο,
μη προσδοκώντας πλούτη να σε δώσει η Ιθάκη.
Η Ιθάκη σ΄ έδωσε τ΄ ωραίο ταξείδι.
Χωρίς αυτήν δεν θά βγαινες στον δρόμο.
Άλλα δεν έχει να σε δώσει πια.
Κι αν πτωχική την βρεις, η Ιθάκη δε σε γέλασε.
Έτσι σοφός που έγινες, με τόση πείρα,
ήδη το κατάλαβες οι Ιθάκες τι σημαίνουν.

Κωνσταντίνος Π. Καβάφης
("Ποιήματα 1897-1933", Ίκαρος 1984)

Στους γονείς μου, με ιδιαίτερη αγαπη.

Chapter 1

Introduction

The principles of the microscopic world that describe the behaviour of particles such as electrons, protons, neutrons, atoms, and molecules can be only explained, up to the present time, by the Quantum Theory or Quantum Mechanics (QM). At this regime, classical theory using Newtonian mechanics fails to treat microscopic elements either as waves or particles of inherent mass, as in the macroscopic world. This failure can be interpreted by Heisenberg's uncertainty principle:

$$\Delta x \Delta p_x \geqslant \frac{\hbar}{2} \tag{1.0.1}$$

which states that the more precisely the position of a particle x is measured the less precise is its momentum p_x. Δ defines the uncertainty of each quantity and $\hbar = \frac{h}{2\pi}$, h is Planck's constant. In QM, the energy is a quantised property, a phenomenon which can be observed when conducting electronic excitation experiments using electromagnetic waves. From quantum theory we obtain the fundamental laws of chemistry as well as explanations for the properties of materials, such as crystals, semiconductors, superconductors, and superfluids. These materials find a plethora of applications in modern science and technology, while biological structures and

mechanisms can be also studied using QM, for understanding and clarifying their role in several life processes.

A radical idea developed by de Broglie at the beginning of the 20^{th} century, introduced the dual nature of particles and waves:

$$\lambda = \frac{h}{p} \Longleftrightarrow p = \frac{h}{\lambda} \tag{1.0.2}$$

where all material particles having a momentum p can also exhibit wave-like properties described by a wave-length λ while, conversely, electromagnetic radiation can also have particle-like properties. The de Broglie hypothesis motivated the discovery of the Schrödinger equation later on (section 1.0.1), a fundamental principle which underpins all of chemistry and a significant part of physics.

Rolling back in time, to the basic fundamentals of wave theory, a sinusoidal wave ψ with position x at time t is described as:

$$\psi(x) = A \sin 2\pi \left(\nu t - \frac{x}{\lambda}\right) \tag{1.0.3}$$

where A is the amplitude of the wave, ν is the frequency of the wave and λ the distance between successive maxima (wavelength).

According to classical mechanics, the energy of a system of particles E is divided into kinetic energy T and potential energy V:

$$E = T + V = \sum_i \frac{m_i u_i^2}{2} + \sum_i V_i = \sum_i \frac{p_i^2}{2m_i} + \sum_i V_i \tag{1.0.4}$$

where m_i is the mass of the particle, u_i its velocity and p_i its momentum.

1.0.1 Schrödinger equation

The laws of QM that are used to explain the wave-like properties of microscopic particles, induce a significant change in the way mathematics, in this case, are solved. In classical mechanics, any variable used, can be directly correlated to a physically measurable property (observables) such as the force F, the momentum p, and the position $\mathbf{r} = \mathbf{r}(x, y, z)$. In QM though, these variables are not directly linked to an observable, but are represented by "operators", which only provide the value of a physical property when they act on a fundamental state function of QM, called the "wavefunction". Each operator contains a specific mathematical operation which can be applied on a wavefunction Ψ. While most variables, such as x, y, z positions are directly represented in QM with the $\hat{x}, \hat{y}, \hat{z}$ operators, momentum operators $\hat{p}$ in the Cartesian space, are defined as $\hat{p}_s = -\imath\hbar\frac{\partial}{\partial s},\ s = x, y, z$

Linear operators satisfy the following conditions:

$$\hat{A}[f(\mathbf{r}) + g(\mathbf{r})] = \hat{A}f(\mathbf{r}) + \hat{A}g(\mathbf{r}) \tag{1.0.5}$$

$$\hat{A}[cf(\mathbf{r})] = c\hat{A}f(\mathbf{r}) \tag{1.0.6}$$

where $\hat{A}$ is an arbitrary operator. $f(\mathbf{r})$, $g(\mathbf{r})$ are arbitrary functions and c defines a constant. Hermitian operators require the expectation value of an observable to be a real number:

$$\int \Psi_i^* \hat{A}\Psi_j d\mathbf{r} = \int \Psi_j (\hat{A}\Psi_i)^* d\mathbf{r} \Longleftrightarrow \langle \Psi_i | \hat{A}\Psi_j \rangle = \langle \hat{A}\Psi_i | \Psi_j \rangle \tag{1.0.7}$$

for all well-behaved Ψ_i and Ψ_j. The function Ψ, in this case, is called "eigenfunction" of the operator $\hat{A}$, and the values obtained when $\hat{A}$ acts on it, are the "eigenvalues" of that operator.

The wavefunction Ψ of a quantum system is a function that contains all the information governing the de Broglie wave-like behaviour of its particles. Each particle, can be described by a set of variables defining its position $\mathbf{r}$, spin s and time t. The probability density function of a particle is given by $|\Psi(\mathbf{r}, s; t)|^2$ and provides the possibility of finding the particle in a volume of space $d\mathbf{r}$ at position $\mathbf{r}$ and time t having a spin s. The probability density integrated over all space is equal to one $|\Psi|^2 = 1$ [23].

When the kinetic T and potential V energy terms, of equation 1.0.4, are written in a quantum mechanical form, they represent the kinetic and potential energy operators $\hat{T}$ and $\hat{V}$. The operator $\hat{H}$ is called Hamiltonian operator and provides the energy of a quantum system E, defined by the wavefunction Ψ:

$$\hat{H} = \hat{T} + \hat{V} \tag{1.0.8}$$

The time-dependent Schrödinger equation [24] is given by:

$$\imath\hbar\frac{\partial\Psi(\mathbf{r};t)}{\partial t} = \hat{H}\Psi(\mathbf{r};t) = \left[\hat{T} + \hat{V}(\mathbf{r};t)\right]\Psi(\mathbf{r};t) \tag{1.0.9}$$

$$\Rightarrow \imath\hbar\frac{\partial\Psi(\mathbf{r};t)}{\partial t} = \left(-\frac{\hbar^2}{2m}\hat{\nabla}^2 + \hat{V}(\mathbf{r};t)\right)\Psi(\mathbf{r};t) \tag{1.0.10}$$

where $\hat{\nabla}^2 = \frac{\partial^2}{\partial x^2} + \frac{\partial^2}{\partial y^2} + \frac{\partial^2}{\partial y^2}$ and m is the mass of the particle.

1.0.1.1 Time-independent Schrödinger equation

The time-dependent form of equation 1.0.9 can be simplified when the potential $\hat{V}(\mathbf{r};t)$ is time-independent. In this case, the potential can be replaced by a time-independent function $v(\mathbf{r})$ while the wavefunction of a single particle $\Psi(\mathbf{r};t)$ can be

separated into a function of time $f(t)$ and a function of spatial coordinates $\psi(\mathbf{r})$:

$$\Psi(\mathbf{r};t) = f(t)\psi(\mathbf{r}) \quad \text{while} \quad \hat{V}(\mathbf{r};t) = \hat{v}(\mathbf{r}) \tag{1.0.11}$$

Thus, equation 1.0.10 becomes:

$$\imath\hbar\frac{df(t)}{dt}\psi(\mathbf{r}) = -\frac{\hbar^2}{2m}f(t)\hat{\nabla}^2\psi(\mathbf{r}) + \hat{v}(\mathbf{r})f(t)\psi(\mathbf{r};t) \tag{1.0.12}$$

which is equal to:

$$\imath\hbar\frac{1}{f(t)}\frac{df(t)}{dt} = -\frac{\hbar^2}{2m}\frac{1}{\psi(\mathbf{r})}\hat{\nabla}^2\psi(\mathbf{r}) + \hat{v}(\mathbf{r}) \tag{1.0.13}$$

when divided by $\Psi(\mathbf{r};t)$.

Looking at the expression of equation 1.0.13, it can be seen that the left part is only dependent on time while the right part depends only on $\mathbf{r}$, thus, both sides are constant. Equating the left part to a constant E, one obtains:

$$\imath\hbar\frac{1}{f(t)}\frac{df(t)}{dt} = E \tag{1.0.14}$$

$$\implies \frac{df(t)}{f(t)} = -\frac{\imath E}{\hbar}dt \tag{1.0.15}$$

$$\implies \ln f(t) = -\frac{\imath Et}{\hbar} + C \tag{1.0.16}$$

$$\overset{by\ integrating}{\implies} f(t) = e^C e^{-\frac{\imath Et}{\hbar}} = Be^{-\frac{\imath Et}{\hbar}} \tag{1.0.17}$$

where B and C are arbitrary constants.

Repeating the same procedure for the right part of equation 1.0.13:

$$-\frac{\hbar^2}{2m}\frac{1}{\psi(\mathbf{r})}\hat{\nabla}^2\psi(\mathbf{r}) + \hat{v}(\mathbf{r}) = E \tag{1.0.18}$$

$$\implies -\frac{\hbar^2}{2m}\hat{\nabla}^2\psi(\mathbf{r}) + \hat{V}(\mathbf{r})\psi(\mathbf{r}) = E\psi(\mathbf{r}) \tag{1.0.19}$$

$$\iff \hat{H}\psi(\mathbf{r}) = E\psi(\mathbf{r}) \tag{1.0.20}$$

the expression for the time-independent Schrödinger equation is obtained. Equation 1.0.20 shows that the Hamiltonian operator is also a Hermitian operator, with E representing the energy eigenvalues and $\psi(\mathbf{r})$ the eigenfunction. Considering equation 1.0.17, these eigenstates are equal to $f(t) = e^{-\frac{\imath E t}{\hbar}}$ and therefore, the expression for the time-dependent wavefunction for different eigenstates becomes:

$$\Psi_n(\mathbf{r};t) = e^{-\frac{\imath E_n t}{\hbar}}\psi_n(\mathbf{r}), \quad n = 0, 1, 2, ... \tag{1.0.21}$$

In practice, the Schrödinger equation is considered as a substantial assumption of quantum theory that needs to be justified. It cannot be proved, but its solutions can justify de Broglie's principle. For the case of a free particle in one dimension (no forces acting on it), the Schrödinger equation takes the following form:

$$-\frac{\hbar^2}{2m}\frac{\partial^2\psi}{\partial\mathbf{r}^2} - E\psi = 0 \tag{1.0.22}$$

where E represents in this case a positive constant which is equal to the kinetic energy of the particle.

1.0.1.2 Molecular Schrödinger equation

For a molecular system consisting of atomic nuclei N, and electrons e, the Schrödinger equation which describes the interactions and energy states between all the particles involved is given by:

$$\hat{H}\psi = \left(\hat{T}_e + \hat{T}_N + \hat{V}_{ee} + \hat{V}_{Ne} + \hat{V}_{NN}\right)\psi \tag{1.0.23}$$

$$= \left[-\sum_{i=1}^{n}\frac{\hbar^2}{2m_i}\hat{\nabla}^2_{\mathbf{r}} - \sum_{I=1}^{N}\frac{\hbar^2}{2M_I}\hat{\nabla}^2_{\mathbf{R}} + \frac{1}{2}\sum_{i=1}^{n}\sum_{j\neq i}^{n}\frac{e^2}{4\pi\epsilon_0\mathbf{r}_{ij}} - \sum_{i}^{n}\sum_{I=1}^{N}\frac{Z_I e^2}{4\pi\epsilon_0\mathbf{R}_{iI}} + \sum_{I}^{N}\sum_{J\neq I}^{N}\frac{Z_I Z_J e^2}{4\pi\epsilon_0\mathbf{R}_{IJ}}\right]\psi \tag{1.0.24}$$

$$= E\psi(\mathbf{r}_1, ..., \mathbf{r}_n, \mathbf{R}_1, ..., \mathbf{R}_N, s_1, ..., s_n, S_1, ..., S_n) \tag{1.0.25}$$

The $\hat{T}_e$ and $\hat{T}_N$ describe the kinetic energy of electrons and nuclei respectively; while the $\hat{V}_{ee}$, $\hat{V}_{Ne}$ and $\hat{V}_{NN}$ define the electron-electron repulsion, the electron-nucleus attraction and the nucleus-nucleus repulsion respectively. $\mathbf{r}_{ij}$ is the distance between electrons i and j, $\mathbf{R}_{iI}$ is the distance between electron i and nucleus I and $\mathbf{R}_{IJ}$ is the distance between nucleus I and nucleus J; Z is the atomic number of nucleus N; N is the number of nuclei; n is the number of electrons and E is the total energy of the system.

In general, the problems where the Schrödinger equation can be solved exactly are very few. To overcome this obstacle, different approximation methods have been developed. Such methods are the variational principle (section 1.0.2), which is based on the variation theorem, and the Born-Oppenheimer approximation (section 1.0.3).

1.0.2 Variational principle

The variation method is an approximation to the ground-state energy E_0, which is the lowest eigenvalue of the Hamiltonian operator $\hat{H}$ of a system described by the time-independent Schrödinger equation 1.0.20, with eigenfunctions ψ_n:

$$\hat{H}\psi_n = E_n\psi_n, \quad n = 0, 1, 2, ... \tag{1.0.26}$$

In several methods with quantum mechanical approach, such as the density functional theory (chapter 3), the knowledge of the ground-state energy is sufficient enough to provide reliable results when studying the behaviour of chemical systems. The variation theorem states that for any trial, normalised, and well-behaved function ϕ, which satisfies the same boundary conditions as ψ_n, the quantity $\mathcal{E}$ is always greater than or equal to the ground-state energy E_0:

$$\mathcal{E} \equiv \langle \phi | \hat{H} | \phi \rangle = \int \phi^*(\mathbf{r}) \hat{H} \phi(\mathbf{r}) d\mathbf{r} \geqslant E_0 \tag{1.0.27}$$

The trial function ϕ, has in most cases an arbitrary expression. If ϕ is identical with the ground-state eigenfunction ψ_0, then the energy state $\mathcal{E}$ is equal to E_0. If ϕ represents one of the excited-state eigenfunctions, then $\mathcal{E}$ will be equal to the corresponding excited-state energy E, which is greater than E_0. However, no matter what trial function ϕ is selected, the quantity $\mathcal{E}$ will never be lower than E_0.

1.0.3 Born-Oppenheimer approximation

In principle, the solution of the above Schrödinger equation for the total wavefunction ψ will give the exact energy of the system. In practice though, for approaching the exact energy of the system, Born and Oppenheimer introduced an approximation scheme in which the nuclei are considered as static, due to their much larger mass than the mass of electrons. Hence, their motion is described by a much longer time scale than that of the electrons. The total wavefunction ψ can be factorised into:

$$\psi(\mathbf{R}, \mathbf{r}) = \Phi_N(\mathbf{R})\Phi_e(\mathbf{r}; \mathbf{R}) \tag{1.0.28}$$

where $\Phi_N(\mathbf{R})$ describes the properties of the nuclei N, and $\Phi_e(\mathbf{r}; \mathbf{R})$ the electrons properties (depending parametrically on the positions of the nuclei). The problem is then reformulated in terms of two separate Schrödinger equations as:

$$\hat{H}\Phi_e(\mathbf{r}; \mathbf{R}) = \left(\hat{T}_e + \hat{V}_{ee} + \hat{V}_{Ne} + \hat{V}_{NN}\right)\Phi_e \tag{1.0.29}$$

$$= \left[-\sum_{i=1}^{n}\frac{\hbar^2}{2m_i}\hat{\nabla}^2_{\mathbf{r}} + \frac{1}{2}\sum_{i=1}^{n}\sum_{j\neq i}^{n}\frac{e^2}{4\pi\epsilon_0\mathbf{r}_{ij}} - \sum_{i}^{n}\sum_{I=1}^{N}\frac{Z_I e^2}{4\pi\epsilon_0\mathbf{R}_{iI}} + \sum_{I}^{N}\sum_{J\neq I}^{N}\frac{Z_I Z_J e^2}{4\pi\epsilon_0\mathbf{R}_{IJ}}\right]\Phi_e \tag{1.0.30}$$

$$= E_e(\mathbf{R}_1, ..., \mathbf{R}_N)\Phi_e(\mathbf{r}_1, ..., \mathbf{r}_n, s_1, ..., s_n, \mathbf{R}_1, ..., \mathbf{R}_N) \tag{1.0.31}$$

and

$$\left[-\sum_{I=1}^{N}\frac{\hbar^2}{2M_I}\hat{\nabla}^2_{\mathbf{R}} + E_e(\mathbf{R})\right]\Phi_N(\mathbf{R}) = E_{B.0.}\Phi_N(\mathbf{R}) \tag{1.0.32}$$

where $E_{B.0.}$ denotes the energy of the system within the Born-Oppenheimer approximation.

The equation 1.0.29 is calculated iteratively and when is converged it enters to equation 1.0.32 to give the motion of the nuclei. The electronic Hamiltonian obtained from Born-Oppenheimer approximation has no electronic degrees of freedom, since all the electronic parameters are incorporated in $E_e(\mathbf{R})$. In classical molecular dynamics (chapter 2) the quantum mechanical description of the nuclear motion is replaced by a Newtonian equation, allowing the nuclei to move classically. The potential energy function, in classical mechanics, is in principle the quantum mechanical potential energy surface (PES).

1.0.4 Potential Energy Surface

The potential energy surface (PES) offers an important tool for visualising and understanding the relationship between energy and molecular geometry, by providing a rigorous way for locating and characterising structures of interest. In computational chemistry, calculations on PES, are mainly used to extract information about the structure and the energy of molecules and of any transition states involved in chemical reactions.

If a pair of atoms, held together by electrostatic forces, can be represented as two spherical particles joined together by a spring of length l, then the potential energy of the system will be larger when the distance between the two atoms is larger or shorter than the equilibrium length l_{eq} of the spring (bond). Although real molecules have similar behaviour, there are some important differences when referring to atoms.

Perhaps the most notable difference is that atoms vibrate continuously around the equilibrium bond length, so that they always possess kinetic and potential energy. The energy at the point where the potential energy takes its minimum value, is

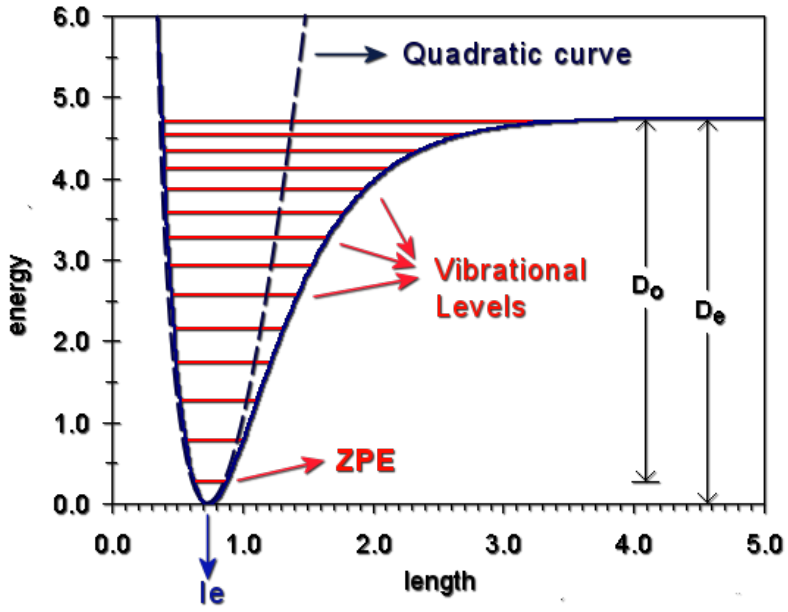

Figure 1.1: PES of a diatomic molecule showing the difference between the harmonic (quadratic curve) and the true quantum behaviour (vibrational levels). At the equilibrium bond length l_e, the quadratic curve approximates the actual PES of the diatomic. ZPE is the energy of the lowest energy level, where the potential energy is minimised to zero.

called zero-point energy (ZPE). The PES of a molecular system is defined by distinct vibrational levels and in the presence of other molecules, these levels are populated according to their spacing and temperature.

The PES of a macroscopic model, of a spring holding a pair of particles or for a real molecule near the equilibrium bond length l_{eq}, is sufficiently described by the simple harmonic oscillator $E = \frac{1}{2}k(l - l_{eq})^2$, where k represents the force constant of the spring). However, in microscopic systems the potential energy deviates from the exact quadratic form, as shown in Figure 1.1, while moving away from l_{eq}. This phenomenon is called anharmonicity.

In a 3-dimensional PES, a stationary point is a point on the surface where an extremum (minimum or maximum) or a saddle point is located. Mathematically, a

stationary point can be found by setting the first derivative of the potential energy with respect to each geometric parameter l to zero:

$$\frac{\partial E}{\partial l_1} = \frac{\partial E}{\partial l_2} = \ldots = 0 \tag{1.0.33}$$

Stationary points that correspond to molecular structures of finite lifetimes (in contrast to transition states), are located at the energy minima on the PES and any small change in the geometry of the system increases the energy. The conformation located at the lowest energy minimum of the whole PES is denoted as the global minimum, while structures corresponding to a minimum of only near by points on the surface are called relative minima. The lowest energy pathway linking two minima, is the path that would be followed by a molecule in going from one minimum to another with just enough energy to overcome the activation barrier, pass through the transition state, and reach the other minimum.

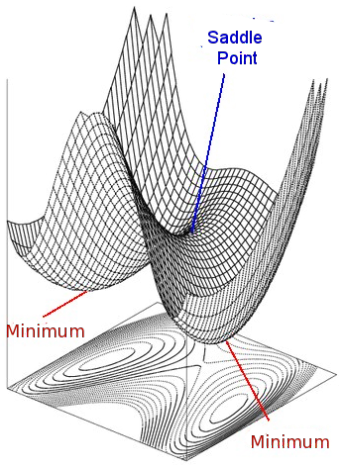

Figure 1.2: Part of 3-dimensional PES surface. A minimum is a minimum in all directions while a saddle point is a maximum in one of the directions [6].

However, in many cases not all reacting molecules follow the lowest-energy path exactly. This is a characteristic of a saddle-shaped surface, where the transition state is defined by a saddle point. Minima and saddle points have both zero first derivatives, but a minimum is a minimum in all directions, and a saddle point is a maximum along the reaction coordinate, whilst a minimum in all other directions.

1.1 Geometry Optimisation

In order to find a stationary point on a PES, we need to ask whether such a point exists, and if yes, then calculate its geometry and energy at that point. This procedure is called geometry optimisation or energy minimisation. The stationary point of interest might be a minimum, a transition state, or, occasionally, a higher-order saddle point. In the case of transition states, the procedure is often referred to as a transition state optimisation. A geometry optimisation calculation, usually starts with an input structure which is believed to resemble the geometry of a molecule at the desired stationary point.

An optimisation problem involves the minimisation of a function over several variables, possibly subjected to restrictions on the values of these variables. Many numerical methods have been developed over the years for locating the stationary points on a PES, depending, in most cases, on the computational method employed for such a calculation. Some of these methods are briefly described below.

1.1.1 First-Order Methods

One of the most simplified schemes for locating minima on molecular potential energy surfaces is the first-order derivative scheme called "Steepest Descent" (SD), which was put forward by K. Wiberg in 1965 [25]. On a molecular potential energy surface the gradient vector points of opposite directions can always be lowered down the surface to reach a local minimum. In the SD method, the function evaluations are performed in the negative gradient direction. Once the function starts to increase, an approximate minimum may be determined by interpolation between the last three points. At this interpolated point a new gradient is calculated and used for the next line search. If the line minimisation is carried out with sufficient accu-

racy it will always lower the function value, and is therefore assured to approach a minimum.

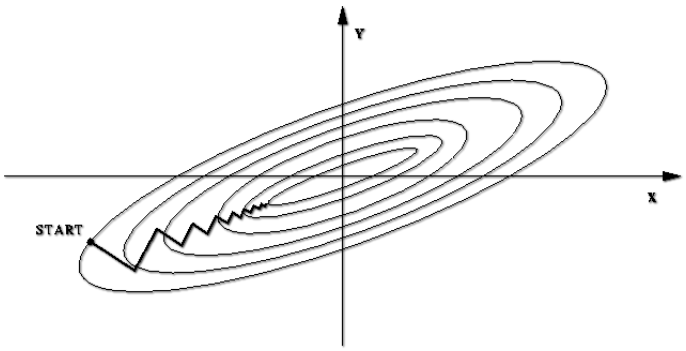

Figure 1.3: Schematic representation of the pathway followed during an SD optimisation. Ellipsoid circles represent the energy levels of a PES with the central being the lowest in energy [7].

However, there are two important drawbacks. Two subsequent line searches have to be perpendicular to each other. If there is a gradient component along the previous search direction, where the energy could be further lowered, a new search line will partly spoil the function lowering obtained by the previous search. The steepest descent path then oscillates around the minimum path. Furthermore, as the minimum is reached, the rate of convergence slows down. The steepest descent will therefore never reach the minimum, but it will crawl toward it with a constant speed.

Sometimes the minimisation along the line is carried out fairly crudely. The step size can be a fixed quantity or taken to depend on the magnitude of the gradient. The guarantee for lowering the function value is lost when approximate line searches are used. By default, the steepest descent method is a very simple numerical technique and can only locate function minima, which makes it reliable for lowering the function value. It can be used to quickly relax a poor starting point, as a pre-optimisation strategy, before a more advanced method is employed.

An improvement over the SD method is achieved with the development of the conjugate gradients (CG) methods. CG methods produce a set of directions that overcome the oscillatory behaviour of steepest descents in narrow valleys. Successive directions are not at right angles to each other, but a line search is constructed so that it is "conjugate" to the previous search direction. If for instance, the surface is purely quadratic, each successive minimisation step will not generate gradient components along any of the previous search directions. Conjugate gradient methods have better convergence features than the steepest descent, but they require slightly more storage than the steepest descent, since the previous gradient also must be saved.

1.1.2 Second-Order Methods

In contrast with SD and CG methods, where the optimisation convergence is linear, in second-order methods the expansion and the convergence of the optimisation function is of second order near a stationary point. This is due to the involvement of the Hessian matrix, which is a matrix of second derivatives of the PES with the atomic coordinates. These methods are mainly referred to as Newton-Raphson (NR) methods [26]. In general, as the stationary point is approached, this method performs better and better; while sufficiently close to the stationary point the gradient is reduced quadratically.

Several schemes have been developed over time, for improving the direction of optimisation and the size of systems studied, such as the Broyden-Fletcher-Goldfarb-Shanno (BFGS) method, where an approximated Hessian is updated during the calculation by contributions from the gradient only [27–30]. Such NR methods are known as quasi-Newton methods. In the current project, any geometry optimisations mentioned using density functional theory, employ the BFGS method by default (sections 4.4, 4.5.1).

1.2 Symmetry in Crystals

A crystal is a regular, ordered arrangement of atoms over a large scale. This arrangement can be constitute by a single type of atoms or by the repetition of a complex pattern of many different types of atoms. Generally, a crystal can be thought as being consisted of two separate parts: the lattice and the basis. The lattice is an ordered layout of points in space, while the basis is the simplest motif of atoms, which by being repeated at every point in the lattice would reconstruct the entire crystal structure. In crystallography the basis is called the "unit or Wigner-Seitz cell".

All the lattices can be obtained by repetition of the unit cell through 3 "primitive", "unit" or "translation" vectors defining the atomic arrangement within the 3D space, that in general are not orthogonal. If $\mathbf{a}_1$, $\mathbf{a}_2$, and $\mathbf{a}_3$ represent the 3 primitive vectors, which leave all the properties of the crystal unchanged after a displacement by any of those vectors then, any lattice point $\mathbf{r}$ could be obtained from another point $\mathbf{r}'$ as:

$$\mathbf{r} = \mathbf{r}' + c_1\mathbf{a}_1 + c_2\mathbf{a}_2 + c_3\mathbf{a}_3 \tag{1.2.1}$$

where c_i, $i = 1, 2, 3$ are integers. Such a lattice of building blocks is called "Bravais" lattice. The volume of a unit cell is given by $\Omega = \mathbf{a}_1 \cdot (\mathbf{a}_2 \times \mathbf{a}_3)$.

The displacement of a lattice by a translation vector is called translation operation and any operation that carries a crystal structure into itself is called symmetry operation. The latter category includes reflection and rotation operations, which are generally called point operations.

Sometimes it is convenient to describe a crystal in terms of a cell that contains more atoms than the unit cell, for simplifying the description of the symmetry operations. In this case, the cell is referred to as a "conventional" cell.

1.2.1 Lattices

The are 5 basic categories of two-dimensional lattices, the oblique and four special lattices, as shown in Figure 1.4; and 14 types of lattices in the 3 dimensions, which can be grouped in seven categories: triclinic, monoclinic, orthorhombic, tetragonal, cubic, triagonal, and hexagonal. Furthermore, there are three lattices in the cubic system: the simple cubic (sc) lattice, the body-centred cubic (bcc) lattice and the face-centred cubic (fcc) lattice, as shown in Figure 1.5.

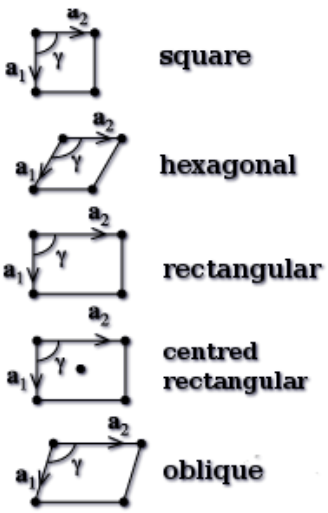

Figure 1.4: 5 basic types of 2-dimensional lattices [8].

1.2.2 The Periodic Potential

In a similar way with the atoms inside a crystal, which occupy positions forming a regular periodic structure, the potential $v(\mathbf{r})$ developed between these atoms is also a periodic function with a period equal to the period of the corresponding Bravais lattice:

$$v(\mathbf{r} + \mathbf{a}_i) = v(\mathbf{r}) \tag{1.2.2}$$

where $\mathbf{a}_i$ are the Bravais lattice vectors ($i = 1, 2, 3$). The period of the potential is of the same order as the de Broglie wave length. In the case of ideal periodic crystals this potential must satisfy the property 1.2.2. Due to the potential periodicity the solution of the single-electron Schrödinger equation 1.0.20 acquires some special properties which are described in the Bloch's theorem.

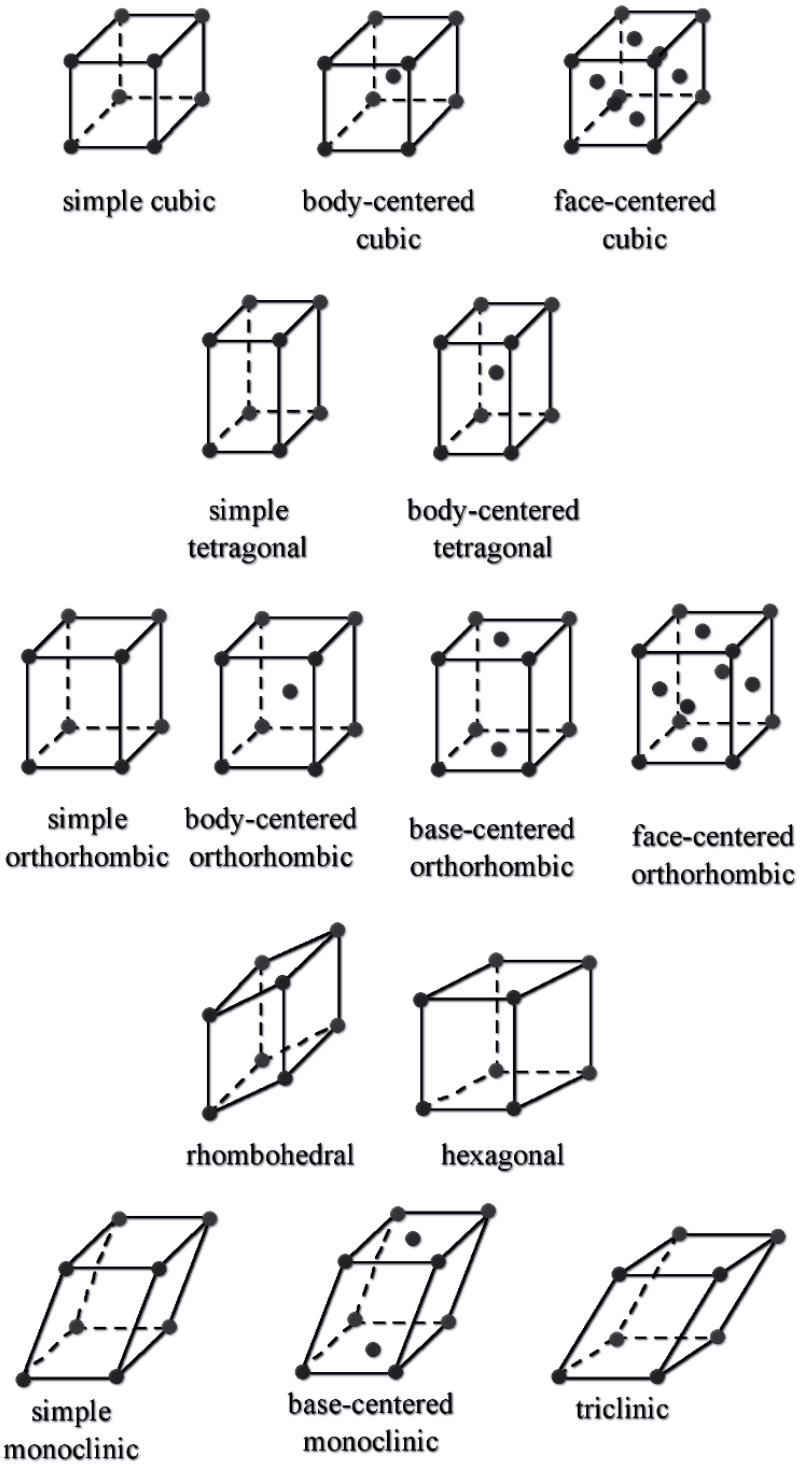

Figure 1.5: 14 types of 3-dimensional lattices [9].

1.2.3 Bloch's Theorem

Bloch's theorem simplifies the expression of Schrödinger's wavefunction ψ of equation 1.0.20, for systems subjected to periodic boundary conditions, by exploiting the periodicity of a crystal. Hence, the infinite number of one-electron wavefunctions to be calculated, is now reduced to the number of electrons in the unit cell of the crystal. The wavefunction is written as the product of a periodic function over the Bravais lattice and a plane wave part:

$$\psi_{\mathbf{k}}(\mathbf{r}) = e^{(\imath \mathbf{k}\cdot\mathbf{r})} u_{\mathbf{k}}(\mathbf{r}) \tag{1.2.3}$$

where the function $u_{\mathbf{k}}(\mathbf{r})$ satisfies the condition:

$$u_{\mathbf{k}}(\mathbf{r} + \mathbf{a}_i) = u_{\mathbf{k}}(\mathbf{r}) \tag{1.2.4}$$

for all lattice vectors $\mathbf{a}_i$. The vector $\mathbf{k}$ used in the expression of Bloch's theorem is called plane wave vector and is a conserved quantity in crystalline systems. The wavefunction $\psi_{\mathbf{k}}$ of the displaced vector $\mathbf{r} + \mathbf{a}_i$ will then take the form:

$$\psi_{\mathbf{k}}(\mathbf{r} + \mathbf{a}_i) = e^{(\imath \mathbf{k}\cdot\mathbf{a}_i)} \psi_{\mathbf{k}}(\mathbf{r}) \tag{1.2.5}$$

so that the probability $|\psi_{\mathbf{k}}(\mathbf{r}|^2$ remains the same due to the periodical symmetry of the system. Therefore, Bloch's theorem indicates that, any required physical property for an infinite system, everywhere in space, can be accurately calculated by only focusing on the properties of electrons within the unit cell.

1.2.4 Brillouin Zones

From the expression of 1.2.5 it can be assumed that, for certain values of the wavevector $\mathbf{k}$, the plane wave $e^{(\imath \mathbf{k}\cdot\mathbf{r})}$ will have the periodicity of a Bravais lattice. Such a set of $\mathbf{k}$ wave vectors, that provide plane waves with the periodicity of a Bravais lattice, is defining the reciprocal lattice. In this case, the phase factor $e^{(\imath \mathbf{k}\cdot\mathbf{a}_i)}$ must satisfy the condition:

$$e^{(\imath \mathbf{k}\cdot\mathbf{a}_i)} = 1, \quad i = 1,2,3 \tag{1.2.6}$$

Equation 1.2.6 states that, for a particular set of vectors $\mathbf{k}$, the wavefunction $\psi_{\mathbf{k}}$ is in phase with all the periodic images of the unit cell. A reciprocal lattice is defined with respect to a particular Bravais lattice, and any Bravais lattice that determines a given reciprocal lattice is often called direct lattice.

For a set of primitive lattice vectors $\mathbf{a}_1$, $\mathbf{a}_2$ and $\mathbf{a}_3$, the reciprocal lattice can be generated by three reciprocal lattice vectors $\mathbf{b}$, respectively as:

$$\mathbf{b}_1 = 2\pi \frac{\mathbf{a}_2 \times \mathbf{a}_3}{\mathbf{a}_1 \cdot (\mathbf{a}_2 \times \mathbf{a}_3)} = 2\pi \frac{\mathbf{a}_2 \times \mathbf{a}_3}{\Omega} \tag{1.2.7}$$

$$\mathbf{b}_2 = 2\pi \frac{\mathbf{a}_3 \times \mathbf{a}_1}{\mathbf{a}_1 \cdot (\mathbf{a}_2 \times \mathbf{a}_3)} = 2\pi \frac{\mathbf{a}_3 \times \mathbf{a}_1}{\Omega} \tag{1.2.8}$$

$$\mathbf{b}_3 = 2\pi \frac{\mathbf{a}_1 \times \mathbf{a}_2}{\mathbf{a}_1 \cdot (\mathbf{a}_2 \times \mathbf{a}_3)} = 2\pi \frac{\mathbf{a}_1 \times \mathbf{a}_2}{\Omega} \tag{1.2.9}$$

The reciprocal primitive vectors $\mathbf{b}_i$, satisfy the condition:

$$\mathbf{b}_i \cdot \mathbf{a}_j = 2\pi\delta_{ij} \tag{1.2.10}$$

where

$$\delta_{ij} = 0,\ i \neq j \tag{1.2.11}$$

$$\delta_{ij} = 1,\ i = j \tag{1.2.12}$$

The primitive reciprocal lattice vectors determine a cell in reciprocal space with a volume Ω_R:

$$\Omega_R = \mathbf{b}_1 \cdot (\mathbf{b}_2 \times \mathbf{b}_3) = \frac{(2\pi)^3}{\Omega} \tag{1.2.13}$$

which defines the first Brillouin zone (BZ). To illustrate this, we can consider a system of non-interacting, free electrons inside a 1D periodic box of length l. The wavefunctions $\psi_k = e^{\imath kx}$ are solutions of the Schrödinger equation 1.0.22 in 1D with eigenvalues:

$$E = \varepsilon(k) = \frac{\hbar^2 k^2}{2m} \tag{1.2.14}$$

which form the energy bands of the system. The values of k are not confined in the first BZ ($-\pi/l < k < \pi/l$). In order to visualise the energy bands within this range of k, it is customary to refold the wavevectors k_n, extended beyond the first BZ, into the first BZ by performing the operation:

$$k_n = k + G_n \tag{1.2.15}$$

where k refers to the first BZ and wavevector $G_n = 2n\pi/l$ with n being an integer. A schematic representation of the energy band folding is shown in Figure 1.6.

Generalising to 3-dimensional lattices, any vector $\mathbf{k}'$ outside the first BZ becomes:

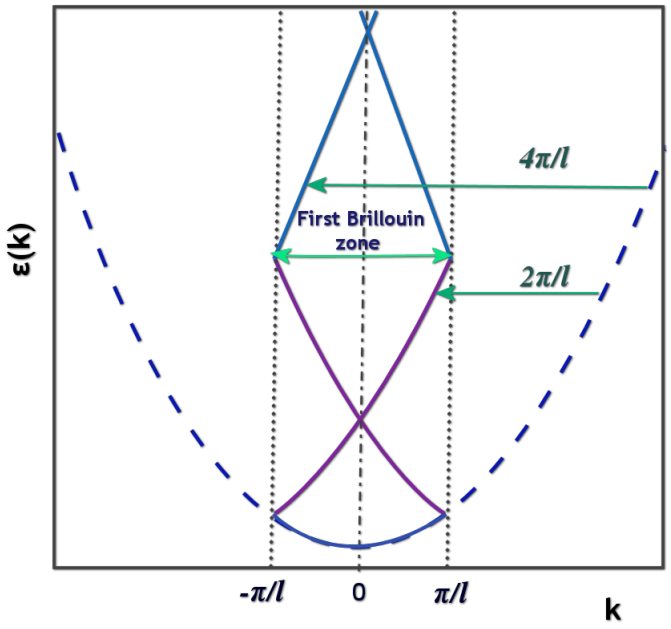

Figure 1.6: BZ energy band refolding on 1D system of non-interacting, free electrons.

$$\mathbf{k}' = \mathbf{k} + \mathbf{G} \tag{1.2.16}$$

where $\mathbf{k}$ is a vector within the first BZ and

$$\mathbf{G} = n_1\mathbf{b}_1 + n_2\mathbf{b}_2 + n_3\mathbf{b}_3 \tag{1.2.17}$$

with n_i integers. $\mathbf{G}$ is a reciprocal lattice vector which satisfies the condition:

$$\mathbf{a}_i \cdot \mathbf{G} = 2\pi n_i \tag{1.2.18}$$

Based on equations 1.2.16 and 1.2.17, the wavefunction of state $\mathbf{k}'$ according to Bloch's theorem (1.2.5) can then be written as:

$$\psi_{\mathbf{k}'}(\mathbf{r}) = e^{i\mathbf{k}'\cdot\mathbf{r}}u_{\mathbf{k}'}(\mathbf{r}) = e^{i\mathbf{k}\cdot\mathbf{r}}\left(e^{i\mathbf{G}\cdot\mathbf{r}}u_{\mathbf{k}'}(\mathbf{r})\right) = e^{i\mathbf{k}\cdot\mathbf{r}}u_{\mathbf{k}}(\mathbf{r}) = \psi_{\mathbf{k}}(\mathbf{r}) \tag{1.2.19}$$

This result justifies the approximation introduced with Bloch's theorem, by representing the infinite number of wavefunctions in a periodic system with a finite number of wavefunctions at each **k**-point located in the first Brillouin zone.

1.2.5 Brillouin zone sampling

While for an infinite system there is a finite number of occupied eigenstates of the Hamiltonian for each **k**-point, the first Brillouin zone also contains infinite **k**-points. Although all of these eigenstates should be calculated, in practice, the only feasible approach is to use a finite number of **k** points, with very minor errors in the wavefunctions and eigenvalues of the Hamiltonian for small changes of **k** [31]. This approach is called Brillouin zone sampling and several methods have been developed for accurately calculate the electronic states over special sets of **k** points within the Brillouin zone.

Based in the general principle that metallic systems should require a very fine sampling of **k**-points, in contrast with semiconductors that require fewer **k**-points, Monkhorst and Pack proposed a general scheme for sampling **k**-points [32]. For a set of vectors q, written in terms of primitive reciprocal lattice vectors **k**:

$$\mathbf{k} = n_1\mathbf{b}_1 + n_2\mathbf{b}_2 + n_3\mathbf{b}_3 \tag{1.2.20}$$

where the integers n_i are defined by the relation:

$$n_i = (2r - q - 1)/2q \quad \text{where} \quad r = 1, 2, 3, ..., q \tag{1.2.21}$$

In the Γ point approximation only a single point is sampled, at $k = 0$.

1.3 Thesis overview

This thesis focuses mainly on the crystalline properties of modelled semiconductor silicon and metallic gold or platinum nanomaterials. Bi-metallic nanoalloys of gold and platinum with copper and palladium are also presented. In more detail, a computational study of silicon nanorods of more than 1000 atoms, with varying aspect ratios and surface passivation by hydrogen is presented in chapter 4. Their structural and electronic properties were investigated at the atomistic *ab initio* level of detail.

A computational approach for simulating extended x-ray absorption fine structure (EXAFS) spectra of gold nanoparticles from force field simulations is presented in chapter 5. A probability distribution function calculated directly from an ensemble of molecular dynamics snap-shots is used to determine the photoabsorbing atoms and their surrounding scattering paths.

Classical molecular dynamic simulations have also been performed on bare platinum nanoclusters and on their bimetallic nanoalloys with copper or palladium, as described in chapter 6. The structural results obtained from the simulations of bare Pt nanoparticles were used as input data for the analysis of extended x-ray absorption fine structure spectra of experimentally synthesised Pt nanoparticles, as a better fitting model from the conventional methods used so far. While the approach detailed in chapter 6, is at a preliminary stage, it has shown promising results for future development.

Furthermore, molecular dynamic simulations on spherical gold nanoparticles with diameters 1.39, 1.94, 2.50 and 3.05 nm have been conducted, as described in the last chapter. Gold nanosurfaces in contact with one or two thiolate molecules were also investigated, using first principles methods.

Chapter 2

Classical Molecular Dynamics

Classical Molecular Dynamics (MD) is a computational technique for simulating materials, with a plethora of applications in various areas of research, such as chemistry, physics, applied mathematics etc. Within the framework of this method, a molecule is modelled as a collection of solid spheres (atoms) held together by springs (chemical bonds), while the motions of the atoms contained in the system are described by using the laws of classical mechanics. The aim is to extract data about the dynamical behaviour of different materials at the atomic scale as well as their thermodynamic properties using statistical mechanics. The energy of a molecular system is expressed as a function of its structural changes, which occur during the simulation, as the springs (bonds) resist towards stretching and bending or the spheres (atoms) repel from being crowded together. This is conceptually similar to the intuitive feel of interacting plastic or metallic atoms going through any necessary conformations in order to find their most energetically stable geometry.

The concept of classical MD seems to have started as an attempt to obtain information about the structural properties of chemical compounds, at a time when the possibility of performing quantum mechanical calculations on anything larger than

the hydrogen atom seemed impossible. Specifically the use of MD as a potential method for studying the variation of energy with respect to the geometry of a molecular system was founded in 1946 by Westheimer and Meyer [33] and by Hill [34]. It has to be stressed, at this point, that the method makes no reference to the electronic behaviour of the atoms within the system, while the Born-Oppenheimer approximation is used implicitly, as a static attractive force between the nuclei and the atoms, which vaguely define the electronic region. Thus, MD methods cannot provide any information about molecular orbitals or any related electronic properties.

Generally, MD is a widely used method for calculating the energies and geometries of large molecular systems, such as proteins, nucleic acids, nanocrystals etc. During a classical MD simulation, the forces and velocities acting on the atoms as a function of their coordinates are evaluated in parallel steps, depending on which integration scheme is used. The mathematical expression of the energy and forces constitutes a "force-field", thus classical MD is sometimes referred to as a force-field method. Each simulation proceeds in discrete steps by calculating the forces and velocities between the particles and solving the equations of motion based on the accelerations obtained from the new forces.

Usually systems studied with classical MD are simulated for a time-period of less than 1 μs but the main factor which affects the reliability of the simulations and also the computational cost of a simulation is the size of the integration time-step. The time-step must be chosen small enough to avoid discretisation errors. Typically, the propagation time-step is chosen to be about $1/10^{th}$ of the smallest period of vibration of chemical bonds contained in the system (usually around 1-6 fs).

Although the electrons contained in the simulated system are "ignored" at the expense of the calculation speed, this does not necessarily lead to non reliable results. By correctly parametrising a force-field, the electronic properties can be approximated with sufficient accuracy, though such results are obtained purely by

analogy. It is important to use an appropriate force-field for the kind of compounds studied, as it is non transferable and is more likely to perform inadequately for other classes of molecules. This is due to that, force field methods are generally ruled by empirical factors. Optimising a hypothetical structure of a molecule may not necessarily lead to the most stable conformation at the global energy minimum. Sometimes a stationary point can be trapped into a transition state during the geometry optimisation. The situation becomes more complex if systems with an overall charge are simulated *in vacuo*. In this case, some discrepancies can be overcome by explicitly including solvent molecules or ions inside the simulation box.

Nevertheless, classical MD methods are fast and computationally more efficient than *ab initio* or semi-empirical methods and hence, can be used for studying very large systems such as large bio-molecules, polymers or nanoparticles. More importantly, they can be used for studying metallic systems containing transition or heavy elements, where other methods depending on the calculation of the energy band structure fail to converge.

2.0.1 The DL_POLY code

The classical MD simulations performed throughout this work were mainly conducted with the DL_POLY2 code [1]. It is a parallel molecular dynamics simulation package developed at Daresbury Laboratory by W. Smith and T.R. Forester. There are two available forms of DL_POLY; DL_POLY2 which is the primary version and is based on a replicated data parallelism and DL_POLY3 which is a domain decomposition version, designed for systems beyond the range of DL_POLY2 (around 10^6 atoms and a maximum number of 1000 processors).

For a typical simulation with the DL_POLY code [18], at least three input files are

necessary: a) The CONFIG file; includes all the spacial coordinates of every atom contained in the system in a Cartesian form and the x,y and z projections of the primitive vectors defining the simulation box. b) the CONTROL file; contains all the parameters defining the thermodynamic state of the system (temperature, pressure, thermodynamic ensemble), the type and duration of the calculation (equilibration time, total time, time-step) and also keywords about the structure of some output files printed (HISTORY, STATIS, RDFDAT). Additionally, cut-off values for the distances of the long-ranged interactions need to be included in the CONTROL file. c) the FIELD file; contains the values of the parameters describing the force field(s) and the kind of interactions developed between the atoms contained in the system.

During a simulation with DL_POLY, all the results and tables are printed in the OUTPUT file. Simultaneously, the STATIS and HISTORY file are also collecting data from the MD simulation. The HISTORY file contains all information describing the trajectory of the system, with the spacial coordinates, the velocities and the forces developed on each atom of the simulated system in every printed frame. The amount of data collected and the number of frames included in the HISTORY file is controlled by keywords given in the CONTROL file. The STATIS file, on the other hand, contains all the details about the thermodynamic parameters and the energy parts of the force field on every MD step. By the end of the simulation, the new geometry of the system in the Cartesian space, is summarised in the REVCON file. For the purpose of restarting a simulation from a previous trajectory, the REVCON file provides the new CONFIG file in a new MD run. In special occasions, the user can output data about the radial distribution function (RDFDAT) or the number of data points in the Z-density function (ZDNDAT). Details about the format of these files and some pre- or post-processing scripts of the input and output files of DL_POLY are shown in the Appendices A, B and C.

2.1 Thermodynamic Ensembles

In each MD simulation, the definition of the thermodynamic state of a molecular system is achieved via a small set of macroscopic parameters, such as the temperature, the pressure, and the number of particles. Also, the microscopic state of a system at a given time is defined by using atomic positions, and momenta. These can also be considered as coordinates in a multi-dimensional space, called phase space.

A thermodynamic ensemble is a collection of these points in a phase space satisfying the conditions of a particular thermodynamic state. For example, in the microcanonical ensemble, (N,V,E), the volume (V), the energy (E) and the number of particles (N) of the system remain constant. Other ensembles, such as the isobaric-isothermal ensemble (N,P,T) or the canonical ensemble (N,V,T), except from the number of particles (N), the pressure (P) and the temperature (T) or the volume (V) and the temperature (T) are also preserved, respectively.

MD simulations begin with an "equilibration period", where the molecular system is allowed to reach a region of the phase-space, near thermodynamic equilibrium. During this period, the temperature is scaled gradually until it reaches a desired value. This is achieved by using temperature stabilisers, called "thermostats", which imitate heat exchange between the system and its surroundings. For an ensemble that keeps the temperature stable, during the equilibrium, an adjustment of the velocities is demanded in every step, since the temperature is related to the kinetic energy. Practically though, this prevents the trajectories from being Newtonian and as a consequence the properties computed are less reliable. To overcome this impact, suitable computational algorithms are used which can treat the molecular system as being in contact with a constant temperature bath (e.g. Berendsen [35] or Hoover thermostat [36]).

In the cases of thermodynamic ensembles which keep the pressure constant, the volume is allowed to change by scaling the space coordinates of the particles. The algorithms used for this purpose are called "barostats" [37].

2.2 Integration Algorithms

For propagating the phase-space trajectory of a molecular system on a computer from its initial position and momenta, methods that proceed in discrete time steps have been developed. This discretisation is dictated by the need to represent on a computer the phase-space points. These propagation methods require the use of small time intervals to avoid trajectory errors. Large time intervals can distort the dynamical behaviour and the thermodynamic properties of the simulated system. One popular and sophisticated integration scheme for propagating trajectories, is the Verlet algorithm [38], in which the coordinates of an atom are expanded as a Taylor series.

In more detail, the derivatives of the particle's position vector are expanded in Taylor series up to the second term by one time-step Δt forward ($\mathbf{r}_i^{(n+1)}$) and one time-step backward ($\mathbf{r}_i^{(n-1)}$). The sum of these expansions gives:

$$\mathbf{r}_i^{(n+1)} = 2\mathbf{r}_i^n - \mathbf{r}_i^{(n-1)} + \frac{\Delta t^2}{m_i}\mathbf{F}_i^n \tag{2.2.1}$$

where $\mathbf{F}_i$ are the forces acting on the particle i and n is the MD step number.

The Verlet algorithm offers a satisfactory accuracy since the error on the first time step calculation is of Δt^3 order, but it propagates the position vector without using the velocities $\mathbf{v}_i$, thus giving no information on the particle's motion or the kinetic energy. For the MD simulations this is a major drawback which can be overcome by

using two improvements of the Verlet algorithm, the Leapfrog Verlet or the Velocity Verlet algorithm.

2.2.1 Leapfrog Verlet

In the Leapfrog Verlet, the velocities $\mathbf{v}_i$ are calculated using the position terms $\mathbf{r}_i$, calculated from the basic Verlet algorithm in every time-step. The velocity vectors are calculated separately from the position of the particles, thus always having a half time-step displacement. A smaller time interval can reduce the numerical error created from this approximation.

$$\mathbf{v}_i^{(n+1/2)} = \mathbf{v}_i^{(n-1/2)} + \frac{\Delta t^2}{m_i}\mathbf{F}_i^n + \vartheta(\Delta t^3) \tag{2.2.2}$$

$$\mathbf{r}_i^{(n+1)} = \mathbf{r}_i^n + \Delta t \mathbf{v}_i^{(n+1/2)} + \vartheta(\Delta t^4) \tag{2.2.3}$$

2.2.2 Velocity Verlet

On the other hand, the Velocity Verlet algorithm, embodies the velocities along with the positions of the atoms in every time-step. Although this avoids the half displacement discrepancy introduced by the Leapfrog Verlet, it still gives results with same accuracy as the basic Verlet algorithm.

$$\mathbf{v}_i^{(n+1/2)} = \mathbf{v}_i^n + \frac{\Delta t}{2m_i}\left(\mathbf{F}_i^n + \mathbf{F}_i^{(n+1)}\right) + \vartheta(\Delta t^3) \tag{2.2.4}$$

$$\mathbf{r}_i^{(n+1)} = \mathbf{r}_i^n + \Delta t \mathbf{v}_i^n + \frac{\Delta t^2}{2m_i}\mathbf{F}_i^n + \vartheta(\Delta t^4) \tag{2.2.5}$$

2.3 Force Fields

Force fields are based on numerous approximations derived from different types of experimental data and quantum calculations. Most force fields in chemistry consist of several parameters defining the bonded forces associated with the chemical bonds, bond angles, and bond dihedrals, and the non-bonded forces such as electrostatic interactions and Van der Waals interactions.

In this respect, the force field energy can be separated into different energy terms, such as the stretching term $E_{stretch}$, the bending energy E_{bend}, the torsional motion $E_{torsion}$, and interactions between atoms or groups which are non-bonded $E_{nonbond}$. Thus, the potential energy of a molecule is given by the combination of these terms and their parameters as:

$$E = \sum_{bonds} E_{stretch} + \sum_{angles} E_{bend} + \sum_{dihedrals} E_{torsion} + \sum_{pairs} E_{nonbond} \tag{2.3.1}$$

Consequently, the stretching energy describes the stretching of a bond length between a pair of atoms, the bending energy, the changes in the angle formed by a sequence of three atoms and the torsional energy, the energy obtained by rotating a series of four atoms along the axis of the two middle atoms.

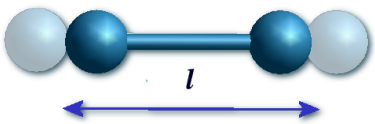

More specifically, the bond stretching term expresses the energy difference of a bond (spring) when is stretched:

$$\Delta E_{stretch} = \frac{1}{2} k_{stretch} \left(l - l_{eq}\right)^2 \tag{2.3.2}$$

where $k_{stretch}$ is the proportionality constant of the spring or bond. As the $k_{stretch}$ gets bigger so the bond/spring becomes stiffer or the more it resists in being stretched; l is the length of the bond which is stretched while l_{eq} is the equilibrium bond length, or else, the "natural" distance of a pair of atoms, whilst in the minimum potential energy value. If the energy corresponding to the equilibrium length is set to zero, then the expression of $\Delta E_{stretch}$ becomes equal to:

$$E_{stretch} = \frac{1}{2} k_{stretch} \left(l - l_{eq}\right)^2 \tag{2.3.3}$$

The angle bending term describes the "angle energy" of the system, which corresponds to the resistance of bending the angle defined by any triatomic unit (A-B-C) within the molecule, as show in Figure 2.3. Approximately, the bending energy is proportional to the square of the increase in the angle α:

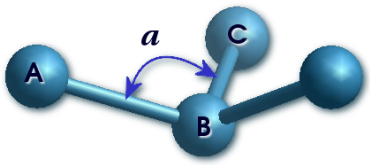

Figure 2.1: α is the angle formed by atoms A-B-C in order

$$E_{bend} = k_{bend} \left(\alpha - \alpha_{eq}\right)^2 \tag{2.3.4}$$

where k_{bend} is a proportionality constant, equal to the one-half the angle bending force constant.

The torsional term defines the energy barrier of changing any "dihedral" angle or "torsional" angle of the system. The dihedral angle is the angle formed between

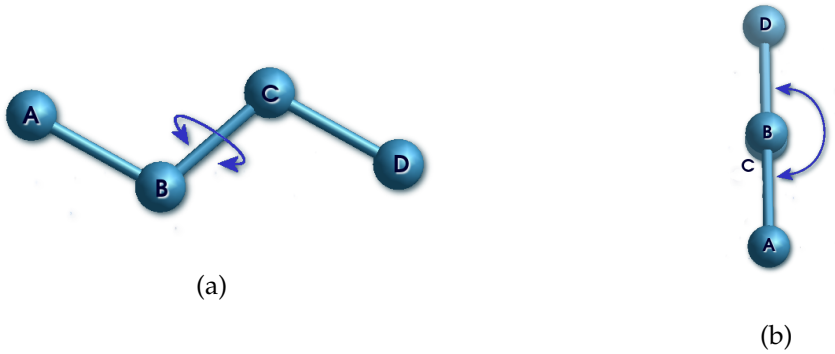

(a) (b)

Figure 2.2: (a) Horizontal and (b) vertical view of the dihedral angle formed by atoms A-B-C-D

a series of four atoms, A, B, C and D, or between the A-B bond and the C-D bond, viewed along the B-C bond, as shown in Figure 2.2. By default, this angle is considered positive if it arises from clockwise rotation of the back bond (C-D) with respect to the front bond (A-B). Since the geometry repeats itself every 360^o, the energy varies with the dihedral angle in a sine or cosine pattern but a combination of sine or cosine functions will reproduce the curve:

$$E_{torsion} = k_0 + \sum_{r=1}^{n} k_r \left[1 + \cos(r\theta)\right] \tag{2.3.5}$$

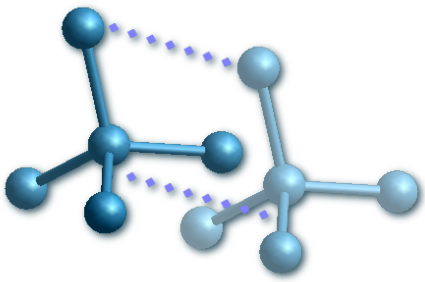

Figure 2.3: Visualisation of non-bonded interactions formed by two different groups of atoms quite far apart

The change in potential energy with distance apart of two groups of atoms that are not directly bonded, is defined by the non-bonded energy term. This energy term contains any short-ranged, such as the Van der Waals interaction, or long-ranged non-bonded interactions, which are mainly pure electrostatic forces between charged atoms of the system. In more detail, these interactions are described in the following sections.

2.3.1 Short Ranged Potentials

2.3.1.1 The Van der Waals energy

The Van der Waals interactions are developed between neighbouring atoms that are not directly bonded. They are relatively weak compared to ionic or covalent bond interactions and are caused by correlations in the fluctuating polarisations of neighbour atoms, molecules or surfaces.

In general, the the Van der Waals energy has a repulsive and an attractive component. For very small distances the potential becomes very repulsive, at distances where the atoms almost interact, it has a slightly negative minimum and goes towards zero for large distances. One of the simplest and most widely used models to describe the Van der Waals interactions is the Lennard-Jones potential.

2.3.1.2 The Lennard-Jones potential

The Lennard-Jones is a pair potential which contains a repulsive term $\frac{1}{\mathbf{r}^{12}}$ and an attractive $\frac{1}{\mathbf{r}^{6}}$ term, where $\mathbf{r}$ represents the distance between a pair of atoms. The repulsive term of the potential is derived by the requirement of the repulsive interaction to fade to zero when $\mathbf{r}$ reaches infinity faster than the attractive term.

$$V(\mathbf{r}_{ij}) = 4\varepsilon \left[\left(\frac{\sigma}{\mathbf{r}_{ij}} \right)^{12} - \left(\frac{\sigma}{\mathbf{r}_{ij}} \right)^{6} \right] \tag{2.3.6}$$

The ε defines the depth of the potential well and σ is the distance at which the inter-particle potential becomes zero.

2.3.2 Long Ranged Potentials

Long-ranged contributions to the potential energy between non-bonded charged atoms or a group of atoms, are essential when dealing with polar or ionic molecular systems. For this purpose, several techniques for simulating Coulomb and dipolar interactions have been developed. Two of the most common methods for describing long-ranged electrostatic forces are the direct Coulomb potential and the Ewald summation technique.

2.3.2.1 Direct Coulomb Potential

The simplest and easiest way to describe the interactions between two point charges is by using the Coulomb potential. According to Coulomb's law, the force acting between two electric charges is radial, inverse-square, and proportional to the product of the charges. Practically, if two points have the same charge then they repel one another, whereas two points with opposite charges attract each other. Hence, if two point charges q_1 and q_2, are located at position vectors $\mathbf{r}_1$ and $\mathbf{r}_2$, then the electrical force acting on the second charge is given by:

$$\mathbf{F}_2 = \frac{q_1 q_2}{4\pi\epsilon_0} \frac{\mathbf{r}_2 - \mathbf{r}_1}{|\mathbf{r}_2 - \mathbf{r}_1|^3} \tag{2.3.7}$$

where ϵ_0 is the permittivity of free space.

The above equation satisfies Newton's third law because it implies that a force of the same magnitude but opposite direction acts on charge q_1 . The forces between the two point charges act along the line joining them.

2.3.2.2 Ewald Summation

Ewald summation was introduced in 1921 [39] as a technique to sum the long-ranged interactions between particles inside a periodic or pseudo-periodic system. The basic cell of a system consists of positively and negatively charged ions mutually interacting via the Coulomb potential, which is repeated infinitely with identical copies of itself. Each ion is effectively neutralised (at long range) by the superposition of a spherical Gaussian cloud of opposite charge centred on that ion. The entire system is then neutral and contains an infinite number of charges situated at points $\mathbf{r}_{j+}$ and $\mathbf{r}_{j-}$, respectively. The total potential at the position of some ion i residing in the basic cell is given by the finite difference of two infinite, diverging series:

$$\phi(\mathbf{r}_i) = q \sum_{j+=1}^{\infty} \frac{1}{|\mathbf{r}_i - \mathbf{r}_{j+}|} + q \sum_{j-=1}^{\infty} \frac{1}{|\mathbf{r}_i - \mathbf{r}_{j-}|} \tag{2.3.8}$$

Instead of evaluating the potential as a sum over the point charges, these charges can be rewritten as delta-like charge densities,

$$\rho(\mathbf{r}) = q \sum_{j+=1}^{\infty} \delta\left(\mathbf{r} - \mathbf{r}_{j+}\right) - q \sum_{j-=1}^{\infty} \delta\left(\mathbf{r} - \mathbf{r}_{j-}\right) \tag{2.3.9}$$

and expanded in a Fourier series whose terms determine the Fourier components $\phi(\mathbf{k})$ of the electrostatic potential. Since the Fourier representation of a delta-function requires infinitely many terms, the Fourier space calculation would again lead to convergence problems.

In Ewald method, the potentially infinite sum in real space, is replaced a by two finite sums: one in real space (**r**-space) and one in reciprocal space (**k**-space). Hence, the combined assembly of point ions and Gaussian charges becomes the (**r**-space) part of the Ewald sum, which is now short ranged. A second set of Gaussian charges, this time with the same charges as the original point ions, centred on the

point ions is superimposed and the potential is then solved as a Fourier series in the (**k**-space). The delta-like point charges by Gaussian charge "clouds" of opposite sign, are augmented by:

$$\rho'(\mathbf{r}) = -q_j \left(\frac{\eta^2}{\pi}\right)^{3/2} \exp^{-\eta^2(\mathbf{r}-\mathbf{r}_j)^2} \tag{2.3.10}$$

By suitably adjusting η, optimal convergence of both series may be achieved. The complete Ewald sum requires an additional correction, known as the self energy correction, which arises from a Gaussian acting on its own site, and is constant. For molecular systems, as opposed to systems comprised simply of point ions, additional modifications are necessary to correct for the excluded (intra-molecular) Coulombic interactions. In the real space sum these are simply omitted. In reciprocal space however, the effects of individual Gaussian charges cannot easily be extracted thus, the correction is made in real space, by removing terms corresponding to the potential energy of an ion due to the Gaussian charge on a neighbouring charge m (or vice versa). This correction appears as the final term in the full Ewald formula:

$$\phi\left(\mathbf{r}_i\right) = \frac{4\pi}{L^3} \sum_{j=1}^{N} q_j \left[\sum_{\mathbf{k}} \exp^{-i\mathbf{k}.\mathbf{r}_{ij}} k^2 \exp^{-k^2/4\eta^2} + \sum_{\mathbf{n}} F\left(\eta|\mathbf{r}_{i,j,\mathbf{n}}|\right)\right] \tag{2.3.11}$$

where

$$F \equiv \frac{2}{\sqrt{\pi}} \int e^{-t^2} dt$$

k are the Fourier vectors of a cubic base cell with side length L and N charges:

$$\mathbf{k} \equiv \frac{2\pi}{L}\left(k_x, k_y, k_z\right), \mathbf{r}_{i,j},\ \mathbf{n} \equiv \mathbf{r}_j + \mathbf{n}L - \mathbf{r}_i \quad (i,j = 1,\ldots,N)$$

and **r** are the inter-particle vectors acting on all periodic images of the base cell, where $\mathbf{n}L$ is a translation vector in the periodic lattice.

2.3.3 Metal Potentials

2.3.3.1 The Gupta Potential

There are several empirical potentials suitable for describing metallic systems that are derived from fitting experimental data into an assumed functional form and usually include a local volume or density dependence in order to describe the metallic binding. The Gupta [40] potential is based on the second moment approximation of Tight-Binding (TB) theory and has been extracted from Gupta's expression for the cohesive energy of a bulk material. The potential is divided into a repulsive (V^r) and many-body attractive terms (V^m) summed over all atoms contained in the molecular system:

$$V_{tot}(\mathbf{r}) = \sum_{i \neq j} \{V^r(\mathbf{r}_{ij}) - V^m(\mathbf{r}_{ij})\} \tag{2.3.12}$$

where

$$V^r(\mathbf{r}) = \sum_{j \neq i} A \exp\left(-p\left(\frac{\mathbf{r}_{ij}}{\mathbf{r}_0} - 1\right)\right) \tag{2.3.13}$$

and

$$V^m(\mathbf{r}) = \left[\sum_{j \neq i} \zeta^2 \exp\left(-2q\left(\frac{\mathbf{r}_{ij}}{\mathbf{r}_0} - 1\right)\right)\right]^{\frac{1}{2}} \tag{2.3.14}$$

where $\mathbf{r}_{ij}$ is the distance between atoms i and j, A is the energy scaling factor for the repulsive energy, ζ is the energy scaling factor for the many-body attractive energy, $\mathbf{r}_0$ the equilibrium bond length of the bulk material, p and q are the range exponents for the pair and many-body potentials respectively.

2.3.3.2 The Sutton-Chen Potential

Another potential with a similar formalism to Gupta is the Sutton-Chen (SC) [41,42] potential which has the form:

$$V_{tot}(\mathbf{r}) = \sum_i \epsilon \left[\sum_{i \neq j} \frac{1}{2} \left(\frac{\alpha}{\mathbf{r}_{ij}} \right)^n - c\rho_i(\mathbf{r})^{\frac{1}{2}} \right] \tag{2.3.15}$$

where ρ_i is a local density accounting for cohesion associated with atom i, given by:

$$\rho(\mathbf{r}) = \sum_{i \neq j} \left(\frac{\alpha}{\mathbf{r}_{ij}} \right)^m \tag{2.3.16}$$

$\mathbf{r}_{ij}$ is the distance between atoms i and j, as previously stated, c is a dimensionless parameter, ϵ is a parameter with dimensions of energy, α is the lattice constant, and m and n are positive integers such that $n > m$.

When describing a bi-metallic system, the parameters ϵ, α, m and n, can be combined using the following mixing rules:

$$\begin{aligned} \epsilon^{AB} = \sqrt{\epsilon^A \epsilon^B}, \quad \alpha^{AB} = \sqrt{\alpha^A \alpha^B}, \\ n^{AB} = \frac{1}{2}\left(n^A + n^B\right), \quad m^{AB} = \frac{1}{2}\left(m^A + m^B\right) \end{aligned} \tag{2.3.17}$$

where A and B refer to different metallic systems.

The parameters used in both the Gupta and the SC force fields are derived from TB calculations performed by Cleri and Rosato [43] on transition metals and alloys, in order to reproduce the cohesive energy, atomic volume and elastic constants of the corresponding real systems at zero temperature. Further works have extended the properties of many-body potentials to include also phonon dispersion, vacancy formation energy, surface energy etc.

2.3.4 The Stillinger-Weber Potential

The Stillinger-Weber potential [44] is an empirical potential, suitable for studying semiconductor nanocrystals [45] [46]. It is a simplified potential which uses geometrical quantities, such as distances and bond angles as variables and is capable of modelling, with a very high precision, the structural and dynamical properties of a large variety of elements [47]. One of its applications concerns the prediction of the dynamical properties of solid and liquid silicon.

In order to study H-terminated Si nanoparticles, the Stillinger-Weber potential was selected due to its efficiency in describing the interactions not only between Si-Si atoms but also between Si-H atoms, according to the work conducted from Kohen et al. [48], who have extended the form of the potential in order to include the Si-H interactions. It is based on a two-body term and a three-body term as shown in the following general form:

$$\Phi = \sum U_{SiSi} + \sum U_{HH} + \sum U_{SiH} + \sum U_{SiSiSi} + \sum U_{HHH} + \sum U_{SiSiH} + \sum U_{SiHH} \tag{2.3.18}$$

where the three first terms are referring to the two-body part and the next four terms are referring to the three-body part.

Although the DL_POLY code [1] comes with several popular force fields implemented by default, the Stillinger-Weber potential, unfortunately, is not currently supported by the versions of the code available so far. For this purpose, the potential had to be imported manually into the DL_POLY source code. The following sections include a summary of the procedure followed for implementing and testing separately each part of the potential for describing the interactions of silicon and hydrogen atoms, as reported in the computational works of Kohen et al [48] and of Hawa and Zachariah [49].

2.3.4.1 Implementing the two-body term

Each term describing the two-body term of the Stillinger-Weber potential has the following generic form:

$$U_2(\mathbf{r}) = \begin{cases} A\left(Br^p - \mathbf{r}^{-q}\right)\exp\left(\frac{\gamma}{\mathbf{r}-\alpha}\right) & \mathbf{r} < \alpha \\ 0 & \mathbf{r} \geq \alpha \end{cases} \tag{2.3.19}$$

where all the contained constants are positive (α, A, B, p, q, γ).

This pair interaction describes in general, the tendency for the formation of a covalent bond. In practice, the three-body term is also needed for the final achievement of a chemical bond.

Since DL_POLY is not providing by default the use of Stillinger-Weber potential as force field, a modification of the code was required. Luckily, using the capability of the program to define a short-ranged pair potential by tabulating the energy values, had limited our task in changing the code, only to the three-body part. Thus, the insertion of the two-body term of the potential was achieved by using an extra input file called TABLE (see Appendix A.4). This file contains all the grid points describing an undefined potential as a function of the distance. The file must contain also in a tabular form the values for the two-body forces as a function of the distance, following the energy values.

2.3.4.2 Testing the tabulated potential with DL_POLY

In order to understand and test the way that the tabulated potential works with DL_POLY and how the program reads the contained data, a diatomic molecule of

two Si atoms located in a different distance from their equilibrium bond length was constructed. If the data contained in the TABLE file are correct then the optimisation will stop at the point where the two atoms have reached their equilibrium bond distance.

The energy grid points and the forces values were obtained by implementing the two-body term of the Stillinger-Weber potential describing the interaction between two Si atoms in Mathematica [50]. The potential, as constructed in the TABLE file, was carefully tested to ensure that its units and format were correct. In this respect, the binding energy and the distance at the minimum was calculated using both Mathematica and DL_POLY, by performing a geometry optimisation in the latter case. Our results were confirmed by the very good agreement between the results obtained by the two codes.

By plotting the potential and differentiating the energy function, the minimum was found to be at distance 2.3516Å. The result also from the geometry optimisation showed that the equilibrium bond length is 2.3516Å. The energy at this point was found to be equal to 50 kcal/mol in both cases. The experimental values for the equilibrium bond distance and the minimum energy were 54 kcal/mol and 2.331Å respectively, which show the good approximation of the calculation and the experiment [51].

2.3.4.3 Implementing the three-body term

The three-body term of the Stillinger-Weber potential has the following general form:

$$U_{j,l,k}(\mathbf{r}) = \begin{cases} \lambda_{j,l,k}\left[1 + \mu_{jlk}\cos(\theta_{jlk}) + \nu_{jlk}\cos(\theta_{jlk})^2\right]\exp\left(\frac{\gamma_{lj}}{\mathbf{r}_{lj}-\alpha} + \frac{\gamma_{lk}}{\mathbf{r}_{lk}-\alpha}\right) & \mathbf{r}_{jlk} < \alpha \\ 0 & \mathbf{r}_{jlk} \geq \alpha \end{cases} \tag{2.3.20}$$

where the constants λ, γ and α, are positive, but μ and ν can also have negative values depending on the interacting atoms. The indices *j*,*l* and *k* refer to the sequence of the three atoms which the three-body term applies to, with the *l* atom located at the centre.

The format of the three-body term is separable into two parts, one angular and one radial cut-off term. It is strictly defined for a sequence of three chemical elements in a specific order. Thus, the angle formed by the atoms Si-H-Si, for example, defines a different potential from the angle formed by the atoms Si-Si-H.

In order to insert the three-body term of the Stillinger-Weber potential into the DL_POLY code, the subroutine which deals with the three-body interactions had to be modified. To start with, a keyword for the program to recognise the potential from its input files had to be introduced. Secondly, since the default three-body potentials of DL_POLY were defined by maximum of five constants, the array in which these constants are stored had to be extended by one more dimension for the inclusion of a sixth parameter needed for the definition of the three-body part. Finally, the new potential had to be consistent with the logic, order and formalism of the whole code. Thus, the insertion of the three-body term is done by dividing it into two parts; the "screening" and the "angular" part.

The screening part contains all the terms depending on the two atom-atom distances $\mathbf{r}_{ij}$ and $\mathbf{r}_{ik}$ and the angular part depends on all the terms described by the angle θ. In this case the screening term is:

$$S(\mathbf{r}) = \exp\left(\frac{\gamma_{ij}}{\mathbf{r}_{ij} - \alpha} + \frac{\gamma_{ik}}{\mathbf{r}_{ik} - \alpha}\right) \tag{2.3.21}$$

and the angular term is:

$$A(\theta) = 1 + \mu_{jik}\cos(\theta_{jik}) + \nu_{jik}\cos^2(\theta_{jik}) \tag{2.3.22}$$

The derivatives of these terms describe the forces exerted on the central and side atoms, in a sequence of three particles. In the DL_POLY code the forces are expressed by the FORTRAN variables *gamma*, *gamsa*, *gamsb* and *gamsc*. The derivative of the angular term gives the *gamma* term, and the derivatives of the exponential term give the *gamsa* and *gamsc* terms. By default, the *gamsb* term which describes the forces on the central atom is set to zero, because the forces on this atom are calculated as a negative sum of the forces on the side atoms. In a mathematical form these terms have the following expression:

$$[gamma] = -S(\mathbf{r}_{ij})S(\mathbf{r}_{ik})\frac{\partial}{\partial r_l{}^{\alpha}}A(\theta_{jik}) \tag{2.3.23}$$

$$[gamsa] = -A(\theta_{jik})S(\mathbf{r}_{ik})(\delta_{lj} - \delta_{li})\frac{\mathbf{r}_{ij}^{\alpha}}{\mathbf{r}_{ij}}\frac{\partial}{\partial r_{ij}}S(\mathbf{r}_{ij}) \tag{2.3.24}$$

$$[gamsc] = -A(\theta_{jik})S(\mathbf{r}_{ij})(\delta_{lk} - \delta li)\frac{\mathbf{r}_{ik}^{\alpha}}{\mathbf{r}_{ik}}\frac{\partial}{\partial r_{ik}}S(\mathbf{r}_{ik}) \tag{2.3.25}$$

where l being one of the atomic labels i,j,k, and α indicating the x,y,z component of the Cartesian space.

For consistency, the modification of the code had to be done with respect to the software's default units. Therefore, the three-body potential is multiplied by a factor of 418.4, the conversion unit of kcal/mol to 10 J/mol, which is the default energy unit of the program. No conversion was needed for the atomic distances, since they are given the same units in both literature and software.

2.3.4.4 Testing of the three-body term

The Stillinger-Weber potential was constructed for describing the behaviour of silicon atoms generally in the liquid phase. Hence, the initial properties of the silicon crystal had to be preserved for the transformation of the bulk crystal to the liquid phase.

By definition this potential gives a minimum at an angle of 109.47 degrees which is the angle of a perfect tetrahedron and the angle observed in the crystalline form of silicon. Also, the distance between two silicon atoms, as defined mainly by the two-body term is 2.35 Å.

For testing the efficiency of the interactions between two hydrogen atoms and one silicon atom, a molecule was constructed which contains two hydrogen atoms bound to a silicon atom. The results obtained from the geometry optimisation are then compared with the results presented in the research article of Kohen et al [48].

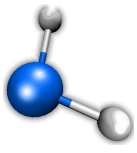

SiH_2

Table 2.1: Results from geometry optimisation of SiH_2

	Energy (kcal/mol)	Bond length (Å)	Angle (deg.)
KTS [48]	145.6	1.474	102.61
This work	145.6	1.474	102.61

Test of the H-H-H sequence By constructing the SiH_3 molecule an additional three-body interaction comes into play; the interaction between three atoms of hydrogen. The two-body interaction between two hydrogen atoms is designed to give the equilibrium bond length of a H_2 molecule when it is absorbed on a catalytic surface and is equal to 0.74 Å, as calculated by Kohen et al. In contrast, the three-body interaction between hydrogen atoms is mainly repulsive and thus the angle formed by H-Si-H is expected to be larger in the SiH_3 than the angle of the same sequence of atoms in SiH_2.

The results obtained from the geometry optimisation with DL_POLY for the SiH_3 molecule revealed a significant variation with the results stated in the paper of Kohen et al. This inconsistency has also been observed by a later work from Hawa and Zachariah [49], who have re-parametrised the variables of the Stillinger-Weber potential as defined in the Kohen et al paper in order to give more satisfactory results.

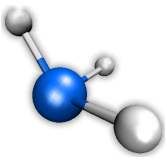

SiH_3

Table 2.2: Results from geometry optimisation of SiH_3

	Energy (kcal/mol)	Bond length (Å)	Angle (deg.)
KTS [48]	222.3	1.471	106.31
This work	208.79	1.582	114.44
HZ [49]	216.13	1.513	109.40
This work	216.47	1.509	109.15

Test for the interactions Si-Si-H and Si-H-Si The three-body interactions between two silicon atoms and one hydrogen, are tested on a Si_2H_6 molecule, being simulated with DL_POLY. Starting from a geometry where all the particles are located in distances smaller than the cut-off distances defined for all the included three-body interactions, the Si_2H_6 molecule is then optimised using the parameters from both articles of Kohen et al and Hawa-Zachariah. The results obtained are shown in the Table 2.3.4.4 below.

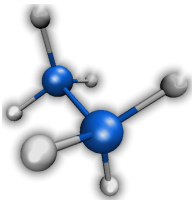

Si_2H_6

Table 2.3: Results from geometry optimisation of Si_2H_6

	Energy (kcal/mol)	Bond length (Å) Si-H	Angle (deg.) H-Si-H
KTS [48]	500.10	1.470	106.6
This work	427.96	1.743	117.19
HZ [49]	483.22	1.510	109.5
This work	491.94	1.505	109.01

Testing the three-body potential forces In each test case mentioned above, the forces computed for every atom were tested by performing finite difference calculations and by differentiating each three-body potential with Mathematica. The atomic forces are given in Cartesian form and thus each atomic force is constituted from its resultant force in the x, y and z direction. The general formula which DL_POLY uses to describe the atomic forces is given by:

$$\mathbf{f}_l{}^{\alpha} = -\frac{\partial}{\partial r_l{}^{\alpha}} U(\theta_{jlk}, \mathbf{r}_{ij}, \mathbf{r}_{ik}) \tag{2.3.26}$$

where $U(\theta_{jlk}, \mathbf{r}_{ij}, \mathbf{r}_{ik})$ is the total potential.

The finite differencing method for verifying the efficiency of the modified code and the calculations performed with Mathematica, were used to validate the accuracy of the result printed by the program. For example, if the value of a force found from finite differencing was not approximating the value printed by the program, this was stating the existence of a bug in the code. On the other hand, if a force printed by the program was approximating the result obtained from finite differencing, but its value was different from the value computed by Mathematica, it meant that a parameter or a constant had been entered incorrectly in the code.

Chapter 3

Density Functional Theory

Density functional theory (DFT) is a first principles approach used in physics and chemistry for extracting the electronic properties of many-body molecular systems. In contrast with other quantum mechanical methods, DFT is based on the evaluation of the electron or charge density $n(\mathbf{r})$ rather than the wavefunction, which does not have a direct physical meaning. While *ab initio* or semiempirical methods are focused on calculating or approximating the practically insoluble Schrödinger equation, DFT employs the electron density which is an experimentally observable entity (X-ray diffraction or electron diffraction).

To extract the structural properties of a molecular system it is sufficient enough to focus only on its ground state. The ground state energy can be obtained, practically exactly, only from knowing the electron density. The innovation of DFT comes with the replacement of the N-electron wavefunction with an overall density function, which allows the disengagement of the energy functional from many electron coordinates. The electron density is a function of position only, requiring only three variables for its definition, the components of $\mathbf{r}$ (x, y, z in Cartesian space). No matter what the size of a molecule may be, the charge density remains a function of

three variables, while the complexity of a wavefunction increases exponentially by increasing the number of electrons.

Because the electron correlation is fundamentally included in DFT, this method can calculate very accurately geometries and relative energies, but perhaps not as accurate as high-level *ab initio* methods. The latter fact results from the lack of knowledge of the exact mathematical form for the DFT functional. In conventional *ab initio* theory, the wavefunction can be improved systematically by using larger basis sets or additional correlation terms, while a further improvement of the functional is a challenging task in DFT. In this sense, DFT cannot be regarded as a special kind of *ab initio* method but the limited use of empirical parameters and the possibility of someday finding the exact functional, make potentially DFT an *ab initio* method.

So far, DFT methods have been extensively used for investigating the structural and electronic properties of semiconductors and several transition metals, where conventional *ab initio* methods break down due to system size limitations. Further improvements in DFT, apart from augmenting or modifying functionals, include also the development of numerical integration schemes in order to extent its applicability in larger and different molecular systems (see section 3.3).

3.0.5 DFT Energy

As in the wavefunction based approaches, the electronic energy E_{el} can be separated into the kinetic energy term T, the nuclei and electrons attraction term E_{ne} and the electron-electron repulsion term E_{ee}. The inter-electronic repulsion term can be divided into the Coulomb J and the Exchange K part, according to Hartree-Fock (HF) theory. While in HF theory, the total energy of a many-body system can be given with an accuracy of 99% the remaining 1% is still important for evaluating the

chemical and physical properties of the molecular system. The missing 1% is called correlation energy E_c and is, in principle, included in the DFT formalism.

$$E_{el}[n] = T(n) + E_{ne}[n] + E_{ee}[n] \tag{3.0.1}$$

$$E_{ee}[n] = J[n] + K[n] + E_c[n] \tag{3.0.2}$$

where $[n]$ indicates that the above terms are functionals of the electron density $n(\mathbf{r})$

3.1 Theorems and Models

The first model for describing the electronic energy as a functional of electron density was developed by Thomas and Fermi [52]. Their theory considers a uniform distribution of electrons forming a "homogeneous" non-interacting electronic gas, which allows the average kinetic energy functional to be expressed only in terms of the particle density.

The omission of exchange and correlation between electrons by Thomas-Fermi theory led to an improvement of the energy functional, made by Dirac, who included the exchange term to the electronic energy, according to his local approximation theory [53]. Despite further improvements made over the years, the Thomas-Fermi-Dirac model has limited applications, mainly on isolated neutral atoms and solids. Density functional theory became an exact theory after the publication of Hohenberg-Kohn theorems (section 3.1.1), while nowadays, DFT calculations are based on the more accurate Kohn-Sham approach (section 3.1.2).

3.1.1 The Hohenberg-Kohn Theorems

The concept of the Hohenberg-Kohn [54] theorems relies on the assumption that the exact prediction of the ground state of an N-electron system is feasible by only using the electron density. Their formulation can be applied on any stationary, non-relativistic many-particle system in an "external" potential $v_{ext}(\mathbf{r})$, which completes the energy required by the electrons to move under the potential of the atomic nuclei and determines all the properties of the ground state.

$$\hat{H} = -\frac{\hbar^2}{2m_e}\sum_i {\nabla_i}^2 + \sum_i v_{ext}(\mathbf{r}) + \frac{1}{2}\sum_{i\neq j}\frac{e^2}{|\mathbf{r}_i - \mathbf{r}_j|} \tag{3.1.1}$$

3.1.1.1 Theorem I

The first Hohenberg-Kohn theorem certifies that any ground state property of a system with interacting particles is a functional of the ground state electron density. Thus, an external potential $v_{ext}(\mathbf{r})$ acting on this system, can be determined by one and only one ground state density $n(\mathbf{r})$.

Assuming that an alternative potential $v'_{ext}(\mathbf{r})$ (with ground state wavefunction ψ'), which produces the ground state density $n(\mathbf{r})$ such that:

$$v_{ext} \longmapsto \hat{H}\psi = E_0\psi \tag{3.1.2}$$

$$v'_{ext} \longmapsto \hat{H}'\psi' = E'_0\psi' \tag{3.1.3}$$

then, from the application of the variational method (section 1.0.2) to the ground state electronic energy:

$$E'_0 = \langle\psi'|\hat{H}'|\psi'\rangle < \langle\psi|\hat{H}'|\psi\rangle = \langle\psi|\hat{H}|\psi\rangle + \langle\psi|\hat{H}' - \hat{H}|\psi\rangle \tag{3.1.4}$$

$$E_0' < E_0 + \int [v_{ext}'(\mathbf{r}) - v_{ext}(\mathbf{r})] n(\mathbf{r}) d\mathbf{r} \tag{3.1.5}$$

Interchanging the primed and unprimed quantities of equation 3.1.5 then:

$$E_0 < E_0' + E_0 - E_0' \Longrightarrow E_0' + E_0' < E_0 + E_0' \tag{3.1.6}$$

which is a contradiction and therefore, the assumption that such a $v_{ext}'(\mathbf{r})$ exists falls apart.

3.1.1.2 Theorem II

The second theorem assures that any trial electron density n provides an energy value higher or equal, if the actual electron density is known, to the ground state energy. Hence, for any trial external potential $v_{ext}(\mathbf{r})$ with an energy functional $E[n]$ the global minimum will always be the exact ground state energy $E[n_0]$ with the exact ground state density n_0.

$$E_0 = E[n_0] \leq E[n] \tag{3.1.7}$$

The theorem is the equivalent of the variation principle of the wavefunction in quantum mechanics (section 1.0.2). This allows the ground state density to be used as the basic variable for minimising the energy when conducting DFT calculations.

Although the original Hohenberg-Kohn theorems are based on some restrictions, like the presence of a non-degenerate ground system, the theorems have been extended to include spin-polarised systems, relativistic systems etc. Nonetheless, both theorems cannot give any information regarding the explicit construction of the kinetic or the exchange and correlation energy functionals.

3.1.2 Kohn-Sham Theory

The real breakthrough in density functional theory came from Kohn and Sham (KS) [55] with the introduction of the KS orbitals for calculating the electron density, which in return, is used to calculate the energy and any other related properties. The central idea in the Kohn and Sham formalism is that the kinetic energy can be separated into two parts, a term which can be calculated exactly and a small residual correction term.

According to the Kohn-Sham approach, the exact ground state density n_0 can be represented by a ground state density n_S of an auxiliary system of N non-interacting particles. This auxiliary system is defined by the Hamiltonian:

$$\hat{H}_S = \hat{T}_S + \hat{V}_{ext} \tag{3.1.8}$$

where $\hat{V}_{ext}$ is the operator of an effective local potential acting on the particles.

The exact ground state density is given by:

$$n_0(\mathbf{r}) = \sum_{i=1}^{N} |\psi_i(\mathbf{r})|^2 d\mathbf{r} \tag{3.1.9}$$

where $|\psi_i(\mathbf{r})|^2 = \psi_i^*(\mathbf{r})\psi_i(\mathbf{r})$ and $\psi(\mathbf{r})$ represents the real Schrödinger wavefunction.

Since the exact ground state density is not known, we assume that the density can be written as a sum of auxiliary one-electron orbitals $\phi_i(\mathbf{r})$ equal to the total number of electrons N of the system. Thus, the exact density for any interacting system $n_0(\mathbf{r})$, would be equal to the density of the auxiliary problem $n_S(\mathbf{r})$:

$$n_0(\mathbf{r}) = n_S(\mathbf{r}) = \sum_{i=1}^{N} |\phi_i(\mathbf{r})|^2 \tag{3.1.10}$$

The independent-particle kinetic energy functional T_S would then have the form:

$$T_S[n_S] = \sum_{i=1}^{N} \langle \phi_i | -\frac{1}{2}\hat{\nabla}^2 | \phi_i \rangle \tag{3.1.11}$$

By including also the classical Coulomb interaction energy E_H (as defined in Hartree-Fock theory) of the electron density n_S, the Kohn-Sham expression of the energy functional using the auxiliary ground state density becomes:

$$E_{KS} = T_S[n_S] + V_{ext}[n_S] + E_H[n_S] + E_{nn} + E_{xc}[n_S] \tag{3.1.12}$$

where E_{nn} is the nuclei-nuclei repulsion term, $V_{ext}[n_S] = \int v_{ext}(\mathbf{r}) n_S(\mathbf{r}) d\mathbf{r}$ and

$$E_{xc}[n_S] = (T[n_0] - T_S[n_S]) + (E_{ee}[n_0] - E_H[n_S]) \tag{3.1.13}$$

The E_{xc} is called exchange-correlation term and represents the deviation of the exact kinetic energy functional $T[n_0]$ of the real system, whose form is not known, from that calculated by using the formula for a non-interacting system $T_S[n_S]$ and also, the electron-electron repulsion energy difference from the classical system (second term of the right part of equation 3.1.13).

By applying the variational principle, as described in the second Hohenberg-Kohn theorem (section 3.1.1.2), Kohn-Sham theory leads to single-particle Schrödinger equations for the orbitals:

$$\hat{H}_{KS}\phi_i(\mathbf{r}) = \left[-\frac{1}{2}\hat{\nabla}^2 + \hat{v}_{KS}(\mathbf{r})\right]\phi_i(\mathbf{r}) = \varepsilon_i\phi_i(\mathbf{r}) \tag{3.1.14}$$

where $\hat{H}_{KS}$ is an effective Hamiltonian acting on the Kohn-Sham orbitals ϕ_i to provide the energy eigenvalues ε_i. The effective potential $v_{KS}(\mathbf{r})$ results from the contribution of:

$$v_{KS}(\mathbf{r}) = v_{ext}(\mathbf{r}) + v_H(\mathbf{r}) + v_{xc}(\mathbf{r}) \tag{3.1.15}$$

where $v_{xc}(\mathbf{r})$ is derived from the minimisation of the exchange-correlation energy functional with respect to the ground state density $n_S(\mathbf{r})$:

$$v_{xc}(\mathbf{r}) = \frac{\delta E_{xc}[n_S]}{\delta n_S} \tag{3.1.16}$$

The Kohn-Sham orbitals are canonical eigenfunctions of the Schrödinger equation 1.0.20 and hence, are required to be orthonormal. In order to find a solution for the ground state density, equations 3.1.14 and 3.1.15 need to be solved self-consistently due to the dependence of the effective potential $v_{KS}(\mathbf{r})$ from the density.

The Kohn-Sham equation (3.1.14) is exact; if the charge density $n_0(\mathbf{r})$ and the expression of E_{xc} are known exactly then the total energy of the molecular system can be computed also exactly. The basic problem in DFT, then, becomes the construction of the exchange and correlation functional $E_{xc}[n_S]$. For this purpose, various expressions of E_{xc} have been developed and proposed.

3.2 Exchange and Correlation Energy

The exchange-correlation energy $E_{xc}[n(\mathbf{r})]$, is a functional of $n(\mathbf{r})$, thus, it depends parametrically on the function $n(\mathbf{r})$ and on its mathematical form, while the exchange-correlation potential $v_{xc}(\mathbf{r})$, the functional derivative of $E_{xc}[n(\mathbf{r})]$, is a function of the components x, y, z of $\mathbf{r}$. In practice, it is common to separate $E_{xc}[n(\mathbf{r})]$ into an exchange $E_x[n]$ and a correlation $E_c[n]$ part:

$$E_{xc}[n(\mathbf{r})] = E_x[n(\mathbf{r})] + E_c[n(\mathbf{r})] \tag{3.2.1}$$

The two components of $E_{xc}[n(\mathbf{r})]$ can be then treated independently. Some of the approximations employed for devising good forms for the exchange-correlation functional are discussed in the following sections.

3.2.1 Local Density Approximation

Within the framework of the Local Density Approximation (LDA) [26], the $E_{xc}[n]$ is calculated exclusively by the local density at the position $\mathbf{r}$ of the particle. This approach, can only be applied in closed-shell, spin-unpolarised systems, that can be treated as a uniform electron gas, where the density n retains the same value or slightly varies at every position; in contrast with non-local methods (section 3.2.2).

In the LDA method proposed by Slater (X_aLDA method), the correlation part of the exchange-correlation energy is neglected and the exchange part used is:

$$E_x^{LDA}[n] = -\frac{3}{4}\left(\frac{3}{\pi}\right)^{\frac{1}{3}} \int n(\mathbf{r})^{\frac{4}{3}} d\mathbf{r} \tag{3.2.2}$$

For extending the applicability of the exchange functional E_x also to open-shell systems, where the spin densities of α and β electrons are not equal, the LDA can be replaced by the more general Local Spin Density Approximation (LSDA). This approach can deal with systems with one or more unpaired electrons, such as radicals. For systems with strictly paired electrons, the LSDA approach becomes equivalent to the LDA.

Several correlation functionals, $E_c[n]$, have been developed to compensate the correlation energy $E_x[n]$, such as the CAPZ (Ceperley, Alder, Perdew and Zunger) [56, 57] or the VWN (Vosko, Wilk and Nusair) [58]. In the latter case, the correlation energy of a uniform electron gas was determined empirically, with the $E_c[n]$ functional interpolating between unpolarised and fully polarised densities.

Although LDA methods have been used over the years in systems with close or similar behaviour to the uniform electron gas, such as bulk metallic systems, calculations performed on systems of chemical interest often produce unsatisfactory results to many chemists. For this purpose, more sophisticated exchange-correlation functionals have been proposed and developed.

3.2.2 Gradient Corrected Methods

A significant improvement over the LDA methods, is based on a non-uniform electron density model. A way to correct the exchange-correlation functional is by infusing its localised description with one or more contributions from the gradient of the electron density. In this case, the electron density is sampled over an infinitesimal distance beyond the "local" region, in contrast to LDA/LSDA methods. Such approaches are called gradient corrected or generalised gradient approximation methods (GGA). Most gradient corrected functionals have an additional correction term

into the expression of the LDA:

$$E_{xc}^{GGA}[n(\mathbf{r})] = E_{xc}^{LDA}[n(\mathbf{r})] + \Delta E_{xc}\left(\frac{|\nabla n(\mathbf{r})|}{n^{4/3}(\mathbf{r})}\right) \tag{3.2.3}$$

The first GGA exchange functional (B or B88) was developed by Becke [59], who proposed a popular correction to the LDA exchange energy:

$$E_x^{B88} = E_x^{LDA} + \Delta E_x^{B88} \tag{3.2.4}$$

Exchange functionals with a similar formlism to Becke's, extended with some additional parameters, found to give better performance over either. Alternative GGA exchange functionals, which are widely used, have also been developed based on the reduced gradient function. These functionals, which do not contain any empirical optimised parameters, include the B86, PBE, and mPBE.

For improving the correlation functionals, corrections to the correlation energy density have been made, by using a different expression for the LDA correlation energy density, as in the popular P86 [60] or PW91 [61] functionals.

$$E_c^{P86} = E_c^{LDA} + \Delta E_c^{P86} \tag{3.2.5}$$

Another popular GGA correlation functional, LYP [62], does not correct the LDA expression but instead computes the correlation energy in total.

3.2.3 Hybrid Functionals

The DFT exchange energy, as defined in GGA methods, can be enhanced with an extra term calculated from Hartree-Fock (HF) theory. In HF theory, the electronic energy for a system of n occupied spatial orbitals will be:

$$E_{HF} = 2\sum_{i=1}^{n} H_{ii} + \sum_{i=1}^{n}\sum_{j\neq i}^{n}(2J_{ij} - K_{ij}) \tag{3.2.6}$$

where H_{ii} represents the system's core electronic energy, as in equations 3.0.1 and 3.0.2, which also include the electrons kinetic energy and the electrons-nuclei attraction. The J and K terms describe the Coulomb and exchange parts of the electron-electron repulsion energy. If the core energy H and the Coulomb energy J are eliminated, then the exchange part K developed between a pair of electrons i and j, illustrates the exchange energy E_x, over the total number of electrons n contained in the system:

$$E_x = -\sum_{i=1}^{n}\sum_{j\neq i}^{n} K_{ij} \tag{3.2.7}$$

Expanding in terms of the KS orbitals ϕ then the above expression of equation (3.2.7) becomes:

$$E_x^{HF} = -\sum_{i=1}^{n}\sum_{j=1}^{n}\langle\phi_i(1)\phi_j(2)|\frac{1}{r_{ij}}|\phi_i(2)\phi_j(1)\rangle \tag{3.2.8}$$

where the E_x^{HF} represents the exact exchange energy of a non-interacting electrons system as a functional of the exact electron density. By adding an LSDA gradient-corrected DFT expression for the correlation energy E_c, the exchange-correlation

energy, $E_{xc} = E_x + E_c$, represents a weighted contribution of the expression for the HF/DFT exchange-correlation functional, which is commonly called "hybrid" DFT functional.

3.2.3.1 B3LYP

One of the most popular hybrid DFT functionals at present, and perhaps DFT exchange-correlation functionals in general, is the Becke3LYP or B3LYP functional [63]. It is based on a modification by Stevens et al. [64] of the exchange-energy functional developed by Becke in 1993 [65], by introducing the LYP [62] correlation-energy functional. Its general form is:

$$E_{xc}^{B3LYP} = (1 - \alpha_0 - \alpha_x)E_x^{LSDA} + \alpha_0 E_x^{HF} + \alpha_x E_x^{B88} + (1 - \alpha_c)E_c^{VWN} + \alpha_c E_c^{LYP} \quad (3.2.9)$$

The E_x^{LSDA} is an LSDA non-gradient-corrected exchange functional, E_x^{HF} is the KS orbital based HF exchange energy functional, E_x^{B88} is the Becke88 exchange functional, E_c^{VWN} is the Vosko, Wilk, Nusair correlation function, which forms part of the accurate functional for the homogeneous electron gas of the LDA and the LSDA, and E_c^{LYP} is the LYP correlation functional. The parameters α_0, α_x and α_c are those that give the best fit of the calculated energy to molecular energies. The B3LYP functional is overall a gradient-corrected, well-tested and sufficiently accurate hybrid functional.

3.3 Methods for DFT calculations

There are several types of basis sets or basis functions for representing the Kohn-Sham orbitals in density functional theory methods. From basis sets that extend through all the space occupied by a molecular system (extended basis sets) to localised functions, centred at the atomic positions or around a chemical bond. In more sophisticated methods, a combination of both types can be achieved, by including localised and extended functions (mixed basis sets) or by augmenting an extended or a localised basis set with atomic-like wavefunctions within a spherical region around the atom.

Generally, in electronic structure calculations, the highest level of accuracy can be reached by using infinite-size basis sets, which is practically impossible. Depending on the numerical method used, the size and kind of atoms contained in the system, these basis functions offer a good compromise for obtaining sufficient accuracy for a limited number of functions. More details about some types of basis sets are discussed in the following sections.

3.3.1 Gaussian Basis Sets

Gaussian basis sets are commonly used in computational chemistry due to their simplicity and efficiency compared to other atomic orbital (AO) basis sets. They are made by contracting primitive Gaussian-type orbitals (GTOs) and there is a wide range of basis sets composed from GTOs. Their complexity depends on the number of basis functions contained for representing all of the electrons on each atom. A list with all the available Gaussian basis sets developed so far can be found on the "Basis set exchange database" [66]. The simplest Gaussian basis set, employs a minimal number of basis functions and for each orbital only one basis function is used.

A primitive Gaussian-type orbital has the general form:

$$\phi_G(x, y, z; \alpha, i, j, k) = N x^i y^j z^k e^{-\alpha(x^2+y^2+z^2)} \tag{3.3.1}$$

where N is normalisation factor, α is an exponent controlling the width of the orbital and i, j, k are non negative integer parameters that determine the nature of the orbital in the Castresian space.

Despite their simplicity, GTOs have some important drawbacks such as the zero slope at the nuclei region, instead of a finite slope (cusp), and the requirement of a large number of basis functions to reach a level of sufficient accuracy. More importantly, calculations employing GTOs, suffer from "basis set superposition error". This is due to the use of incomplete localised basis sets that results in the binding energy being overestimated. Additional parameters or variables can be introduced for improving the quality of GTOs, as described further on.

The first improvement in the utilisation of Gaussian basis sets can be achieved by increasing the multiplicity of all the basis functions. Therefore, doubling all the basis functions will lead to a Double Zeta (DZ) type basis. Equivalently, Triple Zeta (TZ), Quadruple Zeta (QZ) or Quintuple Zeta (5Z) basis sets can be employed.

The most common addition to minimal basis sets is probably the addition of polarisation functions, denoted by an asterisk, *. Polarisation is added to a basis set when higher angular momentum functions are important, especially when some additional flexibility within the basis set is needed, for allowing the KS orbitals to be more asymmetric around the nucleus or along a bond distance. In terms of atomic orbitals, p-orbitals can be used to introduce polarisation in s-orbitals. Similarly, d-type functions can be added to a basis set with valence p orbitals, and f-functions to a basis set with d-type orbitals, and so on.

Another common addition to basis sets is the addition of diffuse functions, denoted by a plus sign or by an additional "aug" keyword (from "augmented"). These additional basis functions can be important in cases of anions or other large molecular systems, where the electron distribution at distances far away from the atomic nuclei is not negligible.

3.3.2 Plane Wave Basis Sets

Plane wave basis sets have lots of applications in quantum chemical simulations, especially when studying properties of crystalline solids. They are appropriate for calculations involving periodic boundary conditions, since the results obtained for an intrinsic property of a unit cell can be considered as an average over the whole crystal. They are solutions to the Schrödinger equation for the case of a particle within a periodic box. The form of a plane wave for a cubic box with side length l is:

$$\psi_{\mathbf{k}}(\mathbf{r}) = \frac{1}{l^{\frac{2}{3}}} e^{\imath(k_x x + k_y y + k_z z)} = \frac{1}{\Omega^{\frac{1}{2}}} e^{\imath(\mathbf{k}\cdot\mathbf{r})} \tag{3.3.2}$$

where $k_x = \frac{2\pi}{l} n_x$, $k_y = \frac{2\pi}{l} n_y$, $k_z = \frac{2\pi}{l} n_z$, with $n_x, n_y, n_z \in \mathbb{Z}$ and Ω is the volume of the box.

When plane waves are used in density functional calculations a much larger number of plane wave basis functions are required compared to the number of Gaussian-type orbitals used in a typical calculation. One of the main advantages of plane wave basis sets is the elimination of the basis set superposition error, since the simulations cell is uniformly covered by the basis functions. A disadvantage is that for calculations on isolated molecules the "supercell" approximation must be made, which involves the construction of a large simulation cell to isolate, as much as possible, the molecule from its periodic image interactions. As a consequence, con-

ventional codes require more computer power to calculate the behaviour of plane waves within the empty space, as the atomic localisation of the orbitals is lost [67].

In practice, plane wave basis sets are combined with an "effective core potential" or pseudopotential, thus focusing mainly at the "valence" charge density. This is a clever way of eliminating the calculation of a large number of wavefunctions and density gradients near the nuclei which are not easily described by plane wave basis sets, since "core electrons" are concentrated near the atomic nuclei. This combined method of a plane wave basis set with a "core" pseudopotential is often described by the abbreviation "PSPW" calculation.

3.3.3 Pseudopotential Approximation

By convention, the electronic states of an atom can be classified into three categories: (a) the "core states", which are localised states closely enough to the nucleus that are not involved in chemical bonding, (b) the "valence" states, which are actively involved states in chemical bonding and (c) the "semi-core" states, which are not directly involved in chemical bonding but are partly localised and more polarisable than core states. Although these terms mainly describe single-particle electronic states, it is customary to refer also to the electrons these states contain by using the same terminology.

In principle, the pseudopotential approximation attempts to replace the wavefunctions of the electrons localised in the vicinity of the nucleus and the nucleus with an effective potential, or pseudopotential, in order to reduce complicated effects derived from the large kinetic energy of the core electrons. This effective potential imposes a weak interaction between the valence electrons and the core electrons, while treating at the same time the nuclei with the core electrons as a rigid

ion centre. Thus, only the chemically active valence electrons are dealt explicitly, as the behaviour of the valence states inside the core region is practically unnecessary. The pseudopotential wavefunctions of the valence electrons generated are required to be orthogonal to all the core states, by construction.

The pseudopotential theory is based on the orthogonalised plane wave (OPW) method, proposed by Herring in 1940 [68], which attempts to replace the steep behaviour of the atomic core wavefunctions with rather smooth plane waves (PW) but, at the same time, reproducing accurately the bonding properties of the true potential. The valence wavefunctions are constructed as a linear combination of PW and core wavefunctions. With careful selection of the expansion coefficients, the constructed pseudo-wavefunction turns out to be orthogonal to the core states.

From the OPW approach, an atomic system is defined by its Hamiltonian $\hat{H}$, the core states $\{|\chi_n\rangle\}$ and the core energy eigenvalues $\{E_n\}$. Each one valence state $|\psi\rangle$ gives an energy eigenvalue E. From these states a smoother pseudostate $|\varphi\rangle$ can be constructed by:

$$|\psi\rangle = |\varphi\rangle + \sum_{n}^{\text{core}} a_n |\chi_n\rangle \tag{3.3.3}$$

The valence state must be orthogonal to all of the core states so that:

$$\langle\chi_m|\psi\rangle = 0 = \langle\chi_m|\varphi\rangle + a_m \tag{3.3.4}$$

which fixes the expansion coefficients a_n. Thus

$$|\psi\rangle = |\varphi\rangle - \sum_{n}^{\text{core}} |\chi_n\rangle\langle\chi_n|\varphi\rangle \tag{3.3.5}$$

Substituting this expression in the Schrödinger equation, $\hat{H}|\psi\rangle = E|\psi\rangle$, gives:

$$\hat{H}|\varphi\rangle - \sum_{n}^{\text{core}} E_n|\chi_n\rangle\langle\chi_n|\varphi\rangle = E|\varphi\rangle - E\sum_{n}^{\text{core}} |\chi_n\rangle\langle\chi_n|\varphi\rangle \tag{3.3.6}$$

which can be rearranged in the form:

$$\hat{H}|\varphi\rangle + \sum_{n}^{\text{core}}(E - E_n)|\chi_n\rangle\langle\chi_n|\varphi\rangle = E|\varphi\rangle \tag{3.3.7}$$

From equation 3.3.7 we can observe that the smooth pseudostate obeys the Schrödinger equation with an extra energy-dependent non-local potential $\hat{V}_{\text{nl}}$:

$$\left[\hat{H} + \hat{V}_{\text{nl}}\right]|\varphi\rangle = E|\varphi\rangle \tag{3.3.8}$$

$$\hat{V}_{\text{nl}} = \sum_{n}^{\text{core}}(E - E_n)|\chi_n\rangle\langle\chi_n| \tag{3.3.9}$$

The additional potential V_{nl}, whose effect is restricted in the core, is repulsive and cancels part of the strong Coulomb potential so that the resulting sum is a weaker pseudopotential. This results in changing the energies of the atomic eigenstates, but if the core states are fairly separated in energy from the valence states, then a reasonable approximation would be the fixing of E in V_{nl} to be the atomic valence eigenvalue.

There are several types of pseudopotentials, depending on the transferability of atomic properties in a variety of systems or the amount of empirical factors introduced for the construction of a pseudopotential. In the first non-empirical approach by Philips and Kleinman [69], the norm of the constructed pseudo-wavefunction inside the core region was different from that of all-electron wavefunction, which led to incorrect charge distribution of the valence states or errors in chemical bonding properties. This could be solved by re-normalising the pseudo-wavefunctions in terms of the all-electron wavefunctions within some radius (cut-off or core radius). Therefore, if the pseudo-wavefunctions are required to preserve the norm inside the core radius, this property is called "norm-conservation" and the relative pseudopotentials "norm-conserving".

3.3.3.1 CASTEP

CASTEP [3] is a PSPW code for performing density functional theory calculations. It can simulate the properties of solids, interfaces, and surfaces for a wide range of materials such as semiconductors, metals etc. First principle calculations within the DFT formalism can be used to simulate a wide range of materials and their properties which can be thought of as an assembly of nuclei and electrons. Its computational requirements scale proportionally to the volume of the simulation cell and with the third power of the total electrons number, depending also on the available computational memory and power.

The code has also the ability to use or directly construct "ultrasoft" pseudopotentials. In contrast with the norm-conserving pseudopotentials reported previously, the ultrasoft pseudopotentials exploit a scheme for relaxing the norm-conservation constraint, thus leading to a much smoother and highly transferable pseudopotential.

3.3.4 Linear-scaling DFT based on the Density Matrix

DFT methods, based on the equations outlined in the previous sections, require a computational effort that scales cubically with the system size N, or they have an $\mathcal{O}(N^3)$ scaling. They have been developed to minimise the energy functional iteratively by having to impose orthonormality constraints on the Kohn-Sham eigenstates. This "conventional" approach sets, in practice, an upper limit on the size of the simulated systems (as in calculations performed with the CASTEP code [3], regardless of the available computational resources). Linear-scaling methods [70], on the other hand, have an $\mathcal{O}(N)$ time scale, where their computational efficiency scales linearly with the system size. Such methods are important for employing a

first principles method accuracy in calculations extended to systems of larger sizes than those accessible with conventional approaches.

3.3.4.1 The ONETEP Approach

ONETEP [4] (Order-N Electronic Total Energy Program) is a linear scaling DFT code, in which the required time for a calculation increases linearly with the number of atoms, in contrast with other conventional DFT approaches mentioned previously. Because of this unique feature, the program is able to model molecular systems larger than ever before with DFT.

According to Kohn-Sham [55] theory 3.1.2, a fictitious system of non-interacting particles can be described by a single-particle density-matrix:

$$\rho(\mathbf{r}, \mathbf{r}') = \sum_i f_i \phi_i^*(\mathbf{r}) \phi_i(\mathbf{r}') \tag{3.3.10}$$

where $\phi_i(\mathbf{r})$ is a set of Kohn-Sham orbitals and f_i is the occupancy state of each $\phi_i(\mathbf{r})$ at zero temperature, therefore $f_i = 0$ or $f_i = 1$.

The diagonal elements of the density matrix define the charge density $n(\mathbf{r})$:

$$n(\mathbf{r}) = 2\rho(\mathbf{r}, \mathbf{r}) \tag{3.3.11}$$

where the factor 2 derives from the inclusion of electron spin, for closed-shell systems.

For a conventional DFT calculation each Kohn-Sham orbital $\phi_i(\mathbf{r})$ is allowed to expand over the entire system's space. Considering the overlap between each orbital and all the possible pairs of the N orbitals, the calculation time becomes eventually proportional to N^3.

In the ONETEP code [71], the expression of the density-matrix is given by:

$$\rho(\mathbf{r},\mathbf{r}') = \sum_{\alpha\beta} \varphi_\alpha(\mathbf{r}) K^{\alpha\beta} \varphi_\beta(\mathbf{r}') \tag{3.3.12}$$

where $\varphi_\alpha(\mathbf{r})$ are a set of spatially localised non-orthogonal functions, called non-orthogonal generalised Wannier functions (NGWFs) and $K^{\alpha\beta}$ is called the density kernel [72]. The density kernel is the density matrix defined by a set of duals φ^β of the NGWFs:

$$\langle \varphi^\beta | \varphi_\alpha \rangle = \int d\mathbf{r} \varphi^{\beta *}(\mathbf{r}) \varphi_\alpha(\mathbf{r}) = \delta_\alpha^\beta \tag{3.3.13}$$

In order to achieve linearity, the NGWFs are strictly localised in a spherical region around the atomic centre at position R and the density kernel is truncated beyond a cut-off distance r_{cut}. The density kernel is required to be a sparse matrix, thus we impose the condition:

$$K^{\alpha\beta} = 0 \text{ , when } r_{cut} < |R_\alpha - R_\beta| \tag{3.3.14}$$

The functions $\varphi_\alpha(\mathbf{r})$ are optimised during the calculation along with the density-kernel using the conjugate gradient method, to ensure strict localisation. The optimisation procedure involves the expansion of the NGWF in terms of "periodic sinc" or "psinc" functions $D_k(\mathbf{r})$ [73]:

$$\varphi_\alpha(\mathbf{r}) = \sum_k D_k(\mathbf{r}) C_{k,\alpha} \tag{3.3.15}$$

The psinc functions are, by construction, orthogonal and are related to plane waves by a Fourier transformation. The quality of the psinc basis set is improved systematically by varying the grid spacing of the psincs, which is equivalent to the kinetic energy cut-off parameter of plane waves. The fact that NGWFs are optimised

in situ allows plane wave accuracy to be achieved with only a minimal number of NGWFs (and hence the smallest possible sparse matrices). Furthermore, as the basis is independent of atomic positions and provides a uniform description of space, ONETEP calculations are not affected by basis set superposition error [74]. The code is parallelised and allows calculations to be performed on large systems containing thousands of atoms [75,76].

3.4 Tight-Binding DFT

Tight binding (TB) methods employ a minimal basis composed of localized atomic-like orbitals, as in linear combination of atomic orbitals (LCAO) method. The TB method has been mainly used for describing the electronic states of non-metallic systems, including covalently bonded materials. Unlike first principles methods, TB methods do not involve the direct computation of overlap and Hamiltonian matrix elements from explicit wave functions, but instead involve empirical fits to experiment or more accurate calculations, derived in most cases from first principles expressions. TB methods are generally less accurate and less transferable than density functional theory methods, but they provide a good alternative for simulating large systems in sufficient time scales, in contradiction with first principles methods.

Depending on their empirical parametrisation, TB methods vary considerably; from completely semiempirical to first principles-based, orthogonal to non-orthogonal, or self-consistent to non-self-consistent. The self-consistent charge (SCC) density functional tight binding (DFTB) method, incorporates a SCC mode into a modified reformulation of the Kohn-Sham total-energy functional, obtained from DFT. This charge dependent energy contribution improves the chemical transferability, resulting in improved values of reaction energies for several categories of molecules.

3.4.1 The DFTB Approach

The code used in this project, for performing TB-DFT calculations is called DFTB+ [2], which exploits the sparsity of the density matrix by using conventional dense diagonalisation algorithms. The matrices size increases linearly with the number of atoms, for large systems, while all the matrices are real for both periodic and non-periodic systems. The method developed in the code is based on a second-order expansion of the Kohn-Sham DFT energy with respect to charge density fluctuations [77]. A generic expression for the total DFTB energy is given by:

$$E_{DFTB} = \sum_{i}^{occ} \langle \phi_i | \hat{H}_0 | \phi_i \rangle + \frac{1}{2} \sum_{\alpha,\beta}^{N} \gamma_{\alpha\beta} \Delta q_\alpha \Delta q_\beta \tag{3.4.1}$$

The first term runs over the occupied single-particle wavefunctions ϕ_i and calculates the Hamiltonian energy for an input density n_0, which is equivalent to a common standard non-self-consistent TB scheme. The second term represents the second order extension of the Kohn-Sham energy of wavefunctions and potentials centred on atoms α and β. The charge fluctuations Δq_α and Δq_β of atoms α and β are defined by a SCC redistribution of Mulliken charges. $\gamma_{\alpha\beta}$ consists of a long-range pure Coulomb term and an exponentially decaying short-range function S:

$$\gamma_{\alpha\beta} = \frac{1}{R_{\alpha\beta}} - S(R_{\alpha\beta}, U_\alpha, U_\beta) \tag{3.4.2}$$

where $R_{\alpha\beta}$ is the distance between atoms α and β while U_α and U_β are the Hubbard parameters for these atoms respectively.

Chapter 4

Computational Study of Silicon Nanoclusters

The applications of silicon nanocrystalline particles have become an extensive and attractive area of research due to their diverse properties. Some of the most important applications involve energy conversion in photovoltaic solar cells [78], biomedical fluorescent imaging as biological sensors [79], electrical response in nanoelectronics as field-effect transistors [80], logic circuits [81], light-emitting diodes [82] etc.

Nearly three decades ago Canham [83, 84] discovered the photoluminescence at room temperature in visible red light of electrochemically etched silicon. As a result a variety of physical, chemical, and electrochemical techniques to produce dispersions of luminescent nanometre sized silicon crystallites were developed. Research led by Nayfeh [85] has demonstrated that by reducing the size of a Si crystal to a few tens of atoms ($\sim$1 nm), without altering its chemical composition, a nanoparticle is created with novel properties.

4.1 Synthetic Methods

4.1.1 Small Si Nanoparticles

Several procedures were developed for synthesising luminescent Si nanoparticles. These include physical, chemical, and electrochemical procedures.

A variety of physical techniques make Si nanoclusters in matrices of glass [86,87] and SiO_2 [88]. Nanocrystals of 3 nm are produced followed by annealing at 1100°C. Another technique involves laser ablation on silicon wafers using a variety of agents to produce isolated Si particles [89].

Isolated particles can be obtained also, by gas-phase preparation from silanes via slow combustion [90, 91], thermal decomposition [92], microwave plasma [93], gas-evaporation [94], or chemical vapour deposition (CVD) [95, 96].

Si nanoclusters in the range 2-10 nm can be chemically synthesised via a reduction of anhydrous ionic salts SiX_4 (X=Cl, Br), dispersed in water-free reverse-micelles solutions, with $LiAlH_4$ [97]. Unlike the physical methods mentioned above, which produce impure Si crystallites that contain a large amount of SiO_2 on the surface, this method produces Si particles with the surface terminated by hydrogen from metal hydride.

In general, SiO_2 inhibits the chemical activity of silicon. On the other hand, Si-O bonds can increase the reactivity of silicon nanosurfaces because these bonds induce polarisation in Si-Si and Si-H bonds of the surface, rendering them more amenable to functionalisation.

A dispersion method of single-crystal silicon wafers using aqueous HF/ethanol electrolyte and hydrogen peroxide (H_2O_2) as cleansing agent, produces ultrasmall

uniform size Si nanoparticles with discrete sizes of 1.0, 1.67, 2.15, 2.9, and 3.7 nm. These nanocrystals have distinct emission in the red, green, and blue light range, an ability which makes then favourable for biomedical tagging, RGB displays, and flash memories [85].

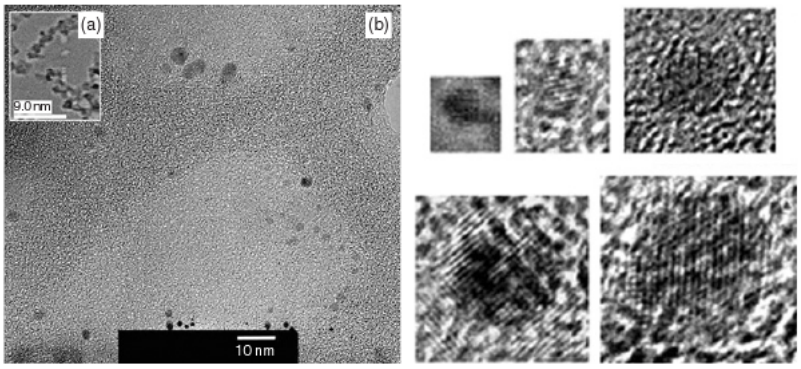

Figure 4.1: (Left) (a) and (b) TEM [10] images of Si particles on a graphite grid. The particles are nearly spherical and can be classified into a small number of discrete sizes. (Right) Closeup TEM images of the 1.0, 1.67, 2.15, 2.9 and 3.7 nm particles (from ref. [11])

4.1.2 Silicon Nanowires

There are two synthetic approaches for creating nanoscale silicon wire structures, which can be characterised as top-down and bottom-up. In the top-down approach, which is the conventional industrial method, silicon nanostructures are patterned in bulk materials by a combination of lithography, etching and deposition to form functional devices [98]. On the other hand, silicon nanowires (SiNWs) can be produced directly and without lithography using the bottom-up approach [99]. A key advantage of the bottom-up approach is that critical nanoscale features are defined during synthesis, which eliminates some of the lithography-based fabrication steps, and moreover, can yield structures uniform at the atomic scale.

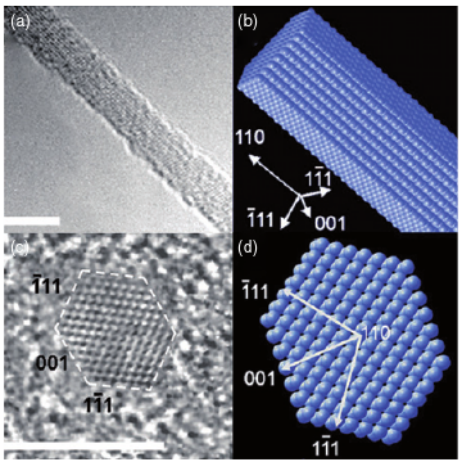

Figure 4.2: (a) TEM [10] images of 3.8 nm diameter SiNWs with [110] growth axis, (c) HRTEM cross-sectional image, and equilibrium shapes for the (b) nanowire and the (d) nanowire cross sections. Scale bars, 5 nm (from ref. [12]).

In general, the preparation of nanowires requires the material to be added during the growth process for restricting the growth to occur along one direction. In systems where atomic bonding is relatively isotropic, such as silicon, achieving 1D growth requires that the symmetry is broken during growth [100]. One common scheme involves the utilisation of a linear growth template to guide the material's growth only in 1D [101].

Another general strategy involves the exploitation of a nanocluster "catalyst" to enforce the growth to happen in 1D. The nanocluster or nanodroplet serves as the site that directs preferential addition of reactant to the main axial direction of a growing nanowire, much like a polymerisation catalyst directs the addition of monomers to a growing polymer chain [102]. The growing procedure is often terminated by using gold nanoparticles. Usually nanocatalytic crystal growth reactions involve the use of chemical vapour deposition (CVD) [103].

4.1.2.1 H-terminated Si nanowires

Perhaps, the best technique for synthesising stable hydrogen terminated SiNWs is the electrochemical dispersion of bulk silicon. Electrochemical dissolution of silicon followed by separation techniques, such as ultrasonic fracturing, produces col-

loidal suspension of particles in a variety of organic solvents which involve HF molecules [104]. The resulting porous layer is made up of one-dimensional crystalline nanowires and zero-dimensional nanocrystallites. These nanowires are hydride terminated, containing mono-($\equiv$ SiH), di-($=SiH_2$) and tri-($-SiH_3$) hydride groups and very little SiO_2 [105]. Hirata et al. [106] reported the production of completely pure H-passivated silicon nanoparticles when oxygen-terminated nanocrystalline silicon films were prepared by using silicon evaporation in ultra-high vacuum with oxygen and argon radicals, and then treated by HF.

4.1.3 Optical Properties of Si nanoparticles

The optical properties of Si nanoparticles can be greatly influenced by their surface chemistry, size and shape. As the size of silicon nanoparticles approaches the quantum regime, their electronic properties are substantially altered compared to a bulk material, due to the strong effect of quantum confinement [107]. Ultrathin silicon nanowires, for instance, demonstrate a blue shift in their optical spectra [83], while silicon quantum dots (QDs) can emit coloured light depending on their synthetic preparation [108]. Quantum confinement induces photoluminesence in the visible range of silicon particles by increasing their optical gap compared to bulk silicon.

Silicon is an indirect gap semiconductor, and requires a phonon in addition to a photon for excitation to the lowest minimum in the conduction band at 1.1 eV. The first direct gap, which requires no phonon for excitation, is at 3.3 eV. In a nanocrystallite, the energy levels become quantised due to confinement. For a 2.5 nm diameter silicon crystallite, the confinement shift is approximately 0.7 eV; this shifts the gap from 1.1 eV, in the infrared, to 1.8 eV, in the visible part of the spectrum.

4.1.4 Structural Properties of Si Nanowires

Synthesised SiNWs are single-crystalline nanostructures with uniform diameters and can be growth-controlled allowing them to be developed not only in different directions but also in various transverse shapes (square, pentagon, hexagon etc.) [109]. Studies on the crystallographic growth directions of SiNWs have also been investigated and revealed that the growth axes of SiNWs are related to their diameters [12, 110].

For diameters between 3 and 10 nm, 95% of the SiNWs were found to grow along the [110] direction; for diameters between 10 and 20 nm, 61% of the SiNWs grow along the [112] direction; and for diameters between 20 and 30 nm, 64% of the SiNWs grow along the [111] direction. These results demonstrate a growth preference along the [110] direction in the smallest SiNWs and along the [111] direction in larger SiNWs. For smaller-diameter SiNWs, the nanowire surface energy plays an increasingly important role in determining the growth direction. To our knowledge the thinnest nanowire reported in literature has a diameter of $\sim$1.3 nm [111].

4.1.4.1 Reconstruction in H-terminated Si surfaces

The surface of H-passivated Si nanoparticles determines to a great extent their chemical behaviour. There are three surface reconstructions reported in the literature. The (1$\times$1), which contains the highest coverage of hydrogen on the surface atoms, the (2$\times$1), which is formed by the reconstruction of unreconstructed H-passivated Si surfaces to (2$\times$1) monohydride phases and the (3$\times$1) reconstruction [112]. The (3$\times$1) phase is a mixture of monohydride and dihydride units (1$\times$1). The reconstruction of H-passivated Si(100) surfaces to form (2$\times$1) monohydride phases has been observed experimentally at 650K [113]. Also a (3$\times$1) reconstruction has been

observed at 370K. The (1×1) phase was mainly observed at room temperature and is consider to be highly disordered. Schematic representations of the observed reconstructions are shown in Figure 4.3.

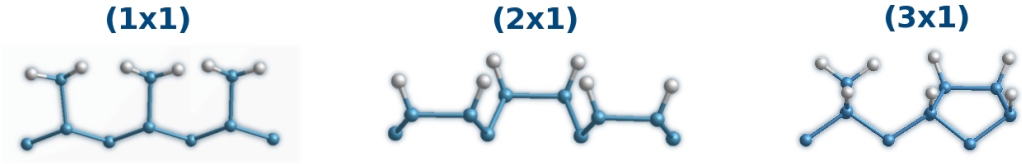

Figure 4.3: Known reconstructions of H-terminated Si nanoparticles. Blue and white spheres represent Si and H atoms respectively.

4.2 Computational Studies on Si Nanostructures

The variety of phenomena of Si nanocrystals makes their theoretical investigation difficult and challenging. Particularly, details regarding their atomic and electronic properties are important for extracting conclusions about their optical, magnetic, dielectric and conductivity properties, chemical reactivity, and stability.

Depending on the number of atoms that each system contains, different computational approaches can be used. In general, tight-binding (TB) methods are used to investigate systems containing from several hundreds to thousands of atoms; DFT methods have been used so far for sizes up to few hundred atoms, by employing the time-dependent density functional theory (TDDFT) approach to study excited states and optical spectra [114]. Other methods for studying excited states are based on the self-energy of a many-body GW approach [115] (direct product of a Green Function and a dynamically screened interaction W). Some accurate calculations which have been carried out for small silicon nanoclusters and periodic silicon systems have used quantum Monte Carlo (QMC) methods [116].

4.2.1 Ultrasmall H-passivated Si nanoparticles

The first structural prototype studied computationally was a spherical Si nanocrystal [117] , which for the experimentally observed size of 1 nm, contained 29 Si atoms (magic number for the Td symmetry and spherical shape). In $Si_{29}H_{36}$, all of the 36 dangling bonds of the Si surface atoms were terminated by hydrogen. However, the corresponding electronic energy gap was calculated at 6 eV, suggesting that the observed clusters possess smaller number of terminating hydrogens, with a part of the dangling bonds saturated by a nanocrystal surface reconstruction. By eliminating 12 H atoms the structure obtained is $Si_{29}H_{24}$ with six reconstructed surface Si-Si dimers.

After relaxation using DFT with the PW91 exchange-correlation functional, the resulting $Si_{29}H_{24}$ (Figure 4.2.1) found to have a band gap of 3.5 eV, close to the one observed experimentally (3.5$\pm$0.3 eV) [118]. The value 3.5 was derived after correction due the DFT gap underestimation.

The surface of a $Si_{29}H_{24}$ cluster can be represented as a 28-atom cage, similar to a filled fulerene structure, with a single silicon atom in the centre, bonded to four surface atoms (related by Td symmetry). The relaxed configuration, has five Si atoms constituting a single tetrahedral core and twenty four Si atoms constituting a H-terminated reconstructed surface. The surface Si atoms form four hexagonal rings while the whole structure of $Si_{29}H_{24}$ has six reconstructed dimers compared to $Si_{29}H_{36}$. The diameter of the prototype was 0.9 nm for the pure Si cluster and 1.066 nm including the H-termination.

In another computational work from Draeger et al. [119], first principles molecular dynamics (FPMD) simulations and QMC calculations were combined in order to determine the structural and optical properties of the 1 nm silicon particle. The

reconstruction of crystalline $Si_{29}H_{36}$ to $Si_{29}H_{24}$ was found to have an optical gap of 3.44 eV, in good agreement with experiment [118]. In addition to the symmetrical single-core, they also found two other configurations of the single-core particles $Si_{29}H_{24}$ with a different hydrogen distribution.

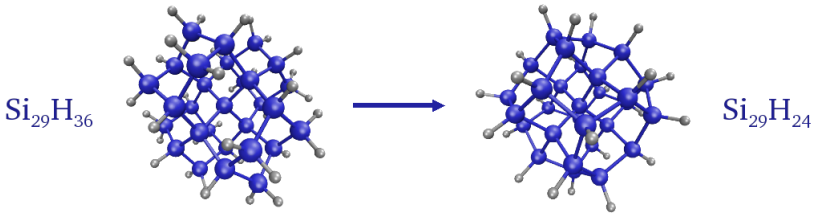

Figure 4.4: Bulk-like unreconstructed $Si_{29}H_{36}$ (Right) configuration and the filled fulerene reconstructed $Si_{29}H_{24}$ (Left) particle. (blue) Si atoms (white) H atoms.

Extending the diameter of the nanoparticles by few angstroms, Puzder et al. [120] studied the structural stability and optical properties of H-passivated Si nanospheres with reconstructed and unreconstructed surfaces and diameters from 0.7 to 2.0 nm (53-331 atoms). The (2×1) reconstructed facets were created by removing a H-atom from neighbouring pairs of SiH_2 groups forming an additional Si-Si bond. The nanostructures were optimised using DFT within the local density approximation, while the calculations regarding the formation energies were performed using QMC.

Their results, showed that the surface with the highest coverage of H-atoms ($Si_{148}H_{120}$) had the lowest formation energy when $\mu_H > -0.3$ eV. The reconstructed $Si_{148}H_{96}$ (2×1) and $Si_{148}H_{72}$ (3×1) found to be more energetically favourable when $\mu_H < -0.3$ and $\mu_H < -0.85$ eV respectively. In general, clusters with reconstructed surfaces were found to have weaker size dependence on their optical gap compared to unreconstructed, but the effect of the dimer reconstructions to the energy gab was less significant when the mean diameter of the nanospheres was larger than 2 nm. Similar conclusions were drawn by Northrup [113], who performed first principles

calculations on the formation energies of H-terminated Si surfaces by modifying the chemical potential of hydrogen μ_H. His results revealed that the (2×1) surface reconstruction is more stable when $-1.28 < \mu_H < -0.24$ eV, while (3×1) and (1×1) reconstructions occur when $\mu_H > -0.24$ and $\mu_H > -0.09$ eV respectively.

4.2.2 H-passivated Silicon Nanowires

Computational works studying silicon nanowires (SiNWs) with first principles methods are usually taking advantage of the periodicity of a crystalline structure in order to perform calculations about their properties. The surfaces of SiNWs are often passivated with an oxidised layer or hydrogen atoms for every dangling bond. An important amount of theoretical studies on SiNWs usually considers hydrogen-terminated structures for practical efficiency in construction and modelling. The effects of the quantum confinement on SiNWs can be understood, sufficiently enough, by using also H-passivated Si nanostructures.

Synthesised H-terminated SiNWs with rectangular shapes (widths 1-2.3 nm) and oriented along [100] direction were found to have a direct band gap that increased with a decrease in the mean diameter of the nanowire due to quantum confinement. Buda et al. [121] studied similar nanowires with diameter 1.5 nm confirming the previous conclusion. In many studies, quantum confinement effects have been considered within an effective mass approximation. However, Read et al. [122] observed deviations from the effective mass theory in nanowires thinner than 2.3 nm.

A theoretical investigation of the atomic and electronic structures, and optical properties of hydrogen-terminated SiNWs carried out by Zhao et al. [107] by performing first principles DFT calculations, showed that all the studied [110] nanowires had a direct energy band gap at the Γ point due to band folding; while the [111]

nanowires were exhibiting a transition from an indirect to direct band gap, on going from large to small diameters. The band gap was increasing sub-quadratically with decreasing thickness. The nanowires were cut from bulk Si along [110] and [111] directions at diameters up to 4.2 nm and were passivated with H such that no SiH_3 complexes would remain on the surface. Similar to studies for porous silicon, quantum confinement was becoming significant for diameters $\leqq$2.2 nm. The LDA band gaps were corrected using a many-body perturbation method based on the GW approximation [115]. The corrected band gaps for [110] SiNWs as obtained by Zhao et al. [107], were in good agreement with experimental values.

Singh et al. [13] studied the electronic and atomic structures of five different classes of hydrogenated SiNWs (NW_n, n=1-5) (Figure 4.2.2) oriented along [110], [100], and [112] for extracting conclusions regarding the role of their mean diameter, morphology, and orientation on their preferential growth behaviour. The nanowires were constructed from a bulk silicon crystal such that these were bounded by low index surfaces.

NW1 was oriented along the [110] direction along, as NW2 also, but with different facets in lateral directions. NW3 had the same structure with NW2 but

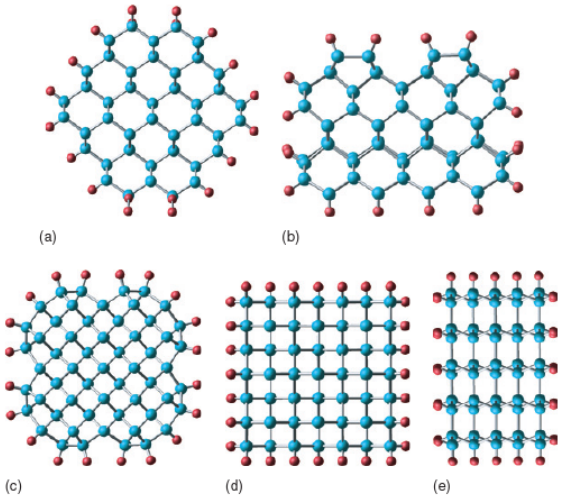

Figure 4.5: Cross-sections of the optimised structures of SiNWs. (a) NW1, (b) NW2, (c) NW3, (d) NW4, and (e) NW5. Red and blue spheres represent H and Si atoms, respectively. NW1 and NW2 are oriented along [110], NW3 and NW4 along [100] while NW5 is oriented along the [112] direction [13].

was oriented along [100] direction. NW4 was elongated along the [100] direction and lastly, the NW5 was similar to the thinnest experimentally observed SiNW, oriented along the [112] direction [111]. The surface of the NWs was terminated with H atoms so that each Si atom is tetra-coordinated. The NW2 and NW3 contained Si dimers, as observed on bulk Si(100) surfaces. In the case of NW5, the calculated Si-Si and Si-H bond lengths (3.85 and 1.5 Å respectively) on the (111) facets were found to agree well with experiments (3.80 and 1.5 Å).

A similar work conducted by Vo et al. [14] on H-passivated SiNWs grown along [100], [110] and [111] directions with diameters ranging from 1-3 nm, emphasises also the dependence of structural stability, band gap and effective mass on the size, growth direction and surface structure of the nanowires. The initial geometries of the NWs were relaxed using quantum Molecular Dynamics (QMD). By using the smallest periodic repeat unit from the optimised structures, geometry optimisations were performed, using LDA-DFT and *ab initio* self-consistent GW energy formation calculations.

Surfaces containing dihydrides in "canted" conformation were more stable than symmetric dihydrides. NWs grown in the [100] direction with surface reconstructions had larger bond length distributions and lower symmetries than the [110] and [111] directions. NWs containing canted dihydrides had no significant differences in bond lengths along the growth directions due to their minimal strain. For $\mu_H > -0.23$ eV the canted dihydride structure with the highest coverage in H-atoms had the lowest formation energy while for $\mu_H < -0.23$ the partial (2×1) reconstruction becomes more favourable. The [111] growth direction was found to be more favourable for $\mu_H > -0.7$ eV. For $\mu_H < -0.7$ the [100] direction is preferred. For NWs with small diameters, the [111] direction is the most favourable.

In the theoretical work of Singh et al. [13], the band gap was found to change

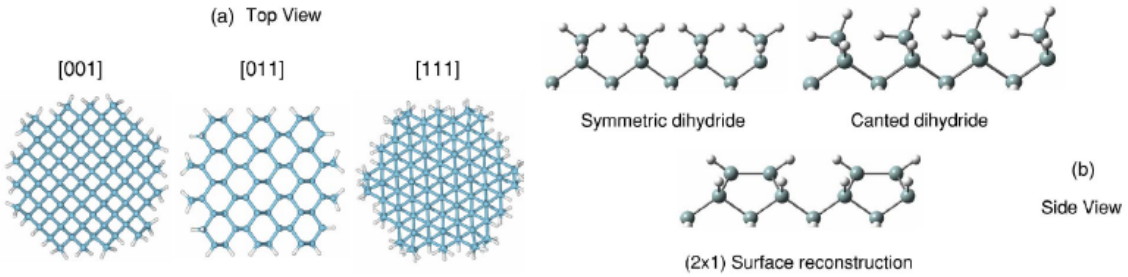

Figure 4.6: Fully relaxed 3 NM Si NWs: (a) in three different growth directions [001], [011], and [111], and (b) with three different surfaces [14].

with the orientation and thickness of the nanowires. In all studied cases the band gap was increasing when the diameter was decreasing due to quantum confinement, but the scaling was dependent on the morphology of the SiNWs (Fig. 4.6). Except for NW3 and NW4, the nanowires were direct band-gap semiconductors. The NW1 and NW2, which were oriented along the same direction, were found to have similar band gaps (1.34 eV). However, the band gaps for NW3 and NW4 were different by as much as 0.40 eV, though both were oriented along the same direction and had nearly the same thickness. This indicates that the scaling of the band gap with the diameter, depends strongly on the nanowire morphology. The band gap was increasing more rapidly for NW4 than in NW3, by decreasing the mean diameter, even though both nanowires were oriented along the same direction. Therefore this is in contrast with the conclusions of Zhao et al. [107], who were claiming that, is possible to fit the band gap in a universal function. The band gap for NW5 oriented along the [112] direction was calculated to be the largest (1.80 eV) among all the SiNWs of similar thickness. The actual band gap, though, is expected to be significantly higher because of the underestimation within the GGA. For [110] and [111] SiNWs with small diameters, Zhao et al. [107] calculated a correction to the band gap using the GW method, which was twice as much as the LDA value. Therefore, the final band gap was estimated close to the experimental value of 3.53 eV.

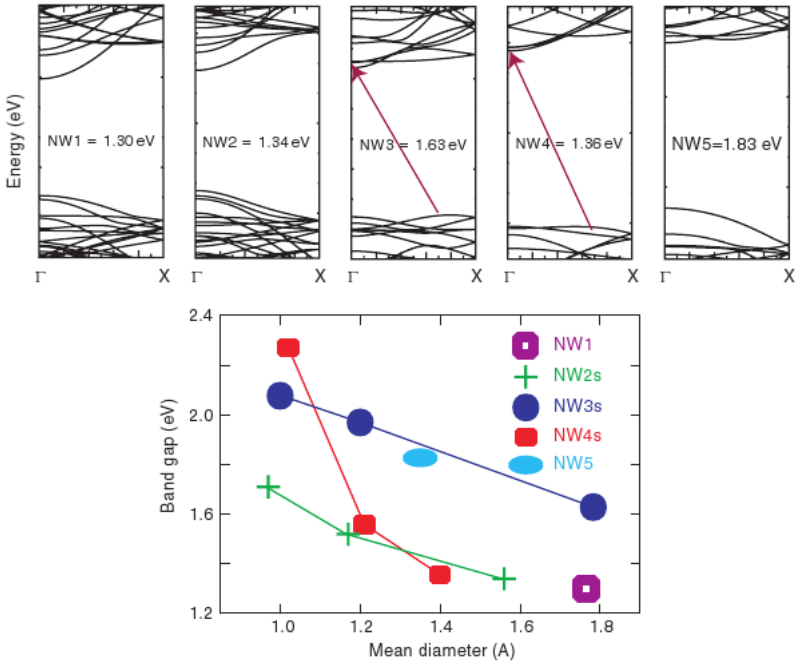

Figure 4.7: (Top) The electronic band structures and band gaps of NWn (n=1-5) SiNWs with comparable mean diameters. Arrows are drawn to show the indirect band gaps in NW3 and NW4. Major ticks on the y-axis are equivalent to 1 eV. (Bottom) Plot of the band gap versus mean diameter of the nanowires shows that in general the gap increases with decreasing diameter and it depends on the orientation of the nanowire. The dependence on mean diameter is similar for NW2 and NW3 but very different for NW4 showing a strong dependence on the morphology of the nanowire [13].

The results obtained from Vo et al. [14], in support of the conclusions made by Singh et al. [13], revealed that the canted dihydride structures had a decreasing band gap, from 2.35 to 0.88 eV for the [100] NWs, from 1.72 to 0.72 eV for the [110] NWs and from 2.12 to 0.85 eV for the [111] NWs, when the diameter was increased from 1.1 to 3 nm. The band gap of the reconstructed structures was varying from 2.03 to 0.64 eV for the [100] NWs, from 1.67 to 0.71 eV for the [110] NWs and from 1.54 to 0.84 eV for the [111] NWs. Nanowires grown along the [100] direction had the largest difference in band gap between the canted and reconstructed structures.

4.3 Calculations on H-Passivated Si Nanorods

Within the framework of this research project, first principle Density Functional Theory (DFT) calculations have been performed on entire silicon nanorods with more than 1000 atoms of varying aspect ratio and levels of surface passivation with hydrogen [21]. These large scale DFT calculations were performed directly for the whole nanostructures, without taking into account periodicity or symmetry effects (as in nanowires), mainly by using the ONETEP program [4].

In the following sections the results of this work are presented and discussed in the context of other works reported in the literature, along with their relevance to technological applications. The conclusions are summarised in the last section. The DFT calculations were performed within the GGA method using the Perdew, Burke and Ernzerhof (PBE) exchange-correlation functional [15]. The structures of the nanorods have been optimised using a density functional tight-binding approach, with the DFTB+ code [2], while energies and electronic properties have been computed with large-scale *ab initio* DFT calculations, using the ONETEP software package.

4.4 Construction and Validation

The H-terminated Si nanorods were constructed using the Accelrys Materials Studio [123]. Initially, pure silicon nanorods were formed from a bulk silicon diamond lattice by truncating a cylindrical shaped nanostructure. The [111] growth direction has been chosen to be the preferential elongation axis, since this is the mainly observed growth direction in several experimental works [14]. All the constructed nanorods had a fixed length of 5.0 nm with diameters varying from 0.8 nm to 1.3 nm. Within these dimensions, the nanorods were carefully shaped in order to avoid the existence of SiH_3 on the surface when saturating the dangling bonds of silicon atoms with hydrogen, as these groups are highly reactive [107]. Thus, the (1×1) unreconstructed H-passivated Si nanorods, had a surface containing both dihydrides (SiH_2) and monohydrides (SiH) while for the (2×1) reconstructed nanorods, the surface contained only monohydrides for allowing a uniform distribution of the reconstructed parts. The final structures were placed in a periodic box with a minimum 1 nm vacuum region, which is considered to be adequate enough for eliminating periodic interactions.

The nanoclusters were then pre-optimised, using tight-binding DFT, within a 0.05 eV/Å force tolerance. For describing the highest angular momentum of the tight-binding DFT Hamiltonian, s, p and d orbitals for Si atoms were included and for the H atoms, only s orbitals. The pre-optimisation of the structures, is required to distinguish the preferred tendencies for reconstruction, mainly for the (2×1) nanostructures. Any single dangling bonds that remained on the surface Si atoms were capped with hydrogens.

A full geometry optimisation was then carried out with DFTB+ for all the nanoclusters, and afterwards, the coordinates of the optimised structures were imported into the ONETEP code, to perform DFT energy and electronic properties calcula-

tions. The calculations were performed directly for the whole nanocluster within the same force tolerance and exchange-correlation functional, using a psinc kinetic energy cut-off of 300 eV. 6 NGWFs with 7.0 Bohr radius, for each Si atom and 1 NGWF with 6.0 Bohr radius, for each H atom, were found to be sufficient for the representation of Si and H atoms in the calculation, after conducting several tests on smaller systems, which are summarised in the next section.

The parameters for our calculations were selected, by performing extensive tests on the $Si_{29}H_{36}$ and $Si_{242}H_{140}$ model clusters using a variety of approaches.

4.4.1 $Si_{29}H_{36}$

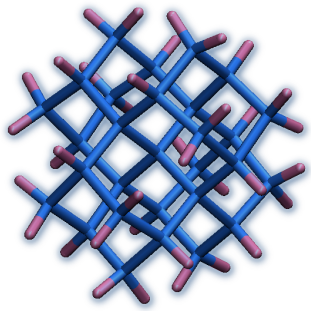

Figure 4.8: Optimised structure of $Si_{29}H_{36}$

DFT geometry optimisations, using the PBE exchange-correlation functional, were performed with ONETEP [4], CASTEP [3] (plane-wave DFT), NWCHEM [19] (Gaussian basis set DFT) and DFTB+ [2] (tight-binding DFT) on the $Si_{29}H_{36}$ quantum dot. An energy tolerance of 0.2 meV and a force tolerance of 0.05 eV/Å were used as convergence criteria for CASTEP, ONETEP and DFTB+. To optimise the geometry of $Si_{29}H_{36}$ with NWCHEM, the 6-31+G* basis set was used to describe both Si and H atoms.

The optimised structures obtained using the above codes showed that the central atom has a tetrahedral coordination which approaches almost identically the symmetry of a Si atom in bulk silicon, while the surface interatomic distances of neighbour silicon atoms are slightly shorter than the core. This is also observed by Dage Sundholm [124], in his simulations on $Si_{29}H_{36}$, with DFT and coupled-cluster

methods. The results summarised in Table 4.1 show the very good agreement between the optimised structures with all these methods.

Table 4.1: Comparison of Si-Si and Si-Si bond lengths as calculated with CASTEP [3], NWCHEM [19], ONETEP [4] and DFTB+ [2] for $Si_{29}H_{36}$

Interaction	**Interatomic Distances (Å)**			
	ONETEP	CASTEP	NWCHEM	DFTB+
Si-Si[a]	2.326	2.335	2.343	2.363
Si-Si[b]	2.319	2.325	2.337	2.339
Si-H[c]	1.503	1.487	1.509	1.503
Si-H[d]	1.498	1.480	1.503	1.498

[a]Si-Si neighbour distances of inner shell
[b]Si-Si neighbour distances of outer shell
[c]Si-H distances of Si atoms containing a single H
[d]Si-H distances of Si atoms containing two H

It is worth noting the remarkable agreement between the Si-H bond lengths described by ONETEP and DFTB+, even though the two programs use different approximation methods but still the same exchange-correlation functional. On the other hand, the Si-Si neighbour distances as calculated with ONETEP tend to agree better with the distances calculated by CASTEP. Both programs are *ab initio* DFT codes which use plane waves to describe the electronic wavefunction in contrast with NWCHEM which uses Gaussian basis sets to describe the atomic interactions.

It has been previously observed in ONETEP that, the best results for crystalline silicon are obtained when 9 NGWFs are used for representing the Si atoms, which is equivalent to the number of valence atomic orbitals [125]. However, to reduce the computational time and effort of the ONETEP calculations on our large nanoclusters, a smaller number of NGWFs and a lower kinetic energy cut-off were selected. By reducing the NGWFs from 9 to 6 and the kinetic energy cut-off from 650 eV to

300 eV, the final geometries of $Si_{29}H_{36}$ were observed to change only slightly ($\sim$ 1% in bond lengths and angles) and therefore, are still acceptable as these errors are less than those due to other approximations involved in DFT calculations.

4.4.1.1 Electronic Properties

The band gap of $Si_{29}H_{36}$ using ONETEP within the local density approximation (LDA) method, for the optimised structure was 3.75 eV, in good agreement with the LDA band gap calculated by Puzder et al. [126] (3.6 eV) and with the band gap reported by Wang et al. [127] (3.67 eV). When the B3LYP [63] exchange-correlation functional is used, the ONETEP calculation yields a 5.3 eV band gap, which is in excellent agreement with QMC results from reference [126] (5.3 eV) and B3LYP/6-31G(d) calculations from reference [127] (5.32 eV). Unfortunately the current implementation of B3LYP in ONETEP is not linear-scaling and does not allow us to study systems larger than $Si_{29}H_{36}$. The experimental excitation threshold of 3.5 eV [118] given to a hydrogenated Si_{29} nanoparticle mainly refers to the $Si_{29}H_{24}$ as supported by several studies [117] [119] [128].

4.4.2 $Si_{242}H_{140}$

In order to test the geometry optimisation effectiveness to provide surface reconstructions, sample calculations using a slice from a 2.0 nm thick nanorod have been performed. The slice, having 242 Si and 128 H atoms, was initially constructed with 24 free dangling bonds on nearby surface Si atoms, for allowing an optimum number of 12 reconstructions to happen. After a few geometry steps, the calculation revealed that only 6 reconstructions were able to occur, thus leaving 12 dangling bonds on the surface. These bonds were then filled with hydrogens yielding at the end the structure of $Si_{242}H_{140}$.

With ONETEP, the calculations were performed using a force tolerance of 0.05 eV/Å and a kinetic energy cut-off of 650 eV. In contrast with $Si_{29}H_{36}$ tests, in which an effectively infinite value for the kernel cut-off distance was used, in this case, the spatial cut-off of the density kernel was set to 13.23 Å. The optimised structure is shown in Figure 4.9, were the reconstructed Si-Si bonds have been highlighted.

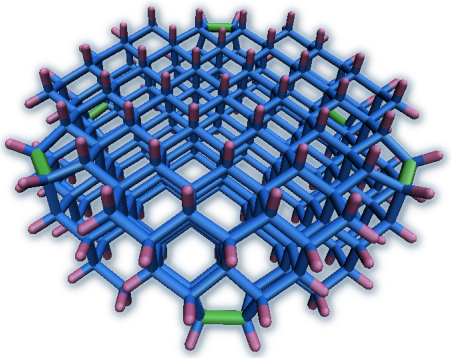

Figure 4.9: Optimised structure of $Si_{242}H_{140}$ using the ONETEP code [4]. Reconstructed Si-Si bonds are shown with green colour.

With the DFTB+ code, the calculation also produced a geometry with 6 surface reconstructions, similar to that of Figure 4.9 where the ONETEP code has been used. The differences in bond lengths between the optimised structures obtained with the two programs were comparable to the differences observed in $Si_{29}H_{36}$.

4.5 Results and Discussion

4.5.1 Structural Properties

Initially, the representative structures for the H-terminated Si nanorods at diameters 0.8, 1.1 and 1.3 nm, for the (1×1) surface reconstruction, were the $Si_{532}H_{308}$, $Si_{766}H_{402}$ and $Si_{1186}H_{462}$ respectively, which had the maximum coverage of H atoms on the surface. The first candidates, aiming to show (2×1) reconstruction on their surface after a structural optimisation, were the $Si_{532}H_{224}$, $Si_{766}H_{258}$ and $Si_{1186}H_{366}$. All the latter nanostructures had free, dangling bonds on pairs of neighbour, surface

Si atoms. After a full geometry optimisation, these parts would be able to "dimerise" and form a new Si-Si chemical bond.

A pre-optimisation on the initial (2×1) H-passivated nanorods revealed that the $Si_{766}H_{258}$ (1.1 nm diameter) was not liable for a complete surface reconstruction. The Si nanorods with diameters 0.8 and 1.3 nm had an even number of nearest neighbour Si atoms on the surface, where a dimerised Si-Si bond could occurred, thus allowing a full (2×1) reconstruction. The surface of the $Si_{766}H_{258}$ nanorod though, was containing free dangling bonds in a series of three neighbouring Si atoms. In this case, two possibilities have been considered: a) the three Si atoms could form a double dimerisation, thus giving two "conjoined", reconstructed Si-Si bonds b) only a pair of Si atoms can create a new bond, while the third Si atom with a free dangling bond should be passivated with an extra H atom. The latter procedure is necessary to obtain closed-shell systems in order to perform calculations with ONETEP. Schematic representations of the possible reconstructions are shown in the image below.

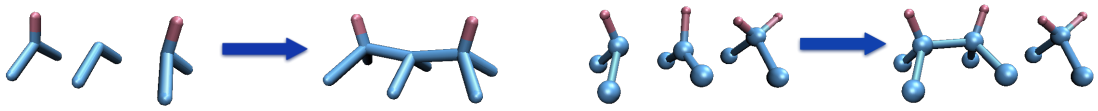

(a) (b)

Although the first possibility seemed quite promising, this kind of reconstruction was impossible to occur in all the parts of the (2×1) reconstructed surface. Hence, the surface of $Si_{766}H_{258}$ was reformed so in every part of the surface were the dimerisation should occur, only pairs of neighbouring Si atoms with one free dangling bond each, would appear. Any surface Si atom with a free dangling bond located next to a pair of Si atoms with free bonds, should hold, in this case, two H atoms instead. Hence, this lead to the representative $Si_{766}H_{318}$ nanostructure for the 1.1 nm diameter nanorod with partial (2×1) surface reconstruction .

Plots of nearest neighbour interatomic distances (bond lengths) between silicon atoms in the optimised geometries, radially away from their axes, are shown in Figure 4.12. To observe the variation of bond lengths along the length of the nanorod, its volume was separated in sections, across the growth axis being aligned at the centre of mass, as can be seen in Figure 4.10. The Si-Si bond lengths were calculated then with respect to the perpendicular distance of a point located at the middle of a bond length from the central axis. The plots located in the top of Figure 4.12 refer to the (2×1) reconstructed nanorods and those located at the bottom refer to the (1×1) unreconstructed nanostructures.

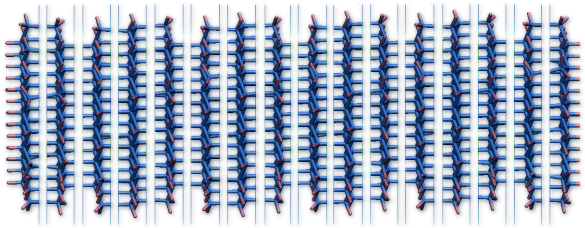

Figure 4.10: Separation of a nanorod in sections

Each diagram of Figure 4.12 shows two kinds of distribution; the distribution of distances along the caps of the nanorod and the distribution along the main part. As expected, due to the different shapes between the caps and the main body of the nanorod, the deformation of interatomic distances creates a bigger dispersion of points which becomes more apparent in the thinnest (2×1) nanostructure and as the diameter increases the fitting curves between the caps and the main part tend to coincide.

As can be seen from Si-Si neighbour distance distribution across the whole volume of the constructed nanorods, from the centre of mass to the surface, there is a homogeneous distribution of the Si-Si distances in the "core" which is later disrupted as the surface is reached. Si-Si bond lengths located at the inner part of the volume, are distributed around 2.36 Å, which is the Si-Si distance in bulk silicon as calculated using the PBE exchange-correlation functional, for all the H-passivated silicon nanostructures. Approximately 25% of the total volume of the

thinnest nanorod maintains the structural properties of the bulk crystal and as the diameter of the nanorod increases this can extend up to 45% for the (2×1) reconstructed nanorods, while for the (1×1) unreconstructed nanorods this range goes approximately from 60% to 75%.

As we move along the diameter of the nanorod and we approach the surface, structural differences between the reconstructed (2×1) and unreconstructed (1×1) nanostructures emerge. The Si-Si bond length in the (1×1) surfaces becomes significantly shorter (∼2.33 Å) and as shown in Figure 4.12 the points around the fitting curve present a similar dispersion with the points located inside the inner volume of the nanorod in all the (1×1) nanorods studied in this work. This tendency, is also observed in several theoretical studies on H-passivated silicon nanowires [14] [129] and can be justified by the steric hindrance the hydrogen atoms exert on the silicon atoms of the surface. The Si-H interatomic distances are distributed around 1.50 Å which are in agreement with the results obtained by Nolan et al. [129] (1.53 Å), who have also performed DFT calculations using the PBE exchange-correlation functional on silicon nanowires with diameters of about 1 nm. Despite that, they have found that a "canted" conformation between surface hydrogen atoms does not occur in (1×1) reconstructed surfaces, while our results show that the "canted" conformation can actually occur in specific parts of the surface, as proposed also by Vo et al. [14]. Schematic representations of "canted" hydrogens observed in our structures are shown in Figure 4.11.

Figure 4.11: Schematic representation of symmetric hydrogens (before geometry optimisation) and "canted" hydrogens (after geometry optimisation) located on a part of the surface of the (1×1) reconstructed $Si_{766}H_{462}$ nanorod

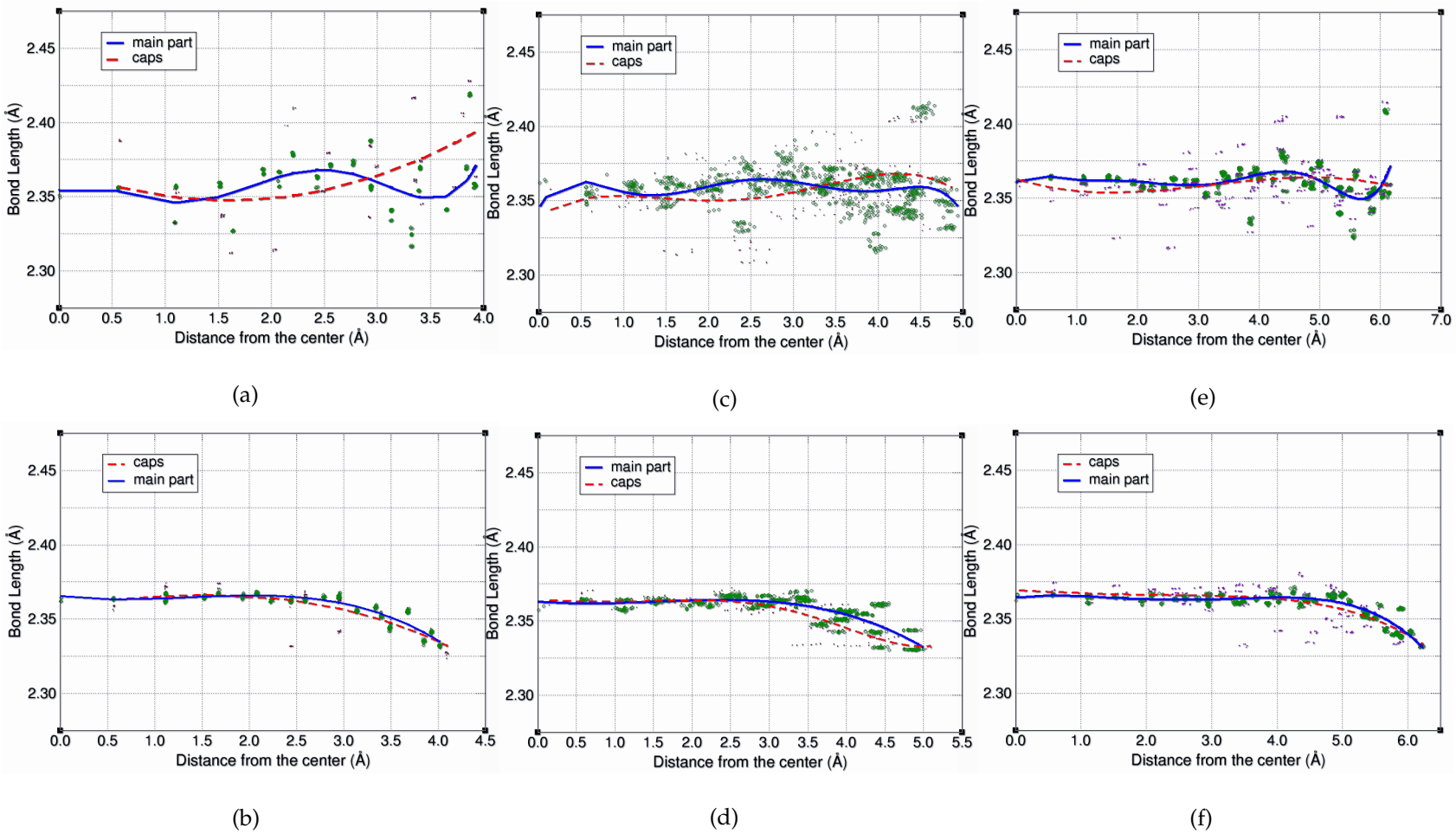

Figure 4.12: Diagrams of nearest neighbour interatomic distances in of $Si_{532}H_{224}$ (a), $Si_{532}H_{308}$ (b), $Si_{766}H_{318}$ (c), $Si_{766}H_{402}$ (d), $Si_{1186}H_{366}$ (e), $Si_{1186}H_{462}$ (f). Si-Si bond lengths located at the caps are represented with dots while bond lengths located in the main part are shown with circles.

While the (1×1) reconstructed surfaces have a similar dispersion of Si-Si interatomic distances for all the studied diameters, this phenomenon cannot be observed in the (2×1) reconstructed surfaces. The dispersion of points along the curve of diagrams (a), (c) and (e) in Figure 4.12 results in a non-uniform behaviour of interatomic Si-Si distances from the thinnest nanorod to the thickest. Despite this, it can be observed that Si-Si distances can have a range between 2.33 Å and 2.42 Å on the (2×1) surface, while the Si-Si distances at the "core" of the (1×1) unreconstructed silicon nanorods are near 2.36 Å.

On the other hand, the diagrams clearly show a grouping of points on specific areas of interatomic distances as we move from the centre to the surface of each nanorod, mainly regarding the main part. This is another factor in support of structural stability and a homogeneous dispersion along the length of the nanorod. Although this scheme applies in the majority of the studied nanostructures, the difference observed mainly in the $Si_{766}H_{318}$ nanorod (diagram (c) of Figure 4.12) results from the presence of both dimers (SiH_2) and monomers (SiH) on the surface. Consequently, the displacement of Si-Si bond lengths located near dimerised atoms is different from the displacement observed in silicon atoms attached to surface dimers.

4.5.2 Formation Energies

In order to investigate the stability of the nanorods and how this is affected by their surfaces and aspect ratios, the formation energies (E_f) have been calculated using the formula [130]:

$$E_f = \frac{(E^{tot} - (n_H E_H))}{n_{Si}} - E_{Si} \tag{4.5.1}$$

where E^{tot} is the total energy of the Si nanorod, n_{Si} and n_H are the number of

silicon and hydrogen atoms contained in it, E_{Si} is the energy of one Si atom in a bulk silicon crystal and E_H the energy H atom in a H_2 molecule. For calculating the energies E_{Si} and E_H single point energy calculations were performed with ONETEP for bulk silicon and for a H_2 molecule.

The structures for bulk Si and H_2 were optimised first with the DFTB+ code. Using the parameters reported in reference [125] for describing the Si atoms within the PBE exchange-correlation functional, single point energy calculations were performed with ONETEP on these structures as well as on the H-passivated Si nanocrystals, to obtain their total energy. The results are shown in Figure 4.13.

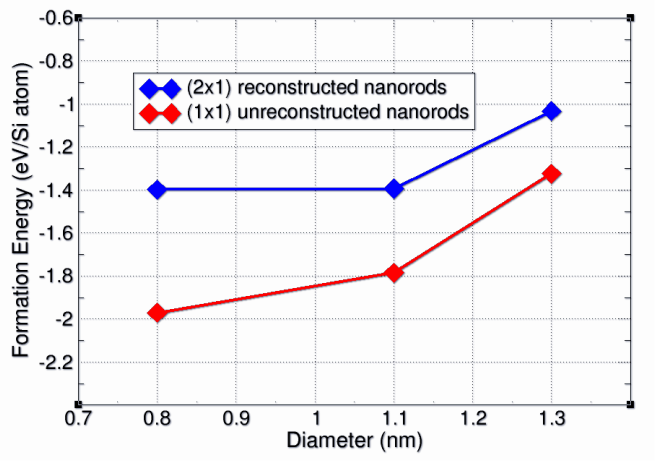

Figure 4.13: Formation energies of the (2×1) reconstructed (blue) and (1×1) unreconstructed (red) nanorods

The plot of Figure 4.13 shows at first the stability of the studied nanoclusters, with formation energies per Si atoms lying between -2.0 to -1.0 eV, as calculated by using equation 4.5.1. The (1×1) unreconstructed structures with the highest coverage in hydrogen, have lower formation energies compared to the (2×1) reconstructed nanorods, which indicates their higher stability. This is also confirmed by the results of Vo et al. [14], who have proved that the "canted" dihydride structures are more favourable when silicon nanowires are exposed to atomic H. Secondly, the trends of the lines in Figure 4.13 reveal that as the number of atoms increases the formation energies are decreased as the size of our nanoclusters approaches the bulk limit, eventually expected to become zero. On the other hand, while the trends

for the (1×1) unreconstructed nanostructures are consistent with the latter scheme, the stabilities of the $Si_{532}H_{224}$ and the $Si_{766}H_{318}$ nanorods seem to be relatively the same. This can be justified by the presence of dihydride (SiH_2) groups on the (2×1) reconstructed surface of the $Si_{766}H_{318}$, which induces less strain between the reconstructed surface parts and consequently lowers the formation energy.

4.5.3 Energy Band Gaps

The energy band gaps of silicon nanostructures can be affected by the diameter, the surface structure and the growth direction in the case of silicon nanowires. As expected, it is observed that as the diameter of a nanocluster is decreased the energy band gap increases, due to quantum confinement effects [107]. This phenomenon is observed in the majority of the silicon structures studied at a nanoscale whether quantum dots [120], nanowires [13] or nanotubes [131]. In the case of silicon nanowires, this trend also applies not only on structures with different growth directions but also between nanowires with different surface reconstructions [132].

As reported in section 1.2.2, Vo et al. [14], found that both (1×1) and (2×1) reconstructed surfaces of [111] grown hydrogenated silicon nanowires reduce their band gaps from 2.12 eV to 0.85 eV and from 1.54 eV to 0.84 eV respectively, as their diameter increases from 1.1 to 3.0 nm. Zhao at al. [107], found that the band gap of [111] Si nanowires was also decreased from 2.3 to 0.8 eV, as their thickness increases from 0.9 to 3.2 nm. In a similar work conducted by Saita et al. [133], the energy band gaps of [111] Si nanowires with diameters 0.55 to 1.0 nm varied from 2.83 to 1.90 eV.

The band gaps obtained from our calculations are shown in Figure 4.14. We can observe a reduction of the band gap as the diameter of the nanorod is increased, which is consistent with the studies mentioned before. On the other hand, the reconstructed surfaces tend to have smaller band gaps from the unreconstructed, as

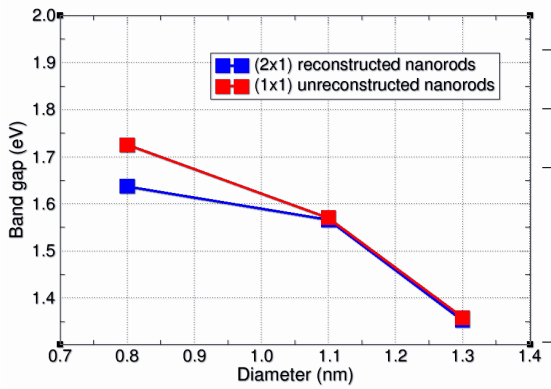

Reconstructions			
(1×1)		(2×1)	
$Si_{532}H_{308}$	1.725 eV	$Si_{532}H_{224}$	1.637 eV
$Si_{766}H_{402}$	1.571 eV	$Si_{766}H_{318}$	1.566 eV
$Si_{1186}H_{462}$	1.358 eV	$Si_{1186}H_{366}$	1.353 eV

Figure 4.14: Energy band gaps of optimised H-terminated Si structures calculated with ONETEP [4] using the PBE exchange-correlation functional [15].

being observed also by Vo et al. Although this trend is obvious in the nanorods with diameters 0.8 nm, the coinciding of the lines between the reconstructed and unreconstructed surfaces for the 1.1 nm and the 1.3 nm thick nanorods in Figure 4.14 indicates the small role played by the surface as the diameter of the nanorod increases.

The values shown in the table of Figure 4.14 represent the HOMO-LUMO gap obtained directly from GGA-DFT calculations using the PBE exchange-correlation functional. Although it is known that GGA methods generally underestimate energy band gaps they can still provide qualitative trends of optical gaps. A self-energy correction method, such as the GW approach, has not been attempted due to the prohibitive amount of computer time such a calculation would require in its application to our nanoclusters.

4.5.4 Density of States

The total electronic density of states (DOS) of bulk crystalline silicon and the nanoclusters $Si_{532}H_{308}$, $Si_{766}H_{402}$, $Si_{1186}H_{462}$, $Si_{532}H_{224}$, $Si_{766}H_{318}$ and $Si_{1186}H_{366}$, are given in Figure 4.15. The DOS for the H-terminated Si nanorods were calculated with

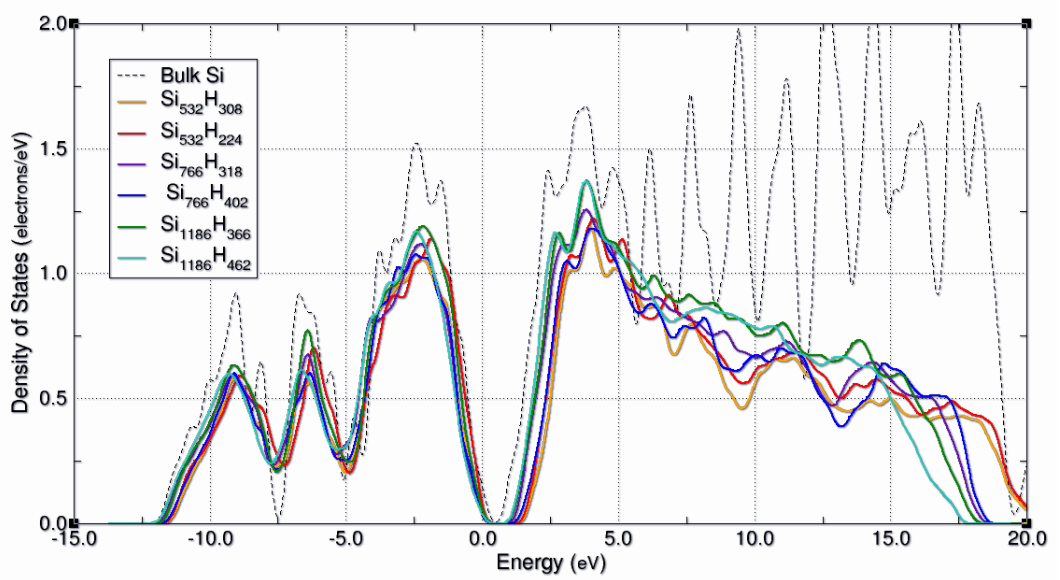

Figure 4.15: Density of states (DOS) of $Si_{532}H_{308}$, $Si_{766}H_{402}$, $Si_{1186}H_{462}$, $Si_{532}H_{224}$, $Si_{766}H_{318}$ and $Si_{1186}H_{366}$ as calculated with ONETEP [4]. The DOS for bulk silicon (dotted line) has been calculated with CASTEP [3].

ONETEP while the DOS for the bulk material was calculated with CASTEP, using a periodic unit cell of 2 Si atoms and an 8 k-point sampling. In both programs the PBE exchange-correlation functional was used.

The plot clearly shows the reduction of the band gap as the diameter of the rod is increased by approaching the bulk limit. While the DOS peaks placed in the valence band area are in close agreement between the two programs, there is strong disagreement for the conduction bands. This phenomenon was also observed in the work of Skylaris and Haynes [125] when they performed DFT calculations within the LDA scheme on a 1000-atom silicon lattice and concluded that the ONETEP NGWFs are usually capable of describing correctly only valence and the low-lying conduction bands. The DOS of the nanorods in the valence area for the (1×1) reconstructed surfaces resemble closer with the DOS of bulk silicon. This also justifies the fact that H-passivated silicon nanostructures can often be sufficient for extracting conclusions regarding the properties of pure silicon nanoparticles.

4.5.5 Orbital Densities

Isosurface plots of the squares of HOMO and LUMO orbitals of the studied hydrogenated silicon nanorods are given in Figure 4.16. The HOMO orbitals of all the nanostructures and the LUMO orbitals of $Si_{532}H_{224}$, $Si_{532}H_{308}$, $Si_{766}H_{402}$ and $Si_{1186}H_{366}$ are localised at the centre of mass ("core"). The LUMO orbitals are degenerate and all the LUMO orbitals of the studied nanorods shown in Figure 4.16 intersect the growth axis at an angle. Surprisingly the LUMO orbitals of the $Si_{766}H_{402}$ and the $Si_{1186}H_{462}$ are showing a localisation closer to the caps of the nanorod with the LUMO orbital of $Si_{1186}H_{462}$ to be localised exclusively at the caps. A quite similar phenomenon was observed in the LUMO orbitals of reconstructed and unreconstructed quantum dots with 0.8 nm diameter [120], although in this case the localisation of the orbital is shifted from the core to the surface when going from an unreconstructed (1×1) to a reconstructed (2×1) surface. As the hydrogen passivation of the surface provides a relatively small barrier for electrons and holes, the HOMO and LUMO orbitals spill out more from the core as the diameter is reduced.

On the other hand, while similar studies have shown the dependence of the band gap on the growth direction, diameter and surface reconstruction and therefore the localisation of HOMO and LUMO orbitals, by extracting conclusions for each factor separately, our results clearly indicate that these factors are strongly inter-related. Consequently, the electronic properties of H-passivated nanorods studied here can be significantly affected by the contribution, weak or strong, of all these factors simultaneously. The shift in the localisation of the HOMO and LUMO densities from the core to the surface for the LUMO, while the HOMO remains in the core, can be compared to the transformation of the energy band gap from "direct" to "indirect".

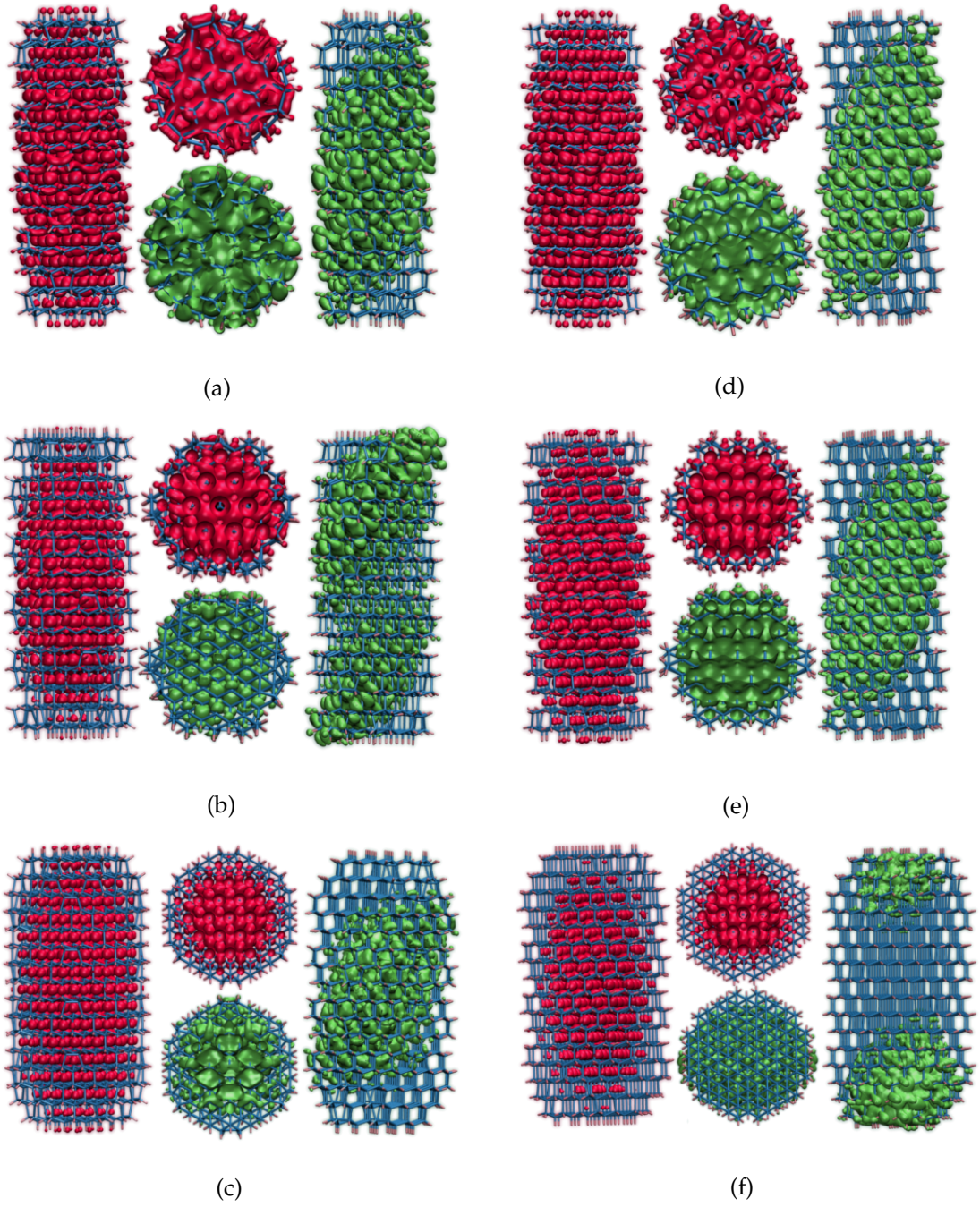

Figure 4.16: Representations of HOMO (red) and LUMO (green) orbital density plots for $Si_{532}H_{224}$ (a), $Si_{532}H_{308}$ (d), $Si_{766}H_{318}$ (b), $Si_{766}H_{402}$ (e), $Si_{1186}H_{366}$ (c), $Si_{1186}H_{462}$ (f) nanorods. Each diagram shows a horizontal view from each orbital, parallel to the nanorod's growth axis, and a vertical view, by clipping the nanorod through a plane at its centre of mass. The isosurfaces were generated by using an isovalue of $1 \times 10^{-5} \frac{e}{a_0^3}$.

4.6 Conclusions

This chapter summarises the results of a DFT study on entire silicon nanorods with varying diameters and surface passivation by hydrogen. The structures chosen were based on several experimental data and the available computational resources, at the time, with the ONETEP [4] and the DFTB+ code [2]. Although the modelled systems may not have a direct representative structure from experiment, they can be considered as an initial step towards the modelling of larger systems that are closer to synthesised silicon nanowires and nanoclusters, which can be investigated at the atomistic *ab initio* level using the "superlattice" approach.

In agreement with experiment, the (1×1) unreconstructed nanorods showed higher stabilities compared to the (2×1) reconstructed nanostructures, which decrease by increasing the thickness of the nanorod. Similarly, a reduction of the energy band gap was observed when the diameter of our H-terminated silicon nanorods was increased from 8 Å to 13 Å. Furthermore, the surfaces of the (1×1) unreconstructed nanorods adopted a "canted" conformation between neighbour H atoms, as also being observed by other theoretical studies.

Chapter 5

Computational Prediction of Au L_{III} EXAFS Spectra

A computational approach for simulating extended x-ray absorption fine structure (EXAFS) spectra of nanoparticles directly from molecular dynamics simulations is presented in this chapter. The method shown consists of two stages. First, a molecular dynamics simulation of a constructed gold nanoparticle is performed, followed by a calculation of an Au L_3-edge EXAFS spectrum using the FEFF 8.4 package [5]. A probability distribution function calculated directly from an ensemble of molecular dynamics snap-shots is used to ensure a balanced sampling of photoabsorbing atoms and their surrounding scattering atoms while keeping the number of EXAFS calculations that need to be performed to a manageable level. The calculated EXAFS resulting from all configurations are merged into an average spectrum.

The work in this chapter was done in collaboration with Dr Otello Roscioni. This work has been recently published in Physical Review B [22].

5.1 Experimental Synthesis and Analysis

Small metal nanoparticles, with diameters in the range of 1-10 nm, present some fascinating physical and chemical properties when compared to their bulk counterparts. These can be attributed to the discretisation of their energy levels which are strongly dependent on their morphology [134, 135]. Therefore their electronic, magnetic and optical properties are "tunable" with regards to their size, shape and surface termination that make them attractive for applications in catalysis, biosensing and electronic devices.

It is important to have reliable synthetic pathways to be able to obtain metal nanoparticles which are uniform and of the desirable chemical and physical properties. Equally important for this goal is the ability to characterise the synthesised nanoparticles in order to ascertain that the desired morphology has been produced. The x-ray diffraction technique (XRD), can provide very precise structure determination in the case of molecular crystals, but in the case of the metallic nanoparticles can result in significant ambiguity in attempts to accurately measure cell parameters and atomic distances.

On the other hand, x-ray absorption spectroscopy (XAS), and more specifically within the extended x-ray absorption fine structure (EXAFS) region, has been able to provide accurate results for the atomic structure of nanoparticles as a function of temperature [136, 137]. Within this framework, factors which can induce structural reconstructions, such as surface tension, capping ligands, steric hindrance effects, and metastable states can significantly alter their physicochemical properties that can be quantified by EXAFS experiments [138].

5.1.1 X-ray Absorption Spectroscopy

X-ray absorption spectroscopy (XAS) is a technique for determining the local electronic and geometric structure of materials, whether in gas, liquid, or solid phase. Amongst its several applications, XAS is used in solid state science, for studying catalytic surfaces and interfaces, in mineralogy, in geochemistry and also in molecular biology. The XAS method has the advantage of being able to probe disordered and amorphous materials with the XAS signal coming from all the atoms of a selected element. It is capable of obtaining structural and chemical information about the atomic environment around the absorbing atom.

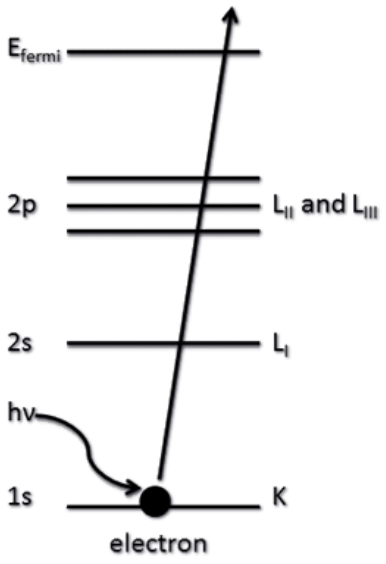

Figure 5.1: A photoelectron from the 1s orbital gives rise to the K edge.

In x-ray absorption spectroscopy the sample is irradiated with tunable monochromatic x-ray radiation. The absorption of the x-rays by the molecular system occurs by exciting electrons into higher-energy unoccupied orbitals or into the continuum (where the electrons are unbound to the atoms). As such the absorption of x-rays is energy dependent. The phenomenon of electron ejection is called the ”photoelectric effect” and the excited electrons are then referred to as ”photoelectrons“. The promotion of an electron to a higher energy orbital empties an orbital, which is then called a ”hole“, and takes place within a femto-second (10^{-15}).

The intensity of the incident x-rays I_0, is reduced when passing through the sample. Consequently, the intensity of the transmitted x-rays I_t from a sample decreases exponentially, depending on the thickness of the sample x and the absorption coefficient of the sample μ:

$$I_t = I_0 e^{-\mu x} \tag{5.1.1}$$

As the incident photon energy is increased, absorption will decrease until the binding energy of a core electron is reached. When an electron inside the core is excited, a sharp rise in absorption occurs, known as the "absorption edge" E_0 (Figure 5.2). The absorption edge depends on the nuclear charge of each element, so that different orbitals will have different energies. The whole spectrum typically covers a $\sim$1 keV region, mostly on the high energy region of the absorption edge.

Beyond the absorption edge, increasing the energy results in a decrease in absorption until the next binding energy is reached. The intensity of the absorption edge is determined by the absorption coefficient μ and each absorption edge is named and ordered in terms of decreasing energy, from K, L_I, L_{II}, L_{III} etc., based on the principal quantum number from which the electron was ejected. Hence, the K shell (n=1) corresponds to an excitation from the 1s orbital, the L shell (n=2) refers to the 2s, $2p_{1/2}$ and $2p_{3/2}$ corresponding to the L_I, L_{II} and L_{III} edges respectively, as shown in Figure 5.1.

The XAS spectrum is approximately divided into two main regions; the XANES (X-ray Absorption Near Edge Structure) and the EXAFS (Extended X-ray Absorption Fine Structure) region. An example of a XAS spectrum with its subdivided areas is shown in Figure 5.2. The following sections are focused only on the EXAFS spectroscopy.

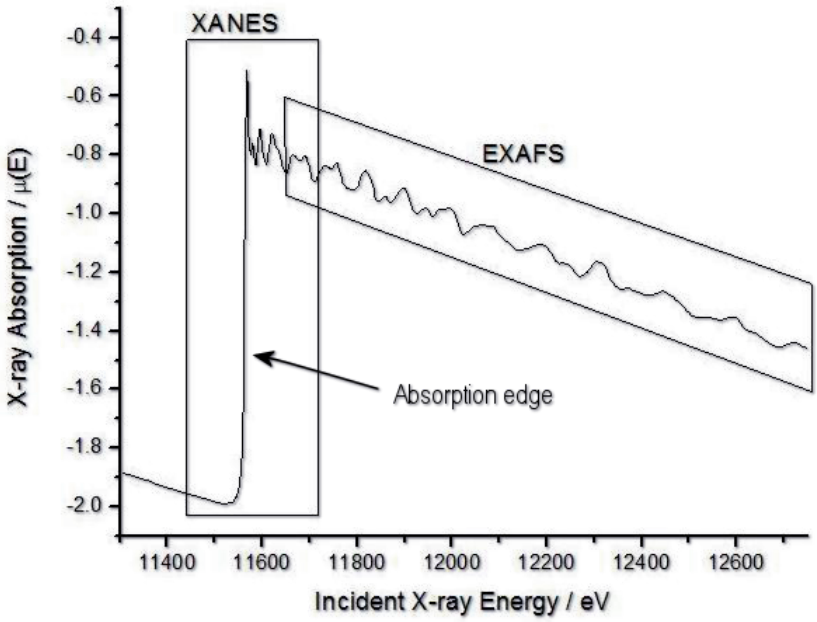

Figure 5.2: Sample of an XAS spectrum at the L_{III} edge, showing XANES and EXAFS regions [16].

5.1.2 Extended X-ray Absorption Fine Structure

Typically the EXAFS region starts at ∼30-40 eV above the absorption edge. The oscillations at this area are defined by the EXAFS fine-structure functions $\chi(E)$ as:

$$\chi(E) = \frac{\mu(E) - \mu_0(E)}{\Delta\mu_0(E)} \tag{5.1.2}$$

where $\mu(E)$ is the measured absorption coefficient, $\mu_0(E)$ is a smooth background function representing the absorption of an isolated atom, and $\Delta\mu_0(E)$ is the measured jump in the absorption $\mu(E)$ at the threshold energy E_0 of the absorption edge.

The photoelectrons can be described as spherical waves, propagating outward from the absorbing atoms. These waves, are scattered from the atoms surrounding

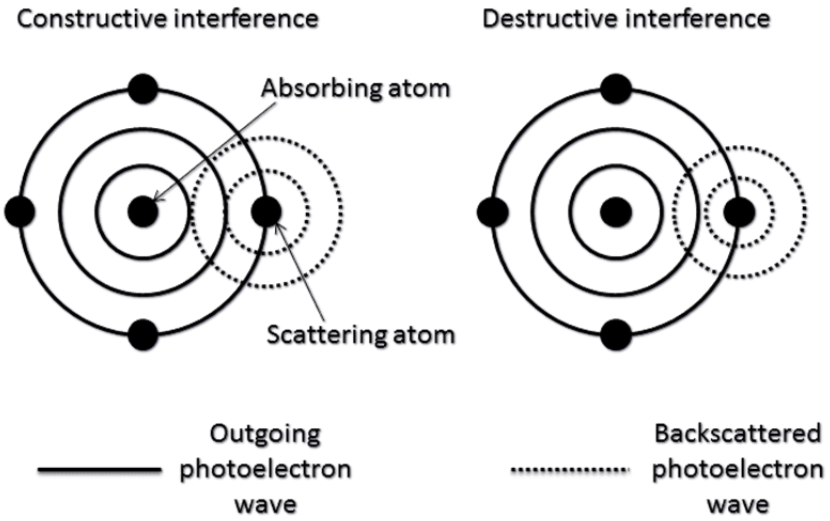

Figure 5.3: Schematic of constructive and destructive interference of an outgoing photoelectron. The circles represent the maxima of the photoelectron waves [16].

the photoabsorber. The relative phase of the outgoing photoelectron wave and the scattered wave at the absorbing atoms affects the oscillations recorded on the EXAFS spectrum. When the waves are out of phase (destructive interference), a minimum absorption occurs and vice versa, as depicted in Figure 5.3.

When the energy of the x-rays incrementally increases, the wavelength of the corresponding photoelectron decreases. The sum of the outgoing and scattered waves at the absorbing atoms oscillates with a periodicity that is related to the average atomic distances between the absorbing and the coordinating atoms. The group of atoms that contribute the same component with the photoabsorbing atom are defining a "shell". Photoelectrons scattered from the photoabsorber to the neighbouring atoms define different scattering paths. Single scattering paths are formed between atoms of the same shell, while paths from atoms in different shells define a multiple scattering path.

The wave behaviour of the photoelectrons participating in the x-ray absorption/emission process is expressed in terms of the wave number k, which is expressed in terms of the x-ray energy:

$$k = \sqrt{\frac{2m(E - E_0)}{\hbar^2}} \tag{5.1.3}$$

where m is the electron mass and E_0 the absorption edge energy.

The primary quantity of EXAFS becomes then $\chi(k)$, which is a function of the photoelectron wave number. $\chi(k)$ is often referred to as "the EXAFS", and provides a general equation which describes the EXAFS spectrum, which is written as a sum of the contribution from all scattering paths of the photoelectron from each shell j:

$$\chi(k) = \sum_j \frac{S_0^2 N_j f_j(k) e^{-2k^2 {\sigma_j}^2}}{kr^2} \sin(2kr_j + \alpha_j(k)) \tag{5.1.4}$$

where $f(k)$ and $\alpha(k)$ are scattering properties of the neighbour atoms of the photoabsorber, N is the number of neighbouring atoms, r is the distance between the photoabsorber and a neighbouring atom, and σ^2 is the atomic pair distance disorder, also known as the Debye-Waller factor. The S_0^2 is an empirical parameter which accounts for the slight relaxation of the remaining electrons when a hole is created by the photoelectron.

Despite its complexity, the EXAFS equation allows the determination of N, r, and σ^2 knowing the scattering amplitude $f(k)$ and the phase-shift $\alpha(k)$. Furthermore, since these scattering factors depend on the properties of the neighbouring atoms, EXAFS can be used to distinguish the atomic species next to the photoabsorber. $\chi(k)$ is often multiplied by a power of k typically k^2 or k^3, in order to emphasise the EXAFS oscillations in the post-processed, final spectrum.

5.2 Calculations on Gold Nanoparticles

The gold nanostructures studied in this work are representative structures of the gold nanoparticles synthesised by Comaschi et al. [20]. More specifically, these refer to the Au L_3 edge XAS data of two non-coated gold nanoparticles with experimentally reported mean diameters of 50$\pm$7Å (Au-NP1) and 24$\pm$8 Å (Au-NP4). The latter nanoparticle samples were either prepared by using the solvated atom dispersion (SMAD) technique or produced under vacuum on a very thin polymer film by consecutive evaporation of gold and Mylar, respectively. The SMAD technique [20,139,140] involves: (a) deposition of an organic solvent on the reactor walls cooled down to very low temperatures, (b) vaporisation of the metal under vacuum and then rapid trapping in a frozen solvent, (c) warming up at room temperature of the solvated atoms, (d) impregnation to a surface of amorphous silica and drying of the samples at room temperature. The gold nanoparticles obtained with this method are non-coated and therefore their x-ray absorption (XAS) spectra depend only on their morphology and size.

Models of gold nanoparticles that correspond to the experimentally determined diameters have been constructed (see Appendix E.2) and their dynamic behaviour and structures at various temperatures have been observed by performing classical molecular dynamics (MD) simulations. Such simulations are often used to study the dynamical behaviour of nanoparticles, even in conditions far from ambient such as, for example, under high external pressure [141]. The reported simulations have been performed with a force field which was designed to reproduce the properties of several bulk, metallic systems. Details regarding the force field are given in chapter 2, section 2.3.3.1.

5.2.1 MD Simulations

All the classical MD simulations have been performed with the DL_POLY software package [1]. The simulations were carried out within the micro-canonical (NVE) ensemble, with an integration time-step of 1 fs. The atomic forces and velocities were equilibrated for a period of 50 ps after which a production calculation of 2 ns followed. Data were collected during the production stage, after confirming that both the energy and temperature were stabilised.

The Au_{429} and Au_{3925} nanoparticles with average diameters of 24 Å and 50 Å respectively, corresponding to the experimentally determined diameters of the nanoparticles, were simulated. Additionally, MD simulations on the Au_{249} (20 Å diameter), Au_{887} (30 Å diameter) and Au_{6699} (60 Å diameter) nanoparticles were also performed, in order to test size effects and verify our results.

The initial structures for the simulated nanoparticles were constructed with Accelrys Materials Studio [123]. The lattice parameters for constructing the nanoparticles were obtained from a unit cell representation of the face-centred cubic (fcc) structure of bulk gold. The unit cell was expanded periodically along each lattice vector and then truncated to form a spherical particle of a specified diameter. Each nanoparticle structure was then relaxed under the effect of the Gupta force field. The MD simulations were conducted at temperatures ranging from 20 K to 300 K.

For the lowest temperature simulations (20K) the classical molecular dynamics ensemble is not entirely appropriate as the atomic motion is expected to be mainly due to phonons, in the form of normal mode vibrations of the nanoparticles, which are populated according to Bose-Einstein quantum statistics. However even in this case, our simulations, to a great extent, agree well with the experimental spectra. This is not completely unexpected as the large atomic weight of Au combined with

the compact shape of the nanoparticles should lead to phonons with small average quantum vibrational amplitudes. This has been also observed for the atomic displacements in the classical simulations at this temperature range, as a result of the reliable representation of the Au potential energy surface by the Gupta potential [142].

5.3 Prediction of EXAFS spectra

The information extracted from the MD simulations can be used to perform a quantitative analysis of XAS data, as has been successfully applied so far to disordered systems, such as aqueous solutions of ions [143–149]. It has also been shown that the damping of the XAS signal associated with the structural disorder, which is expressed normally through the Debye-Waller factor, can be reproduced through the average of XAS spectra computed from a statistically representative number of computer-generated configurations ("configurational average") [144].

In calculating the XAS spectrum of a nanoparticle, asymmetry effects due to the finite size of the nanoparticles have to be taken into account, which increase as the nanoparticle size decreases. Thus, we have assumed that every atom inside the nanoparticle can give rise to absorption, and therefore the resulting XAS spectrum should include the contributions of atoms in different atomic environments. This is achieved by sampling several absorption sites in different positions, starting from the centre of mass of the nanoparticle and ending at the nanoparticle's surface. Since several atoms share an equivalent atomic environment, they are grouped into "shells", which in this case are defined by the distance from centre of mass of the nanoparticle. The details regarding the choice of the absorption sites are analysed and discussed in section 5.4, along with a brief description of the MD trajectory production.

5.3.1 EXAFS calculations

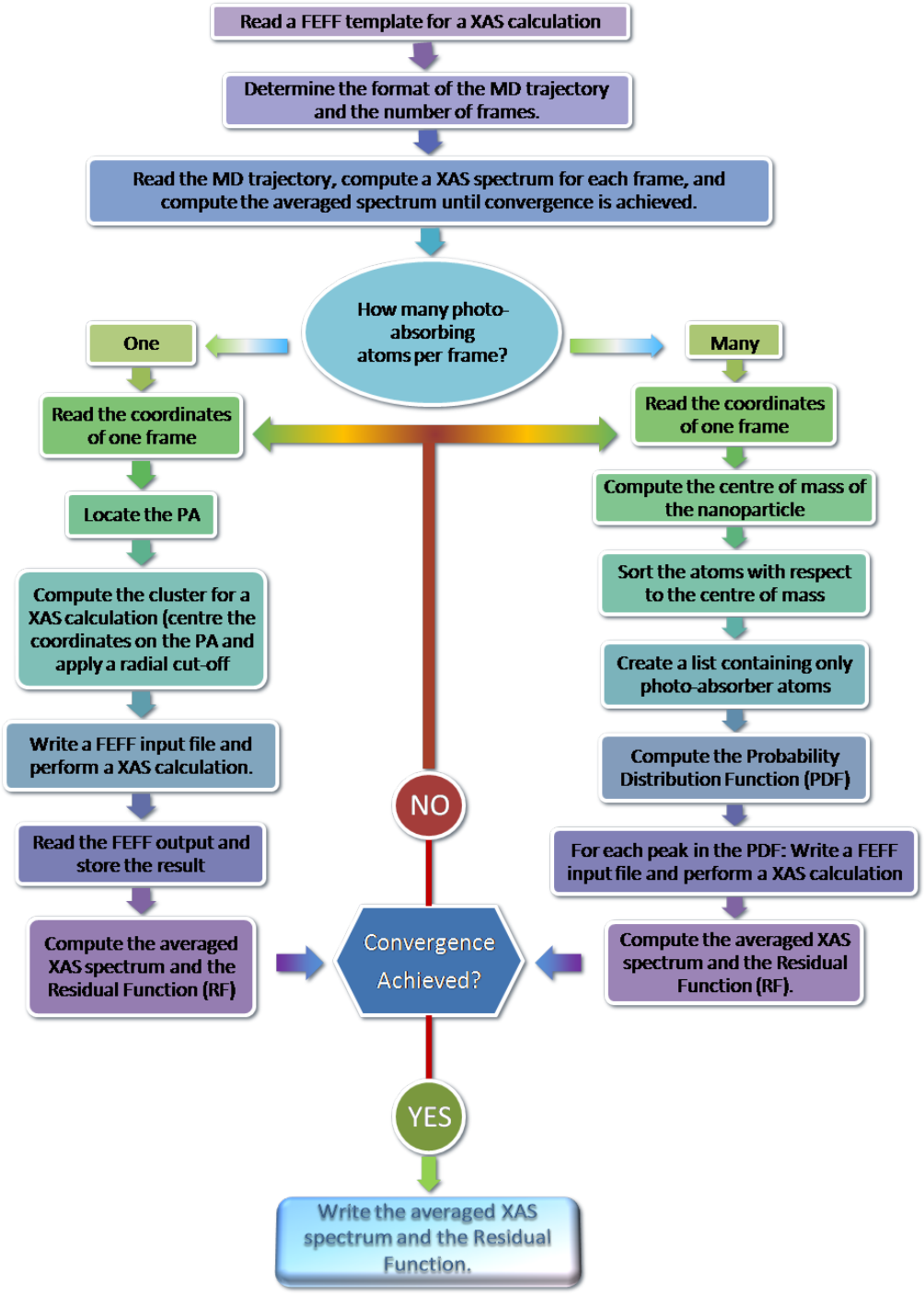

Figure 5.4: Flow chart of the algorithm used to compute the configurational average of XAS spectra using the structural information derived from MD simulations.

To calculate the EXAFS spectrum for a gold nanoparticle from MD simulations, an XAS quantitative analysis code has been developed by Dr Otello Roscioni. The algorithm on which the code is based is summarised in the flowchart of Figure 5.4. The program extracts the required information from a MD trajectory, by reading the coordinates of a gold nanoparticle from each of a fixed set of MD "snap-shots". For each snap-shot several absorption sites at different positions inside the nanoparticle are sampled and an EXAFS spectrum is computed. The calculated XAS data are then averaged together to give a mean spectrum. The procedure is iterated by increasing the number of MD snap-shots sampled until convergence in the resulting XAS spectrum is achieved.

Each mean XAS spectrum is obtained by taking a large number of MD configurations into account. For each configuration, the atoms of the nanoparticle are grouped into "shells" with respect to their distance from the centre of mass. For each shell, a photoabsorbing atom is arbitrarily chosen to represent the absorption behaviour of the Au atoms inside that shell and to contribute to the XAS spectrum from this region for this particular snap-shot (configuration) [144]. The atomic shells are defined by using a probability distribution function (PDF), which is obtained as the sum of Gaussian functions centred on each atom of the nanoparticle.

The statistical weight of each peak i in the PDF is proportional to the number of photoabsorbing atoms whose distance r_j from the nanoparticle's centre of mass satisfies the conditions:

$$r_j \geqslant p_i + \Delta_i^+$$
$$r_j < p_i - \Delta_i^-$$

where p_i is the position of the peak i in the PDF, $\Delta_i^+ = (p_{i+1} - p_i)/2$ is the distance between the peaks i and $i+1$ and $\Delta_i^- = (p_i - p_{i-1})/2$ is the distance between the peaks i and $i-1$. Therefore, each peak (and the corresponding absorption site) will have a statistical weight proportional to the number of atoms sharing the same

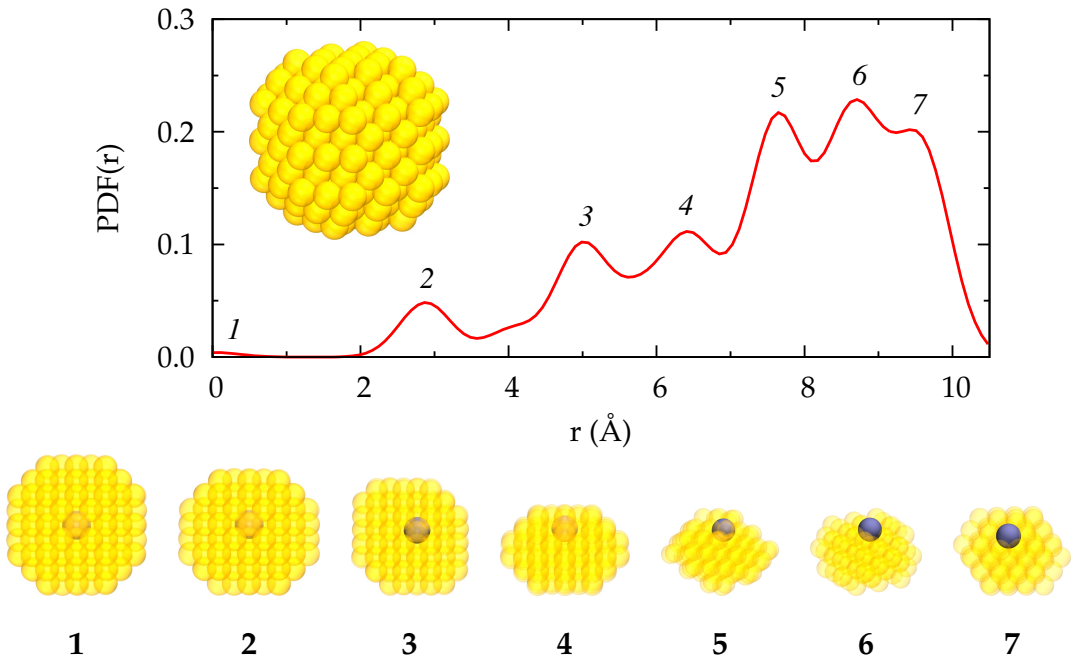

Figure 5.5: Probability distribution function (PDF) computed for a gold nanoparticle with a diameter of 20 Å. The PDF is proportional to the number of atoms found at a given distance from the centre of mass of the nanoparticle. The bottom panel shows the input structures for XAS calculations obtained by applying a cut-off radius of 10Å around gold atoms chosen from within each shell defined by the peaks of the PDF. The photoabsorbing gold atoms are shown in blue, while the gold atoms that define the scattering region are translucent yellow.

physical environment. An example of the PDF generated for a gold nanoparticle structure of 20 Å diameter, divided into absorbing shells, is shown in Figure 5.5. The accuracy of the PDF depends on the standard deviation of the Gaussian functions and can be tuned accordingly to control the number of peaks in the PDF and therefore, the number of locations of absorbing atoms being selected (Figure 5.6).

The Au L_3-edge EXAFS spectra were computed with the FEFF 8.4 [5, 150] program using the Hedin-Lundqvist model of the exchange potential. Atoms up to 10 Å from the photoabsorbing atom were included to obtain converged XAS spectra. In agreement with the data analysis performed previously by Comaschi et al. [20], the

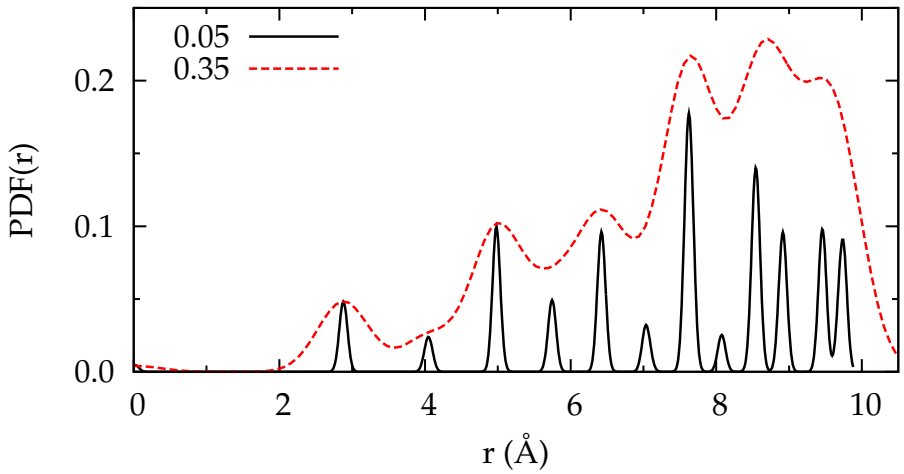

Figure 5.6: Comparison between the PDF computed for a gold nanoparticle with a diameter of 20 Å using standard deviations of 0.05 (solid line) and 0.35 Å (dotted line). A small standard deviation value results in a fine sampling of atomic shells within the nanoparticle and, as a consequence, a higher number of locations of absorbing atoms being selected.

amplitude reduction factor S_0^2 was set to 0.9, the energy shift was set to 7.1 eV and the experimental broadening factor to 1.0 eV. By applying these settings the computed Fermi energy for Au nanoparticles was found to be around 7.3 below the L_3 edge of bulk Au (11919 eV). The Debye-Waller factor has not been taken into account in the calculation, as the thermal damping of the signal is reproduced explicitly through the averaging the XAS spectra over the nanoparticle configurations.

The number of configurations required to obtain a statistically representative averaged spectrum is determined by calculating a residual function (RF), which is the root mean square of the differences between all the energy points of the averaged XAS spectra computed over $N-1$ and N configurations [144]. A XAS spectrum is considered converged when the corresponding RF value falls below the threshold of 10^{-4} and remains below this value for the following 10 iterations. For gold nanoparticles, about 50 configurations are necessary to achieve convergence of the EXAFS spectra.

5.4 Results and Discussion

5.4.1 Effect of the PDF on the mean EXAFS spectrum

To validate our approach, the dependence of the calculated EXAFS spectrum from several factors and parameters has been investigated, which can affect the XAS calculations. One such factor is the resolution of the PDF. For this purpose, the dependence of the computed mean Au L_3-edge EXAFS spectrum on the number of absorption environments for a gold nanoparticle with a diameter of 20 Å at 20 K, has been studied. This choice was made after observing that smaller nanoparticles are affected more strongly by asymmetry effects compared to their larger counterparts. Mean EXAFS spectra for this nanoparticle were computed using PDFs with standard deviations of 0.05 and 0.35 Å, corresponding to a fine and a coarse sampling of absorption sites, respectively. The first case yielded a PDF with 13 different atomic shells while the second case exposed 7 atomic shells, as shown in Figure 5.6. The resulting mean EXAFS spectra and their Fourier transforms (FT) for both cases, are shown and compared in Figure 5.7.

Comparing the two sampling methods, we can observe that the mean spectrum computed with the coarse sampling of the absorption environments shows a phase shift in the EXAFS signal and a displacement of the peaks towards larger bond distances in the corresponding FT, with respect to the more accurate case of the fine sampling. This result suggests that the contribution of the atomic environments with short Au-Au bond lengths is underestimated in the final spectrum. Indeed, the PDF computed with a coarse sampling, as shown in Figure 5.6, does not include the contribution of the outer shell at 9.7 Å, which is present in the PDF computed with a fine sampling and has a statistical weight of 9.5%. As the surface atoms form shorter bond lengths compared to the neighbour pair distances in the core, a poor

sampling of the nanoparticle's outer shell underestimates their contribution in the mean EXAFS spectrum and results in the observed phase shift between the spectra computed with a coarse and a fine sampling of the absorption sites.

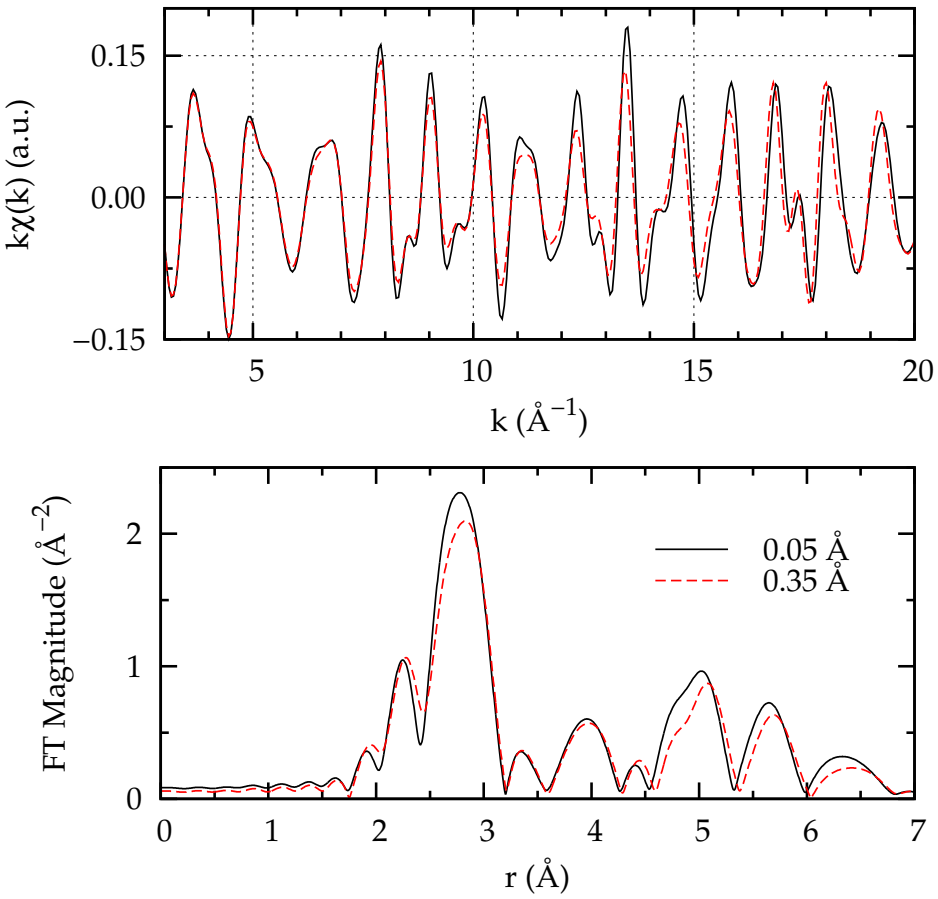

Figure 5.7: Comparison between the simulated EXAFS spectra and the corresponding Fourier transforms of a gold nanoparticles with a diameter of 20 Å at 20 K. The spectra were computed using a fine sampling (solid line) and a coarse sampling (dotted line) of the photo-absorbing sites through PDF standard deviations of 0.05 and 0.35 Å, respectively.

This behaviour is consistent with the experimental observation of atomic surface contraction in gold nanocrystals [151]. For this purpose, the surface compression in our nanocrystals by measuring the nearest neighbour distances of Au atoms as a function of their distance from the centre of mass has been investigated, in or-

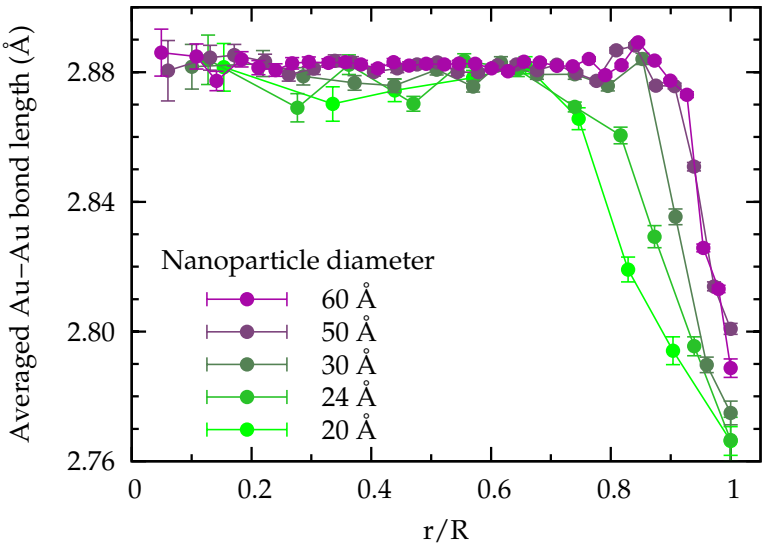

Figure 5.8: Au-Au bond lengths distribution, averaged over MD snap-shots, as a function of the distance from the nanoparticle's core.

der to quantify the effects of the surface tension [152]. A diagram of the resulting bond length distributions, averaged over all the snap-shots, is shown in Figure 5.8. All nanoparticles display a clear shortening of the Au-Au bond length, moving along the nanoparticle's core towards the surface, where it reaches a minimum value. Therefore, the different phases of the mean EXAFS spectra originate from the contribution of surface atoms and account for 9.5% in the final spectrum.

5.4.2 Effect of size

Another parameter being investigated is the dependence of the spectra on the nanoparticle size. It is desirable to be able to use EXAFS spectra to determine the size of the nanoparticles being measured. Therefore, several gold nanoparticles with diameters ranging from 20 Å to 60 Å were studied. The resulting spectra, shown in Figure 5.10, reveal that the intensity of EXAFS oscillations increases with the size of the nanoparticle. No shift was observed in the phase of EXAFS oscillations, in con-

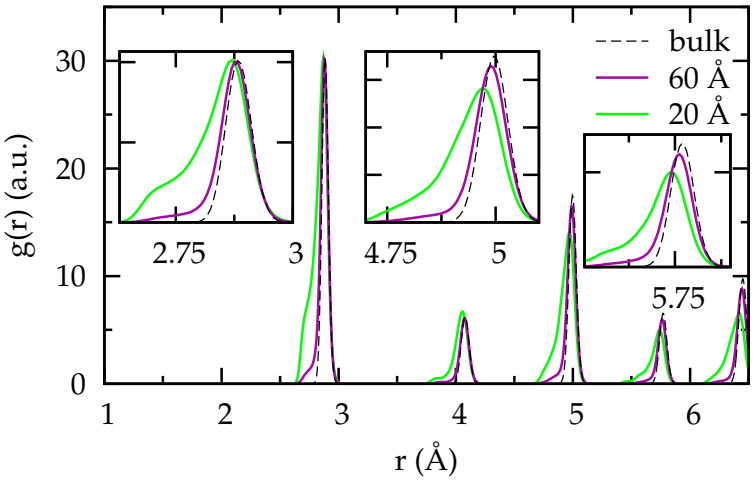

Figure 5.9: Radial distribution functions $g(r)$ extracted from MD trajectories at 20 K. The insets show the details of peaks 1, 3 and 4.

trast to the reported shift between the experimentally obtained EXAFS spectra of Au nanoparticles with mean diameters of 50 Å and 24 Å. The latter, can give rise to a difference of 1% between the best-fit of Au-Au bond lengths [20].

However, the radial distribution functions (RDFs), derived from the MD trajectories and shown in Figure 5.9, demonstrate that the shape of the peaks in a small nanoparticle is strongly asymmetric and very sensitive to its size, when compared with bulk gold. Furthermore, the position of the peaks is displaced towards smaller values than those of the bulk phase, as a result of the contribution from surface atoms. These effects decrease rapidly with respect to the nanoparticle size; for a nanoparticle with a diameter of 60 Å the peaks of the RDF are barely distinguishable from the peaks of the bulk phase. Hence, for a nanoparticle of this size, the region influenced by the surface tension can account approximately for 20% of its volume (Figure 5.8) while for a nanoparticle with a diameter of 20 Å, the same region accounts roughly for 64% of the nanoparticle's volume[1].

[1]For this estimate we have approximate the shape of the nanoparticle to a sphere.

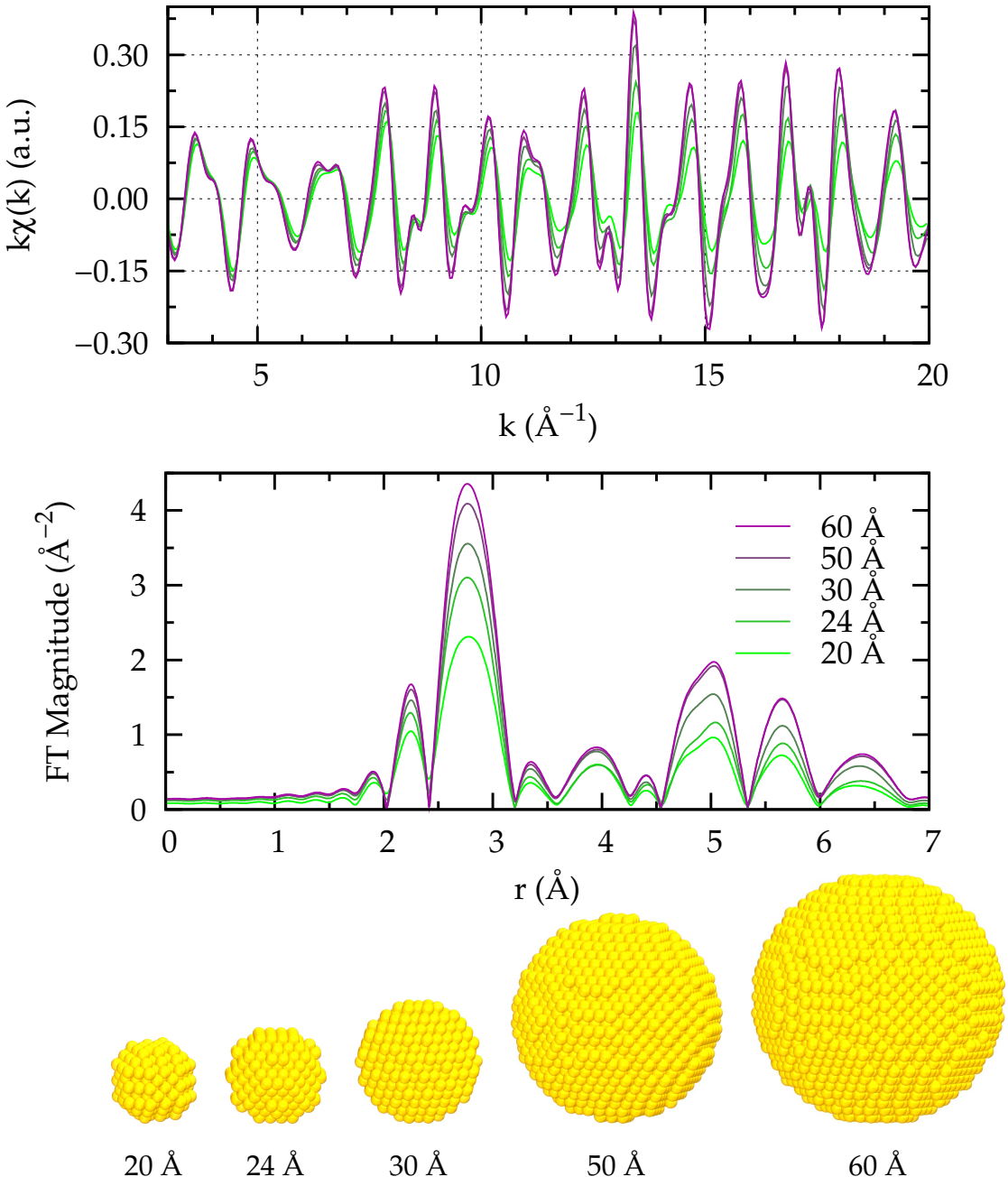

Figure 5.10: Simulated $k\chi(k)$ EXAFS spectra (top panel) and their Fourier Transform (middle panel) as a function of nanoparticle size. The bottom panel shows a pictorial view of each gold nanoparticle.

To explain the observed behaviour, two factors need to be considered. First, the contribution of surface atoms in the RDF decreases rapidly when the particle size increases, as the RDF is averaged over all the atoms. Second, the EXAFS signal is sensitive to atoms up to 10 Å from the photoabsorbing atom (this is visually represented by a spherical probe of 20 Å diameter) when sampling different positions inside the nanoparticle.

For a nanoparticle with a diameter of exactly 20 Å, all the photoabsorbing atoms experience an asymmetrical atomic environment, as the contribution of the core and surface atoms are both included in the same probe. For a particle with a diameter of 60 Å, though, where the radius of the spherical probe is smaller than the radius of the nanoparticle, different scattering regions can then be distinguished. Thus, a virtual sphere located in the inner region of the nanoparticle, accounts only for photoabsorbing atoms experiencing a symmetrical bulk-like environment; while a spherical probe located at the surface scans a scattering region which is mainly asymmetrical. In the case of the largest nanoparticle, this asymmetrical region still represents 70% of its total volume.

5.4.3 Effect of temperature

The effect of temperature on the mean EXAFS spectrum of a gold nanoparticle with a diameter of 60 Å has also been studied. Figure 5.11 shows the spectra computed in a temperature range from 20 K to 300 K. The increasing disorder of the nanoparticle structure caused by the increase in temperature causes a signal damping, leading eventually to a suppressed region in the $\chi(k)$ above 9 $Å^{-1}$ at 300 K.

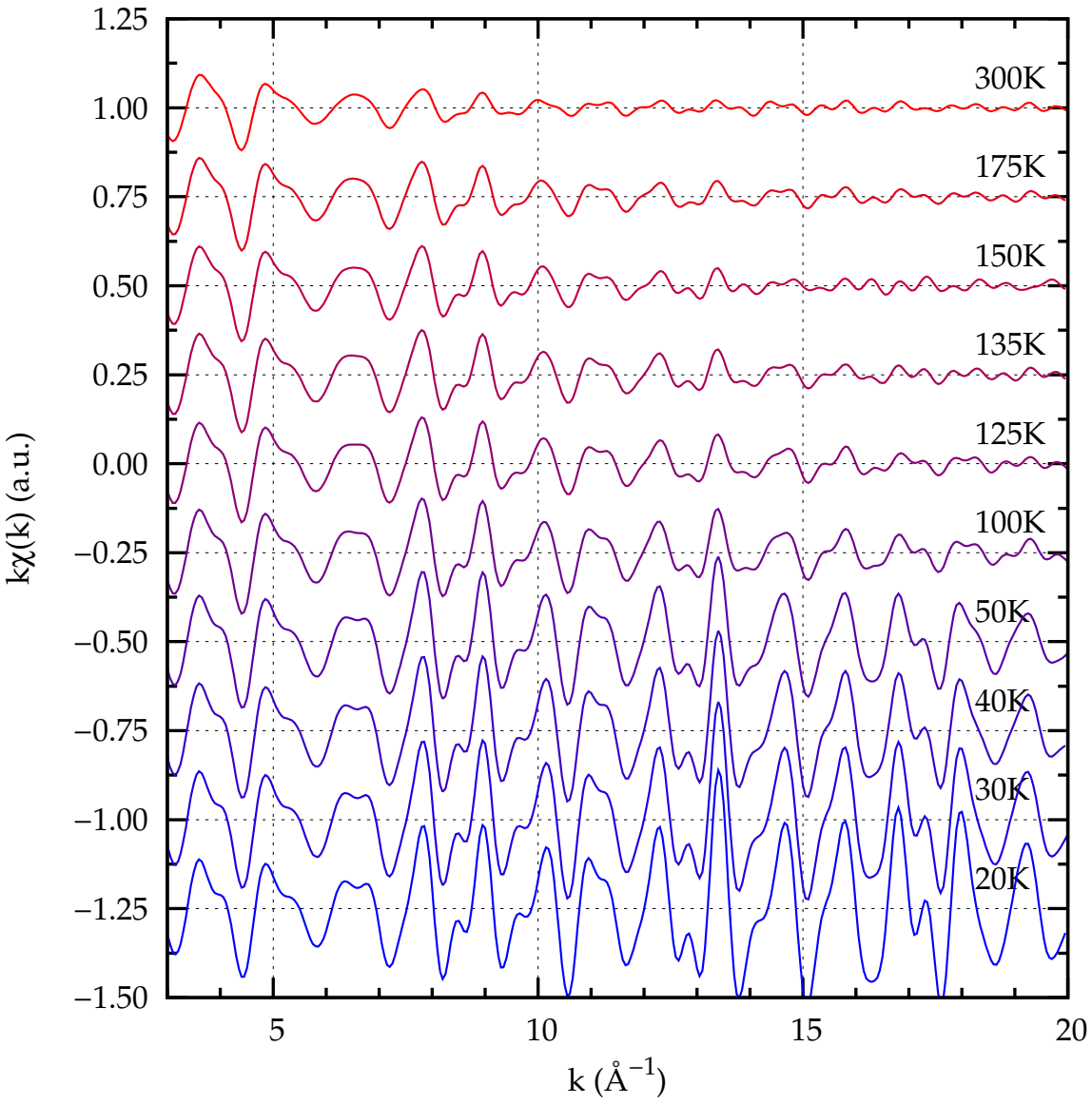

Figure 5.11: Effect of temperature on the simulated EXAFS spectra of a nanoparticle with a diameter of 60 Å.

5.4.4 Comparison with experimental data

When comparing the mean EXAFS spectra of gold nanoparticles with diameters 24 and 50 Å with the experimentally determined spectra of nanoparticles with diameters 24±8 Å and 50±7 Å, an underestimation of the bond lengths is observed in our MD simulations. To correct this error, the structural models obtained from the MD "snap-shots" were scaled by a numerical factor corresponding to the mean ratio between the experimental and the simulated bond lengths at 20 K. From the values reported in Table 5.1 scaling factors of 0.9918 and 0.9971 were calculated to represent the spectroscopic properties of the nanoparticles with diameters of 24 Å and 50 Å respectively.

Figure 5.12 shows the EXAFS spectra of a gold nanoparticle with a diameter of 24 Å at 20 K and 300 K in k space, while Figure 5.14 shows the EXAFS spectra in r space at 20 K. A very good agreement is shown between the simulated spectra and the experimental data. In particular, the phase and the shape of the oscillations are correctly reproduced from k=3 to k=20. The thermal damping of the EXAFS signal at the experimentally determined temperatures is not reproduced correctly in this case. The simulated mean EXAFS spectrum at 20 K has oscillations far too intense compared to the relevant experimental spectrum, while the damping of the simulated mean EXAFS spectrum at 300 K is overestimated compared to experiment.

The best agreement between the simulated mean EXAFS spectra and their experimental counterparts at 20 K and 300 K is found using MD trajectories at 60 K and 150 K respectively. A further investigation of the origin of this discrepancy has been conducted, by carrying out MD simulations of the Au_{429} nanoparticle at 20 K and 300 K with a different force field, in this instance, the Sutton-Chen potential [153, 154]. The mean EXAFS spectra obtained from these MD calculations were practically coincident with the mean EXAFS spectra previously computed.

Table 5.1: Comparison between the shell distances (Å) for two gold nanoparticles at 20 K. Experimental values from Ref. [20]. Calculated values from the radial distribution functions of Au_{429} (24 Å) and Au_{3925} (50 Å) at 20 K.

Au 24±8 Å	R_1	R_2	R_3	R_4
exp.	2.847(2)	4.026(8)	4.931(6)	5.694(6)
calc.	2.867	4.062	4.974	5.742
Au 50±7 Å	R_1	R_2	R_3	R_4
exp.	2.876(2)	4.061(8)	4.975(6)	5.745(6)
calc.	2.879	4.076	4.989	5.760

Similar observations were made for the EXAFS spectra of a gold nanoparticle with a diameter of 50 Å at 20 K and 300 K in k space and r space (Figures 5.13 and 5.14). However, for this system there is a better agreement between the simulated and the experimental EXAFS spectra at 300 K, as the bigger size of the nanoparticle results in more intense oscillations of the EXAFS signal at high k values.

In summary, our results indicate that the unique features in the EXAFS spectra of gold nanoparticles arise mainly from the asymmetric scattering region, which is dominant in nanoparticles with diameters ranging from 20 Å to 60 Å. Furthermore, the discrepancies between the calculated and experimental EXAFS spectra can be attributed to the structural models of gold nanoparticles derived from the MD simulations. In particular, we have found that in our models the effect of surface compression is underestimated and it results in Au-Au bond lengths being longer than the experimentally determined values. This effect is more apparent in small nanoparticles, where the theoretical mean Au-Au bond lengths are on average 0.8 % longer than the experimentally determined bond lengths, while for large nanoparticles this difference shrinks to 0.3 %.

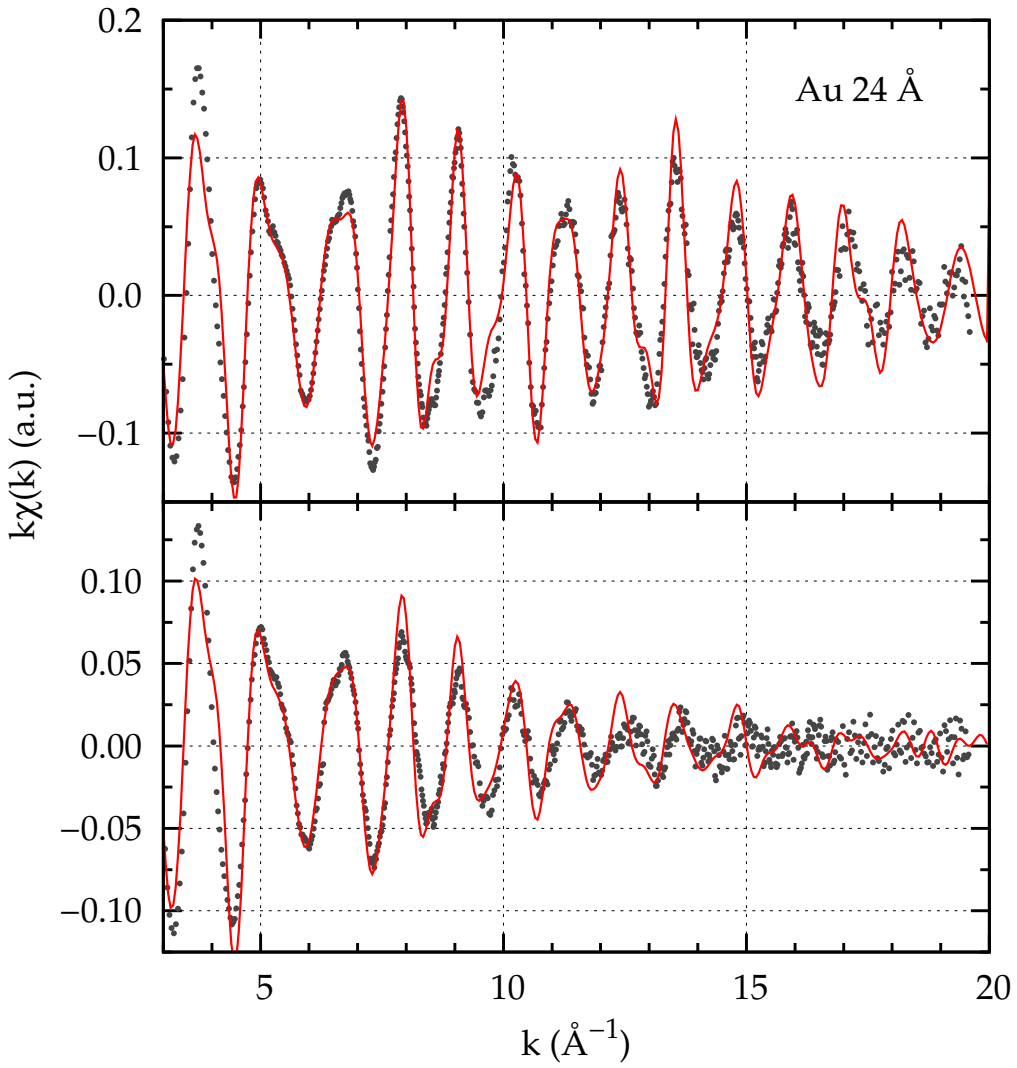

Figure 5.12: Experimental (dotted line) Au L_3-edge EXAFS spectra of a gold nanoparticle with a diameter of 24 Å, measured at 20 K (top panel) and 300 K (bottom panel). The theoretical spectra (solid line) have been obtained by averaging several structures obtained from MD simulations carried out at 60 K (top panel) and 150 K (bottom panel).

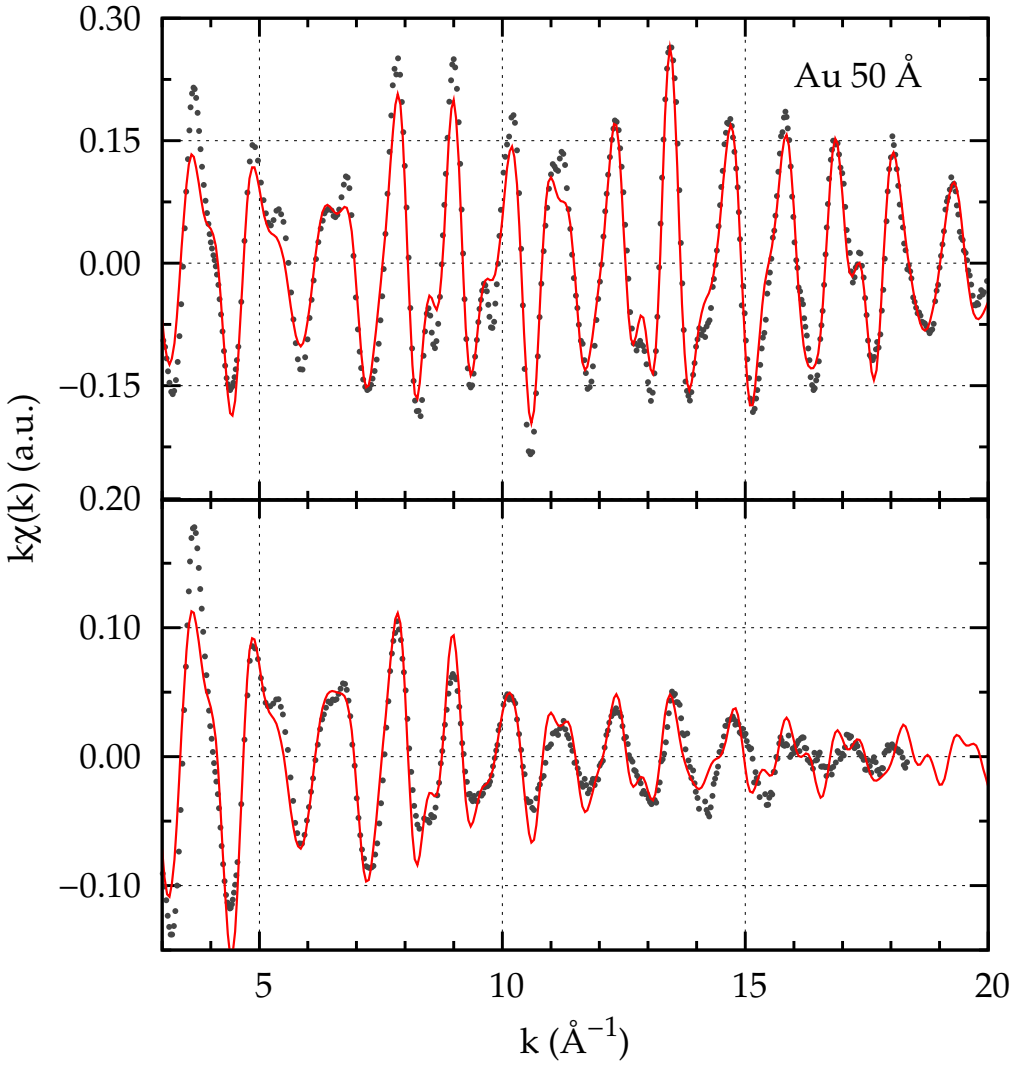

Figure 5.13: Experimental (dotted line) Au L_3-edge EXAFS spectra of a gold nanoparticle with a diameter of 50 Å, measured at 20 K (top panel) and 300 K (bottom panel). The theoretical spectra (solid line) have been obtained by averaging several structures obtained from MD simulations carried out at 40 K (top panel) and 150 K (bottom panel).

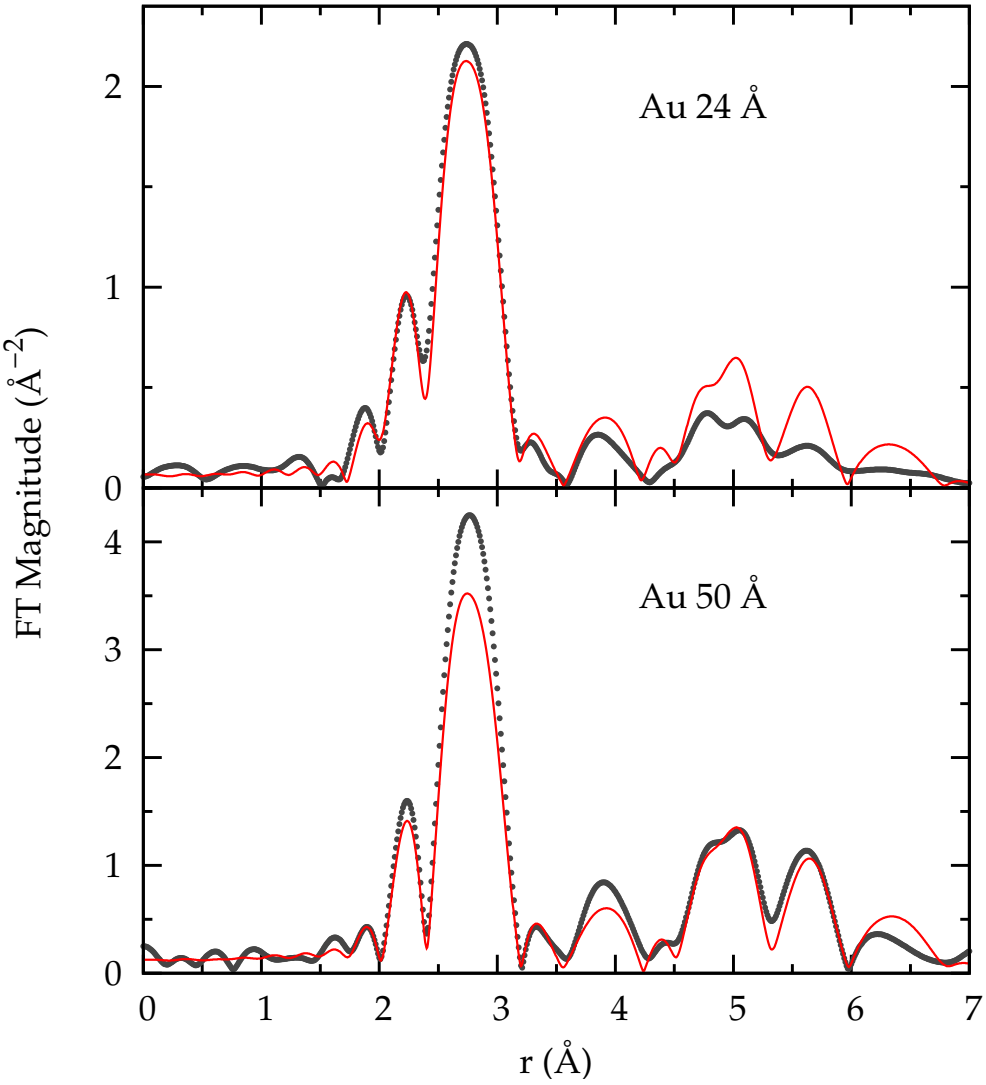

Figure 5.14: Experimental (dotted line) Au L_3-edge EXAFS spectra in r space of gold nanoparticles with a diameter of 24 Å (top panel) and 50 Å (bottom panel), at 20 K . The theoretical spectra (solid line) have been obtained by averaging several structures obtained from MD simulations carried out at 60 K (top panel) and 40 K (bottom panel).

5.5 Conclusions

The computational approach presented in this chapter, for simulating EXAFS spectra of gold nanoparticles directly from classical MD simulations is in good agreement with experimental Au L_3-edge EXAFS spectra. The simulation of EXAFS spectra provides also a route for assessing the quality of the MD simulations, regarding both structural properties and thermal dynamics. Although a fine-tuning of the MD simulations is required to reproduce the correct degree of disorder in the simulated EXAFS spectra, this approach can be further extended by predicting EXAFS spectra of any kind of nanoparticles, given that a suitable force field is available and that the simulation time can adequately sample its conformational space.

The average bond lengths in our MD simulations were about 1% larger than those fitted from analysis of the experimental EXAFS data. On the other hand, the effect of surface reconstruction, as observed in Figure 5.8, shows the significant contribution of surface atoms to the simulated EXAFS spectra (Figure 5.7). The surface tension is underestimated in our simulations compared to the tension observed experimentally [151], perhaps due to the larger Au-Au bond lengths at the surface, with respect to the models presented in Ref. [152]).

Though the thermal damping in the EXAFS simulations steadily increases with the temperature (Figure 5.11), it does not reproduce the signal damping of experimentally determined EXAFS spectra at 20 K and 300 K. The MD simulations at 20 K show small vibrational motions, resulting in an underestimation of the thermal damping, while the vibrations at 300 K are large enough to produce a thermal disorder greater than the experiment. Nevertheless, in our case, the approximation made by representing the atomic interactions with a classical force field still provides reliable results for the structural properties of gold nanoparticles, even though the vibrational motion is not reproduced accurately.

Chapter 6

Platinum Nanoparticles and Nanoalloys

The field of metallic or bimetallic nanoclusters is of particular interest due to their applications in catalysis and optoelectronics, mainly when fabricating materials with well-defined and controllable properties on the nanometre scale. The chemical and physical properties of nanoparticles can be tuned by varying their composition, size and shape. More specifically, nanoalloy clusters can display structures and properties which are distinct from those of pure metallic systems. Surface and segregation properties of nanoalloys are also important in determining their chemical and catalytic reactivity and also their optical and electronic properties.

This chapter summarises the results obtained from classical Molecular Dynamics (MD) simulations on pure platinum nanoparticles along with their copper and palladium nanoalloys. A brief description of the major synthetic methods reported so far for the currently studied Pt nanoparticles is given in sections 6.1.1 & 6.3.1 while the results from the calculations performed on these systems are given in sections 6.2, 6.1.2 & 6.3.3 and 6.1.3 & 6.3.4.

6.1 Platinum Nanoparticles

6.1.1 Experimental Methods

Platinum nanoparticles have recently become a prominent area of research due to their potential applications as catalysts. Perhaps the most popular method reported for the synthesis of controlled size and shape Pt nanoparticles is that of Rampino and Nord [155]. According to this method colloidal platinum nanoparticles are produced in aqueous solution. The Pt is incorporated in the form of potassium platinum chloride solution (K_2PtCl_4). The platinum ions are reduced to neutral platinum atoms by citrate or bubbling H_2. The Pt nanoparticles emerge as the solution becomes more saturated with neutral Pt atoms. To prevent the particles from aggregating, an organic stabilising agent which caps the nanoparticle surface is usually added.

The Pt nanoparticles studied in this work are representative structures of experimentally synthesised nanoparticles, as supplied by Johnson Matthey, supported on 10, 20, 40 and 60 wt% carbon (Ketjen EC600JD) [16]. These were analysed and characterised by using XRD, TEM and EXAFS techniques. The samples were prepared as boron nitride pellets and reduced under flowing H_2 for 30 minutes. Spectra were acquired in transmission mode at temperatures from 20 to 300 K.

The combination of the above techniques is essential for characterising the general structures of the nanoparticles, by averaging their sizes and explaining their differences. Although TEM [10] is limited by its local approach, it provides good estimation of the particle size distribution within the sample. On the other hand, XRD methods often fail to measure an average crystallite size at low sample loadings. At low Pt loadings, in this case, the atomic debris is scattered over the carbon support, in the form of tiny species, which are invisible to XRD, and to all but the highest res-

olution TEM; whilst EXAFS will record the contribution from all of the debris within the x-ray beam at the time of measurement. It is worth noting that these smallest species, are only visible within high angle annular darkfield TEM images.

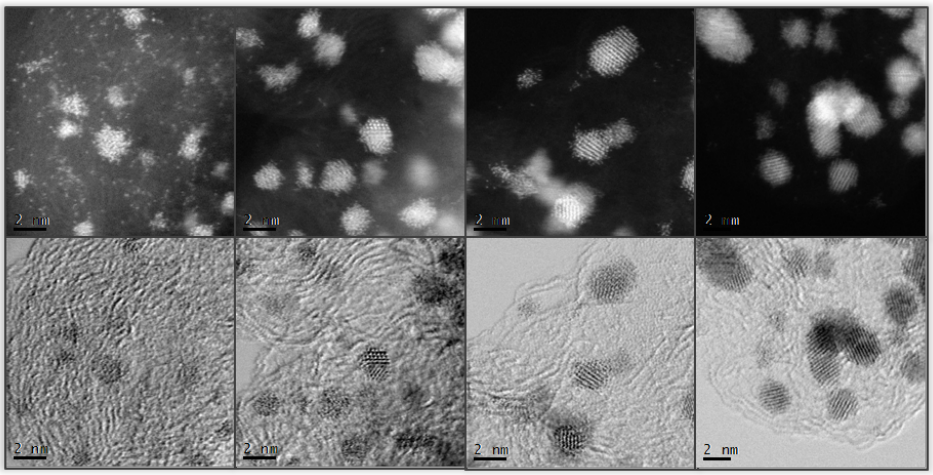

Figure 6.1: Darkfield (top) and brightfield (bottom) aberration corrected STEM images of 10, 20, 40 and 60 wt% Pt/C [16].

In contrast, EXAFS measurements averaged over every atom, where the atomic debris can cause a reduction in the estimation of the average coordination number, results in the EXAFS average particle size being smaller than that of TEM. It has been shown that for highly disordered systems, EXAFS underestimates coordination number and thus particle size when compared with theoretical values. Similarly, when cross-correlating EXAFS with other techniques, such as TEM and XRD, EXAFS gives smaller sizes [16]. The failure to accurately measure the coordination number is due to a failure to account for the high degree of disorder present. Additionally, the assumption of a harmonic disorder made over the standard EXAFS analysis, and the presence of atomic debris near-invisible, increases the errors in determining the EXAFS average particle size. By employing MD simulations to improve the EXAFS analysis, can improve the systematic error derived from the anharmonic disorder, and thus, the discrepancy between EXAFS and TEM results can be reduced. Details about the MD simulations are reported in the following section.

6.1.2 Classical MD Simulations

Classical molecular dynamics simulations were performed on spherical, bare Pt_{13}, Pt_{55}, Pt_{177}, Pt_{381}, Pt_{767} nanoparticles, using two different metallic potentials; the Gupta [40] and the Sutton-Chen [41] force fields. These include "zero" temperature MD simulations, as a geometry optimisation technique, and simulations at 20 K, 85 K, 150 K and 300 K within the microcanonical ensemble (NVE). The optimised geometries are shown in Figure 6.2. A time-step of 1 fs and a total time of 2 ns were considered sufficient for performing the MD simulations. A 50 ps time has been used as an "equilibration" period at the beginning of every simulation.

Additionally, classical MD simulations have also been performed on hemispherical, cuboctahedral and icosahedral structures of pure Pt nanoparticles: Pt_{183}, Pt_{379} (hemispherical); Pt_{147}, Pt_{309} (cuboctahedral) and Pt_{147}, Pt_{309} (icosahedral). Visual representations of the input structures on the systems studied in this work are shown in Figures 6.2 and 6.3. All the reported geometries have been generated with Accelrys Material Studio [123].

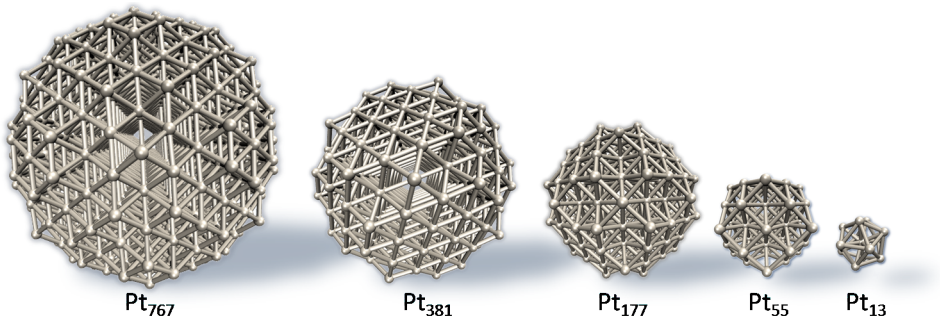

Figure 6.2: Initial/unoptimised structures of spherical Pt_{13}, Pt_{55}, Pt_{177}, Pt_{381}, Pt_{767} nanoparticles

Table 6.1: Comparison results between the force fields used, for the optimised geometries of the Pt_{13}, Pt_{55}, Pt_{177}, Pt_{381}, Pt_{767} nanostructures, obtained using DL_POLY [1]. The results show the remarkable agreement between the Gupta and the Sutton-Chen (SC) potential, especially with respect to the nearest neighbour interatomic distances of the optimised structures.

Nano-particle	Average Nearest Neighbour Distance (Å)		Total Number of Chemical Bonds	Total Energy (eV/atom)	
	Gupta	SC		Gupta	SC
Pt_{13}	2.694	2.694	42	-4.992	-4.611
Pt_{55}	2.703	2.700	216	-5.293	-5.040
Pt_{177}	2.725	2.725	804	-5.462	-5.286
Pt_{381}	2.739	2.737	1872	-5.570	-5.434
Pt_{767}	2.746	2.743	3900	-5.614	-5.507

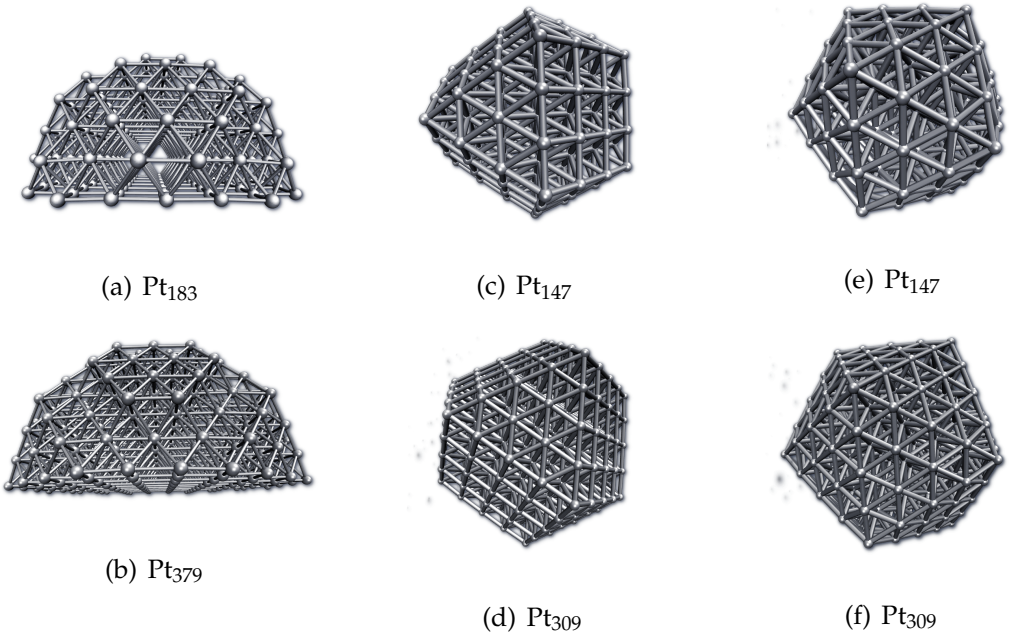

(a) Pt_{183} (c) Pt_{147} (e) Pt_{147}

(b) Pt_{379} (d) Pt_{309} (f) Pt_{309}

Figure 6.3: Optimised geometries of Pt_{183} (a), Pt_{379} (b) (hemispherical); Pt_{147} (c), Pt_{309} (d) (cuboctahedral) and Pt_{147} (e), Pt_{309} (f) (icosahedral).

6.1.2.1 Debye temperature

The Debye temperature is the temperature above which the material behaves classically and where thermal vibrations are more important than quantum effects. In general, by increasing the temperature the amount of dynamic (thermal) disorder within the system also increases. Any increase in the disorder produces a variation in the nearest neighbour atomic distances or else, the bond lengths, which is modelled as a Gaussian distribution, and is known as the pair or radial distribution function (RDF). In more detail, the RDFs of the Pt nanoparticles studied in this work, are described in section 6.1.3 below.

Measurements at low temperature, in particular below the materials Debye temperature, are required to reduce the thermal disorder in the system, and thus the anharmonic contribution effect [156]. For bulk systems, this can be enough to give an accurate value of the coordination number and the amount of disorder. With the dynamic (thermal) disorder greatly reduced, what is left is the static disorder occurring from any surface distortion around the core atoms of the synthesised nanoparticles. For this purpose the simulations mentioned above, extend from very low to room temperatures, and the results obtained, especially at 20 K, are aimed to approximate the experimental results more closely than other relevant methods currently in use for analysing the EXAFS spectra.

6.1.3 Radial Distribution Functions

The radial distribution function $g(\mathbf{r})$ (RDF) or pair correlation function, describes the probability to find a particle within a distance $\mathbf{r}$ away from a reference particle i. In order to construct a RDF plot, the number of atoms surrounding particle i, within a distance interval $\mathbf{r}$ and $\mathbf{r} + d\mathbf{r}$ is counted. This visually creates a number of concentric spheres around the reference particle, where the distance $d\mathbf{r}$ between two

consequent spheres describes the volume of a spherical shell, with an infinitesimal particle density $\rho(\mathbf{r})$, as shown in Figure 6.4.

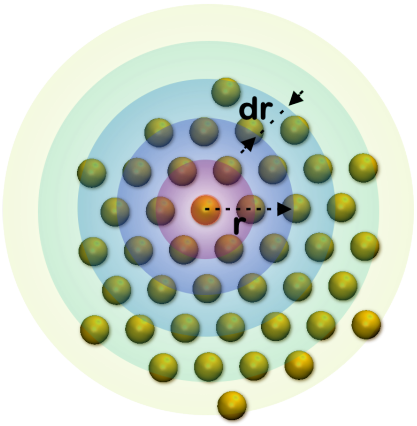

Figure 6.4: Spherical shells around a reference atom of a 55-atom nanoparticle.

The number of particles contained in each shell is equal to the number of particle pairs formed between the reference particle and its surrounding particles. In a MD simulation using DL_POLY, a snapshot of the molecular system is taken at regular intervals and all the pair distances for all the particles N are calculated, sorted and placed in an average histogram which is characteristic for the system simulated. At the same time, the average number of atoms $n(\mathbf{r})$ found in each shell is also calculated by the code.

A table of the mean number of atoms $n(\mathbf{r})$ as a function of the pair distance $\mathbf{r}$ is provided in the OUTPUT file, after an MD simulation with DL_POLY has been performed. To confirm the correctness of an RDF plot constructed with DL_POLY, a script that computes the number of neighbour pair distances and the average number of atoms in each shell for the final structure of a molecular system has been written. The division in coordination shells is based on the RDF data obtained from DL_POLY.

The diagram of Figure 6.5 shows a histogram of the average number of neighbour atoms on the different shells of a 55-atom nanocluster, calculated directly with DL_POLY (black line), merged with the results (blue points) obtained by processing the final structure of the atomic system (table 6.2). In order to match the mean values of neighbour atoms shown on the table 6.2 with the values calculated using DL_POLY, the values are summed while moving from the inner to the outer shell. The perfect agreement between the blue points and the curve prooved the accuracy

Table 6.2: Average number of atoms in every shell of a 55-atom nanoparticle

Shell	Average Distance (Å)	Total number of neighbour pairs	Average number of neighbour atoms
1^{st}	2.814	432	7.855
2^{nd}	3.995	180	3.273
3^{rd}	4.870	528	9.600
4^{th}	5.499	228	4.145
5^{th}	6.294	384	6.982

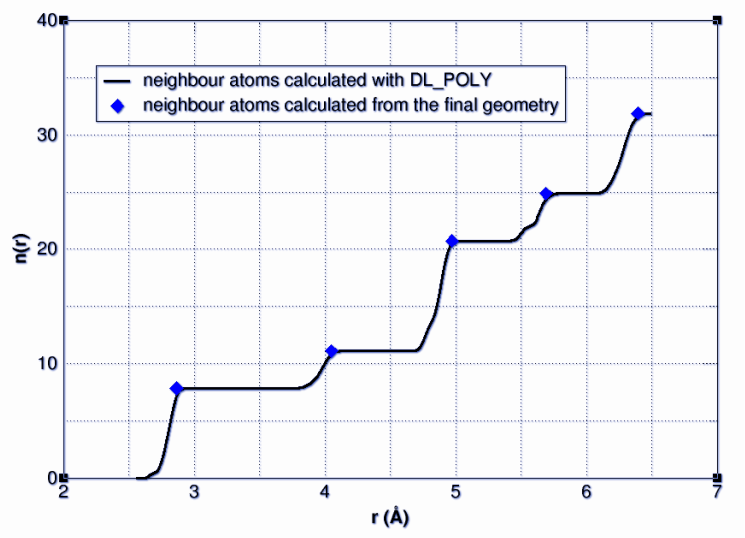

Figure 6.5: Mean number of atoms in the coordination shells of a 55-atom nanoparticle calculated with DL_POLY [17].

of the results obtained by the program.

The RDF plots of the Pt_{55}, Pt_{177}, Pt_{381}, Pt_{767} nanoparticles as simulated at 20 K, 85 K, 150 K and 300 K using the Sutton-Chem potential are shown in Figure 6.6. From a first look at the RDFs of the platinum nanoparticles, two distinctive peaks can be seen; one at the first ($\sim$ 2.7 Å) and one at the third shell ($\sim$ 3.8 Å). As the size of the nanoparticles becomes larger the peaks of the RDF plots are decreased

due to the smaller number of atoms contained in each of the first five shells with respect to the total density of atoms in the whole molecular system. On the other hand, the RDF peaks gradually become long and broader as the temperature of the simulation increases. This is due to the increase of the vibrational motion of the system in higher temperatures which causes the expansion of the peaks in a larger range of atomic pair distances.

Secondly, the displacement of the RDF peaks in smaller distances, mainly observed at the RDF plot of the Pt_{55} nanoparticle, indicates a structural deformation occurring at higher temperatures. As this distortion is more obvious at the last shells of the plot, this suggests a contraction of the pair atomic distances on the surface, also observed experimentally [16]. Although a similar surface contraction is also obvious in the larger Pt nanoparticles studied in this work, this is not shown in the RDFs as the range of the pair distances calculated is restricted within 6.5 Å. Furthermore, the structural stability observed in all the plots is a strong indication of a robust core with bulk-like properties.

Similar conclusions can be drawn for the non-spherical simulated Pt nanoparticles, with some important exceptions. The smallest cuboctahedral and hemispherical Pt nanoparticles (Pt_{147} and Pt_{183} respectively) undergo a structural contraction in almost their full volume at very low temperatures. The hemispherical Pt_{183} shows a double peak at the fourth shell of the RDF plot, which can be attributed to the distortion of the interatomic distances at the edges between the hemispherical and the flat surfaces of the nanoparticle. Both icosahedral Pt nanoclusters (Pt_{147} and Pt_{309}) show a rather complex pair distribution function in very low temperatures which can be attributed to the preservation of their polyhedral shape, with some atomic distances being more contracted or expanded in order to form flat surfaces around the nanoparticle. As the temperature increases and the nanoclusters gain more kinetic energy the RDF resembles more to the RDFs of the spherical Pt nanoparticles.

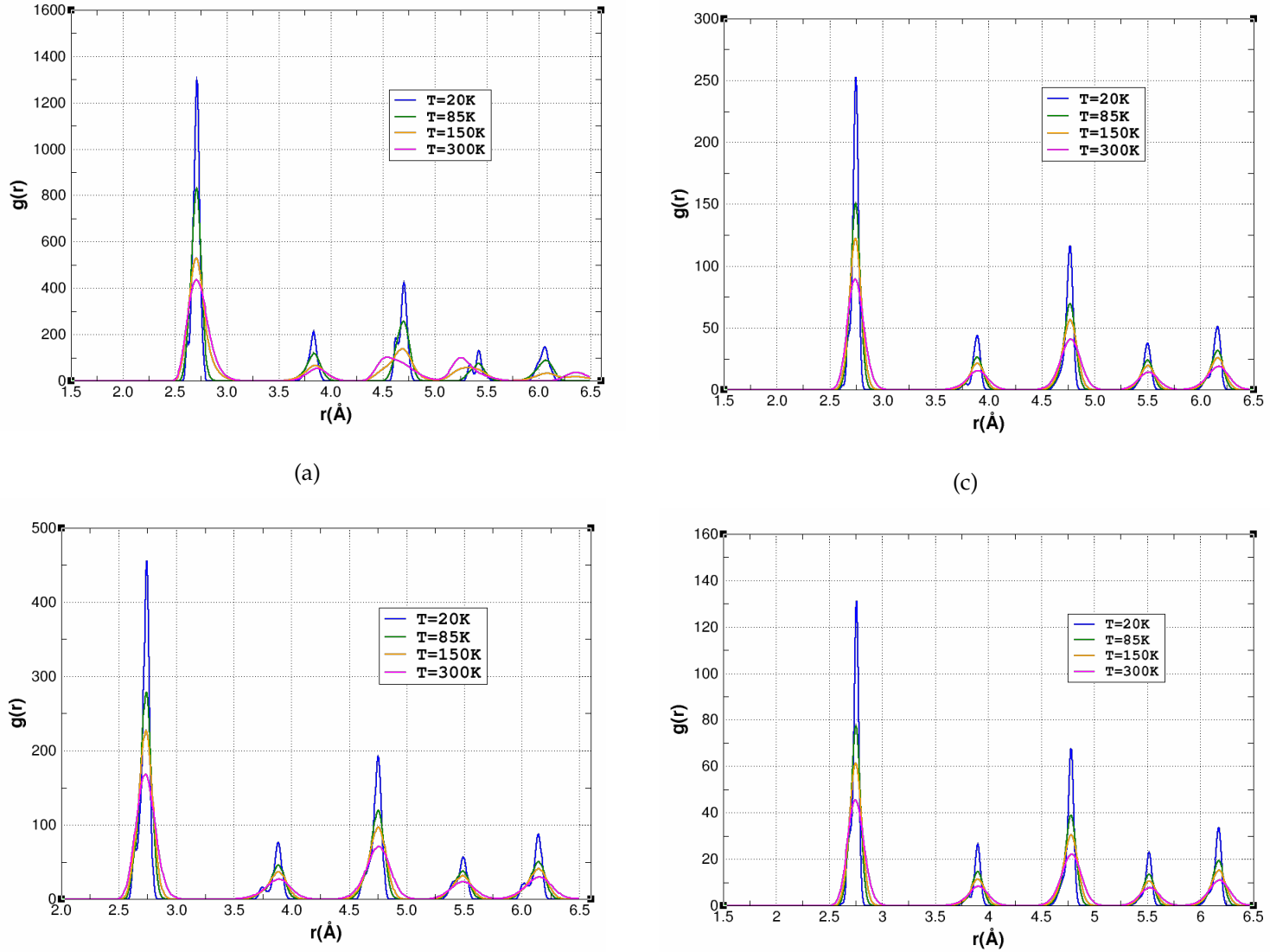

Figure 6.6: Radial Distribution Functions (RDFs) of Pt_{55}, Pt_{177}, Pt_{381}, Pt_{767} nanoparticles at 20 K, 85 K, 150 K and 300 K.

These structural defects result from the contraction of the surface atoms towards the core to minimise the surface energy, a phenomenon observed for both bulk materials [157] and nanoparticles [151]. Surface distortion is present in the bond length distribution and the thermal disorder [151], as surface atoms tend to rearrange themselves in order to reduce the surface tension. For bulk materials, surface reconstructions can be considered negligible, as the bulk contribution dominates; while for nanoparticles below 5 nm, the surface area occupies approximately 25% of the nanoparticle's volume, and for nanoparticles below 2 nm, exceeds 75%. Therefore, the contribution of surface atoms to the average bond length, and to the final EXAFS signal becomes increasingly dominant. Thus, the assumption of a Gaussian distribution in the "standard" EXAFS analysis, breaks down in highly disordered systems, either through thermal or quantum size effects.

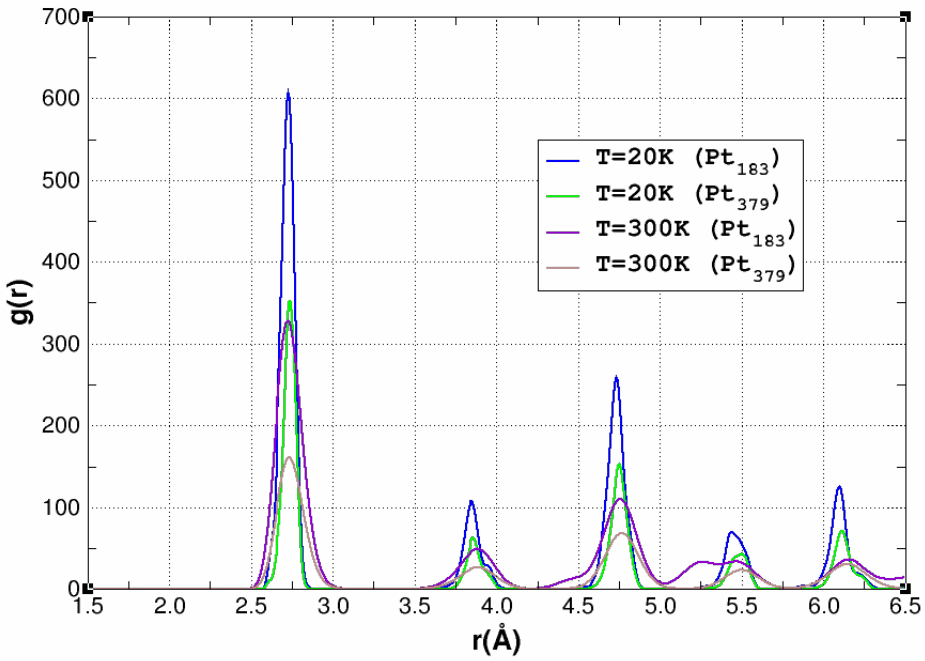

Figure 6.7: RDFs of hemispherical Pt nanoparticles

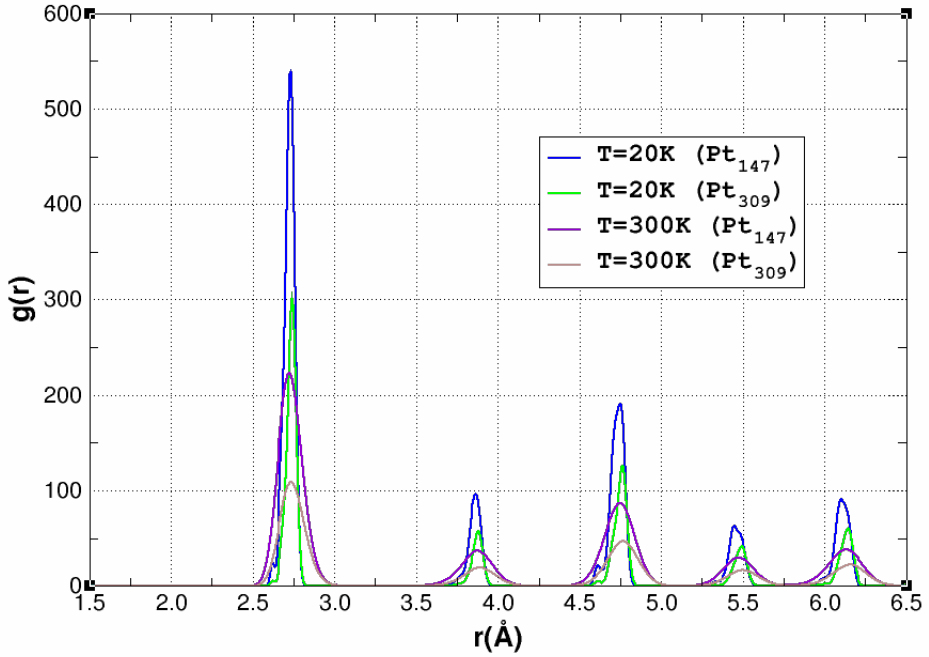

Figure 6.8: RDFs of cuboctahedral Pt nanoparticles

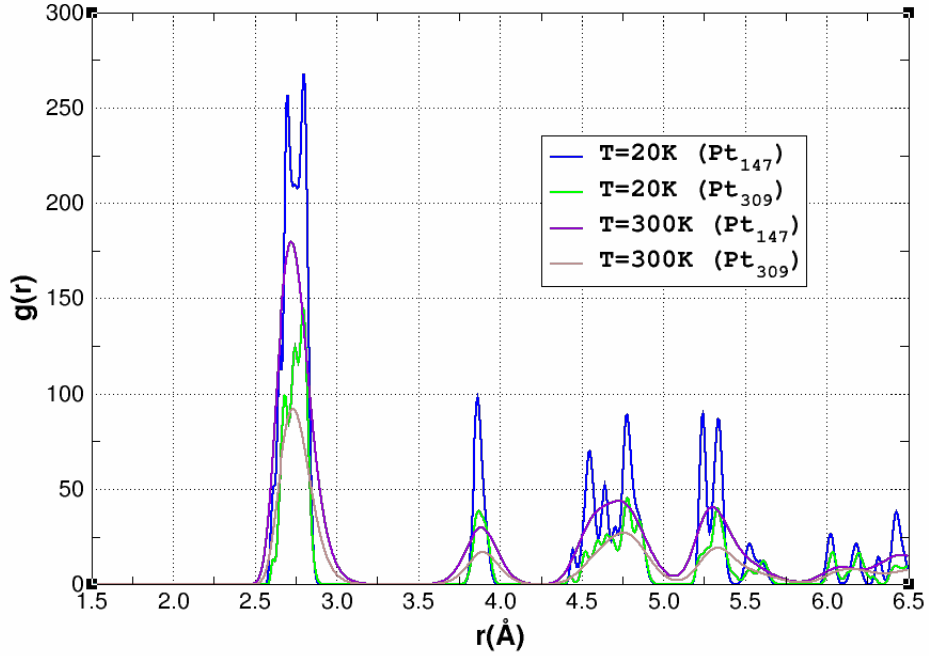

Figure 6.9: RDFs of icosahedral Pt nanoparticles

6.2 Prediction of EXAFS spectra

In order to take into account the high disorder of surface atoms in nano-sized systems, to the atomic pair distribution, the fitting procedure must be able to analyse the EXAFS spectra with a more flexible scheme. So far the existing models for obtaining the structural properties of the nanoparticles are using single distribution for each coordination shell. If the contributions from surface bonds are important enough then, the distribution will become bi- or tri-modal and any attempt to fit a single peak over the split distribution will result in false results.

Several theoretical works have been addressing the need to accurately determine the coordination number from EXAFS, by looking at the relationship between the surface anharmonicity and the particle's geometry [158–160]. Despite demonstrating the difference in the position and intensity of each nearest neighbour shell of the RDF, using different geometries, these studies were still employing an even distribution of bond lengths from the core to the surface, without accounting any termination effects at the surface.

Okamoto [161] and Gilbert et al. [162], have reported using MD simulations for predicting EXAFS, by comparing their results with real structural data, while only in a few studies have attempted to use MD to more accurately determine the average coordination number from EXAFS [163,164]. Theoretical works from Clausen et al. were focused on nanoparticles below 5 nm, while larger particles were also studied [163]. The disorder modelled in these systems however still remained a single pseudo-Gaussian distribution, unlike in this work. In the majority of these works data have been collected at high temperature, where thermal disorder dominates any fine structural disorder. As such, the disorder is fairly poor and can be modelled by using a few adjustments in order to account for small degrees of asymmetry within the distribution [165–167]. Below 3 nm, the disorder becomes significantly

non-Gaussian and the use of extra cumulants will fail to give an accurate result. Applying the information obtained from MD to real EXAFS data is step forward to determine whether the disorder has a significant effect on the EXAFS fit and how much this degree is.

6.2.1 Application of MD to EXAFS

The histogram (RDF) generated from the MD simulations was used to fit the EXAFS data, instead of using the Pt fcc structure of the bulk crystal, as in the standard analysis. In nanoscale systems, the correct treatment of the atomic radial distribution is demanded, in order to account for the effects of the high proportion of disordered surface atoms with decreasing particle size. In contrast, the effects induced by the anharmonic thermal motion and surface termination, in bulk materials, can be considered negligible.

In the standard analysis, the raw EXAFS spectra were energy calibrated, aligned and background subtracted using the AUTOBK algorithm, which is implemented in the ATHENA code [168]. The structural parameters were determined using the ARTEMIS code [169], with photoelectron momentum **k** and non-phase corrected radial distance **r** ranges of 3-18 $Å^{-1}$ and 2-3.2 Å respectively. The scattering paths were calculated using FEFF6 [170].

In both analytic methods, the standard analysis and the procedure employed in the current work, the EXAFS data were parametrised using 4 variables: the amplitude **N**, the isotropic expansion coefficient $\boldsymbol{\alpha}$, the energy correction $\mathbf{\Delta E_0}$ and the disorder σ^2. In the current analysis, only the first coordination shell is considered as the software used to fit the EXAFS data is unable to manage large numbers of scattering paths required for a full multiple scattering analysis. The fitting analysis

in both methodologies in this work was conducted by Stephen Price.

Table 6.3: Structural parameters for 10 (top) - 20 (bottom) wt% Pt/C nanoparticle at 20 K, 150 K and 300 K, acquired in a reduced H_2 environment at the Pt L_{III} edge.

10 wt% Pt/C	**Fitting Method**	**N**	α^2	σ^2 (Å^{-2}) (x10^4)	ΔE_0 (eV)	R_f
20 K	Standard	7.89±0.60	-0.012±0.001	50±3	8.11±0.70	0.009
	Gupta[1]	10.02±0.58	0.000±0.000	19±2	7.41±0.62	0.005
	Sutton-Chen[1]	9.52±0.39	0.003±0.001	25±1	8.33±0.37	0.003
150 K	Standard	8.96±0.30	-0.008±0.001	46±1	8.14±0.29	0.002
	Gupta[1]	9.45±0.55	-0.001±0.001	29±2	7.14±0.53	0.003
	Sutton-Chen[1]	9.08±0.34	0.002±0.001	36±1	7.88±0.35	0.002
300 K	Standard	8.70±0.45	-0.006±0.001	62±3	5.46±0.52	0.010
	Gupta	9.56±1.27	0.002±0.002	46±6	4.66±1.20	0.014
	Sutton-Chen	9.02±0.65	0.005±0.001	52±3	5.34±0.63	0.009

20 wt% Pt/C	**Fitting Method**	**N**	α^2	σ^2 (Å^{-2}) (x10^4)	ΔE_0 (eV)	R_f
20 K	Standard	8.24±0.56	-0.012±0.001	55±3	7.71±0.59	0.009
	Gupta	8.64±0.56	-0.004±0.001	38±3	6.90±0.62	0.010
	Sutton-Chen	8.35±0.54	-0.001±0.001	45±3	7.51±0.56	0.008
150 K	Standard	8.41±0.66	-0.014±0.002	62±4	7.23±0.72	0.014
	Gupta	8.88±0.67	-0.006±0.001	45±4	6.62±0.74	0.015
	Sutton-Chen	8.53±0.65	-0.003±0.001	52±4	7.05±0.68	0.010
300 K	Standard	8.88±0.59	-0.004±0.001	68±4	5.60±0.62	0.015
	Gupta	9.67±1.25	0.004±0.002	52±6	4.51±1.01	0.016
	Sutton-Chen	9.15±0.63	0.007±0.001	58±3	4.96±0.53	0.010

[1]best fit with the 177 Au atoms cluster

Table 6.4: Structural parameters for 40 (top) - 60 (bottom) wt% Pt/C nanoparticle at 20 K, 150 K and 300 K, acquired in a reduced H_2 environment at the Pt L_{III} edge.

40 wt% Pt/C	**Fitting Method**	**N**	α [2]	σ^2 (Å^{-2}) (x10^4)	ΔE_0 (eV)	R_f
20 K	Standard	9.37±0.43	-0.007±0.001	35±1	8.72±0.50	0.004
	Gupta	10.02±0.58	0.000±0.000	19±2	7.41±0.62	0.005
	Sutton-Chen	9.52±0.39	0.003±0.001	25±1	8.33±0.37	0.003
150 K	Standard	8.96±0.30	-0.008±0.001	46±1	8.14±0.29	0.002
	Gupta	9.45±0.55	-0.001±0.001	29±2	7.14±0.53	0.003
	Sutton-Chen	9.08±0.34	0.002±0.001	36±1	7.88±0.35	0.002
300 K	Standard	8.70±0.45	-0.006±0.001	62±3	5.46±0.52	0.010
	Gupta	9.56±1.27	0.002±0.002	46±6	4.66±1.20	0.014
	Sutton-Chen	9.02±0.65	0.005±0.001	52±3	5.34±0.63	0.009

60 wt% Pt/C	**Fitting Method**	**N**	α [2]	σ^2 (Å^{-2}) (x10^4)	ΔE_0 (eV)	R_f
20 K	Standard	9.64±0.31	-0.008±0.001	42±1	7.92±0.29	0.002
	Gupta	10.46±0.79	-0.001±0.001	26±3	6.72±0.73	0.003
	Sutton-Chen	9.85±0.40	0.003±0.001	31±1	7.49±0.44	0.001
150 K	Standard	9.40±0.31	-0.008±0.001	46±1	8.43±0.34	0.002
	Gupta	9.91±0.68	-0.001±0.001	29±3	7.36±0.67	0.009
	Sutton-Chen	9.60±0.44	0.003±0.001	36±2	8.10±0.41	0.002
300 K	Standard	9.04±0.54	-0.004±0.001	59±3	5.79±0.62	0.010
	Gupta	9.96±1.31	0.003±0.002	43±6	4.81±1.23	0.015
	Sutton-Chen	9.36±0.68	0.007±0.001	49±3	5.39±0.62	0.009

[2] A bond length correction term (linear expansion coefficient α) was used as a fitting parameter for the MD input as well as the standard input.

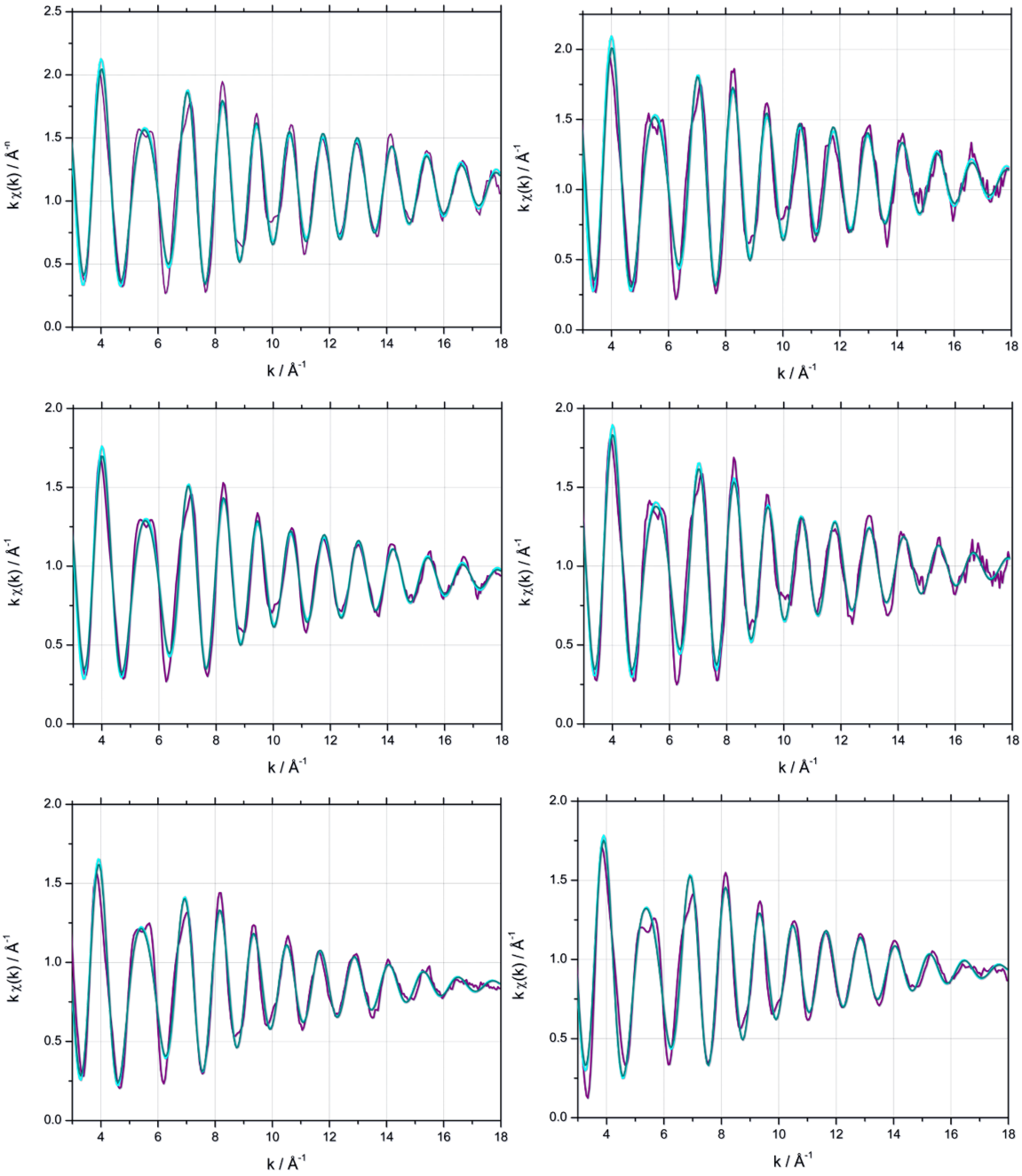

Figure 6.10: k weighted experimental data (purple) and fit to Gupta (tirquoise) and Sutton-Chen (green) potentials, of the 10 and 20 wt% Pt/C at 20 K (top), 150 K (middle) and 300 K (bottom).

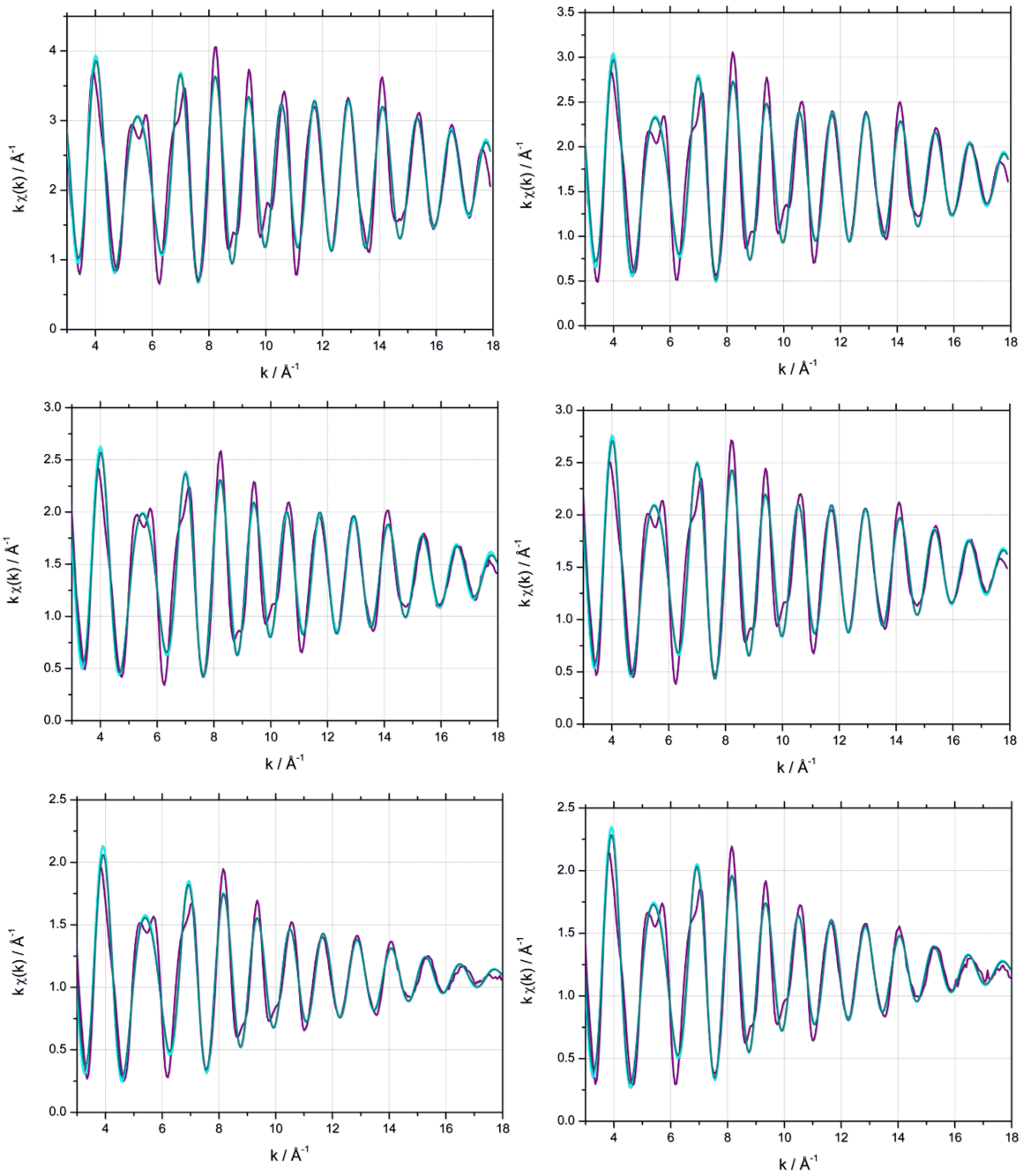

Figure 6.11: k weighted experimental data (purple) and fit to Gupta (tirquoise) and Sutton-Chen (green) potentials, of the 40 and 60 wt% Pt/C at 20 K (top), 150 K (middle) and 300 K (bottom).

Each histogram, from every modelled nanostructure, in all the temperatures simulated, was tried during the EXAFS analysis for determining which gives the best fit. The results are summarised in Tables 6.3 & 6.4 above. The data collected from the 300 K simulations were impossible to be fitted to the EXAFS data at all. As in the case of gold nanoparticles MD simulations (section 5.4) the higher the temperature the greater the disorder. Consequently, a negative σ^2 term would be required to fine-tune the fit and as this is physically unrealistic, these results were discounted. Simulations performed at 150 K were able to be fitted to the data for the 150 K and 300 K within the same error as in the 20 K simulations. On the other hand, the RDF data produced for the smallest (55 atom) and the largest (767 atom) Pt clusters had disorders too great or too small, respectively, that in consequence, failed to be fitted to the EXAFS data. The 381 atom cluster yielded all the best fits.

Comparing the adaptability of the two force fields employed in the classical MD simulations, with respect to the quality of the fit, the Sutton-Chen potential gave better results, from the Gupta potential, when compared with the standard analysis. Whilst, on average, there is no significant difference between the two MD fitting approaches, as also mentioned earlier (Table 6.1), the values in Tables 6.3 & 6.4 clearly indicate that the Sutton-Chen potential is more reliable for simulating Pt nanoparticles, at least in this case. Taking this into account the results reported here, mainly refer to the Sutton-Chen potential.

Although the MD simulations provide an improved input for EXAFS analysis, they do not completely account for all the structural and thermal disorder present and the fits using the RDF histograms as an input require an additional σ^2 parameter. Despite this, the values of σ^2 obtained from the MD histogram are smaller than those obtained from the standard model. In conclusion, the use of molecular dynamic simulations to fit real experimental data, not only provides a significant improvement over the fitting method, but also a measurable metric for evaluating

the quality of a particular force field at replicating nanoparticles behaviour, bearing in mind though that the empirical potentials used were mainly designed to reproduce the properties of bulk metallic systems.

6.3 Platinum Nanoalloys

Although pure metals have a plethora of technological applications, the range of properties of metallic systems can be greatly extended by considering mixtures of elements to generate inter-metallic compounds and alloys. Mixtures of platinum with palladium or copper are of a major interest mainly due to their application as catalytic converters in auto-mobiles. They can be used in the hydrogenation of aromatic compounds in fuel and consequently the reduction of the exhaust gases. This process, however suffers from the catalytic poisoning by H_2S due to the sulphur-containing impurities. There are several works claiming that platinum nanoalloys are more catalytically active and more resistant to sulphur poisoning.

6.3.1 Experimental Works

6.3.1.1 Pt-Pd nanoalloys

Nanoalloys of Pt with Pd have been an attractive and extensive case study for their catalytic applications. Both pure bulk elements and their alloys exhibit face-centred cubic (fcc) symmetry. Due to their relatively low enthalpy of formation (Pt-Pd 1:1 = -4 kJ mol^{-1}) the bulk Pd-Pt alloys have several compositions where the atoms are randomly mixed. In some cases, Pd-Pt alloys may show a strong surface segregation as reported in the experimental work of Watson and Attard [171].

Renouprez, Rousset, and colleagues conducted extensive research studies on rods of bulk Pd-Pt nanoalloys with diameters between 1-5 nm and various compositions [172, 173]. The nanoalloys mainly had cuboctahedral structures, with fcc packing, as their bulk counterparts, while EXAFS measurements revealed that the Pd-Pt particles are intermixed with more Pt-Pt interactions than expected. This indicated that some segregation has occurred. Further experiments showed that the surfaces of these Pd-Pt particles are enriched in Pd, with the relatively largest segregation occurring at low Pd concentrations. Therefore, Pd-Pt nanoalloys with small diameters can be considered as having a fairly isolated Pt core capped with a Pd shell.

Fiermans et al., who studied Pd-Pt particles supported on β-zeolites confirmed the results of Renouprez and Rousset [174]. The particles were composed by a Pd:Pt ratio of 1:3 and a segregation of the Pd to the surface of the nanoparticles was also observed. Toshima et al. reported the synthesis of Pd-Pt colloids (1.5-5.5 nm) with tunable core-shell segregation ($Pt_{core}Pd_{shell}$) for catalytic applications, which was confirmed by EXAFS measurements [175–177]. They had also reported the synthesis of inverted $Pd_{core}Pt_{shell}$ nanoalloys. In contrast, NMR studies on PVP-protected $Pd_{0.2}Pt_{0.8}$ and $Pd_{0.8}Pt_{0.2}$ nanoparticles with average diameter 2.4 nm, revealed a homogeneous Pd-Pt nanoalloy with bulk-like and surface-like Pt atoms [178, 179].

6.3.1.2 Pt-Cu nanoalloys

Toshima and Wang, reported the synthesis of colloidal Cu-Pt particles, by applying catalytic hydrogenation in solution [180]. Several potential applications of Cu-Pt alloys include the catalysis-reduction of NO_x [181]. $Cu_{core}Pt_{shell}$ and $Pt_{core}Cu_{shell}$ nanoparticles have also been synthesised by Eichhorn et al. as well as intermixed particles [182]. The $Cu_{core}Pt_{shell}$ particles (mean diameter 8.8 nm) and their relative

$Pt_{core}Cu_{shell}$ particles (mean diameter 18.3 nm), were found to have approximately equal concentrations of Cu and Pt. The synthesised $Pt_{core}Cu_{shell}$ particles had an fcc Pt core with a $Pt_{0.2}Cu_{0.8}$ shell. Annealing at 370 ^{o}C for 5 h produced an intermixed Cu-Pt particle. In contrast, the $Cu_{core}Pt_{shell}$ particles, with fcc Cu cores and fcc Pt shells, were slightly intermixed by annealing at 370 ^{o}C for 5 h, that generated a Cu-rich/Cu-Pt core and a pure Pt shell. This difference is believed to derive from the higher kinetic stability of $Cu_{core}Pt_{shell}$ core-shell particles.

6.3.2 Theoretical Works

A genetic algorithm describing interatomic interactions of Pd, Pt, and Pd-Pt nanoclusters with the Gupta many-body potential was implemented by Massen et al. [183]. The Gupta potential parameters for Pd-Pt interactions were obtained by averaging the parameters for Pd-Pd and Pt-Pt interactions. According to their results the Pd-Pt nanoalloys had a large number of capped decahedral structures and a reduced tendency to display icosahedral packing in their lowest energy level, compared to pure Pt or Pd nanoclusters [183,184]. The structures for the Pd-Pt clusters were also more distorted than the Pd clusters. These Pd-Pt clusters tend to segregate in shells with the surface being richer in Pd and the core becoming richer in Pt. This segregation, also reported by several experimental studies on Pt-Pd particles, is believed to arise from the contribution of the lower surface energy of Pd and the greater cohesive energy of Pt. Additionally, varying the Pd-Pt interaction parameters of the Gupta potential affects also the tendency towards segregation between the Pt and Pd atoms of the Pt-Pd geometries.

Lloyd et al. extended the work of Massen et al., by studying the dependence of the binding energy on coordination for several cluster sizes, shapes (icosahedral and cuboctahedral shell clusters) and compositions [184]. They showed that

the most stable isomers generally have the largest number of Pt-Pt bonds or Pt-Pd bonds respectively. All the atoms in the cluster were included in order to find the preferred site for segregation on a particular atom. The $Pt_{core}Pd_{shell}$ segregation, as a result of the correlation between average binding energies and atomic distribution parameters, was consistent with the experimental studies of Renouprez and Rousset [172, 173]. Similar results have been obtained by Cheng et al., who used the same Gupta potential parameters in Monte Carlo simulations on icosahedral and decahedral Pd-Pt nanoalloys with 55 atoms [185].

Pd-Pt nanoalloys of 34 and 38 atoms were studied by Rossi et al. [186] by also employing the Gupta potential. Many of the 34-atom clusters adopted incomplete decahedral geometries, in abundance of Pt while for the Pd-rich and intermediate compositions, icosahedral structures were more prominent. For the 38-atom clusters, the truncated octahedral (fcc) geometry dominated the other structures. Fernandez et al. carried out DFT re-optimisations of low-energy isomers generated using the Gupta potential for $(PdPt)_N$ clusters, with N=5-22 [187] had observed $Pt_{core}Pd_{shell}$ segregation, while similar findings were reported also by Paz-Borbon et al. [178].

6.3.3 Classical MD Simulations

Classical MD simulations have been performed using the Sutton-Chen potential [41] on the Pt-core nanoalloys $Pt_{177}Pd_{204}$, $Pt_{381}Pd_{386}$, $Pt_{177}Cu_{204}$ and $Pt_{381}Cu_{386}$ at temperatures 20 K, 85 K, 150 K and 300 K. Additional MD simulations on the intermixed Pt nanoalloys $Pt_{189}Pd_{192}$ and $Pt_{375}Pd_{392}$ at 20 K and 300 K were also attempted. The data collected from these simulations, as in the case of bare Pt nanoparticles, are aimed to be used as inputs for analysing EXAFS data, although the fitting procedure in this case is far more complicated from the method described previously. Optimised structures of the systems studied are given in Figure 6.12.

While simulations for Pt-Cu and Pt-Pd nanoalloys using the Gupta potential have also been performed, this report will focus only on the results obtained with the Sutton-Chen force field. This is mainly due to the flexibility of the latter potential when applied to alloys, by providing a very simple and general scheme for mixing the parameters used in pure metals to represent their relative alloys (section 2.3.3.2).

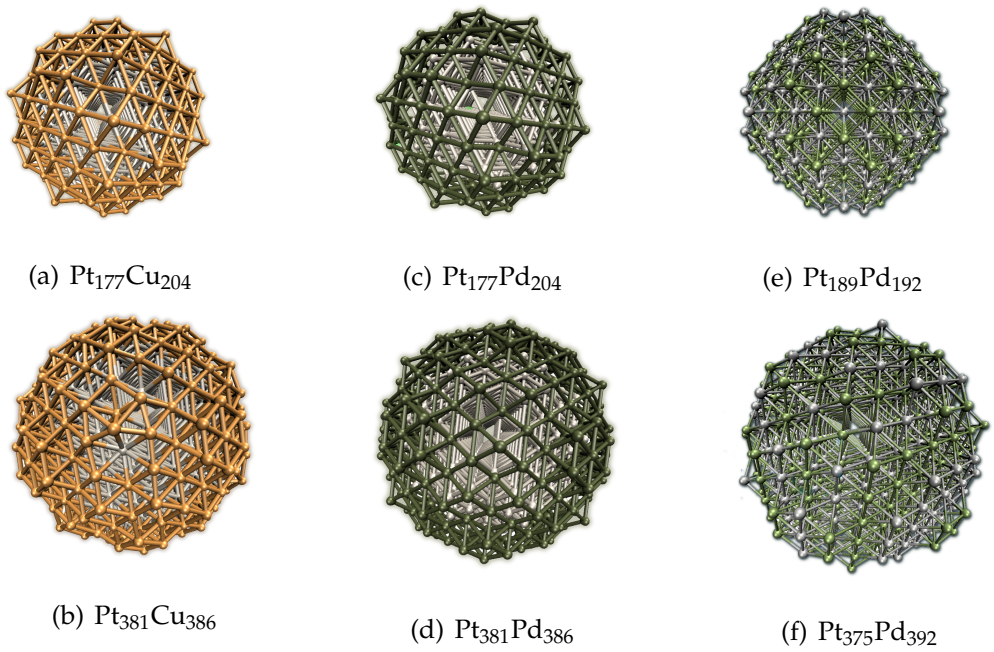

(a) $Pt_{177}Cu_{204}$ (c) $Pt_{177}Pd_{204}$ (e) $Pt_{189}Pd_{192}$

(b) $Pt_{381}Cu_{386}$ (d) $Pt_{381}Pd_{386}$ (f) $Pt_{375}Pd_{392}$

Figure 6.12: Optimised geometries of $Pt_{177}Cu_{204}$ (a), $Pt_{381}Cu_{386}$ (b), $Pt_{177}Pd_{204}$ (c), $Pt_{381}Pd_{386}$ (d), $Pt_{189}Pd_{192}$ (e) and $Pt_{375}Pd_{392}$ (f).

6.3.4 Distribution of bond lengths

The plots of Figures 6.13, 6.14 and 6.15 show the distribution of nearest neighbour atomic distances (bond lengths), from the centre of mass of the nanoparticle to the surface, for the $Pt_{177}Cu_{204}$, $Pt_{381}Cu_{386}$, $Pt_{177}Pd_{204}$, $Pt_{381}Pd_{386}$, $Pt_{189}Pd_{192}$ and $Pt_{375}Pd_{392}$ nanoalloys, obtained from classical MD simulations performed at 20 K and 300 K with the DL_POLY code.

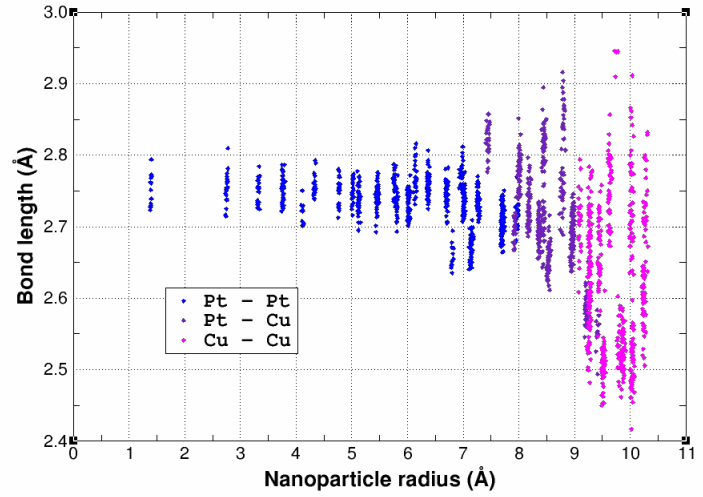

(a)

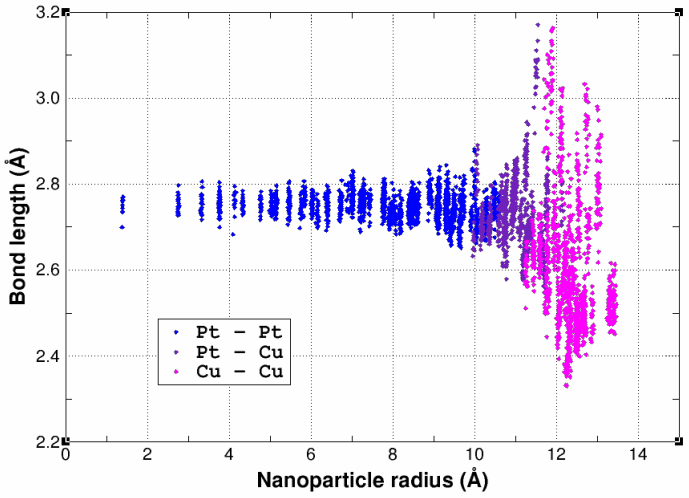

(c)

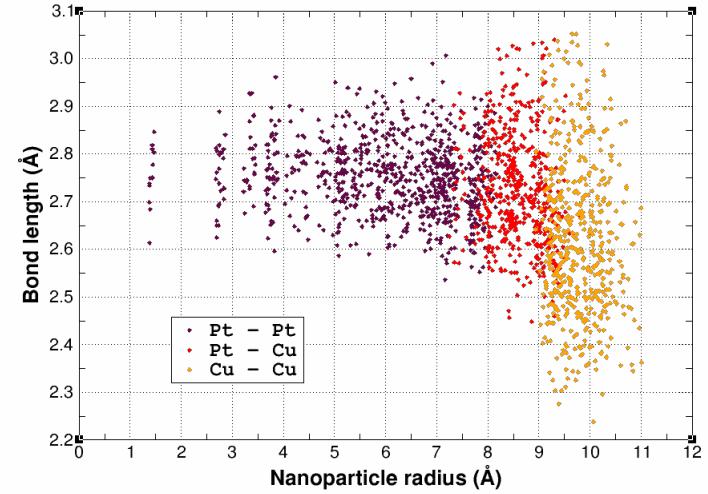

(b)

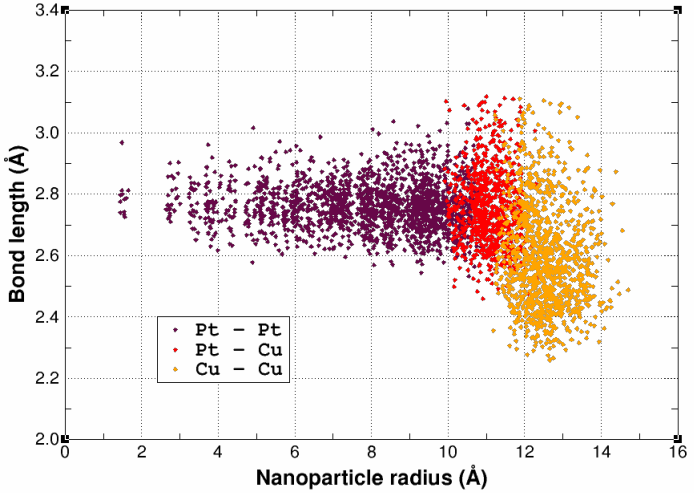

(d)

Figure 6.13: Bond length distribution across the radii of $Pt_{177}Cu_{204}$ (left), $Pt_{381}Cu_{386}$ (right) nanoparticles at 20 K and 300 K.

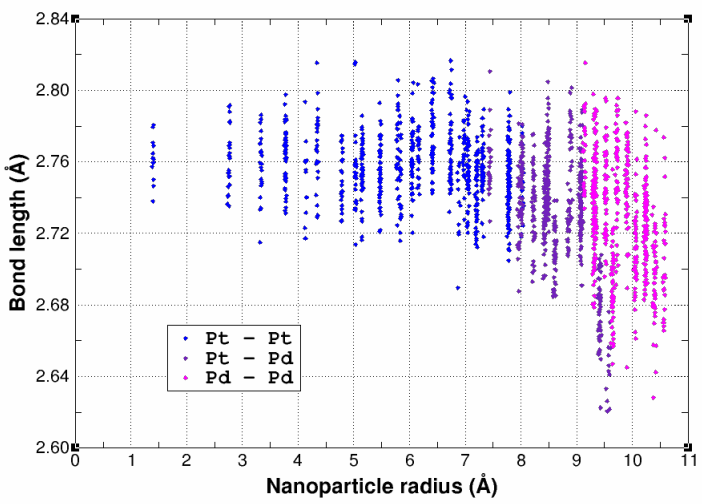

(a)

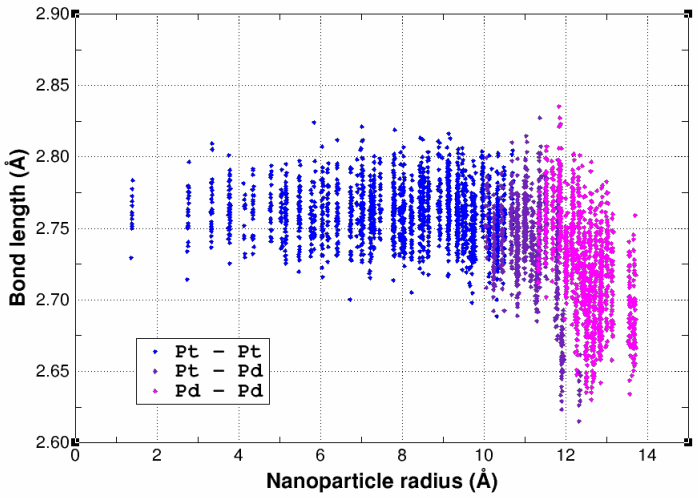

(c)

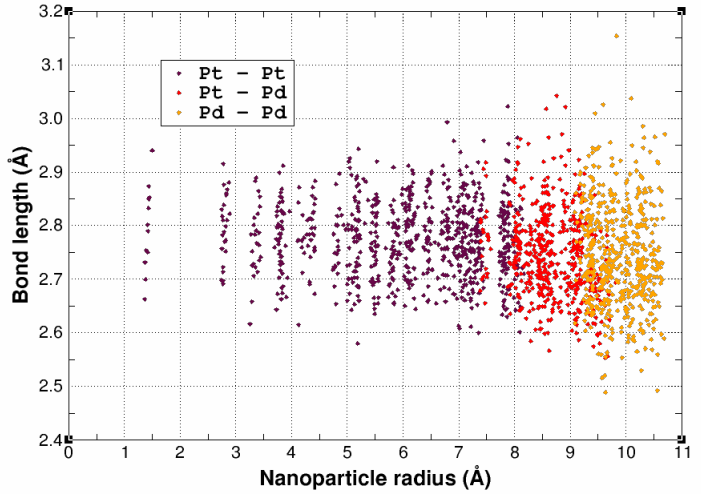

(b)

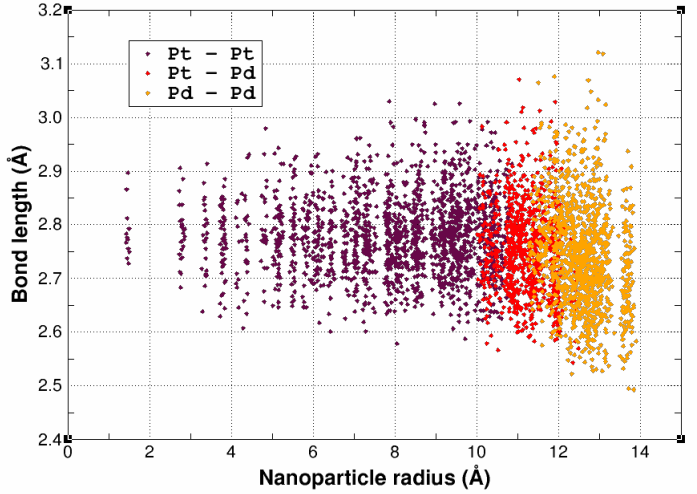

(d)

Figure 6.14: Bond length distribution across the radii of $Pt_{177}Pd_{204}$ (left) and $Pt_{381}Pd_{386}$ (right) nanoparticles at 20 K and 300 K.

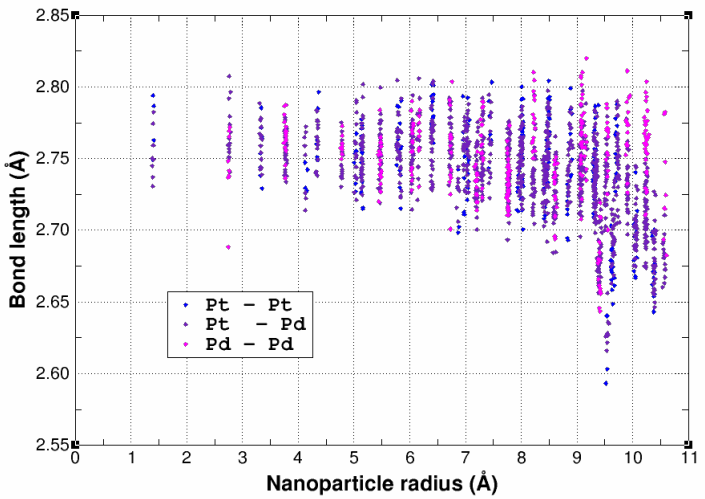

(a)

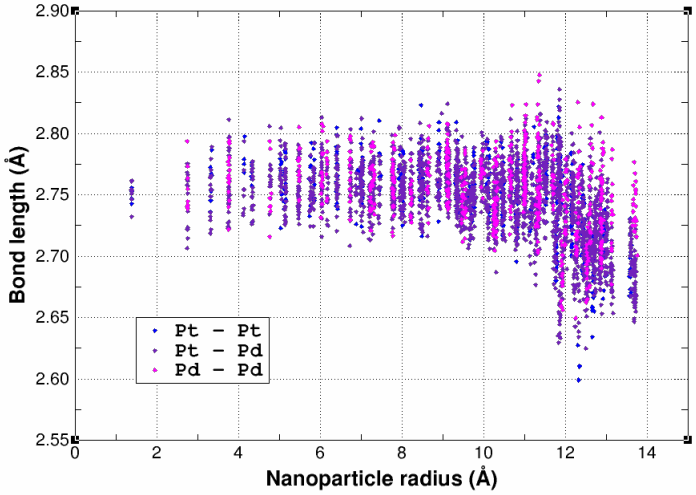

(c)

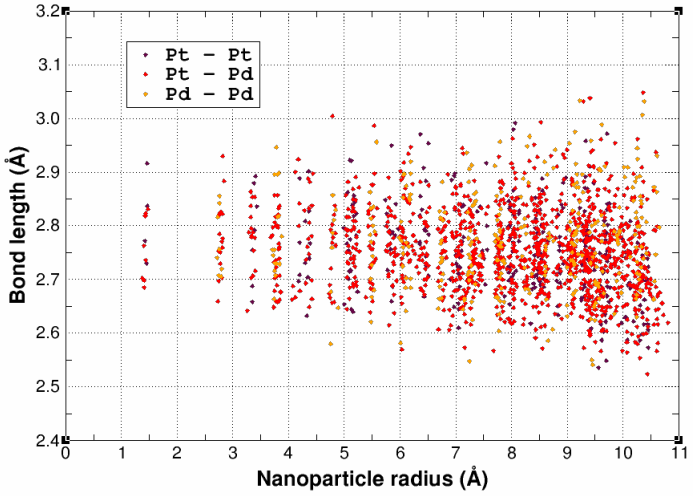

(b)

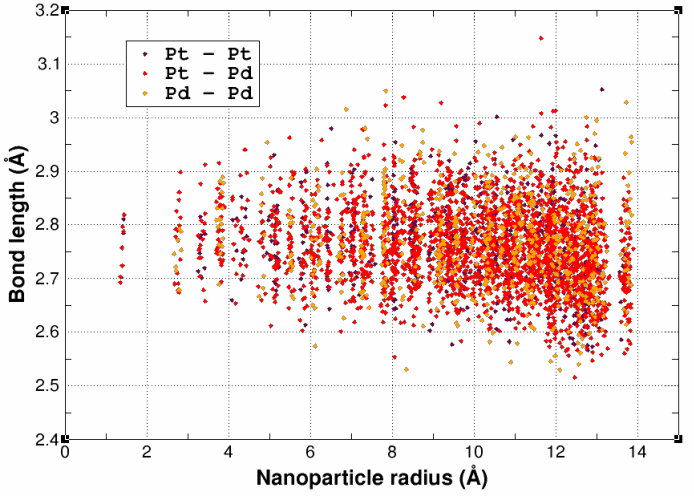

(d)

Figure 6.15: Bond length distribution across the radii of $Pt_{189}Pd_{192}$ (left), $Pt_{375}Pd_{392}$ (right) nanoparticles at 20 K and 300 K.

All the bond length distribution diagrams of the simulated nanoalloys at 20 K, show a robust structure, from the core to the surface, which is shown by the vertical grouping of points along the radius of the nanoparticle. These regions are dispersed across the volume of the nanoparticle as the temperature is raised and the atoms increase their vibrational and rotational motion. Platinum nanoalloys with palladium show a larger contraction at the surface which is more intensive for the $Pt_{core}Pd_{shell}$ rather than the intermixed structures. In room temperature the pair atomic distances of Pt-Pd nanoalloys are more relaxed compared to the Pt-Cu nanoalloys, as can be observed by the slight increase of the average atomic distances mainly inside the core region. The $Pt_{core}Cu_{shell}$ nanoalloys also show a surface reconstruction which seems to be stronger for the $Pt_{381}Cu_{386}$ at room temperature.

On the other hand, as the size of the nanoparticles and the temperature increase, the surface atoms of the non-intermixed structures seem to sink more inside the platinum core with the copper atoms showing larger intermixing rate than palladium atoms. Copper atoms in the outer shell of the Pt-Cu nanoalloys also have a larger range of bond lengths at 20 K which indicates the structural differences of the crystallographic morphology between the two metals, while palladium atoms with similar crystalline features with platinum show an even distribution of bond lengths along the radii of the nanoparticles.

6.4 Conclusions

The work in this chapter focuses on the challenging prospects of analysing EXAFS spectra for nanoparticles by combining theoretical data, from molecular dynamic simulations, with experimental data. Classical MD simulations performed on bare, spherical platinum nanoparticles, were used to fit experimental EXAFS data, mainly with respect to the first coordination shell. Data from simulated models of

Pt nanoparticles, where any structural disorder can be predicted, were used to interpret the anharmonic structural disorder in the EXAFS fit results, for several particle sizes, which is in better agreement with TEM data than the standard approach. The approach described in this chapter is a promising step towards the extension of the current EXAFS analysis to higher coordination shells.

Within this framework, other possible geometries of platinum nanoparticles such as icosahedral, cuboctahedral, or hemispherical were modelled, for future use in the EXAFS fit. Similarly, classical MD simulations of bi-metallic nanoalloys of Pt and Pd or Pt and Cu have also been performed. So far, studies trying to incorporate theoretical and experimental data, have assumed an even distribution of bond lengths throughout the nanoparticle. By being able to use MD data also regarding higher coordination shells would provide a significant improvement over the determination of particle morphology from EXAFS.

Chapter 7

Gold Nanoparticles and Nanosurfaces

This chapter summarises the results from calculations performed on three different categories of gold nanoclusters. In the first two sections, calculations on ultrasmall, bare gold nanoparticles are reported using density functional theory (DFT). Following the work from chapter 5, additional classical MD simulations have been also performed on different spherical gold nanoparticles, of sizes 1.39, 1.94, 2.50 and 3.05 nm.

The third section describes the outcome of geometry optimisations and some attempted *ab initio* MD simulations on gold nanosurfaces, in contact with small thiol molecules; and finally, the last section contains the results of classical MD simulations on a $Au_{core}Cu_{shell}$ nanoparticle and its predicted EXAFS spectrum, as calculated with the method employed in chapter 5.

7.1 Classical MD simulations on gold nanoparticles

Classical molecular dynamics simulations, using the Gupta [40] and the Sutton-Chen [41] force fields on the spherical Au_{13}, Au_{55}, Au_{177}, Au_{381}, Au_{767} and the icosahedral Au_{309} nanoparticles, have been performed (Figure 7.1). These configurations were chosen as representative structures, to aid the EXAFS analysis of synthesised gold nanoparticles. As in the MD simulations reported in chapter 5, the initial structures were optimised at "zero" temperature and later on simulated at 20 K, 85 K, 150 K and 300 K within the micro-canonical ensemble (NVE). A time-step of 1 fs and a total time of 2 ns were considered sufficient to perform the MD simulations. A 50 ps time has been used as an "equilibration" period at the beginning of every simulation.

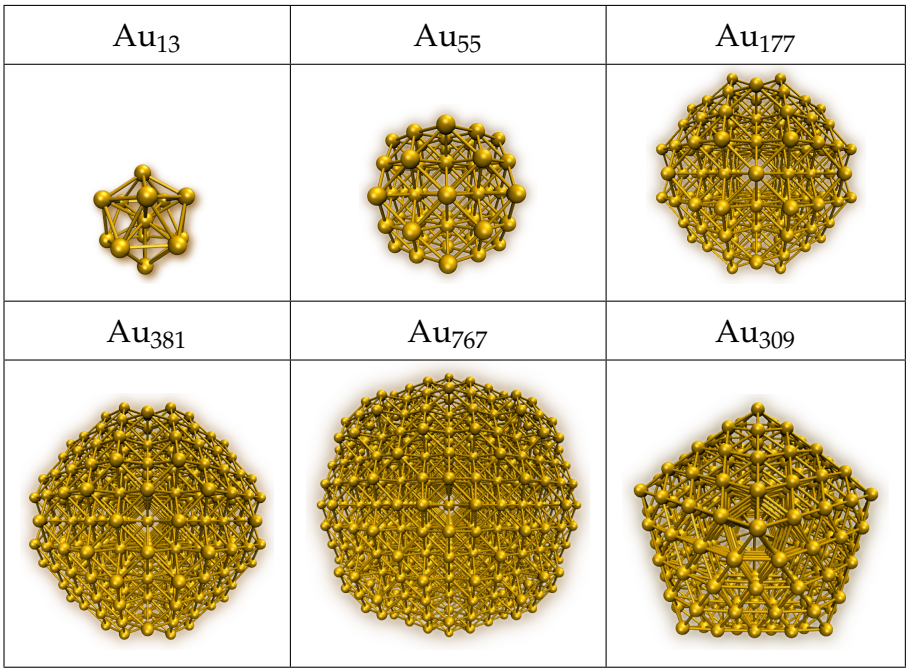

Figure 7.1: Optimised geometries of small gold clusters using DL_POLY [1]

The RDF plots of Figures 7.2 and 7.3, show the differences between the structures simulated at low and room temperatures. At low temperature, the RDF plots are constituted by high, sharp peaks due to the restricted motion of the atoms, in comparison with the RDFs of the nanoparticles simulated at room temperatures, where chemical bonds are relaxed and the vibrational and rotational motions are increased. While the agreement between the RDFs for the larger nanoparticles indicates a structural stability throughout the simulation, in the case of the Au_{55} nanocluster, a shifting of the last coordination shells to the left results from the strong effect of surface contraction, in both the temperatures shown.

On the other hand, when comparing the spherical Au_{381} and the icosahedral Au_{309}, it can be seen, that the Au_{309} nanoparticle has a more complex RDF, due to the different arrangement of atoms to form the icosahedral geometry. Starting from low temperatures, where the structures are almost frozen, the complexity of the Au_{309} plot is gradually reduced, becoming almost similar to the RDFs of the spherical nanoparticles at room temperature. This denotes a breaking of the particle's symmetry in higher temperature, which consequently leads to a distorted geometry with smoother features.

All the simulated structures showed a stable core, in contrast with the smallest nanoparticles, where the surface disorder is significantly large. Despite that, the ultrasmall Au_{13} and Au_{55} nanoparticles have essentially maintained their spherical shape throughout the simulation. The discrepancy observed between the final geometries of the Au_{13} and Au_{55} nanoparticles and the structure of their larger relatives, led us to perform a further investigation of these ultrasmall structures by employing a first principles method, as reported in the following sections.

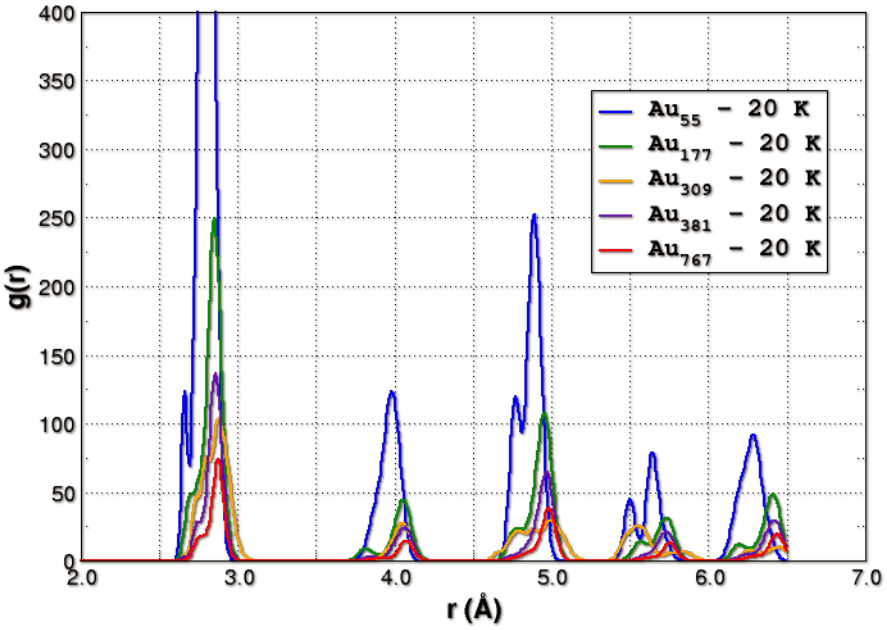

Figure 7.2: RDF of small gold nanoparticles at 20 K calculated with DL_POLY [18]

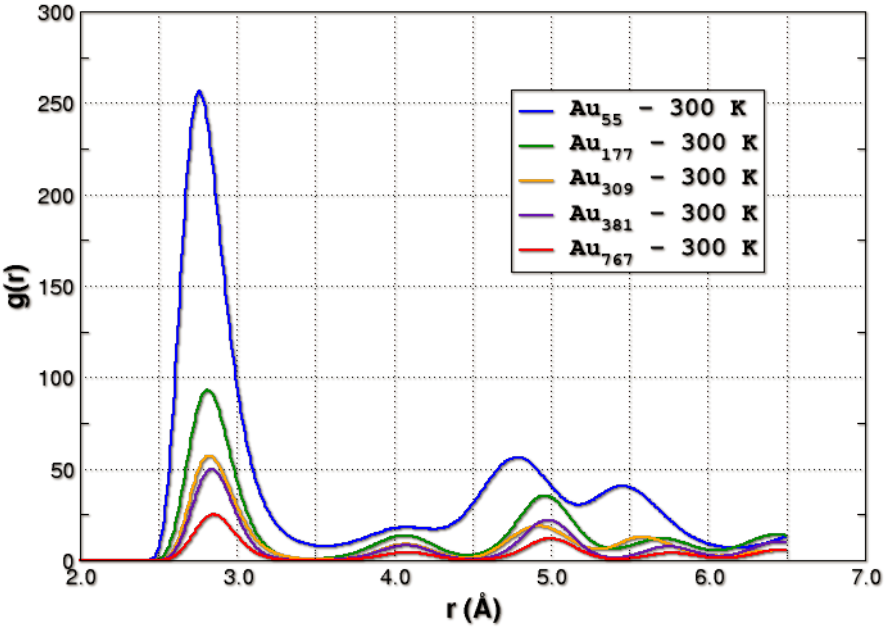

Figure 7.3: RDF of small gold nanoparticles at 300 K calculated with DL_POLY [18]

7.2 Ultrasmall Gold Nanoparticles

Ultrasmall gold nanoclusters, of sizes smaller than 200 atoms, have been extensively reported to show unique properties, in comparison with other nanoclusters from similar metals, due to their large relativistic effects [142, 188–191]. Confining the nanoparticles into quantum sizes, the de Broglie wavelength of valence electrons becomes of the same order as the particle's size and thus, the nanoparticles behave electronically as zero-dimensional quantum dots. These effects are responsible for their unique physical properties, the nanoparticles' size and shape, their amorphous features, observed experimentally, and the strong tendency of gold atoms to form contracted metallic bonds, mainly on their surface.

7.2.1 Theoretical Studies

Perhaps the breakthrough in the science of gold nanoparticles, which promoted the theoretical investigation of gold ultrasmall nanoparticles using first principles methods, emerged from the pioneering work of Schmid et al. [192]; who managed to isolate gold quantum dots and study their properties for the first time. The smallest cluster contained 13 Au atoms in dense packing, followed by layers of $10n^2 + 2$ atoms. The nanoparticle with 55 atoms was well characterised by Schmid's group, while larger nanoparticles of 147, 309, 561, 923, 1415 and 2057 ($n = 3 - 7$) atoms were also isolated.

Despite the existence of sophisticated experimental methods for analysing the structural properties of gold nanoclusters, some problems still remain unsolved. From comparison between experimental imaging methods or resonance methods, in the case of gold nanoparticles with sizes 1-2 nm, the resolution is not good enough to decompose explicitly their geometry features and provide a conclusive determina-

tion of their structure [142]. Thus, several theoretical calculations have been applied in order to shed light on their configurations at this size range.

Theoretical studies, employing DFT calculations and semiempirical potentials, have attempted to perform global minimisations on isolated gold nanoparticles, yielding controversial results due to the complexity of the Au potential energy surfaces (PES) [142,188,191]. Within this framework, attempting to utilise *ab initio* methods for computing the PES, involves significant difficulties for treating gold systems, even at this scale. Nonetheless, even at such a small scale, gold nanoparticles were shown to preserve their metallic properties, independent of their symmetry and structure [191].

For ultrasmall nanoclusters, simulations using empirical many-body potentials, such as the Gupta or the Sutton-Chen potential, which are used in studying the melting of bulk gold systems or in nucleation studies (sections 2.3.3.1 and 2.3.3.2), do not account correctly for the many-body effects required to obtain their correct shape and configurations and in general this applies for the majority of metallic clusters. At this size range, the calculations show that there are many energetically favourable configurations with little or no spatial symmetry, which strongly suggests that ultrasmall gold nanoparticles should be amorphous-like.

One of the works that supports the above argument is provided by Garzon et al. [191]. They have studied the structural stability of Au_n (n=38,55,75) amorphous and ordered nanoparticles, with MD simulations and the *n*-body Gupta potential [193] through dynamical optimisations. By additionally applying extremely low temperatures they have found that both kinds of isomers are of equal stability, with the energy difference between the amorphous and the ordered structures to be very small. Ercolessi at al. [194], reported that the melting temperature of gold nanoparticles of sizes smaller than 90 atoms, became zero, which suggests that ultrasmall gold nanoparticles should have a broken symmetry. Assadollahzadeh and

Schwerdtfeger [189] and Wang et al. [188], have also calculated the zero-point vibrational energy of several neutral gold nanoclusters, from 2-56 atoms, by using DFT based methodologies and found that this accounts for roughly $\sim$1% of the binding energy per atom.

A disordered structure has also been predicted for the lowest energy configuration of Pt_{13} (section 6.1.2) by performing DFT-LDA calculations [195]. These conclusions were in contrast with the classical MD simulations of Au_{13}, Au_{55}, Pt_{13} and Pt_{55} nanoparticles, reported in sections 7.1 and 6.1.2. Both the Gupta and the Sutton-Chen many-body potentials gave an optimised structure of high symmetry with ordered atoms as in the bulk fcc crystal; in contrast with the results mentioned in the above theoretical works. The structural properties of Au_{13}, Au_{55} were further investigated by conducting DFT calculations. The results of these calculations are reported in the following section.

7.2.2 DFT Calculations

7.2.2.1 Geometry optimisation

Trial energy minimisations on the smallest spherical nanoclusters using density functional theory have been attempted with different codes. DFT geometry optimisations on the Au_{13} and Au_{55} nanoclusters with ONETEP [4] and NWCHEM [19] (Gaussian basis set DFT) were impossible to converge. In contrast, calculations attempted with CASTEP [3] (plane-wave DFT), were able to complete successfully by using the ensemble density functional approach (EDFT). The calculations were performed by using the PBE exchange correlation functional [15] and a kinetic energy cut-off of 650 eV.

Geometry optimisations of metallic systems, with first principles methods, are extremely difficult to perform due to the constant variation of the occupancies of electrons and, consequently, the change in the energy band structure during the calculation, which often leads to non-convergence. The EDFT method developed in CASTEP allows the wavefunctions to be updated without invalidating the occupancies during the optimisation. This is achieved by minimising a free-energy functional with variable occupancies across some extra conduction bands, instead of minimising the energy with respect to only the valence bands. As a result, energies are tightly converged and forces can be calculated accurately.

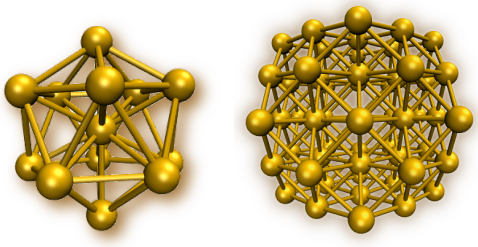

(a) (b)

Average Interatomic Distance (Å)			
Nano-particle	Surface	Core	Total
Au_{13}	2.872	2.731	2.832
Au_{55}	2.816	2.850	2.835

Figure 7.4: Optimised geometries with PBE-DFT of Au_{13} (a) and Au_{55} (b). Table: Average interatomic pair distances of Au atoms within Au_{13} and Au_{55} nanoparticles.

The table of figure 7.4 reports the nearest neighbour interatomic distances of the gold atoms in the Au_{13} and Au_{55} nanoparticles. It is worth noting that in the case of the smallest Au_{13} nanoparticle, the interatomic distances between the central atom, which is the only atom without free dangling bonds, are significantly shorter than the atomic distances calculated for the core atoms of Au_{55}, which are relatively closer to the distances reported for the bulk gold crystal (2.88 Å).

7.2.2.2 *Ab initio* Molecular Dynamics

After the successful optimisation of the above ultrasmall nanoparticles, molecular dynamics simulations of the Au_{13} and Au_{55} nanoparticles have also been attempted using a recently developed feature of the CASTEP code. In contrast with the classical MD scheme reported throughout this work, where an empirical potential or force field is required to describe the way atoms interact between them, the type of MD method implemented in the CASTEP code is defined as "ab initio" or "quantum" molecular dynamics.

The basic idea underlying every *ab initio* MD method is that the forces acting on the atoms are derived from electronic structure calculations, performed "on-the-fly", as the molecular dynamics trajectory is generated. In this way, the electronic variables are not integrated out beforehand, but are considered as active degrees of freedom. This implies that, for a suitable approximate solution of the many-electron problem, "chemically complex" systems can be treated effectively by molecular dynamics. While both classical and *ab initio* molecular dynamics employ the same principles, in practice, the latter method is shifted from manually selecting the model force field to the level of selecting a particular approximation for solving the Schrödinger equation.

The MD simulations of the ultrasmall Au_{13} and Au_{55} were performed at 300 K within the NVE ensemble. The same exchange-correlation functional and kinetic energy cut-off, as in the optimisation calculations, were used. The simulations showed a breaking in the ordered geometry of the systems, as reported also by Grazon et al. [191]. Furthermore, the energy diagrams of Figures 7.5 and 7.6, for each system respectively, show a characteristic variation of the energy throughout the MD trajectory due to the tendency of the systems to adopt a more amorphous structure at the expense of energy stabilisation. Although the *ab initio* MD simulations have been

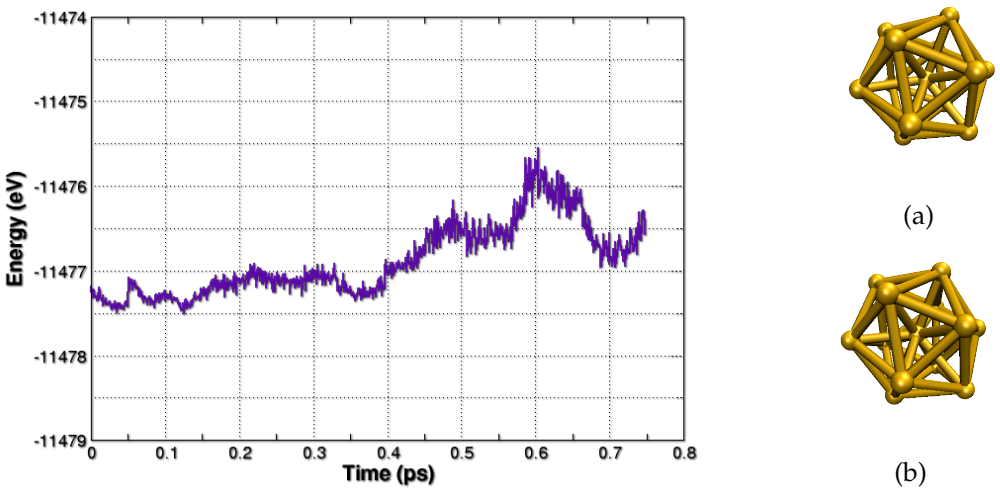

Figure 7.5: [Left] Energy diagram of Au_{13} at 300 K. [Right] Initial (a) and final (b) geometries of Au_{13} after a 0.15 ps of an *ab initio* MD simulation.

carried out for a very short time, even at such a small scale, the distortion of the total structure of the Au_{13} and Au_{55} nanoparticles is distinguishable, as can be seen in the right part of Figures 7.5 and 7.6.

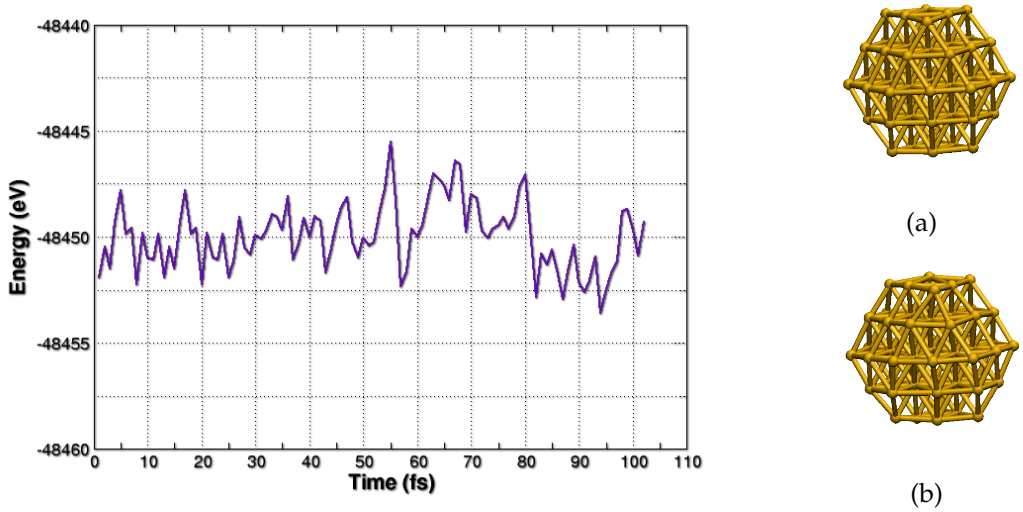

Figure 7.6: [Left] Energy diagram of Au_{55} at 300 K. [Right] Initial (a) and final (b) geometries of Au_{13} after a 0.18 ps of an *ab initio* MD simulation.

7.3 Thiol-Passivated Gold Nanosurfaces

The simulations reported so far regarding ultrasmall gold nanoparticles, have considered the studied systems being completely bare and in vacuum, without any interaction with solvent molecules or capping ligands. In reality though, to produce and isolate gold nanoparticles, organic compounds are used as capping ligands or stabilising agents. In the pioneering work of Schmid and co-workers [192], reported previously, the 55-atom gold nanocluster was encapsulated within phosphine molecules, and more precisely, the isolated compound was characterised as $Au_{55}(PPh_3)_{12}Cl_6$. Perhaps, nowadays, the most popular method for stabilising gold nanoparticles is the use of alkenothiols; firstly reported by Mulvaney and Giersing [196], who showed the possibility of using thiols of different chain lengths and structures in the synthesis of gold nanoclusters.

7.3.1 Synthesis and assembly

For a long time, among the conventional methods employed for the synthesis of gold nanoparticles was the citrate reduction of $HAuCl_4$ in water, introduced by Turkevitch [197]. Frens [198], later on, attempted to control the formation of gold nanoparticles by varying the ratio of reducing/stabilising compounds, leading to pre-chosen sizes of 16 to 147 nm diameter long gold(III) derivatives.

Following the works of Schmid et al. [192] and Mulvaney and Giersing [196], Brust and Schiffrin [199, 200] proposed a synthetic procedure for producing thermally and air-stable gold nanoparticles of controlled size, with a considerable impact on the overall field. The thiol ligands strongly bind on gold due to the soft character of both Au and S [138], which occurs from the reduction of $AuCl_4^-$ by $NaBH_4$ in the presence of dodecanethiol [201]. The proportion of thiol/$AuCl_4^-$ controls the size of the produced gold nanoparticles.

7.3.2 Theoretical studies

Luedtke and Landman [202, 203] have studied the structural and thermodynamic properties of dodecanethiol ($C_{12}H_{25}S$) and butanethiol (C_4H_9S) self-assembled monolayers (SAMs) on small and larger gold(III) nanoparticles, from 140 to 1289 Au atoms, using classical molecular dynamics. Self-assembly, is the property of the passivating ligands to spontaneously stick onto the surface of the nanometallic cluster. They found that the adsorption and arrangement of thiol chains on the surface is strongly depended on the size of the nanoparticles and their surface area. At low temperatures, the dodecanethiol molecules were grouped into anti-parallel orientations while at higher temperatures, they observed disordering and melting of the SAMs, with the transition for the larger cluster to be higher (T$\sim$294 K) than that for the smaller one (T$\sim$280 K).

In a similar work, Ta-Wei et al. [204] have investigated the packing structures of different types of alkanethiols on Au(III) surfaces with an all-atoms force field [205], within the NVT ensemble at 298 K. They found that the flexibility of the thiol headgroup (sulfur) aids and controls significantly the packing of the alkyl chains. Zhang et al. [206], on the other hand, have developed their own all-atoms force filed, based on *ab initio* results from DFT calculations, for studying the packing of alkenothiol SAMs on Au(III) surfaces with various chain lengths. According to their findings the packing, where the thiol chains have adopted a perfect parallel orientation but slightly tilted, was the most favourable, in terms of energy minimisation.

A Au_{38} core nanoparticle, coated with methylthiols, has been investigated via density functional theory by Häkkinen et al. [207]. Starting from a pre-optimised structure of the gold core with a classical force field, the nanoparticle was passivated with 24 methylthiol (MeS) molecules and optimised within the LDA approximation. From the calculated density of states of the bare and the coated Au_{38}, a 1.9 eV shift in the energy bands has been observed. In another theoretical study with density

functional theory, a 25-atom gold nanoparticle passivated with 18 thiols, has been studied [208]. Akola and co-workers have identified its lowest energy structure to be a compact Au_{13} core protected with 6 $[(MeS)_3Au_2]$ complexes.

While several works on thiol-passivated gold nanoparticles argue that the thiol molecules can dimerise, forming a disulfide on the Au(III) surfaces, Andreoni et al. [209] performed DFT calculations, based in the LDA method with some corrections from the BLYP [59, 62] and PBE [15] exchange-correlation functionals. From their calculations, the chemisorption of thiolates (H_3CS) was thermodynamically more favoured from the adsorption of thiols (H_3CSH). Disulfides (R-CH_2S-S-CH_2-R') were found to favour dissociation into strongly bound thiolates. Studying also the adsorption of thiolates onto the surface of a Au_{38} nanocluster (similarly with Häkkinen et al. [207]) and comparing with Au(III) surfaces saw that their chemical and thermodynamic properties were significantly different, from those of thiols.

Following the work of Andreoni and co-workers [209], the calculations reported in this work are focused on the interaction of methylthiolates with gold surfaces. As also reported in Ref. [209], the mechanism taking place during the growth of thiol SAMs is still unclear. In this case, two possibilities are available. The first supports the existence of intact thiols on the surfaces, which has been the case of an extensive experimental study by Nuzzo et al. [210] and the second suggests that when thiols stick to the gold surface, the S-H bond breaks, forming thiolate groups.

While Nuzzo and co-workers [210] defended the adsorption of unbroken methanethiols on the surface of gold nanoparticles, they reported some unexpected features found on some of the collected spectra. A peak assigned for the interaction of Au atoms with the S of the intact thiol, is questioned by the authors of Ref. [209], as this feature is characteristic of the stretch of the Au-S bond of thiolates, which originates from the adsorption of disulfides rather the weak stretch of Au and S atoms of the adsorbed thiols [211].

Furthermore, all the calculations performed by Andreoni et al. support this, by showing that the formation of thiolates by thiol dissociation on gold surfaces is accompanied by hydrogen chemisorption. This is the mechanism which is energetically favoured. As the energy difference between the thiol and thiolate adsorbates is quite small ($\sim$3 kcal/mol) this may be an indication of the co-existence of the two possible mechanisms. On the other hand, the latter authors found that formation of molecular hydrogen, which subsequently desorbs from the surface, can aid the stabilisation of thiolates by an additional amount of 1-3 kcal/mol.

7.3.3 Construction of nanosurfaces

In order to study the impact of organic ligands attached to gold surfaces, DFT calculations have been performed by using the CASTEP code [3]. Similarly with Ref. [209], the PBE exchange-correlation functional has been employed for all the calculations performed on Au(III) surfaces.

As an initial step, the calculation parameters were chosen according to the convergence of the total electron energy E_{tot} with respect to energy cut-off E_{cut}, the k-point grid and the fast Fourier Transform (FFT) numerical grid. For this purpose, DFT calculations on a 3-dimensional periodic image of bulk gold crystal have been completed successfully.

The convergence of the total energy of the bulk gold unit cell, with respect to the energy cut-off is shown in Figure 7.7. From the plot of the total energy with respect to the energy cut-off it can be observed that by using an energy cut-off of 500 eV it is sufficient enough to obtain results with a fine accuracy. Meanwhile, by several other trial calculations performed, a k-point MP grid spacing of 0.05 $Å^{-1}$ was observed to provide satisfactory results.

In general, a relatively large number of k-points is required for an accurate k-point sampling of small unit cells such as in this case, whereas a few points are required for large unit cells. For very large unit cells, only a point at k = 0 (known as the Γ point) is used for calculations in the reciprocal space (section 1.2.5). Additionally, the number of k-points increases as the distance between k-points decreases. In this case, the number of k-points to be is generated by a k-point spacing of 0.05 $Å^{-1}$. The advantage of specifying the k-point spacing instead of a fixed grid is to assure a constant sampling in the k-space independently of the unit cell size, which may have an impact when transferring the parameters chosen to perform calculations on periodic gold nanosurfaces.

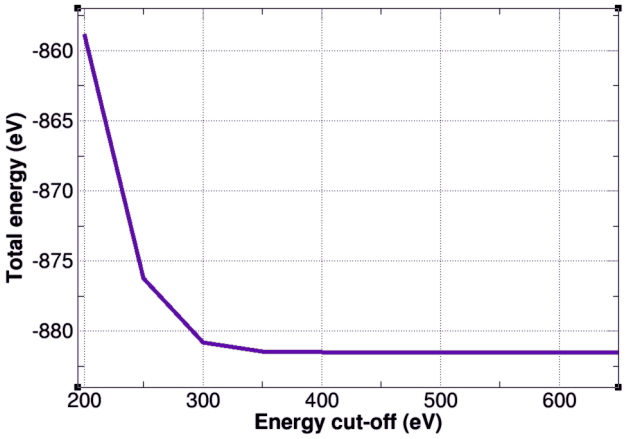

Figure 7.7: Total energy convergence of Au unit cell with respect to the energy cut-off

7.3.3.1 Geometry optimisations

Calculations with the CASTEP code [3] on periodic Au(111) surfaces have been performed. Figure 7.8 shows the geometries of the molecular systems being studied. The Au(111) surfaces were constructed by slicing the bulk structure in the [111] crystallographic direction and coupling the resulting slab with a vacuum gap of about 10 Å. The slab is then fitted on the xy plane and then simulated using periodic boundary conditions. The x and y directions are allowed to vary, while the z-direction is kept fixed. The reliability of the results and the quality of the simu-

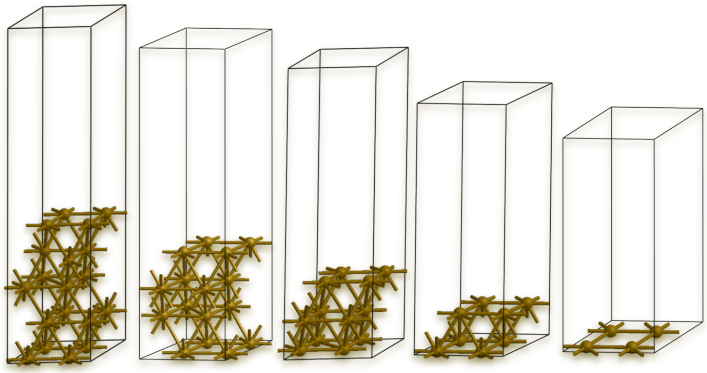

Figure 7.8: Structures of Au(111) surfaces studied with CASTEP [3]

lations are checked by studying the variation of the surface free energy (E_{surf}) with respect to the Au(111) surface thickness and its vacuum gap until convergence is achieved [212]. The surface energy is defined as:

$$E_{surf} = \frac{E_{slab} - E_{bulk}}{A} \tag{7.3.1}$$

where A is the total area of the Au(111) surface, E_{slab} is the computed energy of the slab and E_{bulk} is the energy of an equivalent amount of atoms in bulk gold.

The results, obtained from the calculations performed, are summarised in the Table 7.1. As can be observed the surface energy (E_{surf}) is decreased as the number of layers increases. Furthermore, the difference in surface energy between the fourth and fifth layer of Au atoms implies that a constructed gold nanosurface with 5 layered thickness, is a reliable representative structure for simulating the properties of real Au(III) surfaces.

Table 7.1: Energy values obtained for the optimised structures of the gold nanosurfaces using the CASTEP code [3]

Layers	$\mathbf{E}_{slab}$ (eV/atom)	$\mathbf{E}_{bulk}$ (eV/atom)	**A** (Å^2)	$\mathbf{E}_{surf}$ (eV/Å^{2}atom)
1	-884.7001	-884.8931	14.623	0.0127
2	-884.7042	-884.8931	15.125	0.0117
3	-884.7249	-884.8931	16.139	0.0115
4	-884.7494	-884.8931	16.216	0.0088
5	-884.7592	-884.8931	16.497	0.0082

Following the results of the above calculations, 4 types of (2×2) superlattices of 5-layered gold nanosurfaces in interaction with a methylthiolate molecule, have been constructed. The spatial parameters of the previously optimised gold slabs were used, by expanding the simulated surface unit cell in the x and y directions by a factor of 2, thus, providing a (2×2) nanosurface. The (H_3CS) molecules were manually placed on the surfaces according to the symmetrical parts of the above layer of Au atoms, as shown in Figure 7.9. These parts are coloured differently, where areas with the same colour have the same spatial symmetry. Consequently, this lead to 4 different structures of a (H_3CS) attached to a Au(III) nanosurface. Visual representations of the simulated systems are shown in Figure 7.10 and are named according to the colouring scheme of Figure 7.9. A vacuum region of 10 Å between the hydrogen atoms of the methythiolate and the top xy-plane of the simulation box has been maintained also here, to avoid any atomistic interaction between periodic images along the z-direction.

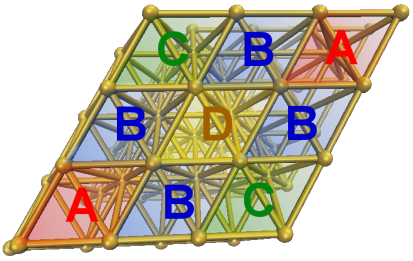

Figure 7.9: Symmetrical parts, shown with different colours, of the simulated Au(III) nanosurface

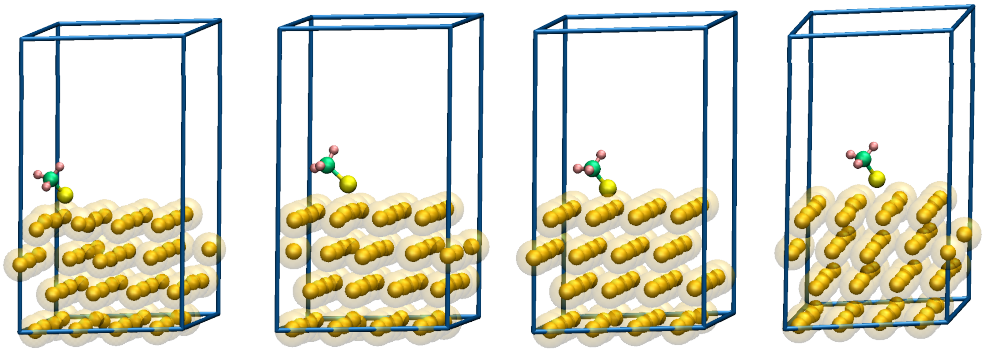

(a) A (red) (b) B (blue) (c) C (green) (d) D (yellow)

Figure 7.10: 4 different (2×2) structures of (H_3CS)-Au(III) nanosurfaces. The assigned letters refer to the colouring scheme of Figure 7.9

The constructed systems were then optimised using the "damped MD method" that has been recently implemented in the CASTEP code [3]. This method allows the direct minimisation of the energy functional, using a second-order equation of motion, by introducing some damping parameters. The first-order dynamics, generally deals with the finding of the ground energy state while the second-order corresponds to the oscillations around the configuration of that energy state. The "damped MD" scheme developed in CASTEP, is significantly faster than the BFGS (section 1.1.2) optimisation technique and besides the critical damping, still maintains the accuracy of a first principles method.

The energy and force tolerances during the energy minimisation of the structures were set to 0.2×10^{-4} eV/atom. A k-point MP grid spacing of 0.05 $Å^{-1}$ and a 650 eV kinetic energy cut-off were used, as in the optimisation of the bare gold nanosurfaces. During the optimisation, the size of the simulation box and the 2 lower layers of Au atoms of the nanosurface were kept fixed.

7.3.4 *Ab initio* Molecular Dynamics

Upon successful optimisation of the constructed (H_3CS)-Au(III) nanosurfaces, *ab initio* molecular dynamics simulations were carried out . A combination of any two of the optimised thiolate-Au nanosurfaces, provided 6 new (2×2) superlattices with two thiolate molecules attached. Along with the MD simulations of (H_3CS)-Au(III) nanostructures, *ab initio* MD simulations have been performed also on the $(H_3CS)_2$-Au(III) nanosurfaces at 300 K within the NVE ensemble. Snap-shots taken at the beginning and the end of the simulations are shown in Figures 7.11 - 7.20. For every configuration, binding energies have been calculated and then obtained as averages.

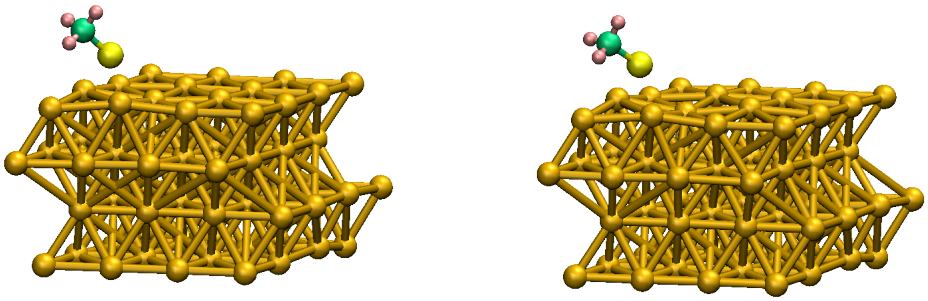

(a) (b)

Figure 7.11: Configurations of A-CH_3S-Au(III) before (a) and after 0.1 ps (b) of a MD simulation at 300 K.

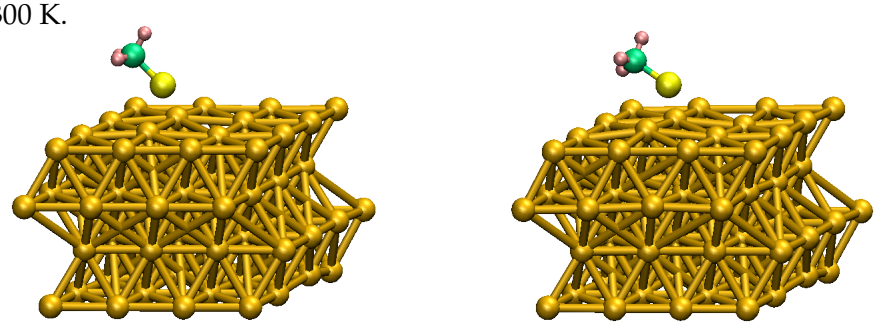

(a) (b)

Figure 7.12: Configurations of B-CH_3S-Au(III) before (a) and after 0.1 ps (b) of a MD simulation at 300 K.

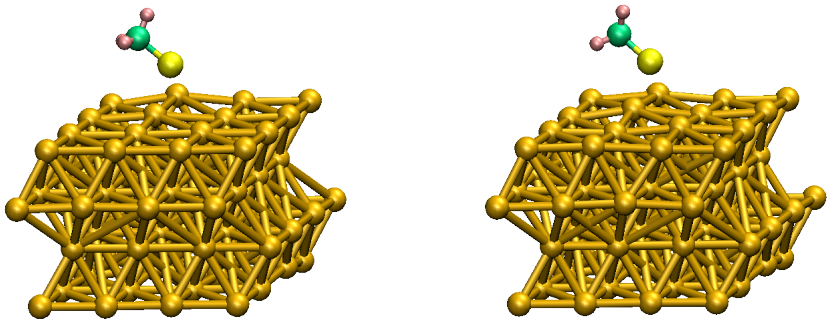

(a) (b)

Figure 7.13: Configurations of C-CH_3S-Au(III) before (a) and after 0.1 ps (b) of a MD simulation at 300 K

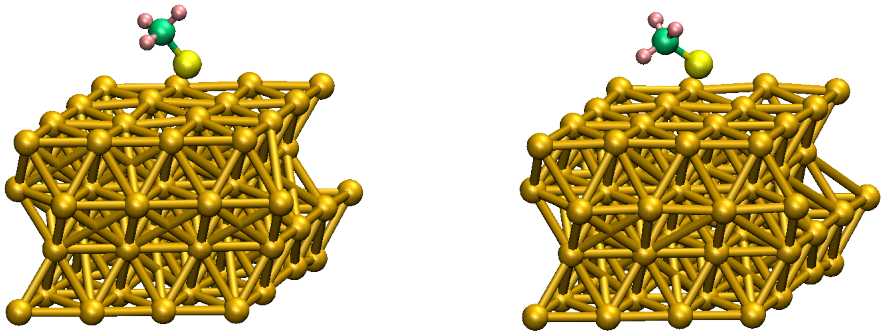

(a) (b)

Figure 7.14: Configurations of D-CH_3S-Au(III) before (a) and after 0.1 ps (b) of a MD simulation at 300 K

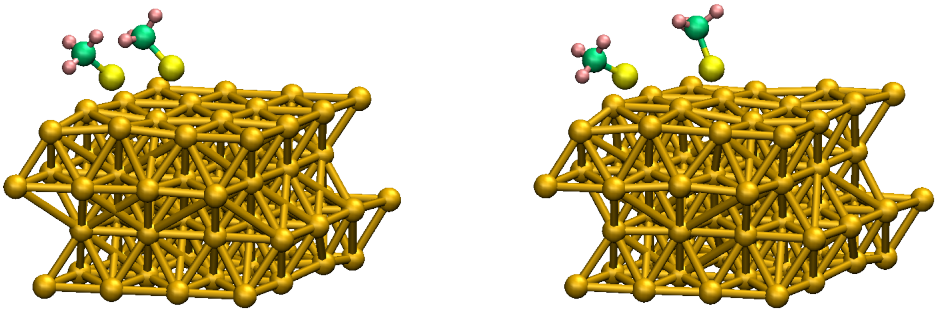

(a) (b)

Figure 7.15: Configurations of AB-$(CH_3S)_2$-Au(III) before (a) and after 0.2 ps (b) of a MD simulation at 300 K

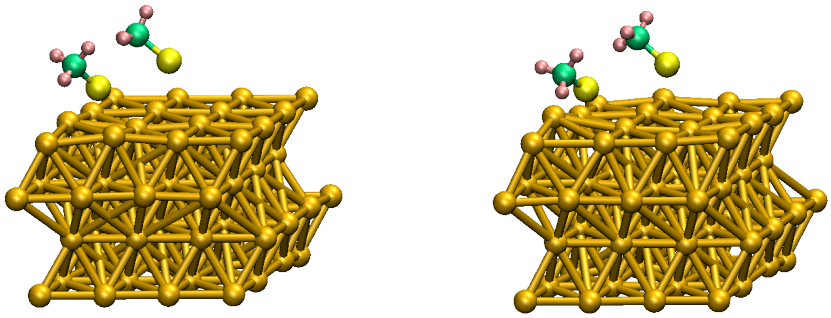

(a) (b)

Figure 7.16: Configurations of AC-$(CH_3S)_2$-Au(III) before (a) and after 0.2 ps (b) of a MD simulation at 300 K

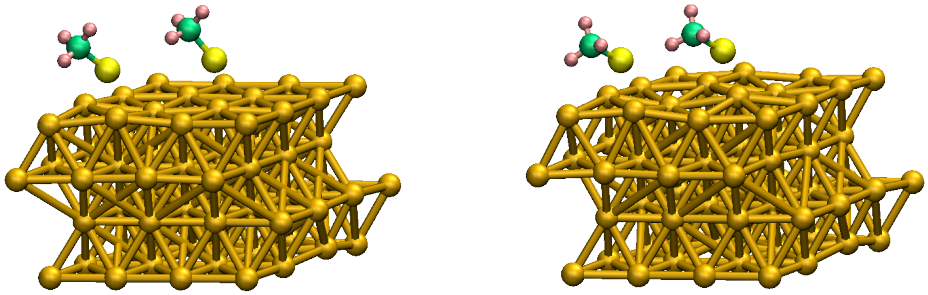

(a) (b)

Figure 7.17: Configurations of AD-$(CH_3S)_2$-Au(III) before (a) and after 0.2 ps (b) of a MD simulation at 300 K

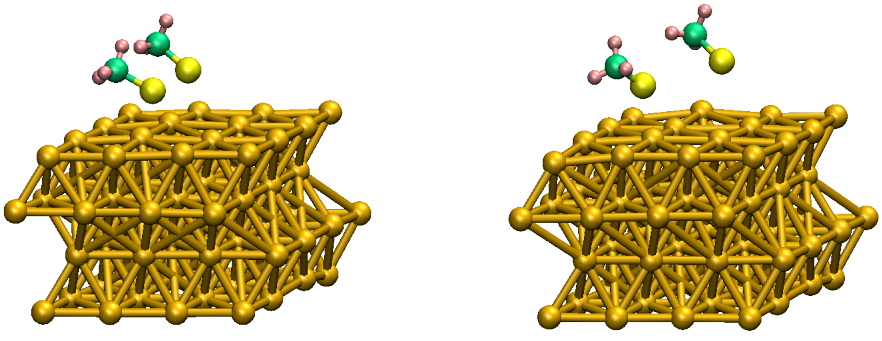

(a) (b)

Figure 7.18: Configurations of BC-$(CH_3S)_2$-Au(III) before (a) and after 0.2 ps (b) of a MD simulation at 300 K

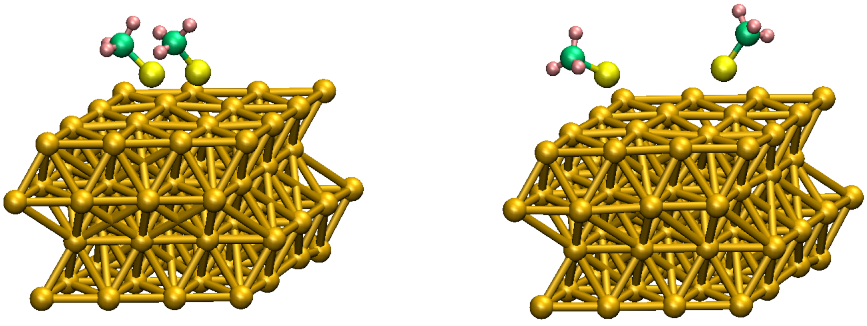

(a) (b)

Figure 7.19: Configurations of BD-$(CH_3S)_2$-Au(III) before (a) and after 0.2 ps (b) of a MD simulation at 300 K

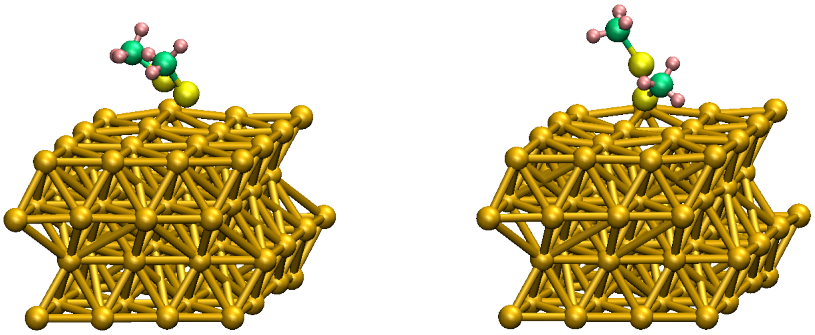

(a) (b)

Figure 7.20: Configurations of CD-$(CH_3S)_2$-Au(III) before (a) and after 0.2 ps (b) of a MD simulation at 300 K

Looking the depicted structures at the starting and final point of the simulations, a surface distortion can be observed at the point where the thiolate is attached. The Au-atom(s) of the top layer that bind to the sulfur atom of the methylthiolate, are extended away from the surface level, creating a small cavity around the neighbour atoms. On the other hand, where 2 thiolate molecules are directly located nearby, in close distance between them (Figures 7.15, 7.18, 7.19 and 7.20), a repulsion force that pulls them away from each other seems to take place.

Table 7.2: Binding energies of mono- and di- methanethiolates

System	**BE** (eV)	**System**	**BE** (eV)
A-CH_3S-Au(III)	1.844	AB-$(CH_3S)_2$-Au(III)	1.993
B-CH_3S-Au(III)	1.858	AC-$(CH_3S)_2$-Au(III)	1.895
C-CH_3S-Au(III)	1.809	AD-$(CH_3S)_2$-Au(III)	1.862
D-CH_3S-Au(III)	1.841	BC-$(CH_3S)_2$-Au(III)	2.673
		BD-$(CH_3S)_2$-Au(III)	2.715
		CD-$(CH_3S)_2$-Au(III)	2.813

Observing the binding energies of single thiolate gold nanosurfaces, at 300 K, the CH_3S-Au(III) systems gain by 0.7-0.8 eV of stabilisation as a 0.1 ps simulation progresses. While the B-CH_3S-Au(III) shows a slightly larger binding energy, the D-CH_3S-Au(III), where the thiolate molecule is located in the centre of the top layer of Au atom, is the system that shows the largest stabilisation during the simulation ($\sim$0.9 eV). On the other hand, the simulated $(CH_3S)_2$-Au(III) systems showed larger binding energies from the CH_3S-Au(III) nanoclusters.

While all the simulated structures seem to have similar binding energies, in the case of the BC-$(CH_3S)_2$-Au(III), BD-$(CH_3S)_2$-Au(III) and CD-$(CH_3S)_2$-Au(III) the binding energies are by 30%-40% larger than the rest of the systems. This is likely due to the strong structural reorganisation taking place between the thiolate molecules, where a conformation with thiolates located quite apart from each other seemed to be preferred. The results shown are in fairly good agreement with the binding energies reported by Andreoni et al. [209] (3.12 eV for $(CH_3S)_2$-Au(III)), where 1.56 eV can be assigned for the Au-S bond of each bound disulfide to the gold surface. Considering also that a part of the energy is used for maintaining the S-S bond in the dimethyl disulfide, the binding energies of the thiolates reported here are expected to be larger.

7.4 Gold-Copper Nanoalloys

7.4.1 Synthesis

Bulk Au-Cu alloys exist in three stoichiometric phases: (a) Cu_3Au, (b) $CuAu_3$ and (c) CuAu. Yasuda et al. [213, 214] studied the separation of copper atoms on a surface of gold nanoclusters supported on an amorphous carbon film , where a rapid mixing was observed at room and lower temperatures. Yasuda and Mori observed stoichiometric $(Cu_3Au)_M$ clusters using TEM, and found that for nanoclusters with sizes around 9 and 20 nm, annealing results in ordering of the initial samples, giving the structure of bulk Cu_3Au [213]. For nanoclusters smaller than 4 nm, the solid solution had the most stable phase. The Cu-Au clusters showed a fcc local packing structure, as in their bulk alloy counterparts.

In a more recent work, Schaak and co-workers described a novel procedure for the synthesis of bimetallic nanoparticles in solution at low temperatures [215, 216]. Cu-Au nanoparticle aggregates were used as precursors to synthesise atomically ordered nanocrystals of intermetallic CuAu, Cu_3Au, and $CuAu_3$. Using several imaging methods they revealed that while the Au nanoparticles are crystalline, the Cu particles appear to be amorphous at the first stage. Then, the Cu-Au aggregates were heated under flowing argon, followed by annealing at 200-300 ^oC which lead to atomically ordered nanocrystals of CuAu, Cu_3Au, and $CuAu_3$.

7.4.2 Computational Works

Lopez and co-workers performed MD simulations, using a many-body Gupta-type potential, on 13- and 14-atom Cu, Au, and Cu-Au clusters, studying their structural properties and melting points [217]. According to their findings, the bimetallic systems showed a closer resemblance to copper clusters rather than the gold clusters,

while the gold clusters, only exhibited a single stage of melting, whereas pure copper and alloy clusters displayed two.

Pauwels and co-workers [218], have studied isolated truncated octahedral clusters of 456 and 786 atoms and a spherical cluster of 959 atoms by performing Monte Carlo (MC) simulations . Their MC simulations predicted that these clusters were not ordered and also not completely homogeneous. The core structure was found to be fully ordered at 300 K, undergoing some distortion at around 600 K. They have also reported possible reasons about the disagreement of their MC simulations with the experimental results, where it appears to be no evidence for core separation with a coated shell of Au [218]. They argued that experimentally the Cu-Au clusters are not generated in an environment of thermodynamic equilibrium, but are being cooled rapidly which can induce structural changes or rearrangement of atoms when interacting with the substrate. On the other hand, the clusters simulated were smaller than the clusters obtained from many of the experiments conducted so far (diameters larger than 4 nm).

Johnston and co-workers have extensively studied Cu-Au clusters with varying compositions and nuclearities [219, 220]. One of their studies was focused on small Cu-Au clusters with either Cu-rich or Au-rich compositions. In Cu-rich clusters they observed disordered structures while for Au-rich clusters provided polyicosahedral structures, such as the Cu_4Au_{30} (incomplete 6-fold pancake) and the perfect core-shell Cu_6Au_{28} and Cu_7Au_{27} (5-fold pancake) clusters. In the case of Cu-rich clusters the intermixing distortion was attributed to the tendency of maximising the Cu-Au bonds, which is greater to the tendency for segregate the Au atoms to the surface [221]. For 38-atom clusters, truncated octahedra dominated the Cu-rich compositions. Their results were in good agreement with the work of Hsu and Lai, who used a hybrid GA-basin-hopping search algorithm, based in the Gupta potential, to study 38-atom Cu-Au nanoalloys [222].

In another work by Johnston et al., stoichiometric structures of bulk-like Cu-Au nanoalloys, $(Cu_3Au)_M$, $(CuAu)_M$, and $(CuAu_3)_M$, were studied and compared with pure Cu and Au clusters, using the Gupta many-body potential [220]. Pure copper clusters adopted regular, icosahedral structures, while gold clusters produced amorphous-like structures, as reported previously by Garzon et al [191]. In the cases of 14, 16, and 55 atoms, replacing a single Au atom with Cu altered the general structure to that of a pure Cu cluster, also supported by Lopez et al [217]. For the stoichiometric nanoalloys, the lowest energy structures were based on icosahedral packing. The $(CuAu)_M$ and $(CuAu_3)_M$ clusters provided layered arrangements of Cu and Au atoms, whereas the Cu and Au atoms were noticeably intermixed in the $(Cu_3Au)_M$ clusters. For all the layered structures observed, the surfaces of the clusters were mainly rich in gold atoms, while the icosahedron-based structures had a Cu atom at the centre. The predicted tendency to Au surface segregation, was in agreement with MD simulations on Cu-Au nanoalloys performed by Rodriguez-Lopez et al [223].

Wilson and Johnston [224] conducted energy calculations on icosahedral and cuboctahedral Cu-Au nanoalloys with 1 to 5 shells with varying composition using again the Gupta many-body potential. For each composition the lowest energy homotops were found to have predominantly Au atoms on the surface and Cu atoms in the core. This was attributed to the lower surface energy of Au compared to Cu and the tendency for mixing or segregation was explained in terms of relative strength of Cu-Cu, Cu-Au, and Au-Au bonding interactions.

Recently, Fernandez et al. performed DFT calculations on $(CuAu)_N$ clusters, with N=5-22, by re-optimising configurations of low-energy isomers provided from a search method based on the Gupta potential [187]. Although the exact ordering of the homotops was quite different between the DFT and Gupta potential calculations, the general stability of icosahedral structures was confirmed.

7.4.3 Classical MD Simulations

Within the perspective of modelling complicated bimetallic systems and predicting their EXAFS spectra, a very limited investigation of the structural and phase equilibria of a spherical gold nanoparticle covered with a copper layer has been studied using the Gupta force field. The parameters used for describing the interactions between the homonuclear atoms (Au-Au and Cu-Cu) were taken to be the same in the nanoalloys as in the pure metallic systems. The heteronuclear interaction parameters (Au-Cu) were obtained by fitting to crystalline Cu_3Au, as derived by Cleri and Rosato [43].

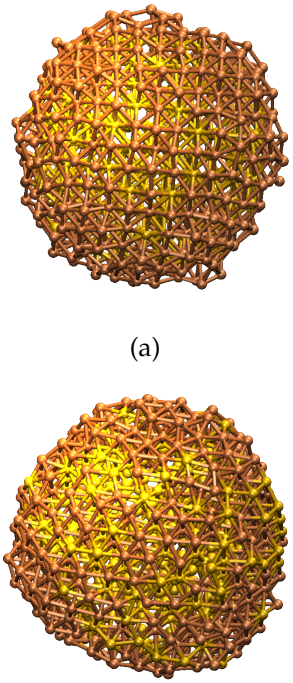

(a)

(b)

Figure 7.21: (a) Initial (equilibrated) and (b) and final structure of the $Au_{381}Cu_{386}$ nanoalloy after a 4 ns MD simulation at 300 K.

The MD trajectory of the $Au_{381}Cu_{386}$ nanoalloy reveals a strong surface and volume distortion, as the copper atoms on the surface sink into the core of gold atoms, during the simulation. This indicates the low segregation rate of the gold-copper nanoalloys and their strong tendency to amalgamate, at this small scale, as supported also by Pauwels and coworkers [218]. On the other hand, the diffusion of the copper atoms inside the systems's centre of mass shows the preference of Cu atoms to be allocated within the core, as suggested also by Johnston et al. [224]. Visual representations of the initial and final structures predicted by the MD simulations are shown in Figure 7.21.

Figures 7.22 and 7.23 show the radial distribution function (RDF) of the $Au_{381}Cu_{386}$ nanoparticle derived from a MD simulations at 20 K and 300 K. Despite the surface

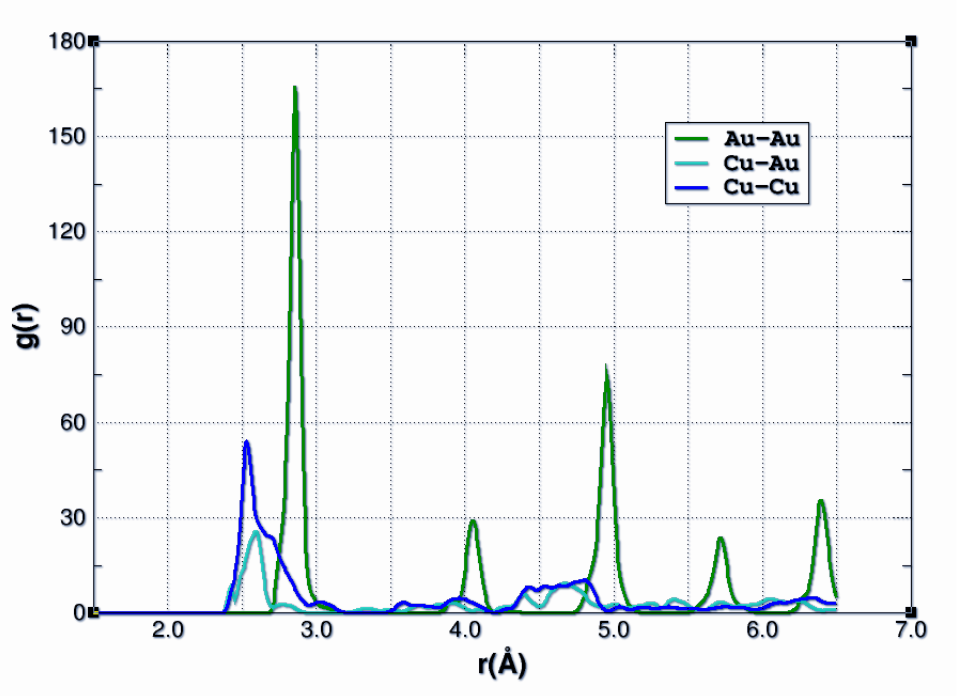

Figure 7.22: Radial distribution diagram of $Au_{381}Cu_{386}$ at 20 K.

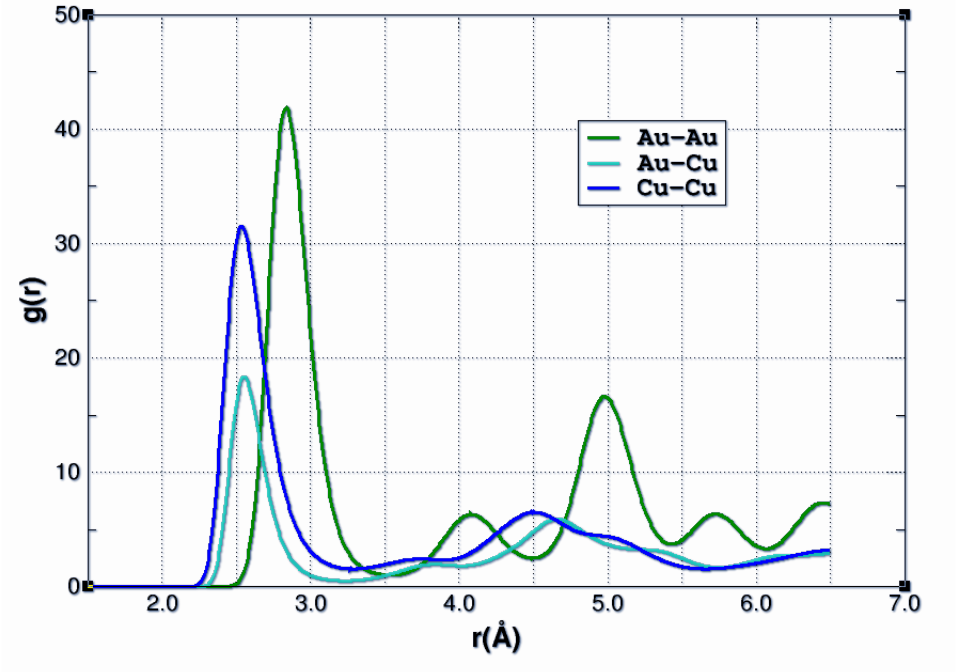

Figure 7.23: Radial distribution diagram of $Au_{381}Cu_{386}$ at 300 K.

distortion, the gold atoms, mainly inside the core of $Au_{381}Cu_{386}$ preserve their structural properties at 20 K and 300 K, as can be seen from the clear definition of the first atomic pair distances in the RDF plot. The surface defects are shown by the large variation of the nearest neighbour atomic distances of the copper atoms while the gold atoms on the surface are strongly affected by the surface Cu atoms which tend to adopt similar conformation, as the simulation proceeds further on.

7.4.4 Calculation of EXAFS

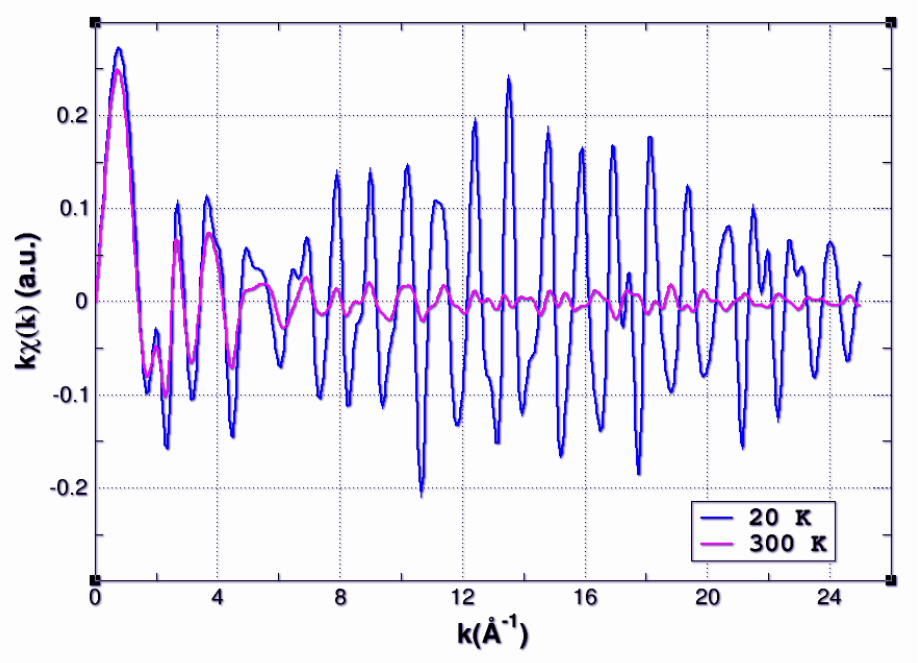

Figure 7.24: Calculated EXAFS spectra of $Au_{381}Cu_{386}$ from classical MD simulations at 20 K (blue) and 300 K (pink).

The strong surface reconstruction induced by the surface Cu atoms to the Au atoms within the core, is apparent in the calculated EXAFS spectra. Figure 7.24 shows the EXAFS spectra calculated for the $Au_{381}Cu_{386}$ nanoparticle, from the MD simulations at 20 K and 300 K, by only using a few MD snap-shots after the equili-

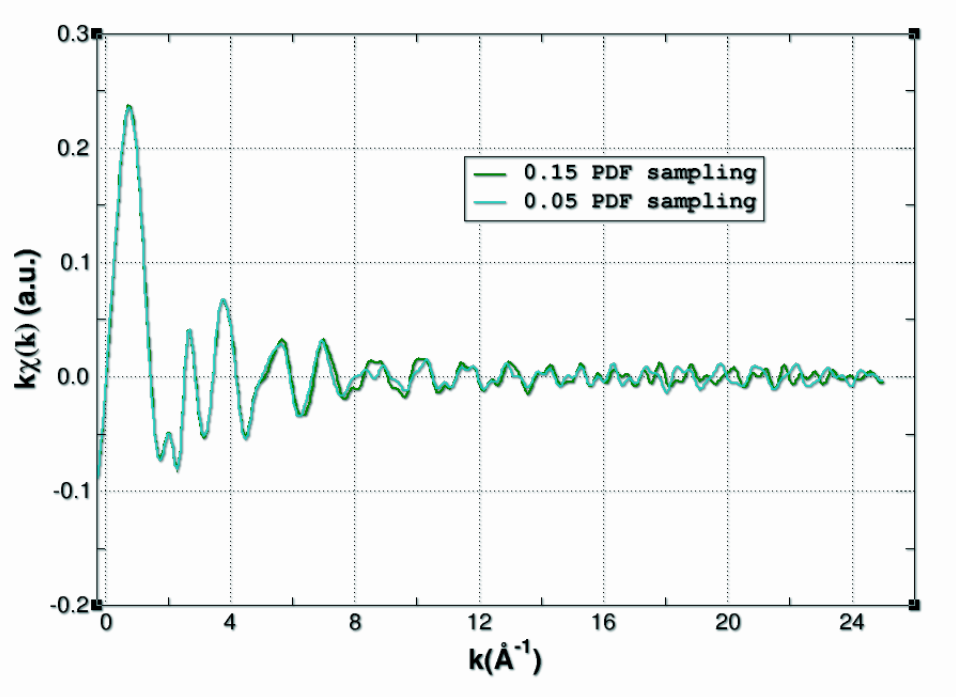

Figure 7.25: Calculated EXAFS spectra of $Au_{381}Cu_{386}$ at 300 K with a fine (turquoise) and a coarser (green) PDF sampling.

bration of the system, at the beginning of the production period of the simulation. Albeit the nanoparticle is not perfectly equilibrated the structure at 20 K is in phase with the structure obtained at 300 K. The difference in the intensity of the peaks can be attributed to the thermal disorder.

The EXAFS shown in Figure 7.25 are derived from the last 20-25 frames of the MD trajectory at 300 K, where a finer PDF sampling has been used with respect to the default value. Even though the EXAFS data seem to coincide in the first values of k, the form of the curvature changes as we move along larger values. This difference is more likely a result of statistical inaccuracy, as the main peaks are identical and in phase. Be comparing the spectra collected at the beginning (Figure 7.24) and at the end (Figure 7.25) of the simulation, the results are significantly different, due to the impact of the Cu atoms sinking into the core of the gold nanoparticle.

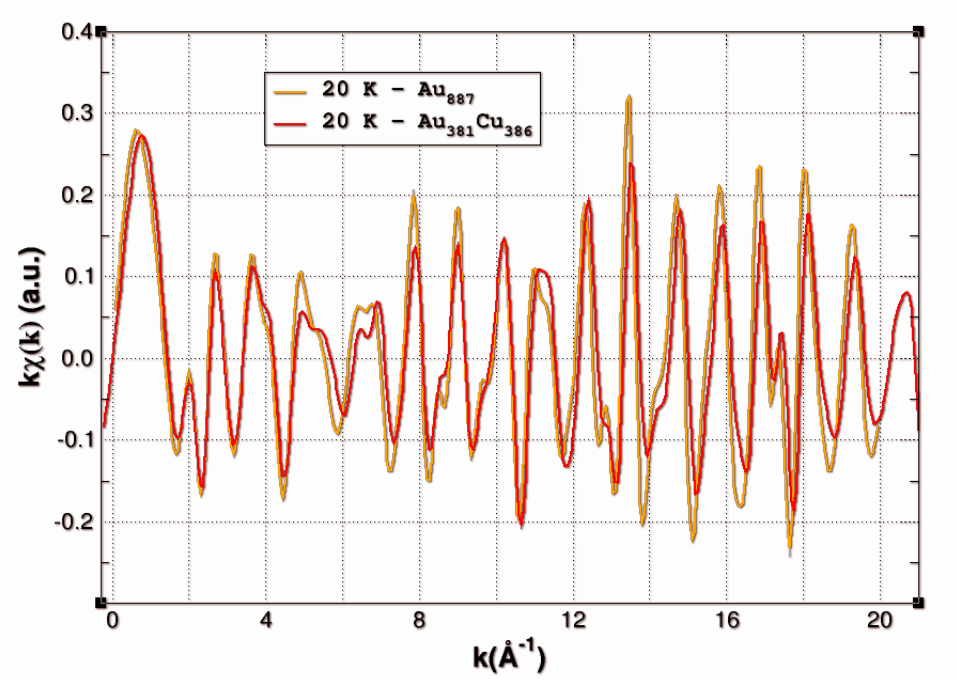

Figure 7.26: Calculated EXAFS spectra of $Au_{381}Cu_{386}$ (red) and the similar Au_{887} (orange) at 20 K.

On the other hand, comparing the EXAFS simulations of the $Au_{381}Cu_{386}$ nanoalloy at 20K with the data collected for the Au_{887} nanoparticle, which has a similar diameter, the spectra have the same shape and intensity, but are slightly shifted. By looking also at the Fourier transformed data, a shift of -0.04 Å for the peak at 2.7 Å of the Au/Cu nanoparticle can be observed, while the peak at 2.3 Å, with respect to the Fourier transform of the Au_{887} EXAFS data, is disappeared. This suggests that the outer shell of copper induces a surface tension greater than gold, which shortens the Au-Au bond distance, as the Cu atoms are entering inside the inner part of the particle. The peak at 2.3 probably results from the surface Au atoms, which are missing on the surface of the $Au_{381}Cu_{386}$ nanoparticle structure at 20 K.

A further improvement of the results reported in this section can be achieved by using longer and more detailed MD approaches in order to explore the properties and behaviour of these systems.

7.5 Conclusions

The last chapter shows the results from calculations performed on gold nanosurfaces in contact with thiolate molecules, using first principles methods. The constructed geometries have been constructed using small periodic images of gold nanosurfaces, in order to make the calculations feasible with the CASTEP code [3]. The structures were then optimised using the "damped MD" method and simulated for 0.1-0.2 ps using *ab initio* MD.

Within the time scales reported, the CH_3S-Au(III) nanosurfaces with one thiolate attached on them showed larger binding energies from the $(CH_3S)_2$-Au(III), with two thiolate molecules bound on their surface. Nanosurfaces where the methylthiolates were near each other, seemed to develop repulsive forces that drive them apart. A few discrepancies observed, in some of the calculations performed, require further investigation. Despite that, the *ab initio* MD simulations performed, indicate that complex metallic systems can be successfully studied within the accuracy of first principles methods.

Chapter 8

Conclusions

From classical molecular mechanics to *ab initio* density functional theory, this thesis summarises the results obtained from calculations on metallic or semiconductor nanoclusters. Due to the complexity of these systems, the current project aims to provide a quantitative approach towards the computational study of their structural and electronic properties. In contrast with simulations performed on biological molecules, where the basic elements contained in these systems, are well described and modelled, even with empirical computational methods, the parameters chosen to model the Si, Au and Pt atoms had to be thoroughly tested and validated before planning a methodology to simulate a chemically relevant system.

The first three chapters mainly contain some general information on the theory behind the methodologies employed in this project, starting from some basic principles of quantum mechanics, to classical molecular mechanics (chapter 2) and finally, to a brief description of density functional theory (chapter 3). The second chapter also contains a detailed description on the way an additional force field has been implemented in DL_POLY [18], in this case, the Stillinger-Weber potential [44]. A section, briefly describing the ONETEP code [4] (linear-scaling DFT), extended by

our research group, is also included.

In chapter 4, a computational study of silicon nanorods with varying aspect ratios and surface passivation by hydrogen is presented. Structures consisting of more than 1000 atoms were studied using both, the ONETEP [4] and the DFTB+ code [2]; the latter for geometry optimisation. The structural, energetic and electronic properties of the nanocrystals were investigated at the atomistic *ab initio* level of detail.

The calculations showed a surface distortion while the inner part of the nanorod retained a stable structure close to bulk Si. In the (1×1) unreconstructed nanorods, the Si-Si bond lengths were more condensed, while in the (2×1) reconstructed nanorods the range of the Si-Si bond length distribution was wider and larger, moving along the core region to the surface. Furthermore, the (1×1) surfaces adopted a "canted" conformation between neighbour H atoms, a property which is consistent with several theoretical studies reported in the past.

The (1×1) unreconstructed H-passivated nanorods presented higher stabilities compared to the (2×1) reconstructed nanostructures, which tend to decrease as the diameter of the nanorod is increased. According to the results of the calculations, when the diameter of the nanorod was extended by 5 Å, formation energies per Si atom decayed almost by 1 eV. Similarly, a reduction of $\sim$ 0.5 eV for the (1×1) nanorods and of $\sim$ 0.3 eV for the (2×1) nanorods in the HOMO-LUMO band gap was observed when their diameter was increased from 8 Å to 13 Å.

EXAFS simulations of gold nanoparticles were presented in chapter 5. The calculations showed a remarkable agreement with the experimentally determined EXAFS spectra, in support of the structural models obtained from classical MD simulations. The simulation of EXAFS spectra provides a route for assessing the quality of the MD simulations, both for studying structural properties and thermal dynamics. However, two main differences between the simulated and experimentally deter-

mined properties of gold nanoparticles were identified.

Firstly, the average bond lengths in the MD simulations performed, were larger than those fitted from analysis of the experimental EXAFS data. The difference, however, is smaller than 1 %. The effect of surface tension is responsible for the shortening of the bond lengths observed in Figure 5.8, and indeed the contribution of surface atoms clearly has a detectable effect on the simulated EXAFS spectra, as shown in Figure 5.7. From these findings, it can be said that, in our MD simulations, the underestimation of the surface tension arises either because the region affected by the surface tension was not as deep as observed experimentally [151], or because the Au-Au bond lengths at the surface were larger than expected (*e.g.* with respect to the models presented in Ref. [152]).

Secondly, though the thermal damping in the EXAFS simulations steadily increases with the temperature (Figure 5.11), it does not reproduce the signal damping of experimentally determined EXAFS spectra at 20 K and 300 K. The MD simulations at 20 K showed small vibrational motions, resulting in an underestimation of the thermal damping. This effect is likely due to the neglect of zero-point vibrational motion by the classical calculations, which allows the system to be more localised near the bottom of the potential energy wells. On the other hand, the vibrations at 300 K were large enough to produce a thermal disorder greater than the experiment. Perhaps, a deeper potential well could reduce the amplitude of vibrations at high temperature and also decrease the bond lengths at the surface, as the resulting forces acting on gold atoms will be stronger.

Better agreement between the computational modelling and the experimental data would have been possible if a more accurate potential energy surface of the gold nanoparticles was used. This work has been based on a force field generated PES due to the prohibitive computational cost that *ab initio* molecular dynamics would have for problems of this size and simulations of this timescale (Ref. [135],

see section 5.1). In our case, the approximation made by representing the atomic interactions with a classical force field still gives reliable results for the structural properties of gold nanoparticles, though the vibrational motion is not reproduced accurately.

A technique that provides a fine-tuning of a force field, by altering the curvature and depth of its potential well, could be a promising step forward for a better agreement between the simulated and experimental EXAFS spectra. Nevertheless, it is expected that significant improvements while using the force field could be achieved by re-parametrisation or an alternative functional form that is more suitable for nanoparticles, given that the Gupta potential [40] and other commonly used many body force fields for metallic systems have been developed with calculations for bulk systems in mind. Furthermore, there is a degree of uncertainly about the actual temperature of the nanoparticles in the experiment which can also be a source of discrepancy with the simulations, as well as the fact that, in the experiment the nanoparticles were supported on an amorphous silica surface, while in the simulations they were treated as isolated.

The discrepancy between classical MD simulations and experimental data is also observed when studying platinum nanoclusters, as shown in chapter 6. Although the MD simulations provide an improved input for EXAFS analysis, resulting in a better fitting model, they do not completely account for all the structural and thermal (dynamic) disorder present in the measurements while the modelled structures were assumed to have a spherical symmetry. Including an additional σ^2 parameter to account the structural disorder in nanoparticles using the MD input, the fitting models were significantly improved, than fits conducted with the standard model at all the desired temperatures. In comparison with TEM measurements [10], the approach used in this work by using data obtained from MD simulations, gives a better agreement about the structural properties of the nanoparticles, instead of us-

ing theoretical models based on the properties of bulk materials when analysing nanoparticles.

The EXAFS approach detailed in chapter 6, showed promising results, although still requires further development. Even though the current fitting scheme was done only in the first coordination shell of the simulated and the synthesised Pt nanoparticles, an extension of the analysis to higher coordination shells could provide a better insight to their structural properties. Work is currently in progress to extend this histogram approach both to higher shells and to three-body correlations, incorporating the contributions from multiple-scattering paths.

Furthermore, Pt nanoclusters of different size and shape are also reported in chapter 6. Classical MD simulations of bimetallic Pt nanoalloys with copper or palladium have been performed, aiming to be used as reference sample structures to interpret recently obtained experimental data. Within the same framework, classical MD simulations on gold nanoparticles with configurations consisted of 55, 177, 381 and 767 atoms, representing sizes of 1.39, 1.94, 2.50 and 3.05 nm respectively, have been also performed, as reported in chapter 7.

In chapter 7, gold nanosurfaces in interaction with thiolate molecules are being investigated, using first principles methods. The constructed geometries were simplified to make the calculations feasible with *ab initio* molecular dynamics in the CASTEP code [3], which allowed the optimisation and simulation of the latter systems.

Within the time scales where the CH_3S-Au(III) and $(CH_3S)_2$-Au(III) have been simulated, the nanosurfaces with one thiolate attached on them showed larger binding energies from the systems with two thiolate molecules. Nanosurfaces where the methylthiolates were near each other, seemed to develop repulsive forces that drive them apart. The discrepancies observed in some of the simulated structures

require further investigation. Despite that, the *ab initio* MD simulations performed within this project, indicate that complex metallic systems can be successfully studied within the accuracy of first principles methods, while the rapidly developing field of linear-scaling DFT in combination with improvements of computational resources, is a promising tool for modelling larger and more complicated systems. Future developments in the ONETEP code are extended to make possible the simulation of entire metal nanoparticles with thousands of atoms and chemical processes on their surfaces. The work done here with CASTEP should serve as a starting point for such studies.

Appendices

Sample files of the procedures used for some of the calculations described in this thesis are included in the following appendices. All the main input and output files of the calculations reported are provided in the attached DVDs.

Appendix A

DL_POLY input files

A.1 FIELD file

The FIELD file contains the force field information, which is defined at the end of the file and the atomic properties of an atom or a molecular group contained in the simulated system given at the beginning of the file. The order of specification of the atoms or molecular types in the FIELD file must follow the order in which they appear in the CONFIG file.

```
Silicon

UNITS
MOLECULES 1
Si
NUMMOL 29
ATOMS  1
Si           28.0855        0.00    1
finish
vdw 1
Si Si  tab
tbp 1
Si  Si  Si  stwb  116.666667  6.0000  9.00000  2.514120  2.514120  3.771180
CLOSE
```

A.2 CONTROL file

```
Si29

integration velocity verlet

temperature         20.00
pressure            0.0010
ensemble nve

#restart
#optim force       1.0E-5

steps             2000000
equilibration       50000
scale                  10
print                  10
stack                  10
stats                  10
rdf                    10
traj      1     4000    2

timestep          0.0010
cutoff            6.5000
delr width        0.5000
rvdw cutoff       6.5000
no electrostatics

print rdf

job time       100000000.00
close time            10.00

finish
```

The CONTROL file contains all the necessary parameters for setting up a simulation. The first section of the file, as shown in the figure aside, includes values for the physical variables affecting the simulated system, such as temperature, pressure and the ensemble used (section 2.1). The middle section includes mainly keywords that control the collection and type of data printed in the output files of DL_POLY while in the last section keywords that define the effect of several atomic interactions are given. The duration of the simulation and the time between each printed MD frame are defined with the keywords "steps" and "timestep", respectively.

A.3 CONFIG file

The CONFIG file contains all the information defining the geometry of very element of the simulated system in tabulated order. The file is divided in 3 columns, representing the x, y and z coordinates of the Cartesian system and 2 sections. The first section contains the x, y and z components of the vectors defining the size of the simulation box, while the second sections indexes all the positions of the atoms

contained in the system. As can be observed, the line above every x, y and z atomic coordinate, denotes the type, index number and atomic mass of that specific atom of the system.

In the figure below, a section from the CONFIG file of a simulated system containing 29 Si atoms is shown.

```
Si29
         0         1
  30.0000000000000000  0.0000000000000000  0.0000000000000000
  0.0000000000000000  30.0000000000000000  0.0000000000000000
  0.0000000000000000  0.0000000000000000  30.0000000000000000
Si               1        14
  -1.3465240000000000  -1.2884960000000000  -4.0817690000000000
Si               2        14
  -1.3465240000000000  -3.9639950000000000  -1.4062690000000000
Si               3        14
  -4.0220240000000000  -1.2884960000000000  -1.4062690000000000
Si               4        14
  -2.6842740000000000  -2.6262460000000000  -0.0685190000000000
Si               5        14
  -1.3465240000000000  -1.2884960000000000   1.2692310000000000
Si               6        14
  -2.6842740000000000   0.0492540000000000  -2.7440190000000000
Si               7        14
  -1.3465240000000000   1.3870040000000000  -1.4062690000000000
Si               8        14
  -4.0220240000000000   1.3870040000000000   1.2692310000000000
Si               9        14
  -2.6842740000000000   2.7247540000000000  -0.0685190000000000
Si              10        14
  -1.3465240000000000   4.0625040000000000   1.2692310000000000
Si              11        14
  -2.6842740000000000   0.0492540000000000   2.6069810000000000
Si              12        14
  -1.3465240000000000   1.3870040000000000   3.9447310000000000
Si              13        14
  -0.0087740000000000  -2.6262460000000000  -2.7440190000000000
Si              14        14
   1.3289760000000000  -1.2884960000000000  -1.4062690000000000
Si              15        14
```

A.4 TABLE file

The TABLE le provides an analytical form for a short range potential that does not exist within the default force fields provided with the DL_POLY code and can be

specified by the user. The option of reading the values from a tabulated potential is specied in the FIELD file (see above) with the "tab" keyword.

The TABLE file shown in the picture below, is a part from the TABLE file used for describing the two-body term of the Stillinger-Weber [45] potential (section 2.3.4). The energy and force values of the pair potential are given in 4 columns, which are read line by line from the code. The units of the energy and force values included in the TABLE file must be compatible with the units of the force field given in the FIELD file.

```
Silicon (Stillinger-Weber)
  7.5420000E-04  3.7711800E+00      5004
Si      Si
  3.0341137E+18  1.8961103E+17  3.7449865E+16  1.1848053E+16
  4.8524224E+15  2.3398351E+15  1.2628440E+15  7.4017349E+14
  4.6203516E+14  3.0310746E+14  2.0700338E+14  1.4614189E+14
  1.0609082E+14  7.8866132E+13  5.9839659E+13  4.6219545E+13
  3.6262800E+13  2.8848179E+13  2.3235146E+13  1.8923053E+13
  1.5566299E+13  1.2921804E+13  1.0815680E+13  9.1216099E+12
  7.7465388E+12  6.6210306E+12  5.6926589E+12  4.9214072E+12
  4.2764227E+12  3.7336944E+12  3.2743731E+12  2.8835412E+12
  2.5493028E+12  2.2621042E+12  2.0142213E+12  1.7993697E+12
  1.6124065E+12  1.4490990E+12  1.3059454E+12  1.1800338E+12
  1.0689317E+12  9.7059744E+11  8.8331050E+11  8.0561473E+11
  7.3627308E+11  6.7423067E+11  6.1858478E+11  5.6856029E+11
  5.2348947E+11  4.8279529E+11  4.4597764E+11  4.1260183E+11
  3.8228896E+11  3.5470792E+11  3.2956861E+11  3.0661623E+11
  2.8562647E+11  2.6640140E+11  2.4876600E+11  2.3256515E+11
  2.1766111E+11  2.0393133E+11  1.9126655E+11  1.7956918E+11
  1.6875193E+11  1.5873653E+11  1.4945272E+11  1.4083733E+11
  1.3283345E+11  1.2538975E+11  1.1845984E+11  1.1200176E+11
  1.0597751E+11  1.0035258E+11  9.5095644E+10  9.0178196E+10
  8.5574275E+10  8.1260204E+10  7.7214369E+10  7.3417011E+10
  6.9850046E+10  6.6496911E+10  6.3342413E+10  6.0372602E+10
  5.7574660E+10  5.4936793E+10  5.2448141E+10  5.0098694E+10
  4.7879215E+10  4.5781176E+10  4.3796694E+10  4.1918476E+10
  4.0139770E+10  3.8454317E+10  3.6856317E+10  3.5340381E+10
  3.3901507E+10  3.2535045E+10  3.1236666E+10  3.0002343E+10
  2.8828323E+10  2.7711106E+10  2.6647428E+10  2.5634242E+10
  2.4668699E+10  2.3748138E+10  2.2870070E+10  2.2032162E+10
  2.1232233E+10  2.0468236E+10  1.9738253E+10  1.9040485E+10
  1.8373240E+10  1.7734932E+10  1.7124069E+10  1.6539247E+10
  1.5979146E+10  1.5442525E+10  1.4928212E+10  1.4435104E+10
  1.3962162E+10  1.3508405E+10  1.3072906E+10  1.2654793E+10
```

Appendix B

DL_POLY output files

B.1 STATIS file

```
Si29
 ENERGY UNITS=DL_POLY Internal Units
         1  1.000000E-03        37
 -8.361706E+05  0.000000E+00 -8.361706E+05 -8.362477E+05  0.000000E+00
  0.000000E+00  7.702204E+01  0.000000E+00  0.000000E+00 -8.063793E+05
  0.000000E+00 -8.937406E+04 -8.980792E+04  0.000000E+00  0.000000E+00
  4.338618E+02  0.000000E+00  0.000000E+00  2.700000E+04  0.000000E+00
  0.000000E+00  0.000000E+00  9.000000E+01  9.000000E+01  9.000000E+01
  0.000000E+00  1.808253E-01  0.000000E+00  1.825811E-01 -3.102446E-14
  1.754125E-06 -3.102446E-14  1.825811E-01 -1.754125E-06  1.754125E-06
 -1.754125E-06  1.825806E-01
         2  2.000000E-03        37
 -8.345864E+05  0.000000E+00 -8.345864E+05 -8.348861E+05  0.000000E+00
  0.000000E+00  2.996920E+02  0.000000E+00  0.000000E+00 -8.827360E+05
  0.000000E+00  1.444487E+05  1.427214E+05  0.000000E+00  0.000000E+00
  1.727299E+03  0.000000E+00  0.000000E+00  2.700000E+04  0.000000E+00
  0.000000E+00  0.000000E+00  9.000000E+01  9.000000E+01  9.000000E+01
  0.000000E+00 -2.922547E-01  0.000000E+00 -2.852650E-01 -1.146662E-13
  4.215205E-06 -1.146662E-13 -2.852650E-01 -4.215205E-06  4.215205E-06
 -4.215205E-06 -2.852657E-01
         3  3.000000E-03        37
 -8.361715E+05  0.000000E+00 -8.361715E+05 -8.362521E+05  0.000000E+00
  0.000000E+00  8.057706E+01  0.000000E+00  0.000000E+00 -8.082201E+05
  0.000000E+00 -8.385421E+04 -8.430833E+04  0.000000E+00  0.000000E+00
  4.541235E+02  0.000000E+00  0.000000E+00  2.700000E+04  0.000000E+00
  0.000000E+00  0.000000E+00  9.000000E+01  9.000000E+01  9.000000E+01
  0.000000E+00  1.696573E-01  0.000000E+00  1.714951E-01 -3.295277E-14
  1.815224E-06 -3.295277E-14  1.714951E-01 -1.815224E-06  1.815224E-06
 -1.815224E-06  1.714946E-01
         4  4.000000E-03        37
 -8.366923E+05  0.000000E+00 -8.366923E+05 -8.367631E+05  0.000000E+00
  0.000000E+00  7.079468E+01  0.000000E+00  0.000000E+00 -8.285748E+05
  0.000000E+00 -2.435263E+04 -2.476630E+04  0.000000E+00  0.000000E+00
  4.136664E+02  0.000000E+00  0.000000E+00  2.700000E+04  0.000000E+00
```

The STATIS file contains analytical information about the total energy, energy components and forces acting on the system at every timestep, as defined by the force field.

B.2 HISTORY file

The HISTORY file provides all the atomic positions, velocities and forces acting on every atom contained in the system, at time intervals during the simulation, which are defined by the user in the CONTROL file. In other words, it gives the "trajectory" of the simulated system and when imported to a visualisation program, such as VMD, one can observe the behaviour of atoms, motions and vibrations, during the simulation.

```
Si29
         2         1        29
timestep          1        29         2         1    0.001000
   30.00       0.000       0.000
   0.000       30.00       0.000
   0.000       0.000       30.00
Si                1   28.085500    0.000000
 -1.3465E+00 -1.2885E+00 -4.1648E+00
  0.0000E+00  0.0000E+00  0.0000E+00
 -8.7888E+01 -8.7860E+01  9.2710E+01
Si                2   28.085500    0.000000
 -1.3465E+00 -4.0470E+00 -1.4063E+00
  0.0000E+00  0.0000E+00  0.0000E+00
 -8.7877E+01  9.2778E+01 -8.7877E+01
Si                3   28.085500    0.000000
 -4.1051E+00 -1.2885E+00 -1.4063E+00
  0.0000E+00  0.0000E+00  0.0000E+00
  9.2710E+01 -8.7860E+01 -8.7888E+01
Si                4   28.085500    0.000000
 -2.7258E+00 -2.6678E+00 -2.6993E-02
  0.0000E+00  0.0000E+00  0.0000E+00
 -1.1003E+03 -1.1004E+03 -1.7109E+03
Si                5   28.085500    0.000000
 -1.3465E+00 -1.2885E+00  1.2692E+00
  0.0000E+00  0.0000E+00  0.0000E+00
 -1.3178E+03 -1.3178E+03  1.3178E+03
Si                6   28.085500    0.000000
 -2.7258E+00  9.0779E-02 -2.7855E+00
  0.0000E+00  0.0000E+00  0.0000E+00
 -1.1003E+03 -1.7109E+03 -1.1003E+03
Si                7   28.085500    0.000000
 -1.3465E+00  1.3870E+00 -1.4063E+00
  0.0000E+00  0.0000E+00  0.0000E+00
 -1.3178E+03  1.3178E+03 -1.3178E+03
```

B.3 OUTPUT file

```
                  DL_POLY Version 2.18

                           Running on    1 nodes

 ********************************************************************************************************************************
 ********************************************************************************************************************************
 ********************************************************************************************************************************
 ***************     Silane                                                                                     ***************
 ********************************************************************************************************************************
 ********************************************************************************************************************************
 ********************************************************************************************************************************


 SIMULATION CONTROL PARAMETERS


 velocity verlet integration selected

 structure optimisation requested
 convergence to minimum force selected
 tolerance for structure optimisation      1.0000E-05

 selected number of timesteps        10000

 temperature scaling on
 temperature scaling interval            5

 data printing interval                  1

 data stacking interval                 10

 statistics file interval                1

 trajectory file option on
 trajectory file start                   1
 trajectory file interval                1
 trajectory file info key                2

 simulation timestep              1.0000E-03

 real space cut off               5.4300E+00

 real space cut off (vdw)         3.7710E+00

 border width of Verlet shell     1.0000E-01


 electrostatic potential terms off

 user allocated job time (s)      1.0000E+04

 job closure time        (s)      1.0000E+01


SYSTEM SPECIFICATION

 energy units=dl_poly internal units


 number of molecular types               1

 molecular species type                  1


 name of species:             Si

 number of molecules                    29

 number of atoms/sites                   1


 atomic characteristics:

                      site     name          mass        charge    repeat    freeze

                         1     Si          28.08550     0.00000         1         0
```

```
 number of specified pair potentials         1

               atom 1  atom 2      key                              parameters

               Si      Si        tab

 potential tables read from TABLE file

 number of specified three body potentials         1

               atom 1  atom 2  atom 3      key                              parameters

               Si      Si      Si          stwb   1.16667E+02  6.00000E+00  9.00000E+00  2.51412E+00  2.51412E+00
 configuration file name:
         Si29

 selected image convention               1

 simulation cell vectors

                       30.000000    0.000000    0.000000
                        0.000000   30.000000    0.000000
                        0.000000    0.000000   30.000000

 system volume            27000.0000000

 link cell algorithm in use

 total degrees of freedom                        84.
 rotational degrees of freedom                    0.
 shell pseudo degrees of freedom                  0.

 sample of starting configuration
      i       x(i)        y(i)        z(i)       vx(i)       vy(i)       vz(i)

      1 -1.3465E+00 -1.2885E+00 -4.0818E+00  0.0000E+00  0.0000E+00  0.0000E+00
      3 -4.0220E+00 -1.2885E+00 -1.4063E+00  0.0000E+00  0.0000E+00  0.0000E+00
      5 -1.3465E+00 -1.2885E+00  1.2692E+00  0.0000E+00  0.0000E+00  0.0000E+00
      7 -1.3465E+00  1.3870E+00 -1.4063E+00  0.0000E+00  0.0000E+00  0.0000E+00
      9 -2.6843E+00  2.7248E+00 -6.8519E-02  0.0000E+00  0.0000E+00  0.0000E+00
     11 -2.6843E+00  4.9254E-02  2.6070E+00  0.0000E+00  0.0000E+00  0.0000E+00
     13 -8.7740E-03 -2.6262E+00 -2.7440E+00  0.0000E+00  0.0000E+00  0.0000E+00
     15  1.3290E+00 -3.9640E+00  1.2692E+00  0.0000E+00  0.0000E+00  0.0000E+00
     17  4.0045E+00 -1.2885E+00  1.2692E+00  0.0000E+00  0.0000E+00  0.0000E+00
     19  1.3290E+00 -1.2885E+00  3.9447E+00  0.0000E+00  0.0000E+00  0.0000E+00
     21  2.6667E+00  4.9254E-02 -2.7440E+00  0.0000E+00  0.0000E+00  0.0000E+00
     23 -8.7740E-03  2.7248E+00 -2.7440E+00  0.0000E+00  0.0000E+00  0.0000E+00
     25 -8.7740E-03  4.9254E-02 -6.8519E-02  0.0000E+00  0.0000E+00  0.0000E+00
     27  2.6667E+00  2.7248E+00 -6.8519E-02  0.0000E+00  0.0000E+00  0.0000E+00
     29 -8.7740E-03  2.7248E+00  2.6070E+00  0.0000E+00  0.0000E+00  0.0000E+00

long range correction for: vdw energy     0.000000E+00
                         : vdw pressure   0.000000E+00

 time elapsed since job start =           0.011 seconds

 ------------------------------------------------------------------------------------------------------------------------
```

```
    step     eng_tot    temp_tot     eng_cfg     eng_vdw     eng_cou     eng_bnd     eng_ang     eng_dih     eng_tet
time(ps)      eng_pv    temp_rot     vir_cfg     vir_vdw     vir_cou     vir_bnd     vir_ang     vir_con     vir_tet
cpu  (s)      volume    temp_shl     eng_shl     vir_shl       alpha        beta       gamma     vir_pmf       press

-------------------------------------------------------------------------------------------------------------------
       1 -8.3617E+05  0.0000E+00 -8.3617E+05 -8.3625E+05  0.0000E+00  0.0000E+00  7.7022E+01  0.0000E+00  0.0000E+00
   0.001 -8.0638E+05  0.0000E+00 -8.9374E+04 -8.9808E+04  0.0000E+00  0.0000E+00  4.3386E+02  0.0000E+00  0.0000E+00
    0.01  2.7000E+04  0.0000E+00  0.0000E+00  0.0000E+00  9.0000E+01  9.0000E+01  9.0000E+01  0.0000E+00  1.8083E-01

 rolling -8.3617E+05  0.0000E+00 -8.3617E+05 -8.3625E+05  0.0000E+00  0.0000E+00  7.7022E+01  0.0000E+00  0.0000E+00
averages -8.0638E+05  0.0000E+00 -8.9374E+04 -8.9808E+04  0.0000E+00  0.0000E+00  4.3386E+02  0.0000E+00  0.0000E+00
          2.7000E+04  0.0000E+00  0.0000E+00  0.0000E+00  9.0000E+01  9.0000E+01  9.0000E+01  0.0000E+00  1.8083E-01
-------------------------------------------------------------------------------------------------------------------
       2 -8.3459E+05  0.0000E+00 -8.3459E+05 -8.3489E+05  0.0000E+00  0.0000E+00  2.9969E+02  0.0000E+00  0.0000E+00
   0.002 -8.8274E+05  0.0000E+00  1.4445E+05  1.4272E+05  0.0000E+00  0.0000E+00  1.7273E+03  0.0000E+00  0.0000E+00
    0.02  2.7000E+04  0.0000E+00  0.0000E+00  0.0000E+00  9.0000E+01  9.0000E+01  9.0000E+01  0.0000E+00 -2.9225E-01

 rolling -8.3538E+05  0.0000E+00 -8.3538E+05 -8.3557E+05  0.0000E+00  0.0000E+00  1.8836E+02  0.0000E+00  0.0000E+00
averages -8.4456E+05  0.0000E+00  2.7537E+04  2.6457E+04  0.0000E+00  0.0000E+00  1.0806E+03  0.0000E+00  0.0000E+00
          2.7000E+04  0.0000E+00  0.0000E+00  0.0000E+00  9.0000E+01  9.0000E+01  9.0000E+01  0.0000E+00 -5.5715E-02
-------------------------------------------------------------------------------------------------------------------
       3 -8.3617E+05  0.0000E+00 -8.3617E+05 -8.3625E+05  0.0000E+00  0.0000E+00  8.0577E+01  0.0000E+00  0.0000E+00
   0.003 -8.0822E+05  0.0000E+00 -8.3854E+04 -8.4308E+04  0.0000E+00  0.0000E+00  4.5412E+02  0.0000E+00  0.0000E+00
    0.02  2.7000E+04  0.0000E+00  0.0000E+00  0.0000E+00  9.0000E+01  9.0000E+01  9.0000E+01  0.0000E+00  1.6966E-01

 rolling -8.3564E+05  0.0000E+00 -8.3564E+05 -8.3580E+05  0.0000E+00  0.0000E+00  1.5243E+02  0.0000E+00  0.0000E+00
averages -8.3245E+05  0.0000E+00 -9.5932E+03 -1.0465E+04  0.0000E+00  0.0000E+00  8.7176E+02  0.0000E+00  0.0000E+00
          2.7000E+04  0.0000E+00  0.0000E+00  0.0000E+00  9.0000E+01  9.0000E+01  9.0000E+01  0.0000E+00  1.9409E-02
-------------------------------------------------------------------------------------------------------------------
       4 -8.3669E+05  0.0000E+00 -8.3669E+05 -8.3676E+05  0.0000E+00  0.0000E+00  7.0795E+01  0.0000E+00  0.0000E+00
   0.004 -8.2857E+05  0.0000E+00 -2.4353E+04 -2.4766E+04  0.0000E+00  0.0000E+00  4.1367E+02  0.0000E+00  0.0000E+00
    0.02  2.7000E+04  0.0000E+00  0.0000E+00  0.0000E+00  9.0000E+01  9.0000E+01  9.0000E+01  0.0000E+00  4.9271E-02

 rolling -8.3591E+05  0.0000E+00 -8.3591E+05 -8.3604E+05  0.0000E+00  0.0000E+00  1.3202E+02  0.0000E+00  0.0000E+00
averages -8.3148E+05  0.0000E+00 -1.3283E+04 -1.4040E+04  0.0000E+00  0.0000E+00  7.5724E+02  0.0000E+00  0.0000E+00
          2.7000E+04  0.0000E+00  0.0000E+00  0.0000E+00  9.0000E+01  9.0000E+01  9.0000E+01  0.0000E+00  2.6875E-02
-------------------------------------------------------------------------------------------------------------------
       5 -8.3650E+05  0.0000E+00 -8.3650E+05 -8.3665E+05  0.0000E+00  0.0000E+00  1.5519E+02  0.0000E+00  0.0000E+00
   0.005 -8.4810E+05  0.0000E+00  3.4809E+04  3.3896E+04  0.0000E+00  0.0000E+00  9.1271E+02  0.0000E+00  0.0000E+00
    0.02  2.7000E+04  0.0000E+00  0.0000E+00  0.0000E+00  9.0000E+01  9.0000E+01  9.0000E+01  0.0000E+00 -7.0427E-02

 rolling -8.3602E+05  0.0000E+00 -8.3602E+05 -8.3616E+05  0.0000E+00  0.0000E+00  1.3665E+02  0.0000E+00  0.0000E+00
averages -8.3480E+05  0.0000E+00 -3.6646E+03 -4.4529E+03  0.0000E+00  0.0000E+00  7.8833E+02  0.0000E+00  0.0000E+00
          2.7000E+04  0.0000E+00  0.0000E+00  0.0000E+00  9.0000E+01  9.0000E+01  9.0000E+01  0.0000E+00  7.4144E-03
-------------------------------------------------------------------------------------------------------------------
       6 -8.3671E+05  0.0000E+00 -8.3671E+05 -8.3679E+05  0.0000E+00  0.0000E+00  8.2007E+01  0.0000E+00  0.0000E+00
   0.006 -8.3307E+05  0.0000E+00 -1.0933E+04 -1.1414E+04  0.0000E+00  0.0000E+00  4.8056E+02  0.0000E+00  0.0000E+00
    0.03  2.7000E+04  0.0000E+00  0.0000E+00  0.0000E+00  9.0000E+01  9.0000E+01  9.0000E+01  0.0000E+00  2.2121E-02

 rolling -8.3614E+05  0.0000E+00 -8.3614E+05 -8.3627E+05  0.0000E+00  0.0000E+00  1.2755E+02  0.0000E+00  0.0000E+00
averages -8.3451E+05  0.0000E+00 -4.8761E+03 -5.6131E+03  0.0000E+00  0.0000E+00  7.3704E+02  0.0000E+00  0.0000E+00
          2.7000E+04  0.0000E+00  0.0000E+00  0.0000E+00  9.0000E+01  9.0000E+01  9.0000E+01  0.0000E+00  9.8655E-03
-------------------------------------------------------------------------------------------------------------------
       7 -8.3673E+05  0.0000E+00 -8.3673E+05 -8.3676E+05  0.0000E+00  0.0000E+00  3.2899E+01  0.0000E+00  0.0000E+00
   0.007 -8.3518E+05  0.0000E+00 -4.6504E+03 -4.8433E+03  0.0000E+00  0.0000E+00  1.9286E+02  0.0000E+00  0.0000E+00
    0.03  2.7000E+04  0.0000E+00  0.0000E+00  0.0000E+00  9.0000E+01  9.0000E+01  9.0000E+01  0.0000E+00  9.4089E-03

 rolling -8.3622E+05  0.0000E+00 -8.3622E+05 -8.3634E+05  0.0000E+00  0.0000E+00  1.1403E+02  0.0000E+00  0.0000E+00
averages -8.3461E+05  0.0000E+00 -4.8438E+03 -5.5031E+03  0.0000E+00  0.0000E+00  6.5930E+02  0.0000E+00  0.0000E+00
          2.7000E+04  0.0000E+00  0.0000E+00  0.0000E+00  9.0000E+01  9.0000E+01  9.0000E+01  0.0000E+00  9.8002E-03
-------------------------------------------------------------------------------------------------------------------
       8 -8.3674E+05  0.0000E+00 -8.3674E+05 -8.3679E+05  0.0000E+00  0.0000E+00  4.7553E+01  0.0000E+00  0.0000E+00
   0.008 -8.3434E+05  0.0000E+00 -7.2131E+03 -7.4917E+03  0.0000E+00  0.0000E+00  2.7863E+02  0.0000E+00  0.0000E+00
    0.03  2.7000E+04  0.0000E+00  0.0000E+00  0.0000E+00  9.0000E+01  9.0000E+01  9.0000E+01  0.0000E+00  1.4594E-02

 rolling -8.3629E+05  0.0000E+00 -8.3629E+05 -8.3639E+05  0.0000E+00  0.0000E+00  1.0572E+02  0.0000E+00  0.0000E+00
averages -8.3457E+05  0.0000E+00 -5.1400E+03 -5.7517E+03  0.0000E+00  0.0000E+00  6.1171E+02  0.0000E+00  0.0000E+00
          2.7000E+04  0.0000E+00  0.0000E+00  0.0000E+00  9.0000E+01  9.0000E+01  9.0000E+01  0.0000E+00  1.0399E-02
-------------------------------------------------------------------------------------------------------------------
-------------------------------------------------------------------------------------------------------------------

    step     eng_tot    temp_tot     eng_cfg     eng_vdw     eng_cou     eng_bnd     eng_ang     eng_dih     eng_tet
time(ps)      eng_pv    temp_rot     vir_cfg     vir_vdw     vir_cou     vir_bnd     vir_ang     vir_con     vir_tet
cpu  (s)      volume    temp_shl     eng_shl     vir_shl       alpha        beta       gamma     vir_pmf       press

-------------------------------------------------------------------------------------------------------------------
       9 -8.3676E+05  0.0000E+00 -8.3676E+05 -8.3679E+05  0.0000E+00  0.0000E+00  3.1563E+01  0.0000E+00  0.0000E+00
   0.009 -8.3474E+05  0.0000E+00 -6.0664E+03 -6.2514E+03  0.0000E+00  0.0000E+00  1.8499E+02  0.0000E+00  0.0000E+00
```

All the information derived from a classical MD simulation, is summarised in the OUTPUT file. At the beginning the OUTPUT file gives an analytical description of the keywords included in the CONTROL file followed by the FIELD file and also by a small random selection of atomic coordinates given in the CONFIG file. When the simulation starts, the data derived from every energy and force component of the force field, at every timestep, are collected and printed in the following sections of the OUTPUT file.

B.4 REVCON file

```
Si29
         2         1        29    0.1000000000E-02
     30.000000000000      0.000000000000      0.000000000000
      0.000000000000     30.000000000000      0.000000000000
      0.000000000000      0.000000000000     30.000000000000
Si              1
    -1.366502462        -1.308475366        -4.141725368
   0.00000000000       0.00000000000       0.00000000000
 -0.224669506711      0.622518080443E-01 -0.157627673295
Si              2
    -1.366502691        -4.023952787        -1.426248103
   0.00000000000       0.00000000000       0.00000000000
 -0.167142368090     -0.273914489820E-01 -0.270964710589E-01
Si              3
    -4.081980579        -1.308475157        -1.426247666
   0.00000000000       0.00000000000       0.00000000000
 -0.110963554474      0.567910468697E-03 -0.146319890770
Si              4
    -2.724245047        -2.666215900       -0.6851415192E-01
   0.00000000000       0.00000000000       0.00000000000
 -0.212602638299     -0.479161086526     -0.347317808886
Si              5
    -1.366509064        -1.308482030         1.289215584
   0.00000000000       0.00000000000       0.00000000000
 -0.353417509238E-01  0.264567602987      0.156446379020
Si              6
    -2.724244659        0.4925897881E-01    -2.783989563
   0.00000000000       0.00000000000       0.00000000000
 -0.314726651533     -0.360031711122     -0.334843592424
Si              7
    -1.366510336         1.406990336        -1.426254857
   0.00000000000       0.00000000000       0.00000000000
  0.326832750091     -0.326832749411      0.205821572101
Si              8
```

The final geometry of the system is printed in the REVCON file, which has the same format with the CONFIG file. In addition with every spatial x, y, and z coordinate of every atom, the x, y and z components of the atoms velocities and forces are given, in the sample shown above. The REVCON file replaces the CONFIG file, when a restart of the MD simulation is required.

Appendix C

Post-processing scripts for DL_POLY

C.1 CONFIG to XYZ

```
#!/usr/bin/perl

open(FILEIN,"<$ARGV[0]") || die "Cannot open input file $ARGV[0]";
open(OUT,">$ARGV[0]".".xyz");

$line=<FILEIN>;
$i=0;
print OUT $line;
print OUT "\n";
while($line=<FILEIN>){
        chomp $line;
        @data = split /[\s\t]+/, $line;
        shift @data if $data[0] eq "";
        if ($data[0] =~ /\D/ && $data[0] !~ /\W/ ){
                my $atom=$data[0];
                $line=<FILEIN>;
                chomp $line;
                @data = split /[\s\t]+/, $line;$i++;
                shift @data if $data[0] eq "";
                printf OUT "%-4s %16.9f%16.9f%16.9f\n",$atom,$data[0],$data[1],$data[2];
        }

}
printf OUT "\n";
printf OUT "Total number of atoms";
printf OUT "%4d\n",$i;

close(FILEIN);
close(OUT);
```

C.2 XYZ to CONFIG

```
#!/usr/bin/perl

# array that contains all the atoms in the periodic table
@periodic=("H","He","Li","Be","B","C","N","O","F","Ne","Na","Mg","Al","Si",
"P","S","Cl","Ar","K","Ca","Sc","Ti","V","Cr","Mn","Fe","Co","Ni","Cu",
"Zn","Ga","Ge","As","Se","Br","Kr","Rb","Sr","Y","Zr","Nb","Mo","Tc","Ru",
"Rh","Pd","Ag","Cd","In","Sn","Sb","Te","I","Xe","Cs","Ba","La","Ce","Pr",
"Nd","Pm","Sm","Eu","Gd","Tb","Dy","Ho","Er","Tm","Yb","Lu","Hf","Ta","W",
"Re","Os","Ir","Pt","Au","Hg","Tl","Pb","83","Po","At","Rn","Fr","Ra","Ac",
"Th","Pa","U","Np","Pu","Am","Cm","Bk","Cf","Es","Fm","Md","No","Lr","Rf",
"Db","Sg","Bh","Hs","Mt");

$name=$ARGV[0];

open(XYZ,"$name");
$i=0;
$check="on";
@atom_type="";
while($line=<XYZ>){
if ($check eq "on"){
$header=$line;
$check="off";
}
@data=field($line);
if ($data[0] =~ /\w/ && $data[1] =~ /\d/ && $data[2] =~ /\d/ && $data[3] =~ /\d/ ){
        $atom[$i][0]=$data[0]; # atom type
        $atom[$i][1]=$data[1]; # X
        $atom[$i][2]=$data[2]; # Y
        $atom[$i][3]=$data[3]; # Z

        # check if $data[$atom_label] is present in @atom_type
        $check=0;
        foreach my $tmp(@atom_type){
                $check++ if $tmp ne $data[0];
        }
        push(@atom_type,$data[0]) if $check > $#atom_type;

        $i++;
}}
# remove the empty value at the beginning of @atom_type.
shift(@atom_type);

# compare the atoms in the system with the periodic table, and write the atomic number
for my $j(0 .. $#periodic){
my $atom2=$periodic[$j];
my $atom3=length($atom2);
for my $k(0 .. $#atom_type){
my $length=length($atom_type[$k]);
$atom_number[$k]=$j+1 if ($atom_type[$k] =~ /^$atom2/i && $length == $atom3);
}}

open(CFG,">${name}.cfg");
$header2="Converted from XYZ\n";
print CFG "$header\n";
```

```
#writing atom types and coordinates into DL_POLY CONFIG
#for($i=1;$i<=$#atomType;$i++){
for my $i(0 .. $#atom){
my $atom2=$atom[$i][0];
for my $j(0 .. $#atom_type){
$Z=$atom_number[$j] if $atom_type[$j] =~ /^$atom2/i;
}
printf CFG "%-8s%10d%10d\n",$atom2,$i+1,$Z;
printf CFG "%20.15f%20.15f%20.15f\n",$atom[$i][1],$atom[$i][2],$atom[$i][3];
}
close(CFG);
close(XYZ);

sub field{
        chomp $_[0];
        my @out = split /[\s\t]+/, $_[0];
        if ($out[0] eq ""){ shift @out};
        return @out
}
```

The above scripts, written in "perl", have been constructed to convert the atomic positions of a simulated system, from the format of the CONFIG file to a typical XYZ file and vice versa. A sampled geometry for the Si_{29} system, in XYZ format in shown below:

```
29

 Si       -1.346500       -1.288500       -4.164800
 Si       -1.346500       -4.047000       -1.406300
 Si       -4.105100       -1.288500       -1.406300
 Si       -2.725800       -2.667800       -0.026993
 Si       -1.346500       -1.288500        1.269200
 Si       -2.725800        0.090779       -2.785500
 Si       -1.346500        1.387000       -1.406300
 Si       -4.105100        1.387000        1.269200
 Si       -2.725800        2.766300       -0.110040
 Si       -1.346500        4.145600        1.269200
 Si       -2.725800        0.007729        2.648500
 Si       -1.346500        1.387000        4.027800
 Si        0.032752       -2.667800       -2.785500
 Si        1.329000       -1.288500       -1.406300
 Si        1.329000       -4.047000        1.269200
 Si        2.708300       -2.667800       -0.110050
 Si        4.087500       -1.288500        1.269200
 Si       -0.050300       -2.667800        2.648500
 Si        1.329000       -1.288500        4.027800
 Si        1.329000        1.387000       -4.164800
 Si        2.708300        0.007728       -2.785500
 Si        4.087500        1.387000       -1.406300
 Si       -0.050299        2.766300       -2.785500
 Si        1.329000        4.145600       -1.406300
 Si       -0.008774        0.049254       -0.068519
 Si        1.329000        1.387000        1.269200
 Si        2.708300        2.766300       -0.026993
 Si        2.708300        0.090780        2.648500
 Si        0.032751        2.766300        2.648500
```

Appendix D

DL_POLY inputs for Au_{13}

D.1 FIELD

```
Gold13
units  ev
molecular types 1
Gold
nummols 13
atoms 1
Au     196.9670       0.0         1
finish
metal 1
Au      Au      gupt   0.4122    2.884     10.229     1.790      4.036
close
```

D.2 CONTROL

```
Au55 with Gupta Potentials

integration velocity verlet

temperature         20.00
pressure            0.0010
ensemble nve

#restart
#zero
#optim force       1.0E-5

steps             2000000
equilibration       50000
scale                  10
print                 100
stack                  10
stats                 100
rdf                    10
traj    1     4000    2

timestep         0.0010

cutoff           6.5000
delr width       0.5000
rvdw cutoff      6.5000
no electrostatics

print rdf

job time       100000000.00
close time            10.00

finish
```

D.3 CONFIG

```
Gold (13 atom cluster)
         2         1        13  -410286.918245
     40.000000000000      0.000000000000      0.000000000000
      0.000000000000     40.000000000000      0.000000000000
      0.000000000000      0.000000000000     40.000000000000
Au               1
    0.1926494748E-01   -0.1642203981E-01   -0.8959976098E-03
  0.281001545082E-01  0.263117160829     -0.271110737667
  -2131.03569527       2492.57261509      -1357.21730189
Au               2
     2.259921999         1.417252624       -0.6337563116E-01
  0.162117718797     -0.587374003811     -0.252394878187E-01
  -267.203079293      -806.675898522       206.942777592
Au               3
    -2.262568391         1.403066555       -0.4512651586E-01
 -0.348366591126     -0.104338060148     -0.472326832320E-01
   1155.78305899      -815.024533102       178.087909825
Au               4
     2.238000912        -1.475459360        0.5620615700E-01
  0.393623796407      0.213870059164E-01 -0.206023497361
   176.096124692       1093.01882725      -498.909281936
Au               5
    -2.254434998        -1.378805284        0.8622297296E-01
  0.176532864037      0.406232066018E-01 -0.153540837723E-01
  -929.321832944       21.1239790699      -1246.95204793
Au               6
     1.389381055         0.6874771515E-01    2.217973462
  0.210393687155      0.850606478478E-01 -0.482414609499E-01
   2153.46890328      -399.804916976       2993.49605182
Au               7
    -1.394355435         0.4419577866E-01    2.284595278
  0.221563263478      0.126825230212      0.219530024142E-01
  -223.515140349       359.663748696      -622.220842911
Au               8
   -0.3098460735E-01     2.270075655         1.359153138
 -0.533976605568      0.535343735041      0.372113155026
   119.182120074       1135.10086543      -195.759028275
Au               9
   -0.4199417751E-01    -2.232770344         1.443853007
 -0.110082136141     -0.155227775255      0.108046860305
   605.953119931      -1396.72380924       826.057519054
Au              10
     1.408130523        -0.6800014253E-01   -2.257736006
 -0.908880071628E-01  0.100422698012      0.434806648860
   892.995040362       591.325959796      -388.291172558
Au              11
    -1.362480966        -0.1708261189E-01   -2.269171337
  0.166917793705     -0.275079573855E-01 -0.162525593036
  -672.106745499       27.2289906946       180.830708103
Au              12
    0.1819522063E-01     2.249832689        -1.426826671
  0.828108820717E-01  0.642263394257E-01  0.238125243217E-01
  -244.693159804      -639.633736714       71.2608782504
Au              13
    0.1392391775E-01    -2.264631233        -1.384871857
 -0.358746820161     -0.362558227286     -0.185004647090
  -635.602714174      -1662.17209147      -147.326169141
```

Appendix E

Construction of nanoparticles with Materials Studio

Accelrys Materials Studio (MS) [123] is a multifunctional platform which allows the modelling, simulation and analysis of chemical compounds, using a large variety of available options. More importantly, it employs some of the most popular computational software for conducting calculations which can be linked to an external server or a computer cluster. The procedure for constructing nanocrystals and nanostructures using MS, is very simple and straight-forward, as described in the following sections.

E.1 Construction of Si nanorods

The unit cells of every element of the periodic table in its bulk crystalline form are already included in MS. For constructing a Si nanorod, the unit cell of bulk silicon has to be imported by selecting *File* > *Import* > *Select crystal structure*. Otherwise, the symmetry of a crystal structure can be defined by the user from the *Build* > *Crystals* menu.

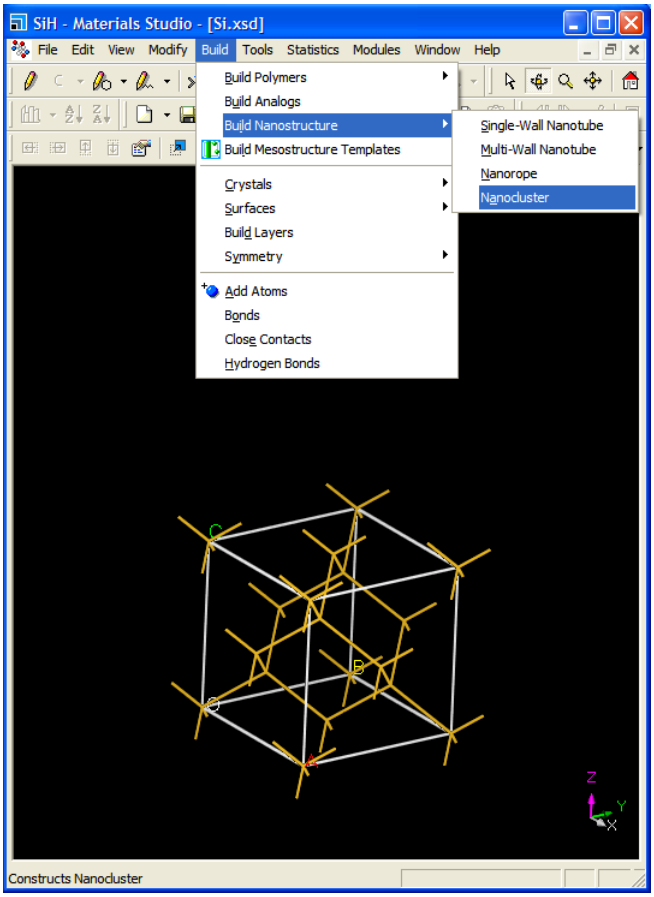

From the *Build* menu select *Build Nanostructure* > *Nanocluster*.

In the *Shape* menu of the *Shape* tab, select *Cylinder* and then insert the values of the cylinder basis radius and its height in Å. At the *Base plane* box, give define the crystal's growth direction by using "Miller indices". By pressing the *Build* button the Si nanorod is now constructed.

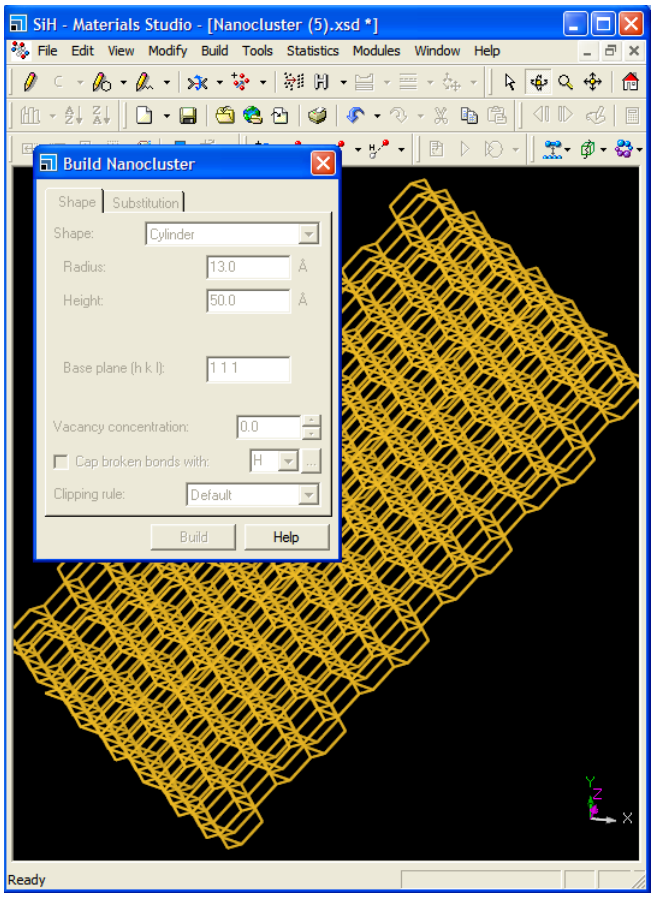

The surface atoms of the constructed Si nanorod which contain free dangling bonds, can be capped with H atoms directly by using the *Auto-update hydrogen* option from the tools bar, right below the menu bar.

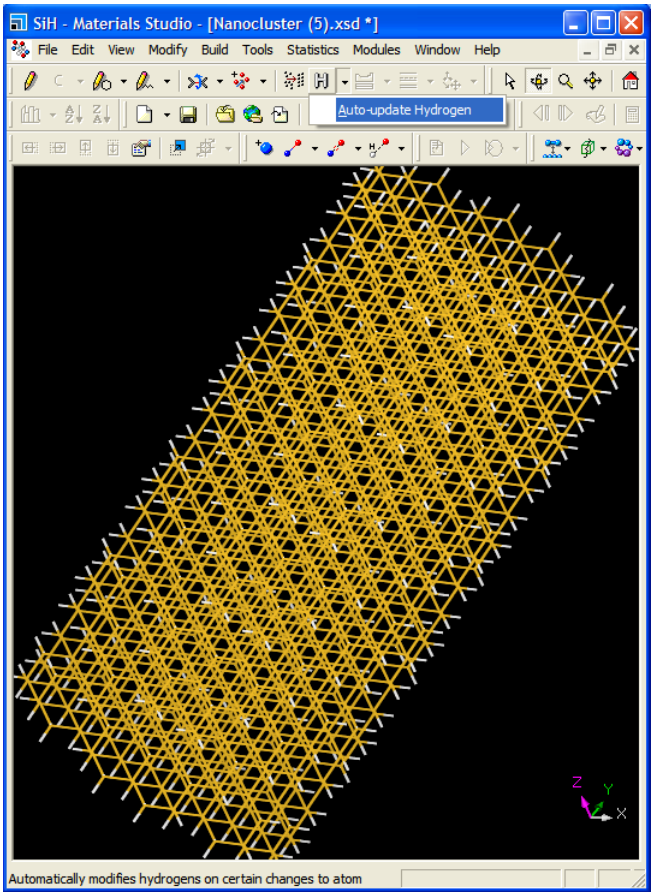

In order to resemble the shape of Si nanorods observed in experimental images, the caps of the nanorod were manually smoothed by selectively removing some surface atoms at the edges.

E.2 Construction of Au/Pt nanoparticles

In a similar manner as described in the previous for constructing Si nanorods, the unit cell of the bulk gold/platinum crystal is imported (*File* > *Import* > *Select crystal structure*). The unit cell of a bulk crystal can also be imported from a geometry optimisation calculation performed on a unit cell structure of the simulated system.

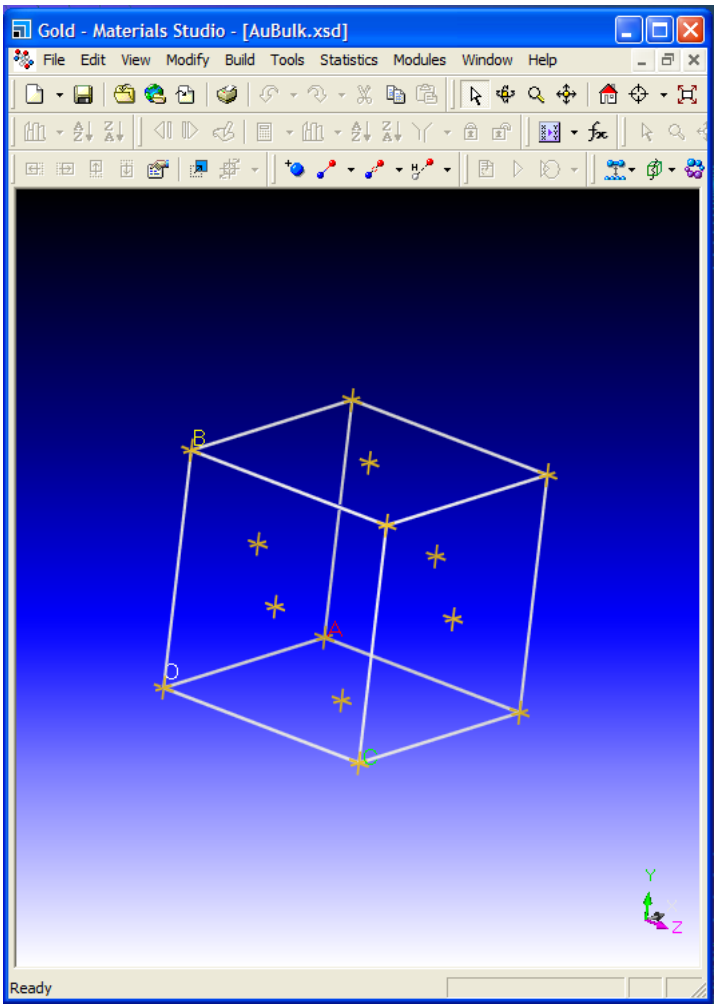

From the *Build* menu select *Build Nanostructure* > *Nanocluster*.

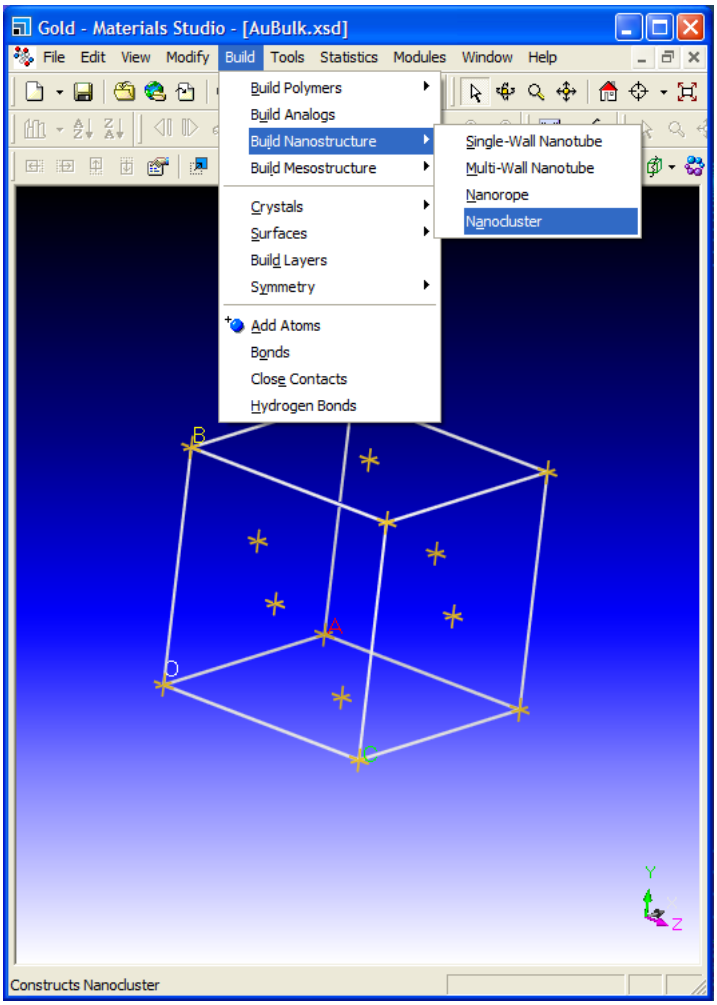

In the *Shape* menu of the *Shape* tab, select *Sphere* and then give the radius in Å.

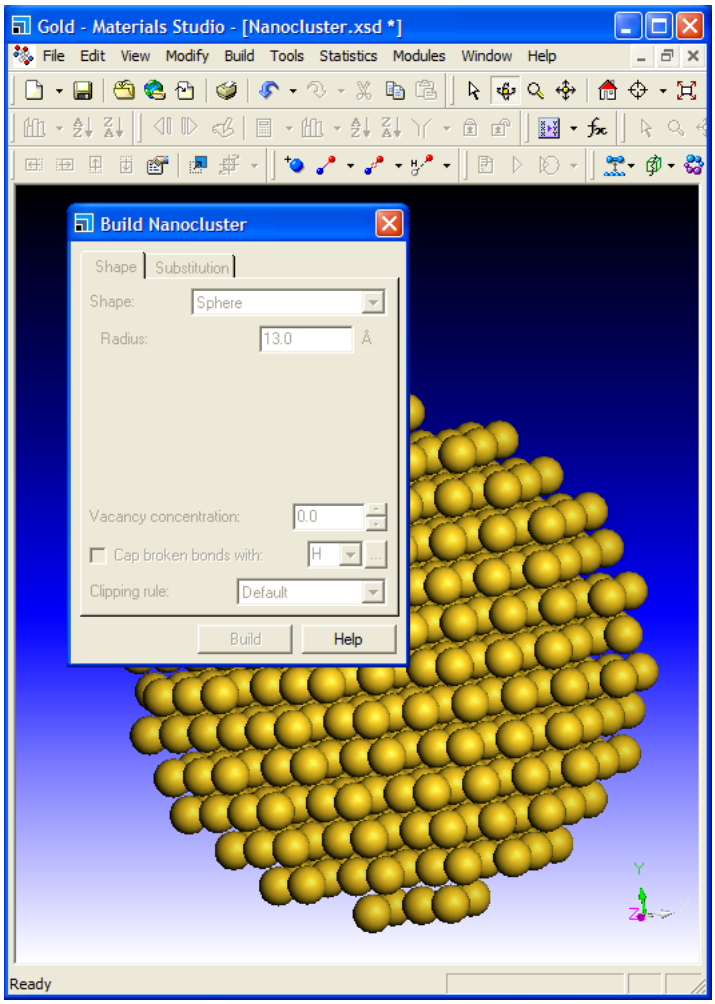

Appendix F

CASTEP input files

Samples of the CASTEP input files for a gold nanosurface in contact with one CH_3S-molecule are displayed below. The .cell file contains all the coordinates and variables defining the geometry of the simulated system, while the .param file contains all the parameters regarding the calculation.

F.1 .param file

```
task=molecular dynamics
iprint=2
XC_FUNCTIONAL = PBE
CUT_OFF_ENERGY = 650 eV
GRID_SCALE = 2.0
metals_method = EDFT
OPT_STRATEGY = speed
md_ensemble    = NVE
md_delta_t     = 1.0 fs
md_num_iter    = 200
md_temperature = 300 K
```

F.2 .cell file

```
%BLOCK LATTICE_ABC
11.614000  11.614000   19.424000
90.000000  90.000000   60.000000
%ENDBLOCK LATTICE_ABC

%BLOCK POSITIONS_ABS
Au        2.826000000     3.429400000     0.205700000
Au        1.403700000     0.899400000     0.190900000
Au        5.775300000     3.371000000     0.217700000
Au        4.316300000     0.886900000     0.193800000
Au        8.634400000     3.419000000     0.214600000
Au        7.197400000     0.902300000     0.201200000
Au       11.592400000     3.366500000     0.212100000
Au       10.118300000     0.890400000     0.195200000
Au        5.738000000     8.411100000     0.245000000
Au        4.437500000     5.827400000     0.162100000
Au        8.694400000     8.591400000     0.011200000
Au        7.479400000     6.220900000     0.407600000
Au       11.559400000     8.410600000     0.231100000
Au       10.203000000     5.820400000     0.210600000
Au       14.497400000     8.575400000     0.031200000
Au       13.313200000     6.193900000     0.407900000
Au        5.794300000     1.669800000     2.588800000
Au        7.239300000     4.196300000     2.582400000
Au        2.894200000     1.669300000     2.585500000
Au        4.347300000     4.185000000     2.582800000
Au       11.606600000     1.690500000     2.562900000
Au       13.047600000     4.182000000     2.595400000
Au        8.704600000     1.668900000     2.582400000
Au       10.152000000     4.193200000     2.576900000
Au        8.700600000     6.595100000     2.690400000
Au       10.147100000     9.229200000     2.574600000
Au        5.741700000     6.760400000     2.579900000
Au        7.306000000     9.181000000     2.560900000
Au       14.481800000     6.576500000     2.734600000
Au       15.953900000     9.247200000     2.556900000
Au       11.581000000     6.746900000     2.561100000
Au       13.087000000     9.193000000     2.575000000
Au        2.920500000     0.016800000     4.891200000
Au        4.361600000     2.510200000     4.914400000
Au        5.750500000     0.044800000     4.945700000
Au        1.450100000     2.493900000     4.879900000
Au        2.867000000     3.453100000     7.434200000
Au        1.419800000     0.819200000     7.138500000
Au        5.911900000     3.399300000     7.118700000
Au        4.400900000     0.739800000     7.476600000
Au        8.707400000     0.034200000     4.859200000
Au       10.160900000     2.518800000     4.858700000
Au        0.006300000     0.007800000     4.831900000
Au        7.265800000     2.468900000     4.847600000
Au        8.757500000     3.356100000     7.285500000
Au        7.292500000     0.856900000     7.205500000
Au       11.610700000     3.334600000     7.196000000
Au       10.158300000     0.812100000     7.235900000
Au        5.788600000     5.080200000     4.843400000
Au        7.242000000     7.536900000     4.891700000
Au        8.686400000     4.955000000     4.952700000
Au        4.329600000     7.573800000     4.880200000
Au        5.791400000     8.377400000     7.254800000
Au        4.392600000     5.894400000     7.225300000
Au        8.709400000     8.382500000     7.224100000
Au        7.275500000     5.919900000     7.271900000
```

```
Au       11.621300000     5.059900000     4.853200000
Au       13.026600000     7.559800000     4.897600000
Au        2.904600000     4.900700000     5.010900000
Au       10.152400000     7.545400000     4.869300000
Au       11.602100000     8.349500000     7.230100000
Au       10.169300000     5.845900000     7.220100000
Au       14.521200000     8.406300000     7.231600000
Au       13.047400000     5.913300000     7.231200000
H         2.108900000     0.881500000    10.048200000
H         2.019200000     2.516600000    10.741500000
H         3.213300000     1.353200000    11.362600000
C         2.685900000     1.698600000    10.475000000
S         3.928700000     2.318300000     9.307100000
%ENDBLOCK POSITIONS_ABS

%block ionic_constraints
1 Au 1  1 1 1
2 Au 2  1 1 1
3 Au 3  1 1 1
4 Au 4  1 1 1
5 Au 5  1 1 1
6 Au 6  1 1 1
7 Au 7  1 1 1
8 Au 8  1 1 1
9 Au 9  1 1 1
10 Au 10  1 1 1
11 Au 11  1 1 1
12 Au 12  1 1 1
13 Au 13  1 1 1
14 Au 14  1 1 1
15 Au 15  1 1 1
16 Au 16  1 1 1
17 Au 17  1 1 1
18 Au 18  1 1 1
19 Au 19  1 1 1
20 Au 20  1 1 1
21 Au 21  1 1 1
22 Au 22  1 1 1
23 Au 23  1 1 1
24 Au 24  1 1 1
25 Au 25  1 1 1
26 Au 26  1 1 1
27 Au 27  1 1 1
28 Au 28  1 1 1
29 Au 29  1 1 1
30 Au 30  1 1 1
31 Au 31  1 1 1
32 Au 32  1 1 1
%endblock ionic_constraints

KPOINTS_MP_SPACING 0.04 1/ang

fix_all_ions : false
fix_com : false
FIX_ALL_CELL : TRUE

%block species_pot
  Au   Au_00.recpot
  C    C_01.recpot
  H    H_04.recpot
  S    S_00.recpot
%endblock species_pot
```

Directory structure with input and output files of calculations from this thesis are provided in the accompanying DVDs

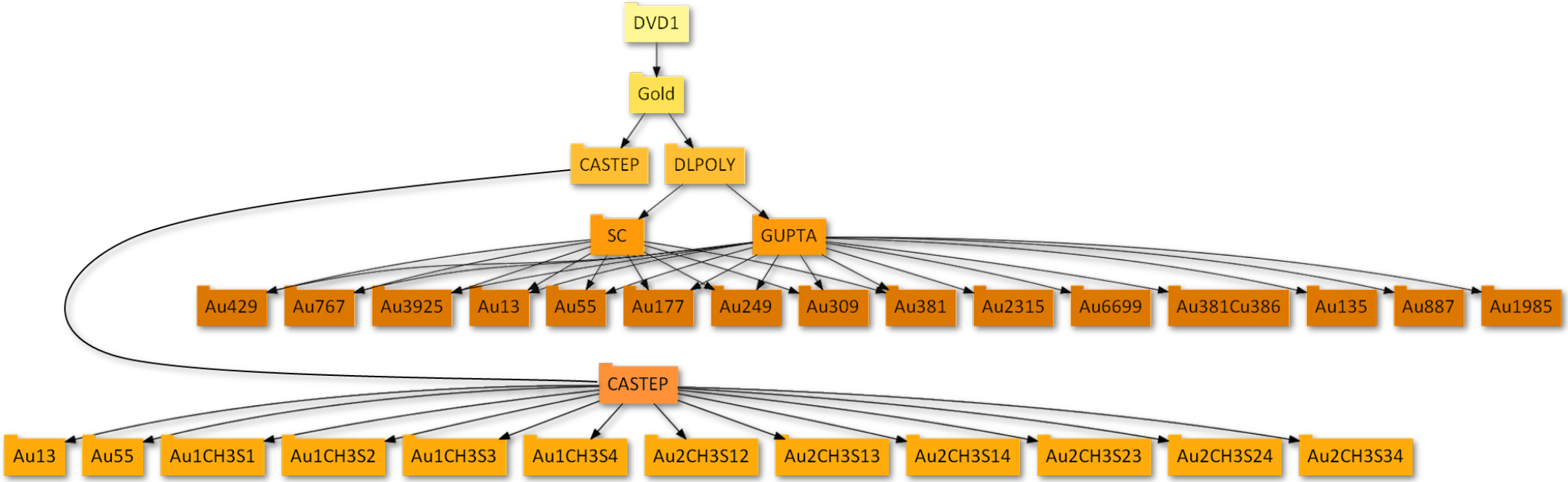

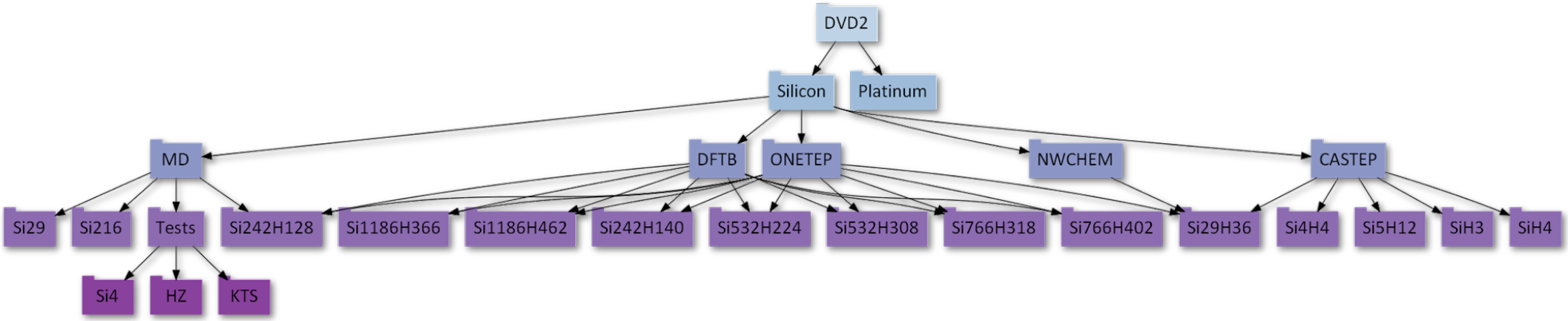
DVD2
Silicon
Platinum
MD
DFTB
ONETEP
NWCHEM
CASTEP
Si29
Si216
Tests
Si242H128
Si1186H366
Si1186H462
Si242H140
Si532H224
Si532H308
Si766H318
Si766H402
Si29H36
Si4H4
Si5H12
SiH3
SiH4
Si4
HZ
KTS

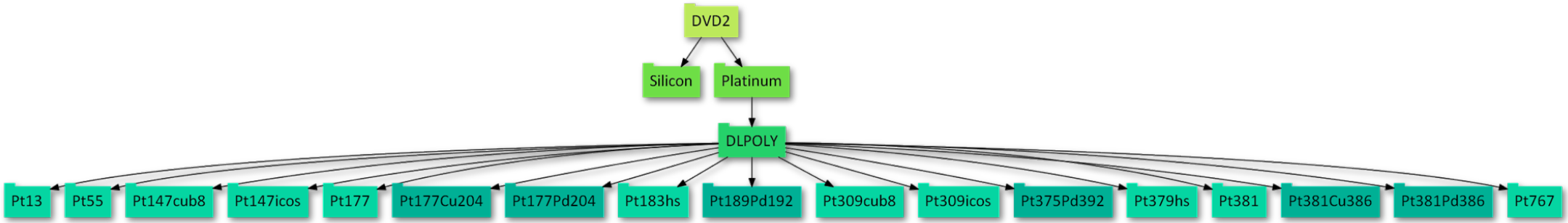
DVD2
Silicon
Platinum
DLPOLY
Pt13
Pt55
Pt147cub8
Pt147icos
Pt177
Pt177Cu204
Pt177Pd204
Pt183hs
Pt189Pd192
Pt309cub8
Pt309icos
Pt375Pd392
Pt379hs
Pt381
Pt381Cu386
Pt381Pd386
Pt767

Bibliography

[1] W. Smith and T. R. Forester. DL_POLY_2.0: A general-purpose parallel molecular dynamics simulation package. *J. Molec. Graphics*, 14(3):136–141, 1996.

[2] B. Aradi, B. Hourahine, and Th. Frauenheim. DFTB+, a sparse Matrix-Based implementation of the DFTB method. *The Journal of Physical Chemistry A*, 111(26):5678–5684, 2007.

[3] M. D. Segall, M. J. Probert, C. J. Pickard, P. J. Hasnip, S. J. Clark, M. C. Payne, and K. Refson. First principles methods using CASTEP. *Zeitschrift für Kristallographie*, 220:567–570, 2005.

[4] C.-K. Skylaris, P. D. Haynes, A. A. Mostofi, and M. C. Payne. Introducing ONETEP: Linear-scaling density functional simulations on parallel computers. *The Journal of Chemical Physics*, 122(8):084119, 2005.

[5] A. L. Ankudinov, B. Ravel, J. J. Rehr, and S. D. Conradson. Real-space multiple-scattering calculation and interpretation of x-ray-absorption near-edge structure. *Phys. Rev. B*, 58(12):7565–7576, 1998.

[6] http://www.chm.bris.ac.uk/pt/harvey/msci_pract/back_qm.html.

[7] T. Hjorteland. http://trond.hjorteland.com/thesis/node26.html.

[8] P. Hofmann. http://www.philiphofmann.net/surflec3/surflec014.html.

[9] A. R. Barron and C. Smith. http://cnx.org/content/m16927/latest/.

[10] http://en.wikipedia.org/wiki/Transmission_electron_microscopy.

[11] G. Belomoin, J. Therrien, A. Smith, S. Rao, R. Twesten, S. Chaieb, M. H. Nayfeh, L. Wagner, and L. Mitas. Observation of a magic discrete family of ultrabright Si nanoparticles. *Applied Physics Letters*, 80(5):841–843, 2002.

[12] Y. Wu, Yi Cui, C. M. Lieber, L. Huynh, C. J. Barrelet, and D. C. Bell. Controlled growth and structures of molecular-scale silicon nanowires. *Nano Letters*, 4:433, 2004.

[13] A. K. Singh, V. Kumar, R. Note, and Y. Kawazoe. Effects of morphology and doping on the electronic and structural properties of hydrogenated silicon nanowires. *Nano Letters*, 6(5):920–925, 2006.

[14] T. Vo, A. J. Williamson, and G. Galli. First principles simulations of the structural and electronic properties of silicon nanowires. *Physical Review B*, 74(4):045116, 2006.

[15] J. P. Perdew, K. Burke, and M. Ernzerhof. Generalized gradient approximation made simple. *Phys. Rev. Lett.*, 77(18):3865–3868, 1996.

[16] Stephen W. Price. *Enhanced Structural Characterisation of Supported Catalysts*. PhD thesis, Chemistry, University of Southampton, 2011.

[17] W. Smith and T. R. Forester. DL_POLY_2.0: A general-purpose parallel molecular dynamics simulation package. *J. Molec. Graphics*, 14(3):136–141, 1996.

[18] W. Smith, T. R. Forester, and I. T. Todorov. *The DL_POLY_2 User Manual*, 2.20 edition, 2009.

[19] E. J. Bylaska, W. A. de Jong, N. Govind, K. Kowalski, T. P. Straatsma, M. Valiev, D. Wang, E. Apra, T. L. Windus, J. Hammond, P. Nichols, S. Hirata,

M. T. Hackler, Y. Zhao, P.-D. Fan, R. J. Harrison, M. Dupuis, D. M. A. Smith, J. Nieplocha, V. Tipparaju, M. Krishnan, Q. Wu, T. Van Voorhis, A. A. Auer, M. Nooijen, E. Brown, G. Cisneros, G. I. Fann, H. Fruchtl, J. Garza, K. Hirao, R. Kendall, J. A. Nichols, K. Tsemekhman, K. Wolinski, J. Anchell, D. Bernholdt, P. Borowski, T. Clark, D. Clerc, H. Dachsel, M. Deegan, K. Dyall, D. Elwood, E. Glendening, M. Gutowski, A. Hess, J. Jaffe, B. Johnson, J. Ju, R. Kobayashi, R. Kutteh, Z. Lin, R. Littlefield, X. Long, B. Meng, T. Nakajima, S. Niu, L. Pollack, M. Rosing, G. Sandrone, M. Stave, H. Taylor, G. Thomas, J. van Lenthe, A. Wong, and Z. Zhang. *NWChem, A Computational Chemistry Package for Parallel Computers*. Pacific Northwest National Laboratory, 2007.

[20] T. Comaschi, A. Balerna, and S. Mobilio. Temperature dependence of the structural parameters of gold nanoparticles investigated with EXAFS. *Phys. Rev. B*, 77(7):075432, 2008.

[21] N. Zonias, P.G. Lagoudakis, and C.-K. Skylaris. Large-scale first principles and tight-binding density functional theory calculations on hydrogen-passivated silicon nanorods. *Journal of Physics: Condensed Matter*, 22(2):025303, 2010.

[22] O. M. Roscioni, N. Zonias, S. W. T. Price, A. E. Russell, T. Comaschi, and C.-K. Skylaris. Computational prediction of l_3 exafs spectra of gold nanoparticles from classical molecular dynamics simulations. *Physical Review B*, 83(11):115409, 2011.

[23] Ira N. Levine. *Quantum Chemistry*. Prentice-Hall, 5 edition, 2000.

[24] E. Schrödinger. An undulatory theory of the mechanics of atoms and molecules. *Phys. Rev.*, 28(6):1049–1070, 1926.

[25] K. B. Wiberg. A scheme for strain energy minimization. application to the cycloalkanes1. *Journal of the American Chemical Society*, 87(5):1070–1078, 1965.

[26] F. Jensen. *Introduction to Computational Chemistry*. John Willey & Sons, 1999.

[27] C. G. Broyden. A class of methods for solving nonlinear simultaneous equations. *Math. Comp.*, 19:577–593, 1965.

[28] R. Fletcher. A new approach to variable metric algorithms. *The Computer Journal*, 13(3):317–322, 1970.

[29] D. Goldfarb. A family of variable-metric methods derived by variational means. *Math. Comp.*, 24:23–26, 1970.

[30] D. F. Shanno. Conditioning of quasi-Newton methods for function minimization. *Math. Comp.*, 24:647–656, 1970.

[31] L. P. Bouckaert, R. Smoluchowski, and E. Wigner. Theory of brillouin zones and symmetry properties of wave functions in crystals. *Phys. Rev.*, 50(1):58–67, 1936.

[32] H. J. Monkhorst and J. D. Pack. Special points for brillouin-zone integrations. *Phys. Rev. B*, 13(12):5188–5192, 1976.

[33] F. H. Westheimer and Joseph E. Mayer. The theory of the racemization of optically active derivatives of diphenyl. *The Journal of Chemical Physics*, 14(12):733–738, 1946.

[34] T. L. Hill. On steric effects. *The Journal of Chemical Physics*, 14(7):465–465, 1946.

[35] H. J. C. Berendsen, J. P. M. Postma, W. F. van Gunsteren, A. DiNola, and J. R. Haak. Molecular dynamics with coupling to an external bath. *Journal of Chemical Physics*, 81(8):3684–3690, 1984.

[36] W. G. Hoover. Canonical dynamics: Equilibrium phase-space distributions. *Phys. Rev. A*, 31(3):1695–1697, 1985.

[37] S. Melchionna, G. Ciccotti, and B. L. Holian. Hoover NPT dynamics for systems varying in shape and size. *Molecular Physics*, 78(3):533–544, 1993.

[38] L. Verlet. Computer "experiments" on classical fluids. I. Thermodynamical properties of Lennard-Jones molecules. *Phys. Rev.*, 159(1):98, 1967.

[39] P. P. Ewald. Die berechnung optischer und elektrostatischer gitterpotentiale. *Ann. Phys. (Leipzig)*, 64:253–87, 1921.

[40] R. P. Gupta. Lattice relaxation at a metal surface. *Phys. Rev. B*, 23(12):6265–6270, 1981.

[41] A. P. Sutton and J. Chen. Long-range Finnis–Sinclair potentials. *Philos. Mag. Lett*, 61:139–164, 1990.

[42] H. Rafii-Tabar and A. P. Sutton. Long-range Finnis-Sinclair potentials for f.c.c. metallic alloys. *Phil. Mag. Lett.*, 63(4):217–224, 1991.

[43] F. Cleri and V. Rosato. Tight-binding potentials for transition metals and alloys. *Phys. Rev. B*, 48(1):22–33, 1993.

[44] Stillinger F. H. and T. A. Weber. Computer simulation of local order in condesed phases of silicon. *Phys. Rev. B*, 31(8):5262–5271, April 1985.

[45] F. H. Stillinger and T. A. Weber. Fluorination of the dimerized Si(100) surface studied by molecular-dynamics simulation. *Phys. Rev. Lett.*, 62(18):2144–2147, 1989.

[46] T. A. Weber and F. H. Stillinger. Dynamical branching during fluorination of the dimerized Si(100) surface: A molecular dynamics study. *The Journal of Chemical Physics*, 92(10):6239–6245, 1990.

[47] Zi Jian, Z. Kaiming, and Xie Xide. Modification of Stillinger-Weber potentials for Si and Ge. *Phys. Rev. B*, 41(18):12915–12918, 1990.

[48] Kohen D., Tully J. C., and Stillinger F. H. Modeling the interaction of hydrogen with silicon surfaces. *Surface Science*, 397:225–236, 1998.

[49] T. Hawa and M. R. Zachariah. Molecular dynamics study of particle-particle collisions between hydrogen-passivated silicon nanoparticles. *Phys. Rev. B*, 69(3):035417, 2004.

[50] *Mathematica Documentation Center (http://reference.wolfram.com/)*.

[51] P. Atkins and J. de Paula. *Physical Chemistry*. Oxford University Press, 7th edition, 2002.

[52] Block F. Bemerkung zur elektronentheorie des ferromagnetismus und der elektrischen leitfähigkeit. *Z. Physik*, 57(545), 1929.

[53] P. A. M. Dirac. Note on the exchange phenomena in the Thomas atom. *Proc. Cambridge Philos. Soc*, 26:376, 1930.

[54] P. Hohenberg and W. Kohn. Inhomogeneous electron gas. *Phys. Rev.*, 136(3B):B864–B871, 1964.

[55] W. Kohn and L. J. Sham. Self-consistent equations including exchange and correlation effects. *Phys. Rev.*, 140(4A):A1133–A1138, 1965.

[56] D. M. Ceperley and B. J. Alder. Ground state of the electron gas by a stochastic method. *Phys. Rev. Lett.*, 45(7):566–569, 1980.

[57] J. P. Perdew and A. Zunger. Self-interaction correction to density-functional approximations for many-electron systems. *Phys. Rev. B*, 23(10):5048–5079, 1981.

[58] S. H. Vosko, L. Wilk, and M. Nusair. Accurate spin-dependent electron liquid correlation energies for local spin density calculations: a critical analysis. *Can. J. Phys.*, 58(1200), 1980.

[59] A. D. Becke. Density-functional exchange-energy approximation with correct asymptotic behavior. *Phys. Rev. A*, 38(6):3098–3100, Sep 1988.

[60] J. P. Perdew. Density-functional approximation for the correlation energy of the inhomogeneous electron gas. *Phys. Rev. B*, 33(12):8822–8824, Jun 1986.

[61] J. P. Perdew, J. A. Chevary, S. H. Vosko, K. A. Jackson, M. R. Pederson, D. J. Singh, and C. Fiolhais. Atoms, molecules, solids, and surfaces: Applications of the generalized gradient approximation for exchange and correlation. *Phys. Rev. B*, 46(11):6671–6687, 1992.

[62] C. Lee, W. Yang, and R. G. Parr. Development of the colle-salvetti correlation-energy formula into a functional of the electron density. *Phys. Rev. B*, 37(2):785–789, 1988.

[63] A. D. Becke. Density-functional thermochemistry. III. The role of exact exchange. *The Journal of Chemical Physics*, 98(7):5648–5652, 1993.

[64] P. J. Stephens, F. J. Devlin, C. F. Chabalowski, and M. J. Frisch. Ab initio calculation of vibrational absorption and circular dichroism spectra using density functional force fields. *The Journal of Physical Chemistry*, 98(45):11623–11627, 1994.

[65] R. M. Dickson and Axel D. Becke. Basis-set-free local density-functional calculations of geometries of polyatomic molecules. *The Journal of Chemical Physics*, 99(5):3898–3905, 1993.

[66] Basis set exchange database.

[67] M. Finnis. *Interatomic Forces in Condensed Matter*. Oxford Series on Materials Modelling. Oxford University Press, Oxford, 2003.

[68] C. Herring. A new method for calculating wave functions in crystals. *Phys. Rev.*, 57(12):1169–1177, 1940.

[69] J. C. Phillips and L. Kleinman. New method for calculating wave functions in crystals and molecules. *Phys. Rev.*, 116(2):287–294, 1959.

[70] S. Goedecker. Linear scaling electronic structure methods. *Rev. Mod. Phys.*, 71(4):1085–1123, 1999.

[71] C.-K. Skylaris, M. C. Payne, A. A. Mostofi, and P. D. Haynes. ONETEP: linear-scaling density-functional theory with plane waves,. *Psi-k Newsletter*, 72:78–91, December 2005.

[72] C.-K. Skylaris, A. A. Mostofi, P. D. Haynes, O. Diéguez, and M. C. Payne. Nonorthogonal generalized Wannier function pseudopotential plane-wave method. *Phys. Rev. B*, 66(3):035119, 2002.

[73] A. A. Mostofi, P. D. Haynes, C.-K. Skylaris, and M. C. Payne. Preconditioned iterative minimization for linear-scaling electronic structure calculations. *The Journal of Chemical Physics*, 119(17):8842–8848, 2003.

[74] P.D. Haynes, C.-K. Skylaris, A.A. Mostofi, and M.C. Payne. Elimination of basis set superposition error in linear-scaling density-functional calculations with local orbitals optimised in situ. *Chemical Physics Letters*, 422(4-6):345–349, 2006.

[75] C.-K. Skylaris, P. D. Haynes, A. A. Mostofi, and M. C. Payne. Implementation of linear-scaling plane wave density functional theory on parallel computers. *Physica Status Solidi (b)*, 243(5):973–988, 2006.

[76] C.-K. Skylaris, P. D. Haynes, A. A. Mostofi, and M. C. Payne. Recent progress in linear-scaling density functional calculations with plane waves and pseudopotentials: the ONETEP code. *Journal of Physics: Condensed Matter*, 20(6):064209 (9pp), 2008.

[77] M. Elstner, D. Porezag, G. Jungnickel, J. Elsner, M. Haugk, Th. Frauenheim, S. Suhai, and G. Seifert. Self-consistent-charge density-functional tight-binding method for simulations of complex materials properties. *Phys. Rev. B*, 58(11):7260–7268, 1998.

[78] M. Stupca, M. Alsalhi, T. Al Saud, A. Almuhanna, and M. H. Nayfeh. Enhancement of polycrystalline silicon solar cells using ultrathin films of silicon nanoparticle. *Applied Physics Letters*, 91(6):063107, 2007.

[79] Yi Cui, Qingqiao Wei, H. Park, and C. M. Lieber. Nanowire nanosensors for highly sensitive and selective detection of biological and chemical species. *Science*, 293(5533):1289–1292, 2001.

[80] Yi Cui and C. M. Lieber. Functional nanoscale electronic devices assembled using silicon nanowire building blocks. *Science*, 291(5505):851–853, 2001.

[81] M. H. Huang, S. Mao, H. Feick, H. Yan, Yiying Wu, H. Kind, E. Weber, R. Russo, and P. Yang. Room-temperature ultraviolet nanowire nanolasers. *Science*, 292(5523):1897–1899, 2001.

[82] Yu Huang, X. Duan, Yi Cui, L. J. Lauhon, Kyoung-Ha Kim, and C. M. Lieber. Logic gates and computation from assembled nanowire building blocks. *Science*, 294(5545):1313–1317, 2001.

[83] L. T. Canham. Silicon quantum wire array fabrication by electrochemical and chemical dissolution of wafers. *Applied Physics Letters*, 57(10):1046–1048, 1990.

[84] A. G. Cullis, L. T. Canham, and P. D. J. Calcott. The structural and luminescence properties of porous silicon. *Journal of Applied Physics*, 82(3):909–965, 1997.

[85] O. Akcakir, J. Therrien, G. Belomoin, N. Barry, J. D. Muller, E. Gratton, and M. Nayfeh. Detection of luminescent single ultrasmall silicon nanoparticles using fluctuation correlation spectroscopy. *Applied Physics Letters*, 76(14):1857–1859, 2000.

[86] S. H. Risbud, L-C. Liu, and J. F. Shackelford. Synthesis and luminescence of silicon remnants formed by truncated glassmelt-particle reaction. *Applied Physics Letters*, 63(12):1648–1650, 1993.

[87] M. Fujii, S. Hayashi, and K. Yamamoto. Growth of Ge microcrystals in SiO_2 thin film matrices: A Raman and electron microscopic study. *Jpn. J. Appl. Phys.*, 30:687–694, 1991.

[88] J. G. Zhu, C.W. White, J. D. Budai, S. P. Withrow, and Y. Chen. Growth of Ge, Si, and SiGe nanocrystals in SiO_2 matrices. *Journal of Applied Physics*, 78(7):4386–4389, 1995.

[89] A. Borghesi, A. Sassella, B. Pivac, and L. Pavesi. Characterization of porous silicon inhomogeneities by high spatial resolution infrared spectroscopy. *Solid State Communications*, 87(1):1–4, 1993.

[90] A. Fojtikor, H. Weller, S. Fiechter, and A. Henglein. Preparation of colloidal silicon and preliminary photochemical experiments. *Chemical Physics Letters*, 134:477, 1987.

[91] A. Fojtik and A. Henglein. Luminescent colloidal silicon particles. *Chemical Physics Letters*, 221:363, 1994.

[92] S. M. Prokes. Study of the luminescence mechanism in porous silicon structures. *Journal of Applied Physics*, 73(1):407–413, 1993.

[93] H. Takagi, H. Ogawa, Y. Yamazaki, A. Ishizaki, and T. Nakagiri. Quantum size effects on photoluminescence in ultrafine Si particles. *Applied Physics Letters*, 56(24):2379–2380, 1990.

[94] R. Okada and S. Iijima. Oxidation property of silicon small particles. *Applied Physics Letters*, 58(15):1662–1663, 1991.

[95] D. J. DiMaria, J. R. Kirtley, E. J. Pakulis, D. W. Dong, T. S. Kuan, F. L. Pesavento, T. N. Theis, J. A. Cutro, and S. D. Brorson. Electroluminescence studies in silicon dioxide films containing tiny silicon islands. *Journal of Applied Physics*, 56(2):401–416, 1984.

[96] S. Berger, L. Schächter, and S. Tamir. Photoluminescence as a surface-effect in nanostructures. *Nanostructured Materials*, 8(2):231, 1997.

[97] J. P. Wilcoxon, G. A. Samara, and P. N. Provencio. Optical and electronic properties of Si nanoclusters synthesized in inverse micelles. *Phys. Rev. B*, 60(4):2704–2714, 1999.

[98] J. D. Meindl, Qiang Chen, and J. A. Davis. Limits on silicon nanoelectronics for terascale integration. *Science*, 293(5537):2044, 2001.

[99] C. M. Lieber. Nanoscale science and technology: Building a big future from small things. *Mater. Res. Soc. Bull*, 28:486–491, 2003.

[100] C. M. Lieber. One-dimensional nanostructures: Chemistry, physics & applications. *Solid State Communications*, 107:607, 1998.

[101] C. R. Martin. Nanomaterials: A membrane-based synthetic approach. *Science*, 266:1961, 1994.

[102] R. S. Wagner and W. C. Ellis. Vapor-liquid-solid mechanism of single crystal growth. *Applied Physics Letters*, 4(5):89–90, 1964.

[103] N. Wang, Y. F. Zhang, Y. H. Tang, C. S. Lee, and S. T. Lee. SiO_2-enhanced synthesis of Si nanowires by laser ablation. *Applied Physics Letters*, 73(26):3902–3904, 1998.

[104] Y. H. Xie, W. L. Wilson, F. M. Ross, J. A. Mucha, E. A. Fitzgerald, J. M. Macaulay, and T. D. Harris. Luminescence and structural study of porous silicon films. *Journal of Applied Physics*, 71(5):2403–2407, 1992.

[105] R. C. Anderson, R. S. Muller, and C. W. Tobias. Chemical surface modification of porous silicon. *J. Electrochem. Soc.*, 140(5):1393–1396, 1993.

[106] M. Hirata, K. Nakamura, and K. Yokota. H-termination of nanocrystalline Si:O films by HF solution treatment. *e-Journal of Surface Science and Nanotechnology*, 3:527–530, 2005.

[107] X. Zhao, C. M. Wei, L. Yang, and M. Y. Chou. Quantum confinement and electronic properties of silicon nanowires. *Phys. Rev. Lett.*, 92(23):236805, 2004.

[108] F. Erogbogbo, Ken-Tye Yong, I. Roy, GaiXia Xu, P. N. Prasad, and M. T. Swihart. Biocompatible luminescent silicon quantum dots for imaging of cancer cells. *ACS Nano*, 2(5):873–878, 2008.

[109] D. Yao, G. Zhang, and Baowen Li. A universal expression of band gap for silicon nanowires of different cross-section geometries. *Nano Letters*, 8(12):4557–4561, 2008.

[110] Yi Cui, L. J. Lauhon, M. S. Gudiksen, Jianfang Wang, and C. M. Lieber. Diameter-controlled synthesis of single-crystal silicon nanowires. *Applied Physics Letters*, 78(15):2214–2216, 2001.

[111] D. D. D. Ma, C. S. Lee, F. C. K. Au, S. Y. Tong, and S. T. Lee. Small-diameter silicon nanowire surfaces. *Science*, 299:1874–1877, 2003.

[112] Y. J. Chabal and K. Raghavachari. New ordered structure for the H-saturated Si(100) surface: The (3×1) phase. *Phys. Rev. Lett.*, 54(10):1055–1058, 1985.

[113] J. E. Northrup. Structure of Si(100)H: Dependence on the H chemical potential. *Phys. Rev. B*, 44(3):1419–1422, 1991.

[114] A. D. Zdetsis, C. S. Garoufalis, M. S. Skaperda, and E N Koukaras. Variation and adjustment of the optical gap of small Si nanocrystals by partial substitution of Si with Ge. *Journal of Physics: Conference Series*, 10:101–104, 2005.

[115] M. S. Hybertsen and S. G. Louie. First-principles theory of quasiparticles: Calculation of band gaps in semiconductors and insulators. *Phys. Rev. Lett.*, 55(13):1418–1421, 1985.

[116] A. Puzder, A. J. Williamson, J. Grossman, and G. Galli. Surface control of optical properties in silicon nanoclusters. *Journal of Chemical Physics*, 117(14), 2002.

[117] L. Mitas, J. Therrien, R. Twesten, G. Belomoin, and M. H. Nayfeh. Effect of surface reconstruction on the structural prototypes of ultrasmall ultrabright Si_29 nanoparticles. *Applied Physics Letters*, 78(13):1918–1920, 2001.

[118] M. H. Nayfeh, N. Rigakis, and Z. Yamani. Photoexcitation of Si-Si surface states in nanocrystallites. *Phys. Rev. B*, 56(4):2079–2084, 1997.

[119] E. W. Draeger, J. C. Grossman, A. J. Williamson, and G. Galli. Influence of synthesis conditions on the structural and optical properties of passivated silicon nanoclusters. *Phys. Rev. Lett.*, 90(16):167402, 2003.

[120] A. Puzder, A. J. Williamson, F. A. Reboredo, and G. Galli. Structural stability and optical properties of nanomaterials with reconstructed surfaces. *Phys. Rev. Lett.*, 91(15):157405, 2003.

[121] F. Buda, J. Kohanoff, and M. Parrinello. Optical properties of porous silicon: A first-principles study. *Phys. Rev. Lett.*, 69(8):1272–1275, 1992.

[122] A. J. Read, R. J. Needs, K. J. Nash, L. T. Canham, P. D. J. Calcott, and A. Qteish. First-principles calculations of the electronic properties of silicon quantum wires. *Phys. Rev. Lett.*, 69(8):1232–1235, 1992.

[123] Accelrys. *Materials Studio*. Inc, Accelrys Software, ©2001-2007.

[124] D. Sundholm. First principles calculations of the absorption spectrum of Si_29H_36. *Nano Letters*, 3(6):847–849, 2003.

[125] C.-K. Skylaris and P. D. Haynes. Achieving plane wave accuracy in linear-scaling density functional theory applied to periodic systems: A case study on crystalline silicon. *Journal of Chemical Physics*, 127(16):164712, 2007.

[126] A. Puzder, A. J. Williamson, J. C. Grossman, and G. Galli. Computational studies of the optical emission of silicon nanocrystals. *Journal of the American Chemical Society*, 125(9):2786–2791, 2003.

[127] B-C. Wang, Y-M. Chou, J-P. Deng, and Y-T. Dung. Structural and optical properties of passivated silicon nanoclusters with different shapes: A theoretical investigation. *The Journal of Physical Chemistry A*, 112(28):6351–6357, 2008.

[128] O. Lehtonen and D. Sundholm. Coupled-cluster studies of the electronic excitation spectra of silanes. *The Journal of Chemical Physics*, 125(14):144314, 2006.

[129] M. Nolan, S. O'Callaghan, G. Fagas, J. C. Greer, and Th. Frauenheim. Silicon nanowire band gap modification. *Nano Letters*, 7(1):34–38, 2007.

[130] T-L. Chan, C. V. Ciobanu, F-C. Chuang, Ning Lu, C-Z. Wang, and K-M. Ho. Magic structures of H-passivated [110] silicon nanowires. *Nano Letters*, 6(2):277–281, 2006.

[131] N. Ming, Guangfu L., Jing L., Lin L., Lu W., Mingwei J., Wei S., Zhengxiang G., Guangping L., N. M. Wang, and Y. Dapeng. First-principles study of hydrogen-passivated single-crystalline silicon nanotubes: electronic and optical properties. *Nanotechnology*, 18(505707), 2007.

[132] M-F. Ng, L. Zhou, S-W. Yang, L. Y. Sim, V. B. C. Tan, and P. Wu. Theoretical investigation of silicon nanowires: Methodology, geometry, surface modification, and electrical conductivity using a multiscale approach. *Phys. Rev. B (Cond. Mat. and Mat. Phys.)*, 76(15):155435, 2007.

[133] A. M. Saitta, F. Buda, G. Fiumara, and P. V. Giaquinta. Ab initio molecular-dynamics study of electronic and optical properties of silicon quantum wires: Orientational effects. *Phys. Rev. B*, 53(3):1446–1451, 1996.

[134] F. Baletto and R. Ferrando. Strucural properties of nanoclusters: Energetic, thermodynamic and kinetic effects. *Rev. Mod. Phys.*, 77:371, 2005.

[135] R. Ferrando, J. Jellinek, and R. L. Johnston. Nanoalloys: From theory to applications of alloy clusters and nanoparticles. *Chem. Rev.*, 108(3):845, 2008.

[136] F. W. Lytle, D. E. Sayers, and E. A. Stern. Extended x-ray-absorption fine-structure technique. II. Experimental practice and selected results. *Phys. Rev. B*, 11(12):4825–4835, 1975.

[137] P. A. O'Day, J. J. Rehr, S. I. Zabinsky, and G. E. Jr. Brown. Extended x-ray absorption fine structure (EXAFS) analysis of disorder and multiple-scattering in complex crystalline solids. *Journal of the American Chemical Society*, 116(7):2938–2949, 1994.

[138] Marie-Christine Daniel and Didier Astruc. Gold nanoparticles: Assembly, supramolecular chemistry, quantum-size-related properties, and applications toward biology, catalysis, and nanotechnology. *Chemical Reviews*, 104(1):293–346, 2004. PMID: 14719978.

[139] K. J. Klabunde, Yong Xi Li, and Beng Jit Tan. Solvated metal atom dispersed catalysts. *Chemistry of Materials*, 3(1):30–39, 1991.

[140] M. P. Casaletto, A. Longo, A. M. Venezia, A. Martorana, and A. Prestianni. Metal-support and preparation influence on the structural and electronic properties of gold catalysts. *Applied Catalysis A: General*, 302(2):309–316, 2006.

[141] C. Bealing, G. Fugallo, R. Martonak, and C. Molteni. Constant pressure molecular dynamics simulations for ellipsoidal, cylindrical and cuboidal nano-

objects based on inertia tensor information. *Phys. Chem. Chem. Phys.*, 12:8542–8550, 2010.

[142] J. M. Soler, M. R. Beltrán, K. Michaelian, I. L. Garzón, P. Ordejón, D. Sánchez-Portal, and E. Artacho. Metallic bonding and cluster structure. *Phys. Rev. B*, 61(8):5771–5780, 2000.

[143] P. J. Merkling, A. Muñoz-Páez, and E. Sánchez Marcos. Exploring the capabilities of x-ray absorption spectroscopy for determining the structure of electrolyte solutions: Computed spectra for Cr^{3+} or Rh^{3+} in water based on molecular dynamics. *J. Am. Chem. Soc.*, 124(36):10911–10920, 2002.

[144] O. M. Roscioni, P. D'Angelo, G. Chillemi, S. D. Longa, and M. Benfatto. Quantitative analysis of xanes spectra of disordered systems based on molecular dynamics. *J. Synchrotron Rad.*, 12:75–79, 2005.

[145] P. D'Angelo, O. M. Roscioni, G. Chillemi, S. Della Longa, and M. Benfatto. Detection of second hydration shells in ionic solutions by XANES: Computed spectra for Ni^{2+} in water based on molecular dynamics. *J. Am. Chem. Soc.*, 128(6):1853–1858, 2006.

[146] F. Carrera, F. Torrico, D. T. Richens, A. Muñoz-Páez, José M. Martínez, R. R. Pappalardo, and E. Sánchez Marcos. Combined experimental and theoretical approach to the study of structure and dynamics of the most inert aqua ion [ir(h2o)6]3+ in aqueous solution. *J. Phys. Chem. B*, 111(28):8223–8233, 2007.

[147] P. D'Angelo, V. Migliorati, G. Mancini, and G. Chillemi. A coupled molecular dynamics and XANES data analysis investigation of aqueous cadmium(ii). *J. Phys. Chem. A*, 112(46):11833–11841, 2008.

[148] P. D'Angelo, A. Zitolo, V. Migliorati, G. Mancini, I. Persson, and G. Chillemi. Structural investigation of lanthanoid coordination: a combined XANES and molecular dynamics study. *Inorg. Chem.*, 48(21):10239–10248, 2009.

[149] E. C. Beret, K. Provost, D. Müller, and E. Sànchez Marcos. Coupling CP-MD simulations and x-ray absorption spectroscopy: Exploring the structure of oxaliplatin in aqueous solution. *J. Phys. Chem. B*, 113(36):12343–12352, 2009.

[150] B. Ravel. A practical introduction to multiple scattering theory. *Journal of Alloys and Compounds*, 401:118–126, 2005.

[151] W. J. Huang, R. Sun, J. Tao, L. D. Menard, R. G. Nuzzo, and J. M. Zuo. Coordination-dependent surface atomic contraction in nanocrystals revealed by coherent diffraction. *Nature Mater.*, 7(4):308–313, 2008.

[152] A. Yevick and A. I. Frenkel. Effects of surface disorder on EXAFS modeling of metallic clusters. *Phys. Rev. B*, 81(11):115451, 2010.

[153] A. P. Sutton and J. Chen. Long-range Finnis-Sinclair potentials. *Phil. Mag. Lett.*, 61(3):139–146, 1990.

[154] H. Rafii-Tabar and A. P. Sutton. Long-range Finnis-Sinclair potentials for f.c.c. metallic alloys. *Phil. Mag. Lett.*, 63(4):217–224, 1991.

[155] L. D. Rampino and F. F. Nord. Preparation of palladium and platinum synthetic high polymer catalysts and the relationship between particle size and rate of hydrogenation. *Journal of the American Chemical Society*, 63(10):2745–2749, 1941.

[156] G. Dalba and P. Fornasini. EXAFS Debye–Waller factor and thermal vibrations of crystals. *Journal of Synchrotron Radiation*, 4(4):243–255, 1997.

[157] M. R. Martin and G. A. Somorjai. Determination of the surface geometry for the aluminum (110) and (111) surfaces by comparison of low-energy-electron-diffraction calculations with experiment. *Phys. Rev. B*, 7(8):3607–3615, 1973.

[158] R. B. Greegor and F. W. Lytle. Morphology of supported metal clusters: Determination by EXAFS and chemisorption. *Journal of Catalysis*, 63(2):476–486, 1980.

[159] A. I. Frenkel. Solving the 3D structure of metal nanoparticles. *Zeitschrift für Kristallographie*, 222(11):605–611, 2007.

[160] J.M. Montejano-Carrizales, F. Aguilera-Granja, and J.L. Moran-Lopez. Direct enumeration of the geometrical characteristics of clusters. *Nanostructured Materials*, 8(3):269–287, 1997.

[161] Y. Okamoto. XAFS simulation of highly disordered materials. *Nuclear Instruments and Methods in Physics Research Section A: Accelerators, Spectrometers, Detectors and Associated Equipment*, 526(3):572–583, 2004.

[162] B. Gilbert, H. Zhang, F. Huang, J. F. Banfield, Y. Ren, D. Haskel, J. C. Lang, G. Srajer, A. Jürgensen, and G. A. Waychunas. Analysis and simulation of the structure of nanoparticles that undergo a surface-driven structural transformation. *The Journal of Chemical Physics*, 120(24):11785–11795, 2004.

[163] B. S. Clausen, L. Grabaek, H. Topsoe, L. B. Hansen, P. Stoltze, J. K. Norskov, and O. H. Nielsen. A new procedure for particle size determination by EXAFS based on molecular dynamics simulations. *Journal of Catalysis*, 141(2):368–379, 1993.

[164] B.S. Clausen, H. Topsøe, L.B. Hansen, P. Stoltze, and J.K. Nørskov. Determination of metal particle sizes from EXAFS. *Catalysis Today*, 21(1):49–55, 1994.

[165] M. Bauer and H. Bertagnolli. The amplitude reduction factor and the cumulant expansion method: Crucial factors in the structural analysis of alkoxide precursors in solution. *The Journal of Physical Chemistry B*, 111(49):13756–13764, 2007. PMID: 18020443.

[166] G. Bunker. Application of the ratio method of EXAFS analysis to disordered systems. *Nuclear Instruments and Methods in Physics Research*, 207(3):437–444, 1983.

[167] P. Eisenberger and G. S. Brown. The study of disordered systems by EXAFS: Limitations. *Solid State Communications*, 29(6):481–484, 1979.

[168] B. Ravel and M. Newville. *ATHENA*, *ARTEMIS*, *HEPHAESTUS*: data analysis for X-ray absorption spectroscopy using *IFEFFIT*. *Journal of Synchrotron Radiation*, 12(4):537–541, 2005.

[169] M. Newville. *IFEFFIT*: interactive XAFS analysis and *FEFF* fitting. *Journal of Synchrotron Radiation*, 8(2):322–324, Mar 2001.

[170] J. J. Rehr and R. C. Albers. Theoretical approaches to x-ray absorption fine structure. *Rev. Mod. Phys.*, 72(3):621–654, Jul 2000.

[171] D. J. Watson and G. A. Attard. Surface segregation and reconstructive behaviour of the (1 0 0) and (1 1 0) surfaces of platinum-palladium bulk alloy single crystals: A voltammetric and leed/aes study. *Surface Science*, 515(1):87–93, 2002.

[172] A. J. Renouprez, J. L. Rousset, A. M. Cadrot, Y. Soldo, and L. Stievano. Structure and catalytic activity of palladium-platinum aggregates obtained by laser vaporisation of bulk alloys. *Journal of Alloys and Compounds*, 328(1-2):50–56, 2001.

[173] J. L. Rousset, L. Stievano, F. J. Cadete Santos Aires, C. Geantet, A. J. Renouprez, and M. Pellarin. Hydrogenation of tetralin in the presence of sulfur over γ-Al_2O_3-supported Pt, Pd, and Pd-Pt model catalysts. *Journal of Catalysis*, 202(1):163–168, 2001.

[174] L. Fiermans, R. De Gryse, G. De Doncker, P. A. Jacobs, and J. A. Martens. Pd segregation to the surface of bimetallic Pt-Pd particles supported on H-β zeolite evidenced with x-ray photoelectron spectroscopy and argon cation bombardment. *Journal of Catalysis*, 193(1):108–114, 2000.

[175] N. Toshima, M. Harada, T. Yonezawa, K. Kushihashi, and K. Asakura. Structural analysis of polymer-protected palladium/platinum bimetallic clusters as dispersed catalysts by using extended x-ray absorption fine structure spectroscopy. *The Journal of Physical Chemistry*, 95(19):7448–7453, 1991.

[176] N. Toshima, T. Yonezawa, and K. Kushihashi. Polymer-protected palladium-platinum bimetallic clusters: preparation, catalytic properties and structural considerations. *J. Chem. Soc., Faraday Trans.*, 89:2537–2543, 1993.

[177] Y. Wang and N. Toshima. Preparation of PdPt bimetallic colloids with controllable core/shell structures. *The Journal of Physical Chemistry B*, 101(27):5301–5306, 1997.

[178] L. O. Paz-Borbón, R. L. Johnston, G. Barcaro, and A. Fortunelli. A mixed structural motif in 34-atom Pd-Pt clusters. *The Journal of Physical Chemistry C*, 111(7):2936–2941, 2007.

[179] Y. Y. Tong, T. Yonezawa, N. Toshima, and J. J. van der Klink. Pt NMR of polymer-protected Pt/Pd bimetallic catalysts. *The Journal of Physical Chemistry*, 100(2):730–733, 1996.

[180] N. Toshima and Y. Wang. Preparation and catalysis of novel colloidal dispersions of copper/noble metal bimetallic clusters. *Langmuir*, 10(12):4574–4580, 1994.

[181] C. U. I. Odenbrand, J. Blanco, P. Avila, and C. Knapp. Lean NOx reduction in real diesel exhaust with copper and platinum titania based monolithic catalysts. *Applied Catalysis B: Environmental*, 23(1):37–44, 1999.

[182] Shenghu Zhou, Bindhu Varughese, Bryan Eichhorn, Greg Jackson, and Kevin McIlwrath. Pt–Cu core–shell and alloy nanoparticles for heterogeneous NOx reduction: Anomalous stability and reactivity of a core–shell nanostructure. *Angewandte Chemie International Edition*, 44(29):4539–4543, 2005.

[183] C. Massen, T. V. Mortimer-Jones, and R. L. Johnston. Geometries and segregation properties of platinum-palladium nanoalloy clusters. *J. Chem. Soc., Dalton Trans.*, pages 4375–4388, 2002.

[184] L. D. Lloyd, R. L. Johnston, S. Salhi, and N. T. Wilson. Theoretical investigation of isomer stability in platinum-palladium nanoalloy clusters. *J. Mater. Chem.*, 14:1691–1704, 2004.

[185] D. Cheng, S. Huang, and W. Wang. Structures of small Pd-Pt bimetallic clusters by Monte Carlo simulation. *Chemical Physics*, 330(3):423–430, 2006.

[186] G. Rossi, R. Ferrando, A. Rapallo, A. Fortunelli, B. C. Curley, and R. L. Johnston. Global optimization of bimetallic cluster structures. II. Size-matched Ag-Pd, Ag-Au, and Pd-Pt systems. *The Journal of Chemical Physics*, 122(19):194309, 2005.

[187] E. Fernandez, P. Balbas, L. Perez, K. Michaelian, and I. Garzon. Structural properties of bimetallic clusters from density functional theory calculations. *International Journal of Modern Physics B*, 19(15-17):2339–2344, 2005.

[188] J. Wang, J. Jellinek, J. Zhao, Z. Chen, R. B. King, and P. von Ragué Schleyer. Hollow cages versus space-filling structures for medium-sized gold clusters: The spherical aromaticity of the Au_50 cage. *The Journal of Physical Chemistry A*, 109(41):9265–9269, 2005. PMID: 16833267.

[189] B. Assadollahzadeh and P. Schwerdtfeger. A systematic search for minimum structures of small gold clusters Au_*n* (n = 2–20) and their electronic properties. *The Journal of Chemical Physics*, 131(6):064306, 2009.

[190] K. Michaelian, N. Rendón, and I. L. Garzón. Structure and energetics of Ni, Ag, and Au nanoclusters. *Phys. Rev. B*, 60(3):2000–2010, Jul 1999.

[191] I. L. Garzón, K. Michaelian, M. R. Beltrán, A. Posada-Amarillas, P. Ordejón, E. Artacho, D. Sánchez-Portal, and J. M. Soler. Lowest energy structures of gold nanoclusters. *Phys. Rev. Lett.*, 81(8):1600–1603, Aug 1998.

[192] Gunter Schmid, Monika Baumle, Marcus Geerkens, Ingo Heim, Christoph Osemann, and Thomas Sawitowski. Current and future applications of nanoclusters. *Chem. Soc. Rev.*, 28:179–185, 1999.

[193] R. P. Gupta. Lattice relaxation at a metal surface. *Phys. Rev. B*, 23(12):6265–6270, 1981.

[194] F. Ercolessi, W. Andreoni, and E. Tosatti. Melting of small gold particles: Mechanism and size effects. *Phys. Rev. Lett.*, 66(7):911–914, 1991.

[195] S. H Yang, D. A. Drabold, J. B. Adams, P. Ordejón, and K. Glassford. Density functional studies of small platinum clusters. *Journal of Physics: Condensed Matter*, 9(5):L39, 1997.

[196] M. Giersig and P. Mulvaney. Preparation of ordered colloid monolayers by electrophoretic deposition. *Langmuir*, 9(12):3408–3413, 1993.

[197] J. Turkevich, P. C. Stevenson, and J. Hillier. A study of the nucleation and growth processes in the synthesis of colloidal gold. *Discussions Of The Faraday Society*, 11(c):55, 1951.

[198] G. Frens. Controlled nucleation for the regulation of the particle size in monodisperse gold suspensions. *Nature Physical Science*, 241:20–22, 1973.

[199] M. Brust, J. Fink, D. Bethell, D. J. Schiffrin, and C. Kiely. Synthesis and reactions of functionalised gold nanoparticles. *J. Chem. Soc., Chem. Commun.*, 16:1655–1656, 1995.

[200] C. A. Waters, A. J. Mills, K. A. Johnson, and D. J. Schiffrin. Purification of dodecanethiol derivatised gold nanoparticles. *Chem. Commun.*, pages 540–541, 2003.

[201] M. Brust, M. Walker, D. Bethell, D. J. Schiffrin, and R. Whyman. Synthesis of thiol-derivatised gold nanoparticles in a two-phase liquid-liquid system. *J. Chem. Soc. Chem. Commun.*, 7:801–802, 1994.

[202] W. D. Luedtke and U. Landman. Structure, dynamics, and thermodynamics of passivated gold nanocrystallites and their assemblies. *The Journal of Physical Chemistry*, 100(32):13323–13329, 1996.

[203] W. D. Luedtke and U. Landman. Structure and thermodynamics of self-assembled monolayers on gold nanocrystallites. *The Journal of Physical Chemistry B*, 102(34):6566–6572, 1998.

[204] Ta-Wei Li, Ito Chao, and Yu-Tai Tao. Relationship between packing structure and headgroups of self-assembled monolayers on Au(111): Bridging experimental observations through computer simulations. *The Journal of Physical Chemistry B*, 102(16):2935–2946, 1998.

[205] S. L. Mayo, B. D. Olafson, and W. A. Goddard. DREIDING: a generic force field for molecular simulations. *The Journal of Physical Chemistry*, 94(26):8897–8909, 1990.

[206] L. Zhang, T. Lu, G. W. Gokel, and A. E. Kaifer. Mixed monolayers formed by the self-assembly on gold of thiol-functionalized anthraquinones and 1-alkanethiols. *Langmuir*, 9(3):786–791, 1993.

[207] H. Häkkinen, R. N. Barnett, and U. Landman. Electronic structure of passivated Au_38(SCH_3)_24 nanocrystal. *Phys. Rev. Lett.*, 82(16):3264–3267, Apr 1999.

[208] J. Akola, M. Walter, R. L. Whetten, H. Häkkinen, and H. Grönbeck. On the structure of thiolate-protected Au_25. *Journal of the American Chemical Society*, 130(12):3756–3757, 2008.

[209] W. Andreoni, A. Curioni, and H. Grönbeck. Density functional theory approach to thiols and disulfides on gold: Au(111) surface and clusters. *International Journal of Quantum Chemistry*, 80(4-5):598–608, 2000.

[210] R. G. Nuzzo, B. R. Zegarski, and L. H. Dubois. Fundamental studies of the chemisorption of organosulfur compounds on gold(111). implications for molecular self-assembly on gold surfaces. *Journal of the American Chemical Society*, 109(3):733–740, 1987.

[211] H. Grönbeck, A. Curioni, and W. Andreoni. Thiols and disulfides on the Au(111) surface: The headgroupgold interaction. *Journal of the American Chemical Society*, 122(16):3839–3842, 2000.

[212] O. M. Roscioni. *A computational study of supported rhodium catalysts*. PhD thesis, Chemistry, University of Southampton, 2010.

[213] H. Yasuda and H. Mori. Effect of cluster size on the chemical ordering in nanometer-sized Au-75at%Cu alloy clusters. *Zeitschrift für Physik D Atoms, Molecules and Clusters*, 37:181–186, 1996. 10.1007/s004600050026.

[214] H. Yasuda and H. Mori. Cluster-size dependence of alloying behavior in gold clusters. *Zeitschrift für Physik D Atoms, Molecules and Clusters*, 31:131–134, 1994. 10.1007/BF01426588.

[215] A. K. Sra and R. E. Schaak. Synthesis of atomically ordered AuCu and AuCu3 nanocrystals from bimetallic nanoparticle precursors. *Journal of the American Chemical Society*, 126(21):6667–6672, 2004.

[216] Raymond E. Schaak, Amandeep K. Sra, Brian M. Leonard, Robert E. Cable, John C. Bauer, Yi-Fan Han, Joel Means, Winfried Teizer, Yolanda Vasquez, and

Edward S. Funck. Metallurgy in a beaker: Nanoparticle toolkit for the rapid low-temperature solution synthesis of functional multimetallic solid-state materials. *Journal of the American Chemical Society*, 127(10):3506–3515, 2005. PMID: 15755172.

[217] M. J. López, P. A. Marcos, and J. A. Alonso. Structural and dynamical properties of Cu–Au bimetallic clusters. *The Journal of Chemical Physics*, 104(3):1056–1066, 1996.

[218] B. Pauwels, G. Van Tendeloo, E. Zhurkin, M. Hou, G. Verschoren, L. Theil Kuhn, W. Bouwen, and P. Lievens. Transmission electron microscopy and monte carlo simulations of ordering in au-cu clusters produced in a laser vaporization source. *Phys. Rev. B*, 63(16):165406, Mar 2001.

[219] R. A. Lordeiro, F. F. Guimarães, J. C. Belchior, and R. L. Johnston. Determination of main structural compositions of nanoalloy clusters of Cu_xAu_y (x + y $\leq$ 30) using a genetic algorithm approach. *International Journal of Quantum Chemistry*, 95(2):112–125, 2003.

[220] S. Darby, T. V. Mortimer-Jones, R. L. Johnston, and C. Roberts. Theoretical study of Cu–Au nanoalloy clusters using a genetic algorithm. *The Journal of Chemical Physics*, 116(4):1536–1550, 2002.

[221] A. Rapallo, G. Rossi, R. Ferrando, A. Fortunelli, B. C. Curley, L. D. Lloyd, G. M. Tarbuck, and R. L. Johnston. Global optimization of bimetallic cluster structures. I. size-mismatched Ag–Cu, Ag–Ni, and Au–Cu systems. *The Journal of Chemical Physics*, 122(19):194308, 2005.

[222] P. J. Hsu and S. K. Lai. Structures of bimetallic clusters. *The Journal of Chemical Physics*, 124(4):044711, 2006.

[223] J. L. Rodríguez-López, J. M. Montejano-Carrizales, U. Pal, J. F. Sánchez-Ramírez, H. E. Troiani, D. García, M. Miki-Yoshida, and M. José-Yacamán.

Surface reconstruction and decahedral structure of bimetallic nanoparticles. *Phys. Rev. Lett.*, 92(19):196102, May 2004.

[224] N. T. Wilson and R. L. Johnston. A theoretical study of atom ordering in copper-gold nanoalloy clusters. *J. Mater. Chem.*, 12:2913–2922, 2002.